Characteristics of Earth's magnetopause from Cluster measurements

Adrian Blăgău

Dissertation
an der Fakultät für Geowissenschaften
der Ludwig–Maximilians–Universität
München

vorgelegt von
Adrian Blăgău
aus Arad, Rumänien

München, den 1. Oktober 2007

Erstgutachter: Prof. Dr. Manfred Scholer
Zweitgutachter: Prof. Dr. Rudolf Treumann
Tag der mündlichen Prüfung: 5. Dezember 2007

Părinţilor mei şi Macăi

Contents

Zusammenfassung **ix**

Summary **xv**

1 Introduction **1**
1.1 The magnetopause 1
1.2 The magnetic reconnection process 8

2 Satellite and instruments **15**
2.1 The Cluster mission 15
2.2 The satellite payload 16
The CIS instrument 16
The FGM instrument 18
The EFW instrument 19
Other Cluster instruments 20

3 A new technique for determining orientation and motion of a non-planar magnetopause **25**
3.1 The timing analysis procedure in the planar case 25
Procedure for obtaining the timing information 27
Arguments for the constant thickness approach 28
3.2 The timing method for a 2-D, non-planar magnetopause 28
The parabolic layer model 29
The cylindrical layer model 30
Optimizing the timing procedure for a 2-D magnetopause 31
3.3 Presentation of the test case 32
3.4 Obtaining the input parameters 38
A case of non-planar magnetopause. Finding the unit vector $\vec{l}$ 38
Obtaining the timing information 43

4 Results for the 24 June 2003 magnetopause crossing: comparison of different methods **47**
4.1 Results from the planar timing technique . . . 47
4.2 Solutions from the 2-D timing technique . . . 51
Finding solutions in the cylindrical model . . . 51
Stability of the solutions . . . 52
4.3 Comparison with planar, single spacecraft techniques . . . 52
4.3.1 Minimum variance analysis of the magnetic field . . . 53
4.3.2 Minimum Faraday residue method . . . 56
Determining the electric field vector . . . 56
Results from the planar MFR technique . . . 58
Faraday residues in the planar and 2-D, non-planar method . . . 60
4.3.3 DeHoffmann-Teller analysis . . . 61
4.4 Comments and discussions . . . 63
Discusions of the solutions . . . 63
Comparison with the planar methods . . . 68
The nature of the 2-D MP feature . . . 71
What is the best 2-D solution? . . . 72
4.5 Relation between the current work and previous approaches . . . 73

5 Observation of magnetic reconnection at the magnetopause **77**
5.1 Jump relations for a rotational discontinuity . . . 77
5.2 Practical issues in the identification of a rotational discontinuity . . . 80
5.3 Overview on the 14 March 2002 event . . . 84
General conditions . . . 84
Inferring the magnetopause thickness. . . . 90
5.4 Analysis of the event from 14 March 2002 . . . 91
The non-constancy of $\rho(1-\alpha)$ in experimental data. . . . 95
The contribution of the current density in the Walén relation. . . . 97
5.5 Overview on the 26 January 2001 event . . . 101
General conditions . . . 101
The favourable circumstances of the 26 January 2001 event. . . . 104
Inferring the magnetopause thickness. . . . 106
5.6 Oxygen influence on the Walén test . . . 110
The magnetopause transition around 10:43:30 . . . 111
The magnetopause transition around 11:03:00 . . . 114
Interpretation of the results . . . 115
5.7 Observations about the Oxygen at the magnetopause . . . 119

6 Conclusions **125**

Appendices

A Minimum variance analysis **133**

B Timing methods **137**
B.1 Timing analysis in the planar model 139
B.2 The parabolic layer model 142
B.2.1 Plain timing analysis 142
B.2.2 Combined analysis 146
B.3 The cylindrical layer model 149
B.3.1 Plain timing analysis 150
B.3.2 Combined analysis 155
B.4 Geometrical and dynamical parameters of the solutions 155
B.4.1 Parabolic layer case 156
B.4.2 Cylindrical layer case 160
B.5 Combining MVAB with the timing analysis 161

C Solutions for the 2-D magnetopause **163**
C.1 Tables and figures description 163
C.2 Solutions from the parabolic model 166
C.3 Solutions from the cylindrical model 172

D Stability of the 2-D solutions **183**

E Magnetic variance in the planar and 2-D, non-planar methods **189**

F The deHoffmann-Teller analysis **197**

G The Minimum Faraday Residue technique **199**

H Computing the ion single - fluid moments **203**

Bibliography **207**

Credits **215**

Acknowledgements **217**

Lebenslauf **219**

Zusammenfassung

Charakteristik der Erdmagnetopause anhand von Messungen mit Cluster

Das Thema dieser Arbeit ist die terrestrische Magnetopause, eine Diskontinuität, welche die Grenzschicht zwischen dem vom Erdmagnetfeld kontrollierten Plasma und dem mit Überschallgeschwindigkeit gegen das Erdmagnefeld anströmenden Plasma der Sonne bildet, dem sogenannten Sonnenwind. Wir interessieren uns sowohl für die Bestimmung der makroskopischen Eigenschaften dieser Diskontinuität (wie für ihre Form, Orientierung, Bewegung und Dicke), als auch für die physikalischen Phänomene, die in ihrer Umgebung stattfinden. Wir haben diese Studie durchgeführt, indem wir in-situ Messungen der verschiedenen Plasmaparameter analysiert und interpretiert haben. Die Daten wurden mit den Satelliten der Cluster-Mission der Europäischen Weltraumbehörde (ESA) während der Durchquerungen der Magnetopause genommen.

Nahezu alle Methoden, die zur Ableitung der Parameter eines Magnetopausendurchganges benutzt werden, beruhen zum einen auf der Annahme einer ebenen Geometrie, zum anderen nehmen sie an, dass alle physikalischen Größen sich nur entlang der Normalenrichtung ändern. Wir können diese Methoden in zwei Kategorien unterteilen. Auf der einen Seite stehen die Methoden, die sich nur auf Daten eines einzelnen Satelliten stützen und auf der Gültigkeit von verschiedenen Erhaltungsgesetzen basieren. Die Minimum-Varianz-Analyse des magnetischen Feldes (MVAB) zum Beispiel basiert auf dem Nichtvorhandensein von magnetischen Monopolen, was die Konstanz der Magnetfeldkomponente entlang der Normalenrichtung zur Folge hat. Somit ergibt sich bei dieser Methode die Normalenrichtung als die jenige Richtung, entlang der die Variationen des Magnetfeldes am kleinsten sind. Eine weitere planare Methode ist die Minimum Faraday Residue (MFR) Methode, die auf der Erhaltung des magnetischen Flusses beruht. In diesem Fall wird zusätzlich zur Richtung die als konstant angenommene Geschwindigkeit entlang dieser Richtung bestimmt, so daß die Variation der Komponente des elektrischen Feldes tangential zu dieser Richtung (das sogenannte Faraday Residuum) minimalisiert wird. Im Unterschied zu diesen Methoden profitiert man bei der Cluster-Mission zum ersten Mal von korrelierten Messungen, die gleichzeitig an vier Punkten im Raum vorgenommen werden. Aus der Kenntnis der Satellitenpositionen und der Zeiten, zu denen die Satelliten die Erdmagnetopause durchqueren, kann man Orientierung, Dicke und Geschwindigkeit des Magnetopausenübergangs unmittelbar bestimmen. Die Vierpunkt-Timing Methode nimmt üblicherweise ebenfalls Planarität an, und bietet damit einen unabhängigen Test der verschiedenen Einzelsatelliten-Methoden.

In dieser Arbeit haben wir die Vierpunkt-Timing Methode weiterentwickelt, um damit realistischere Situationen behandeln zu können, bei denen sich die Magnetopause auf der Größenskala des Satellitenabstandes wie eine zweidimensionale, nichtplanare Diskontinuität verhält. Eine solche Konfiguration kann durch lokale Ein- bzw. Ausbuchtungen der Magnetopause verursacht werden, oder sie wird durch eine Oberflächenwelle mit großer Amplitude hervorgerufen, die sich entlang der Magnetopause ausbreitet. Die neue Methode ist in solchen Fällen anwendbar, wenn die Einzelsatelliten-Methoden an verschiedenen Orten unterschiedliche Normalenrichtungen für die Magnetopause ergeben, alle Normalen aber näherungsweise in einer gemeinsamen Ebene liegen, die wir als *Ebene der Normalen* bezeichnen. Wir haben in solchen Fällen die Magnetopause lokal durch eine parabolische bzw. zylindrische Form modelliert. In beiden Fällen haben wir angenommen, dass die Diskontinuität eine konstante Dicke besitzt und sich ihre Form senkrecht zur *Ebene der Normalen* nicht ändert. In dieser Ebene ordnen wir der Schicht eine einheitliche Bewegung oder eine Bewegung entlang zweier zueinander senkrechter Richtungen zu. Mit einem derartigen Modell können wir zwei Eigenheiten der nichtplanaren Magnetopause beschreiben: ihre Bewegung entlang der Normalenrichtung und, indem wir einen zweiten Freiheitsgrad zulassen, die großskaligen Wellen, die häufig entlang der Magnetopausenoberfläche laufen.

Mathematisch ergibt sich bei jeder der Implementierungen des Modells (parabolische oder zirkulare Geometrie, ein oder zwei Freiheitsgrade in der Bewegung der Magnetopause) ein System von acht gekoppelten Gleichungen. Diese Gleichungen entsprechen den Bedingungen, dass die inneren und äußeren Begrenzungen der Magnetopause mit den Satellitenpositionen übereinstimmen, so wie sie sich aus den Timing-Informationen der Daten ergeben. Die zu bestimmenden Unbekannten sind die Bewegungsrichtung der Magnetopause, die räumliche Skala der Gesamtstruktur, die Magnetopausendicke, die anfängliche Position der Struktur, sowie drei Koeffizienten, welche die Zeitabhängigkeit der Geschwindigkeit in Form eines Polynoms beschreiben. Im Grunde vertraut diese Vorgehensweise einzig auf die Timing-Information, und deswegen haben wir sie als *einfache Timing Analyse* bezeichnet.

Da in unserem Modell die Richtung der Magnetopausenbewegung vollständig durch einen Winkel in der *Ebene der Normalen* beschrieben wird, haben wir unsere *einfache Timing Analyse* wie folgt verbessert: Wir haben verschiedene Werte für diesen Winkel im Bereich $[-\pi, \pi]$ angenommen, und das Gleichungssystem für diese Winkel gelöst. Für jede Lösung wurde die magnetische Varianz entlang der momentanen (d.h. entlang der geometrischen) Normalen für jeden der Satelliten gesondert berechnen. Danach haben wir diejenige Richtung der Magnetopausenbewegung ausgewählt, für welche die *globale* normale magnetische Varianz ein Minimum ist, wobei wir unter global das gewichtete Mittel über die vier Satelliten verstehen. Die auf diese Weise gefundene Lösung hat zwei Vozüge: erstens bezieht sie die MVAB Methode ein, und zweitens liefert sie eine bessere Beschreibung der Magnetopausenbewegung. Da nämlich der Winkel nun ein Input-Parameter ist, stehen jetzt vier, statt drei Koeffizienten zur Bestimmung der Geschwindigkeits-Zeit-Abhängigkeit der Magnetopause zur Verfügung. Wir haben diese Methode als *kombinierte Timing-MVAB Analyse* bezeichnet.

Die neue Methode wurde auf eine Magnetopausendurchquerung angewendet, bei der die planaren Techniken miteinander unvereinbare Resultate zeigten. Im Gegensatz dazu sind die Lösungen, die mit den unterschiedlichen Implementierungen der neuen zweidimensionalen Methode gewonnen wurden, konsistent und stabil, und ergeben eine konvexe Form der Magnetopause. Aus Sicht der globalen magnetischen Varianz und des globalen Faraday Residuums erweisen sich diese Lösungen als den planaren Lösungen überlegen. Ausserdem sind in den Einzelsatellitentechniken sowohl die individuellen Normalen als auch die Geschwindigkeiten entlang der Normalen bei den vier Satelliten voneinander entkoppelt. Bei der zweidimensiona-

len Methode suchen wir dagegen nach einer globalen Lösung, deshalb sind die Normalenrichtung und die Geschwindigkeit durch die angenommene Geometrie und die ermittelte Bewegung gekoppelt, woraus eine realistischere Beschreibung der Magnetopause resultiert.

Die relativ große Scherung der Plasmaströmung an der Magnetopause und deren Orientierung in Bezug auf die Magnetfeldrichtung deutet auf die Kelvin-Helmholtz Instabilität (welche 'Wind-über-Wasser'-artige Wellen erzeugt) als mögliche Ursache für die von Cluster für diesen Fall gefundene zweidimensionale Form hin. Dieser Mechanismus ist einer der vorgeschlagenen physikalischen Prozesse, um den Transfer von Energie, Impuls und, in seiner nichtlinearen Phase, auch Masse durch die Magnetopause hindurch zu erklären. Mit der in dieser Arbeit entwickelten Methode ist es relativ einfach, die Wellenlänge und Periodizität einer solchen Struktur abzuschätzen. Betrachten wir zum Beispiel das parabolische Modell und erlauben zwei Freiheitsgrade für die Bewegung der Magnetopause, dann ergibt sich für den von uns untersuchten Fall eine Wellenlänge von ~ 8 Erdradien und eine Periode von $\sim 10-11$ Minuten.

Der wichtigste Prozess für den Transfer von Masse, Impuls und Energie ist allerdings die magnetische Rekonnexion. Dieser Prozess konvertiert magnetische Energie in Strömungsenergie und in Heizung und wird verantwortlich gemacht für viele dynamische Vorgänge auf der Sonne, in planetaren Magnetosphären und in vielen astrophysikalischen Objekten wie zum Beispiel magnetischen Sternen und Sternwinden. Die Magnetopause bietet die einzigartige Gelegenheit, dieses Phänomen mit in-situ Messungen zu studieren. Es tritt auf, wenn die Plasmen zu beiden Seiten der Magnetopause, also auf der Magnetosheath- und der Magnetosphärenseite, antiparallele Magnetfeldkomponenten aufweisen. Durch Rekonnexion werden interplanetare und terrestrische Magnetfelder verbunden, das Plasma kann auf diese Weise entlang den miteinander verknüpften Magnetfeldlinien durch die Magnetopause hindurchfließen. Somit ist die Magnetopause in diesem Fälle keine undurchdringliche Barriere mehr.

Im Kontext der Magnetopause sagen alle Modelle der magnetischen Rekonnexion vorher, daß sich an der Grenzfläche eine Rotationsdiskontinuität ausbildet. Um anhand von Satellitendaten festzustellen, ob sich die Magnetopause wie eine Rotationsdiskontinuität verhält, führen wir den sogenannten Walén-Test durch, der die Erhaltung der tangentialen Komponente der Strömungsgeschwindigkeit des Plasmas, des Massenflusses entlang der Normalenrichtung und des tangentialen elektrischen Feldes voraussetzt. Mit diesem Test prüfen wir, ob das Plasma in einem Bezugssystem, in dem die Plasmaströmung überall parallel zum Magnetfeld erfolgt (dem sogenannten deHoffmann-Teller System), mit der lokalen Alfvéngeschwindigkeit fließt. Dies ist eine Bedingung für das Vorhandensein einer Rotationsdiskontinuität. Während der Walén-Test sich als sehr erfolgreich bei der Identifizierung der Magnetopause als Rotationsdiskontinuität erwiesen hat, bleibt als ein wunder Punkt, dass der Proportionalitätsfaktor zwischen der Plasmageschwindigkeit im deHoffmann-Teller System und der Alfvéngeschwindigkeit meist unter dem idealen Wert von eins liegt, der von der Theorie gefordert wird. Diese Diskrepanz könnte ihre Ursache in den vereinfachenden Annahmen haben, die der Walén-Analyse zugrunde liegen.

Eine dieser Annahmen bezieht sich auf die Rolle der Elektronen in der Analyse, die üblicherweise wegen der geringen Masse der Elektronen vernachlässigt wird. Gleichzeitig ist es aber schwierig, einen Beweis für einen Beitrag der Elektronen zu liefern, weil Elektronenmessungen durch das Auftreten von Photoelektronen beeinflußt werden, die durch auf die Oberfläche des Satelliten auftreffende Sonnenstrahlung erzeugt werden, und weil deren Strömungsgeschwindigkeit viel kleiner als ihre thermische Geschwindigkeit ist. Eine zweite vereinfachende Annahme, die allgemein gemacht wird, ist, alle Ionen als Protonen anzunehmen, eine Näherung, die durch den hohen relativen Anteil von Protonen an den Ionen einigermaßen gerechtfertigt wird. Wie im Fall der Elektronen, so ist auch die Messung der weniger häufig vorkommenden Ionensorten, sofern sie vorhanden sind, mit derzeitigen Satelliteninstrumenten eine experimentelle Heraus-

forderung. In Verbindung mit diesen Problemen haben wir zwei Magnetopausendurchgänge untersucht, bei denen wir Hinweise gefunden haben, daß die Grenzfläche sich wie eine planare, zeitunabhängige Rotationsdiskontinuität verhielt. Die magnetohydrodynamische Behandlung war in beiden Fällen gerechtfertigt, da die Magnetopausendicke sich als viel größer als der Ionengyroradius und die Ioneninertiallänge herausstellte.

Im ersten Rekonnexionsfall erlaubte die Vier-Punkt Methode von Cluster wegen des kleinen Abstandes zwischen den Satelliten im Verhältnis zur Magnetopausendicke, aus dem Ampère'schen Gesetz das Stromdichteprofil der Magnetopause zu bestimmen. Nach den Messungen des Plasma-Ionenspektrometers spielten die weniger häufig auftretenden Ionensorten (He^+, He^{2+}, oder O^+) keine Rolle und wurden deswegen vernachlässigt. Es handelt sich also um ein Elektronen-Protonen Plasma, und aufgrund der Ladungsneutralität sollte die Elektronendichte gleich der (gemessenen) Protonendichte sein. Die Protonenströmungsgeschwindigkeit wurde ebenfalls gemessen, und so liess sich aus dem Ausdruck für die Stromdichte die Elektronengeschwindigkeit berechnen. Mit der Kenntnis der Elektronendichte und -Geschwindigkeit konnten wir den Beitrag von Elektronen zum Walén-Test bestimmen, mit dem Ergebnis, daß es sich tatsächlich um einen zweitrangigen Beitrag handelte. In der Tat lag die Verbesserung des Proportionalitätsfaktors bei nur etwa 8%, von 0.60 auf 0.65 für Cluster 1, und bei etwa 5%, von 0.81 auf 0.85 im Fall von Cluster 3.

Dieses Ereignis ist zudem ideal geeignet, ein weiters Problem zu untersuchen, nämlich die Gültigkeit der Relation $\rho(1-\alpha) = konst$, wo ρ die Plasmadichte und α der Anisotropiefaktor des Plasmadrucks ist. Diese Relation basiert auf denselben Erhaltungssätzen wie der Walén-Test und sollte deshalb ebenso für eine Rotationsdiskontinuität gelten. Obwohl die Magnetopause sich hier wie eine dicke, planare, stationäre Diskontiuität verhielt, konnten wir experimentell zeigen, dass die Relation in diesem Fall nicht erfüllt ist. In der Tat haben wir hier Gründe gefunden, warum dies ein generelles Resultat ist, und nicht nur eine Eigentümlichkeit des behandelten Falles. Umso erstaunlicher ist es deshalb, daß man bei der Verwendung eines modifizierten Walén-Tests, der die Relation $\rho(1-\alpha) = konst$ einbezieht (und somit seine Gültigkeit voraussetzt), typischerweise bessere Resultate erzielt. In unserem speziellen Fall erhöhte sich der Proportionalitätsfaktor im Walén-Test um den nicht unbedeutenden Betrag von $\sim 23\%$ auf 0.84.

Im zweiten Rekonnexionsfall erlaubte uns der hohe Gehalt an aus der Ionosphäre stammendem O^+, in Zusammenhang mit dem geeignet gewählten Messmodus, zu testen, ob die Präsenz einer weniger häufig auftretenden Ionensorte auf signifikante Weise zum Ergebnis des Walén-Tests beitragen würde. In diesem Fall ergab das Plasma-Ionenspektrometer eine relative Häufigkeit (in der Anzahldichte) von etwa 1% für die O^+ Ionen, die 16 mal schwerer als Protonen sind. Wir untersuchten zwei Magnetopausendurchgänge, die zum zweiten Rekonnexionsfall gehörten. In beiden Fällen fanden wir durch die Verwendung des im Massenschwerpunkt der beiden Ionensorten ermittelten Momentes anstelle des Protonenmomentes eine Verbesserung im Ergebnis des Walén-Tests. Der Proportionalitätsfaktor erhöhte sich um 12% bis 15%, wobei ein Intervall sogar eine Erhöhung von 22.5% auf 0.74 zeigte, und somit der eins näher kam. Im allgemeinen ist der Einfluss der weniger häufig auftretenden Ionensorten gering, aber unser Resultat zeigt, daß in seltenen Fällen, wie dem von uns untersuchten Fall mit hohem O^+ Anteil, ihr Einfluss eine wichtige Rolle bei der Frage nach dem Charakter der Diskontinuität spielen kann.

Zusätzlich zum Einfluss auf das Resultat des Walén-Tests, erlaubte uns der hohe Anteil an O^+ im zweiten Rekonnexionsereignis eine weitere bemerkenswerte Beobachtung. Wir stellten eine Korrelation zwischen der Änderung der Magnetfeldrichtung und derjenigen der O^+-Strömungsgeschwindigkeit fest, ähnlich wie man es im Fall einer Rotationsdiskontinuität

zwischen der (auf den Massenschwerpunkt bezogenen) Geschwindigkeit und dem Magnetfeld erwarten würde. Wenn man den Walén-Test nur mit den O^+ Größen durchführt, zeigen die Daten eine Korrelation zwischen der O^+ Geschwindigkeit im (O^+ basierenden) HT System und der (O^+ basierenden) Alfvén Geschwindigkeit, auch wenn die Bestimmung des HT-Systems nicht besonders gut bestimmt war. Eine derartige Relation passt nicht in den Rahmen der generellen Theorie der Rotationsdiskontinuität, in der sich alle Konzepte (deHoffmann-Teller System, Alfvén Geschwindigkeit, etc.) auf die Massenschwerpunkts-Flüssigkeit beziehen.

Summary

The subject of this study is the terrestrial magnetopause, which is the boundary separating the plasma environment controlled by the Earth magnetic field from the plasma originating at the Sun and carried away by the solar wind. We were interested both in determining the macroscopic properties of this discontinuity (like its shape, orientation, motion and thickness) as well as in the physical phenomena taking place at that location. We carried out the study by analysing and interpreting the in-situ measurements taken on-board the European Space Agency's Cluster mission, during the times when the spacecraft crossed the magnetopause.

Almost all the methods used in inferring the magnetopause crossing parameters assume a planar geometry for this boundary and consider that all physical quantities vary only along the normal direction. We can divide them into two categories. On the one hand there are single-spacecraft techniques, based on the validity of various conservation laws. For example, the minimum variance analysis of the magnetic field (MVAB) is based on the absence of magnetic poles, which implies the constancy of the magnetic field component along the normal. Consequently, in this method the direction of minimum magnetic variance provides the direction of the magnetopause normal. Similarly, the planar method of minimum Faraday residue (MFR) is based on the magnetic flux conservation across the discontinuity. In this case the algorithm finds a direction in space and a velocity (assumed constant) along this direction so that the variation in the tangential component of the electric field (the so called Faraday residue) is minimized. On the other hand, the Cluster mission provides for the first time correlated measurements taken simultaneously at four points in space. The differences in the position and time of the satellites' encounter with the terrestrial magnetopause can be used to infer the magnetopause orientation, thickness and velocity. This four-point timing method usually assumes a planar discontinuity as well, and offers an independent check for the various single-spacecraft techniques.

In this thesis we extended the four-point timing method in order to accommodate the more realistic situations when the magnetopause behaves like a two-dimensional (2-D), non-planar discontinuity on the scale of the inter-spacecraft separation distance. Such non-planarity occurs when the magnetopause has a local bulge or indentation, or when a large amplitude wave travels on the magnetopause surface. The new method is designed to deal with the situation when the single-spacecraft techniques provide individual magnetopause normals that, although different, are contained roughly in a plane (which we call the *plane of the normals*). We locally modelled the magnetopause as a layer which has either a parabolic or a cylindrical shape. In both

cases we assumed that the discontinuity has a constant thickness and that its shape does not change along the direction perpendicular to the *plane of the normals*. In the same *plane of the normals* we allowed for the layer to have either a unidirectional movement or a motion along two mutually perpendicular directions. With this model we can describe two features of the non-planar magnetopause: its normal motion and, by allowing for a second degree of freedom, the large-scale waves that often travel along that surface.

Mathematically, in each implementation of the model (parabolic or circular geometry, one or two degrees of freedom in the magnetopause movement) we have established a system of eight equations. These equations correspond to the conditions that the magnetopause leading and trailing edges meet the positions of the satellites according to the timing information extracted from the measurements. The unknowns to be found were: the direction of movement, the spatial scale of the structure, the magnetopause thickness, the initial position of the structure and three coefficients describing the velocity-time dependence, assumed polynomial. Basically, this approach relies on the timing information alone and therefore we termed it as *plain timing analysis*.

Because in our model the direction of the magnetopause movement is fully described by an angle in the *plane of the normals*, we improved the *plain timing analysis* in the following way: we imposed different values for this quantity in the range $[-\pi, \pi]$, and solved the system of equations with this condition. For each solution, the magnetic field variance along the instantaneous (i.e. geometrical) normal at each satellite was computed. Then, we selected that direction of magnetopause movement for which the *global* normal magnetic field variance was minimum. By *global* we mean a weighted average over the four spacecraft. The solution obtained in that way has two advantages: first, it incorporates the MVAB technique. Second, because the angle is now an input parameter, four coefficients. instead of three, are available to describe the magnetopause velocity-time dependence, which yields a much improved description of the magnetopause motion. We called this approach the *combined timing - MVAB analysis*.

The new method was applied to a magnetopause transition for which the various planar techniques provided inconsistent results. In contrast, the solutions obtained from the different implementation of the new 2-D method were consistent and stable, indicating a convex shape for the magnetopause. These solutions 'perform' better than the planar solutions from the global magnetic field variance and global Faraday residue perspectives. Note also that in the single-spacecraft techniques, the estimated individual normal directions and velocities are decoupled from each other. In the 2-D method, however, we are looking for a global solution, and thus the normal direction and velocity are linked through the geometry we adopted and through the determined motion, giving a more realistic description of the magnetopause.

The relative large flow shear across the magnetopause and its orientation with respect to the magnetic field direction suggests the Kelvin - Helmholtz instability (producing 'wind over water' type waves) as the possible cause for the 2-D feature encountered by Cluster in this event. The mechanism is one of the proposed physical processes to explain the transfer of energy, momentum and, in its non-linear phase, mass across the magnetopause. With the method developed in this thesis it is straightforward to estimate the wavelength and the periodicity of such a structure. For example, by considering the parabolic model and allowing for two degrees of freedom for the magnetopause movement, we obtained a wavelength of ~ 8 Earth radii and a period of $\sim 10-11$ minutes in the analyzed case.

The most important process, however, for transferring mass, momentum and energy across the magnetopause is magnetic reconnection. The process has the effect of converting magnetic field energy into bulk kinetic energy and heating, and is being invoked to explain many dy-

namical processes at the Sun, in planetary magnetospheres, and in other astrophysical objects. At the magnetopause we have the unique opportunity to study the reconnection phenomenon with in-situ measurements. It occurs when the plasmas in the regions adjacent to the magnetopause, i.e. in the magnetosheath and in the magnetosphere, have antiparallel magnetic field components. Through reconnection the interplanetary and terrestrial magnetic fields become interconnected, and the magnetopause thus ceases to act as an impenetrable barrier, the plasma being now able to flow across it and transfer momentum and energy to the magnetosphere.

In the magnetopause context, all magnetic reconnection models predict the formation of a rotational discontinuity at this boundary. In order to establish whether the magnetopause behaves like a rotational discontinuity we perform the so called Walén test, which combines in a single relation the conservation of the plasma tangential momentum, of the normal mass flux and of the tangential electric field. By doing this test, we check whether the plasma flows at the local Alfvén velocity in a frame of reference (the so-called deHoffmann-Teller frame) in which the flow is field aligned everywhere. While the Walén test has proven very successful in establishing whether a discontinuity has rotational character or not, a long standing issue remains, namely that at the magnetopause the factor of proportionality between the plasma velocity in the deHoffmann-Teller frame and the Alfvén velocity is usually less than the ideal value of one required by the theory. This discrepancy could have an explanation in the fact that the Walén analysis relies on some simplifying assumptions.

One of these assumptions refers to the role of electrons in the analysis, which is usually neglected due to their relative low mass. At the same time it is difficult to experimentally test their contribution because the electron measurements are affected by the presence of photoelectrons, produced by the solar radiation incident on the spacecraft surface, and because their bulk velocity is much smaller than their thermal velocity. A second simplifying assumption commonly made is to consider all the ions as being protons, an approximation justified by the prevalence of protons in the magnetopause environment. As in the electron case, obtaining reliable measurements for the minor ion species is an experimental challenge for the present satellite instrumentation. In connection with these issues, we presented two events of magnetopause crossings, providing evidence that the boundary behaved like a planar, time-stationary rotational discontinuity. The magnetohydrodynamic treatment was justified in both cases because the magnetopause thickness was found to be much greater than the ion gyro-radius and ion inertial length.

In the first of these events, due to the small inter-spacecraft separation distance relative to the magnetopause thickness, the four-point capability of Cluster allowed us to determine, via Ampère's law, the corresponding magnetopause current density profile. According to the measurements of the ion composition detector, the minor ion species (like He^+, He^{2+} or O^+) did not seem to play a role and therefore their presence was neglected. In this situation we have a case of an electron-proton plasma and, according to the charge neutrality assumption, the density of electrons should be equal to that of protons, the latter being experimentally measured. The proton flow velocity is also measured and, from the expression of the electric current density, the electron flow velocity is indirectly obtained. Knowing the electron density and flow velocity allowed us to asses the contributions from electrons in the Walén test, concluding that it is of second order. Indeed, the improvement in the Walén factor of proportionality was only around 8%, from 0.60 to 0.65 in case of Cluster 1 and around 5%, from 0.81 to 0.85 in case of Cluster 3.

The first reconnection event presented in the thesis is almost ideally suited to study another important issue related to the reconnection process. This issue refers to the relation $\rho(1-\alpha) = const$, with ρ being the plasma density and α the plasma pressure anisotropy factor. The

relation should hold for a rotational discontinuity, being based on the same conservation laws as the Walén relation. However, despite the strong evidence that the magnetopause behaves like a thick, planar and stationary discontinuity for this transition, we have experimentally proven that the quantity $\rho(1-\alpha)$ is not constant across the discontinuity. In fact, we provided arguments that this experimental invalidation seems not to be a peculiarity of the transition in question, but a more general result. An even more baffling aspect adds to this issue: when we use a variant of the Walén relation that incorporates the $\rho(1-\alpha) = const$ relation (therefore assuming its validity), we typically obtain better results in the test. In our particular case the factor of proportionality in the Walén test has improved by around 23 %, to 0.84.

For the second reconnection event, the large content of O^+, originating at the ionosphere, and the appropriate instrument mode allowed us to test whether the presence of a minor ion species contributes in a significant manner to the outcome of the Walén test. In this event, the plasma ion spectrometer detected a relative abundance (in number density) of around 1% for the O^+ ions, which are 16 times heavier that the protons. We investigated two magnetopause transitions belonging to the second reconnection event. In both cases, by using the centre-of-mass moments and not simply the proton moments in the Walén test, we found an improvement in the outcome. The factor of proportionality increased by between 12 - 15 %, with one interval showing an increase of even 22.5 %, to 0.74, and thus become closer to one. In general, the influence of minor ions is small, but our result shows that in the rare events like the one we investigated, with large O^+ contribution, their influence could be an important factor in determining the character of the discontinuity.

In addition to the effect of influencing the result of the Walén test, the large content of O^+ particles in the second reconnection event allowed us to make another noteworthy observation. We noticed a correlation between the change in magnetic field direction and in the direction of the O^+ bulk velocity at the magnetopause, similar with what we expect to happen for a rotational discontinuity between the plasma centre-of-mass velocity and the magnetic field. When performing a Walén test by using only O^+ quantities, the data clearly indicate a correlation between the O^+ velocity in the (O^+ based) HT frame and the (O^+ based) Alfvén velocity, although the identification of the HT frame was not as good. No such relation is prescribed in the general theory of the rotational discontinuity, where all concepts (deHoffmann-Teller frame, Alfvén velocity etc.) and quantities refer to the centre-of-mass fluid.

CHAPTER 1

Introduction

1.1 The magnetopause

Due to their low density and taking into account the spatial scales involved, space plasmas are considered as collisionless. This means that the collisions between the constituent particles are so infrequent when compared with the variations in the field or in the particle dynamics that they can be neglected. In general this also means that the magnetic field is 'frozen' into the plasma, because two plasma particles that at one moment were connected by a magnetic field line will still be connected at any later moment by such a line. Therefore, space plasmas behave like ideal conductors, i.e. they are impenetrable by outside magnetic fields. When plasmas of different origins are coming into contact they have the tendency to form cellular structures, where domains of plasma and magnetic field of different regimes remain isolated from each another. So is the case of the Earth magnetosphere, where in the first order approximation, plasma and magnetic field from inside are isolated from the solar-wind regime by a relatively thin membrane - the magnetopause. This impenetrable layer, which is also the place of an electric current system to account for the change in the magnetic fields across it, behaves like a tangential discontinuity, i.e. there is no magnetic field component, nor any plasma flow along its normal direction.

The concept of magnetopause appeared in the early work of *Chapman and Ferraro* [1931]. The authors had the intuition of a cavity forming around the Earth (what is now called magnetosphere), as a consequence of interaction between a stream of neutral ionized gas of solar origin and the terrestrial magnetic field. They proposed a system of currents to flow on the surface of this cavity, called afterwards the Chappman-Ferraro current, to account (through the Lorentz force) for retarding and deflecting the advancing stream.

One of the early clear identifications of the magnetopause (MP) boundary, appeared in the work of *Cahill and Amazeen* [1963], reporting on Explorer 12 data. Figure 1.1 (taken from *Cahill and Patel* [1967]) shows the magnetic field measured by this satellite on 21 August 1961. The MP is evident around 11.4 R_E, when a sharp change in magnetic field direction occurred, accompanied by a decrease in magnitude. After the transition, the magnetic fluctuations are also increased. The measured field magnitude just inside the MP is approximately two times

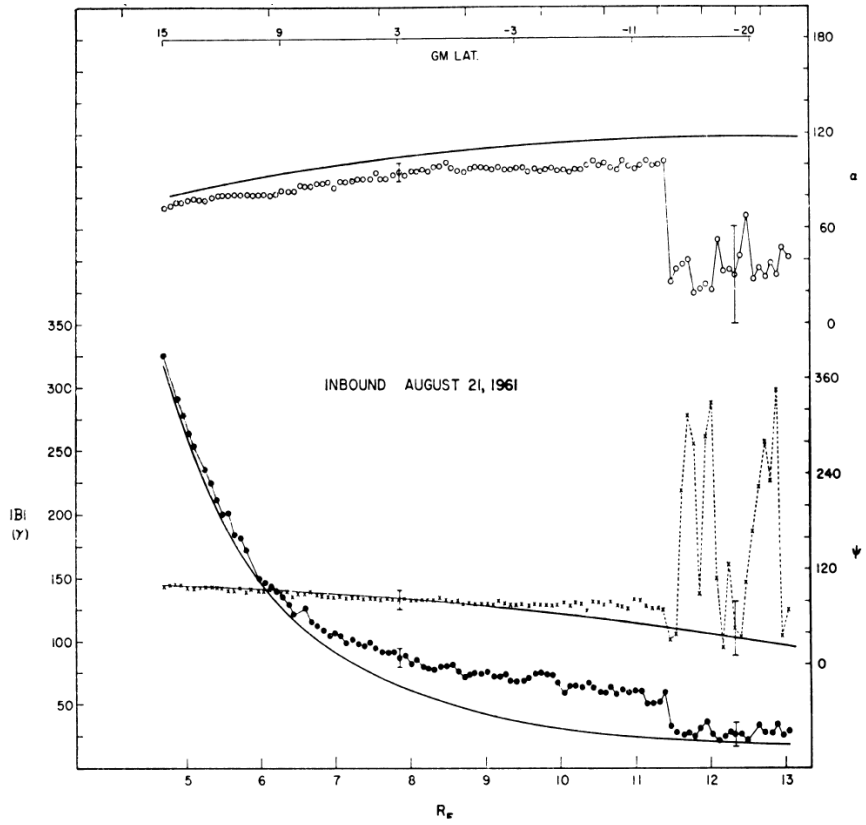

Figure 1.1: Identification of the MP by Explorer 12. The magnetic field magnitude (solid dots) and orientation (given by two angles, indicated with crosses and circles) of the recorded field are shown as function of radial distance (in Earth radii, R_E). These values are compared with the magnitude and orientation of a model field (continuous lines), resulting from a spherical harmonic analysis of the ground recorded magnetic data. The MP appears in the satellite data around 11.4 R_E, when a sharp change in magnetic field direction occurred, accompanied by a decrease in magnitude.

greater than the magnitude of the model field, resulting from a spherical harmonic analysis of the ground recorded magnetic data, due to the compression exerted by the solar wind flow.

Figure 1.2 (an adaptation from *Kivelson and Russell* [1995]), reflects the present understanding of the magnetosphere structure. The solar-wind is coming from the left, with bulk velocity exceeding the velocity of compressional (fast magnetosonic) waves, and encounters the obstacle of the terrestrial, dipole-like magnetic field. A bow-shock (not shown) is formed, upstream of the magnetopause (the surface shown in light blue), where the solar-wind plasma is slowed down and part of its kinetic energy is converted into heat. The region between the bow-shock and the magnetopause is called magnetosheath.

The shape of the MP is given by the equilibrium between the total pressure on the two sides of the boundary. In a simple model, we have the plasma pressure in the magnetosheath (which in turn is determined by the solar-wind dynamic pressure) and the magnetic pressure in the magnetosphere. A better approximation would also consider the plasma pressure in the magnetosphere and would take into account the solar-wind magnetic field as well. A typical value for the location of the magnetopause sub-solar point is at $\sim 10 \div 11$ R_E from the Earth centre, while on the flanks the magnetopause is located at a distance of roughly 15 R_E. The distant tail of the magnetosphere has a circular cross-section with a radius of $\sim 25 \div 30$ R_E (*Stern* [1995]).

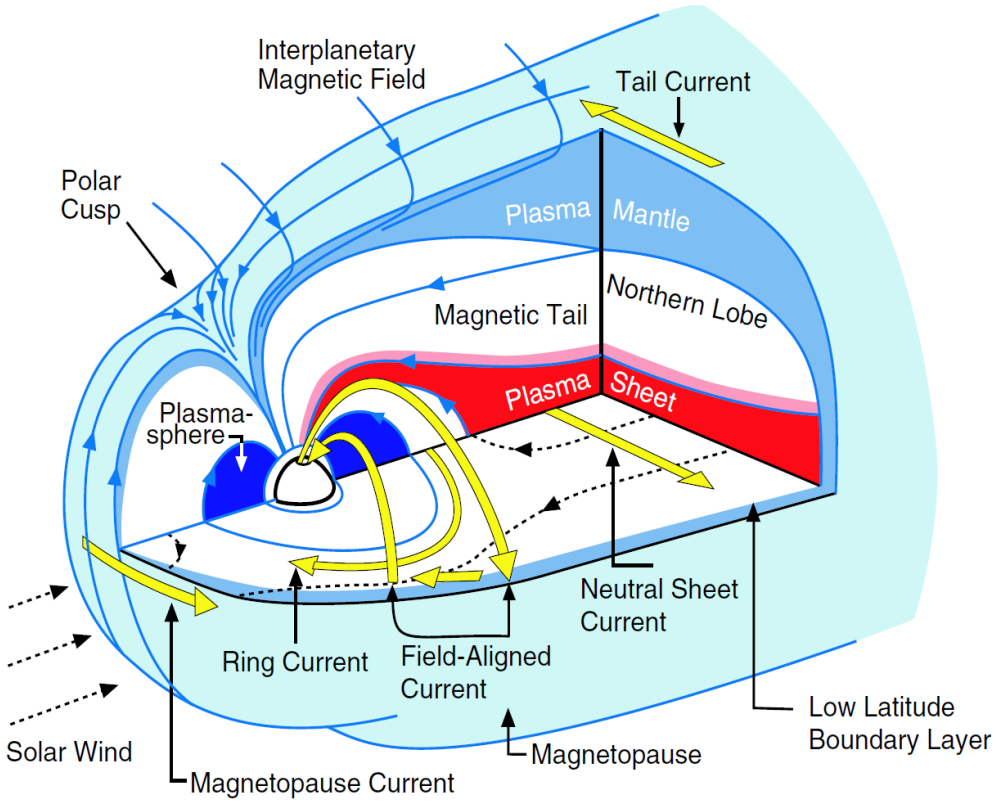

Figure 1.2: Three-dimensional model of the magnetoshere. The magnetopause and magnetopause boundary layer appear in light blue and darker blue, respectively. Different electric current systems are shown in yellow. Solar wind is coming from left.

The above numbers are averages, based on data collected on-board various missions. As the solar-wind dynamic parameters (density, velocity) are rapidly changing, the magnetopause shrinks or expands. It was found that the orientation of the interplanetary magnetic field (IMF) also controls the shape and location of the MP; a southward oriented IMF moves the MP sub-solar point Earthward and increases the cross-section of the magnetospheric tail (see for example *Fairfield* [1995]).

The measurements taken on-board satellites proved that the MP is far from being a simple impenetrable layer, isolating the interior of the magnetosphere from the magnetosheath plasma. Just inside the magnetopause current layer, boundary layers were detected most of the time with characteristics (plasma moments and velocity distribution function) intermediate between that of the two adjacent plasma regimes. Depending on the location, they are called the low latitude boundary layer, LLBL (*Eastman et al.* [1976]) , plasma mantle or high latitude boundary layer, HLBL (*Rosenbauer et al.* [1975]) and high altitude cusp or entry layer, EL (*Haerendel and Paschmann* [1975] and *Paschmann et al.* [1976]). In Figure 1.2 they appear in blue. Not only inside, but usually also outside the MP, a layer of magnetospheric particles is observed. This layer, termed magnetosheath boundary layer provides support for magnetospheric plasma transfer across the MP.

It is generally agreed that the HLBL and the EL are situated on open magnetic field lines (i.e. having one end on the Earth surface and the other in the solar-wind) and that they are formed by the magnetosheath plasma entering along the open field lines in the cusp region.

The cusp is the funnel-shaped indentation in the MP surface, where the magnetic field lines closing at the dayside or on the nightside separate (see Figure 1.2). LLBL may be partially on open field lines (especially during southward IMF, when the process of magnetic reconnection is thought to be active) and partially on closed field lines. All these layers are mapping at low altitude in a limited region around day-side auroral oval (*Vasyliunas* [1979]). The LLBL is also the site of the so-called region-1 current system, connecting the solar-wind and ionosphere, directed downward in the morning side and upward in the after-noon side.

In general, the characteristic signature of the MP in satellite data is the magnetic field rotation in the plane of the discontinuity. This rotation identifies the electric current system flowing in the layer. However, other markers have to be used in cases of transitions with low magnetic shear, like the sudden increase in the proton temperature or temperature anisotropy when coming from the magnetosheath to the magnetosphere (*Paschmann et al.* [1993]). The drop in plasma density is another indication of entering the magnetosphere but this usually happens in the boundary layer.

Processes taking place at the magnetopause

The existence of boundary layers indicates that the MP is not impenetrable. In order to explain the formation of these layers and, more general, the transfer of energy, momentum and mass between the solar-wind and the magnetosphere, several physical processes were proposed:

- *Magnetic reconnection.* This is a process that involves a local break-down of the 'frozen-field' situation when a sharp change in magnetic field direction exists across a plasma boundary. It could be depicted as a phenomenon in which two magnetic field lines from the adjacent domains get cut at some position and the resulting branches reconnect at the later moment so that plasma elements from the previously separated regimes are now linked by the newly connected magnetic field lines (see Figure 1.3 from the next section). In case of the MP, the interplanetary and terrestrial magnetic fields become interconnected and thus the MP ceases to act as an impenetrable barrier, with the plasma being now able to flow across it. Since in our thesis we are dealing with the experimental identification of this phenomenon, we will treat it in more detail in the next section.
- *Cross-field diffusion.* This process implies a mechanisms for particle scattering, which are thus distorted from their trajectories. In case of collisionless plasmas we speak about 'anomalous' collisions, caused by the interaction between particles and plasma waves, as the responsible phenomenon for the scattering. There are many mechanisms proposed, from current driven instabilities to macroscopic turbulence. From the investigation of the electric and magnetic field spectra in the LLBL region, the conclusion emerged that the rate of this mechanism is too slow to account for the thickness of this boundary (see *Treumann et al.* [1995]). But nevertheless, the anomalous collision frequency could locally be high enough for the onset of magnetic reconnection, opening in this way a simpler way for magnetosheath plasma to enter the LLBL (see *Sibeck et al.* [1999]).
- *Kelvin-Helmholtz instability.* The flow of the magnetosheath plasma along the magnetopause may cause ripples on this boundary in the same way as water is agitated by a breeze. In some conditions this undulations can grow non-linearly to form rolled-up vortices that can engulf plasma from both sides of the MP. There are several conditions that favour such a development, like high density in the solar wind, high velocity shear across the MP, magnetic field orientation transverse to the magnetosheath flow and low rotation of the magnetic field in the MP. These requirements are often met at the dawn- and dusk-flanks of the magnetopause, at times when IMF is predominantly northward

oriented. Convincing evidence of this phenomenon using Cluster data was reported by *Hasegawa et al.* [2004].

- *Finite Larmor radius effects.* Typically the MP thickness is several times larger than the ion gyro-radius, computed by using their mean thermal velocity. It is argued that the particles having more energy, for which the Larmor radius is comparable to or even greater than the boundary thickness, induce a series of effects at the MP (like curvature drift or gradient B drift) that can account for the observed plasma presence in the adjacent boundary layer. There are observations in support of particle transfer across the MP due to the finite Larmor radius, like for example *Marcucci et al.* [2004], reporting on O^+ exit in the magnetosheath. However, the present general view is that only a small fraction of the particles may enter the LLBL through this process (see *Hill* [1983], *Treumann and Baumjohann* [1988]), largely because plasma charge-neutrality has to be preserved.
- *Impulsive penetration.* According to this mechanism, solar wind plasma-field irregularities, or plasmoids, impinging on the Earth's geomagnetic field with an excess momentum can penetrate into the magnetospheric cavity. At the edge of the plasmoid, in the direction perpendicular to the magnetic field and plasma velocity, a polarization electric field is induced which leads to a $\vec{E} \times \vec{B}$ drift (see for example *Lemaire and Roth* [1978]). While in the laboratory experiments this mechanism has been proved, there is to date no direct indisputable evidence for its occurrence at the magnetopause. We should add that in *Lundin et al.* [2003] the authors reported solar-wind plasma clouds protruding into the dayside magnetopause, having characteristics implied by the impulsive penetration.

The structure of the magnetopause region

The structure of the MP region has been studied by many authors, either by investigating individual events considered representative in one way or another, or in a statistical manner. From the latter, we mention the studies appearing in the work of *Berchem and Russell* [1982b] devoted to the dayside MP, and *Paschmann et al.* [2005a] referring to the flank of the MP. Also, in connection with the statistical analysis of the MP transitions, we mention the superposed epoch analysis technique, where average variations of the key plasma and magnetic field parameters are obtained from a set of transitions sharing the same characteristics. For example, using this technique, the structure of the low-latitude dayside MP region when the magnetic shear is low at this interface (i.e. below 30 °) was analyzed by *Paschmann et al.* [1993]. In a complementary investigation, the same region was analyzed for cases of high magnetic shear (i.e. above 45 °) by *Phan and Paschmann* [1996]. Below we summarize some of these findings.

At the dayside MP, for low magnetic shear, a gradual decrease in the plasma density was often observed, simultaneous with an increase in the magnetic field strength and in plasma anisotropy. The formation of this layer, called 'plasma depletion layer' was attributed to the escape of the more energetic particles, moving along the magnetic field lines away from the subsolar region. As *Phan et al.* [1994] showed by a superposed epoch analysis, the feature is present only for low magnetic shear, the interpretation being that in the case of high magnetic shear the reconnection process is active and dominates over the formation of the depletion layer (*Russell* [1995]).

The width of the current flow region (often taken as the MP thickness as well) is on average many times the magnetosheath thermal ion gyro radius (10 times according to *Berchem and Russell* [1982b] and *Paschmann et al.* [2005a] and 14 times according to *Phan and Paschmann* [1996]), ranging typically between 400 and 1000 km. But there are extreme cases when the MP thickness, expressed in ion gyro radii, could be as low as around one ion gyro radius or higher

than 100. So far, despite all efforts, it is not clear what parameters in the solar-wind (IMF orientation or magnitude, plasma parameters etc) determine the values of the MP thickness.

The study of individual cases shows that the MP is in continuous inward-outward motion, changing very rapidly its normal velocity. This is a consequence of MP's very low mass per unitary cross-section, resulting in big acceleration even in case of a relatively small pressure imbalance. Typical values for the normal velocity are around tens of km/sec but there are cases of very rapid crossings, when velocities higher than 300 km/sec were determined (*Paschmann et al.* [2005a]). The amplitude of the MP excursion in the radial direction can be several R_E.

The electric current density at the magnetopause ranges typically from 20 to 80 $\mathrm{nA/m^2}$ (see *Paschmann et al.* [2005a]). This quantity can be estimated from Ampère's law when we know the magnetic jump across the MP and the thickness of this boundary. In general, the change in direction of the tangential magnetic field component, from the magnetosheath to the magnetosphere, occurs in a single rotation of less than 180 °.

At the mesoscale level (i.e. below the scale of MP thickness), there is much substructure in the current carrying region, which invalidates the initial picture of a one-dimensional current layer. The study of this substructure was boosted with the availability of Cluster. In this respect we mention here the curlometer technique, (see for example *Dunlop et al.* [2002b]), allowing a direct estimation of the current density by applying the Ampère's law to the magnetic field measurements recorded at the four satellites. Another powerful tool, based on the Grad-Shafranov equation, permits the local reconstruction of the current-layer region. Two-dimensional magnetic field maps are produced, which reveal structures such as magnetic islands or X-type null points (see for example *Sonnerup and Guo* [1996] and *Hasegawa et al.* [2005]).

The thickness of the LLBL was found to be comparable with the width of the current flow region (*Phan and Paschmann* [1996]). By studying the same region, *Bauer* [1997] showed that often this layer exhibits a steplike profile in the plasma density, with two plateaus. In such situations, the outer part was identified as situated on open field lines, whereas the inner part being on closed field lines. According to a study by *Eastman et al.* [1976], investigating equatorial and mid-latitude regions, magnetopause crossings without boundary layer are found to occur in about 10 % of all magnetopause crossings.

Determining the macroscopic parameters of the magnetopause

The motivation for finding the MP orientation and velocity is threefold. First, it is the problem of studying the large-scale dynamical processes that take place at this interface, like for example the large amplitude surface waves. For that purpose, only a moderately accurate knowledge of the MP normal direction and MP normal velocity is sufficient. The second problem consists in establishing whether the magnetosphere and the magnetosheath regions are magnetically connected, or in other words, whether the MP behaves like a rotational (having an average normal magnetic field component $\langle B_n \rangle \neq 0$) or tangential ($\langle B_n \rangle = 0$) discontinuity. Generally, even if one is dealing with a rotational discontinuity, the normal component of the magnetic field at this interface is very small (around 10% of the total magnetic intensity) and therefore in this problem an accurate knowledge of the normal direction is needed. The same requirement of accurate normal determination appears when we want to establish whether a plasma flow exists across the MP.

Third, from the normal velocity and the crossing duration one can easily compute the MP thickness. This is an important parameter, giving an estimation for the spatial scale characterizing the processes taking place in that region. For example, by comparing the MP thickness with the kinetic parameters like the gyro radius and the inertial length, we obtain an

indication whether the MHD approximation can be used or a kinetic treatment is inevitable in studying the discontinuity. Also, knowing the MP thickness and the magnetic change at this boundary we can estimate (via Ampère's law) the MP current density, which is an important quantity in studying the plasma instabilities that may occur in that region.

Initially the techniques used in determining the MP orientation were single-spacecraft methods, relying on some simplifying assumptions for the boundary like planar geometry and variation of all physical quantities along the normal direction only. Nowadays different single-spacecraft techniques exist, each based on the conservation of some particular physical quantity across the discontinuity. A detailed and unified description of these techniques is provided in *Sonnerup et al.* [2006].

The first single-spacecraft technique, called minimum variance analysis of the magnetic field (MVAB), was developed by *Sonnerup and Cahill* [1967]. It is based on the $\nabla \cdot \vec{B} = 0$ condition, which with the above mentioned assumptions imply a constant component of the magnetic field along the MP normal. Consequently, the normal is found by searching for the direction in space that minimizes the magnetic variance. The MP velocity is not found in the analysis, but in some cases we can combine MVAB with the so-called deHoffmann-Teller (HT) analysis (see for example *Khrabrov and Sonnerup* [1998]). In the latter, we are searching for the existence of a specific reference frame where the plasma flow becomes aligned with the magnetic field and thus the motional electric field vanishes. If the identification of such a HT frame is successful, then the projection of $\vec{V}_{HT}$ (the velocity of HT frame with respect to the measurement frame) along the MP normal is the normal MP velocity.

Another single-spacecraft method called Minimum Faraday Residue (MFR) was developed based on the conservation of magnetic flux across the discontinuity (see *Khrabrov and Sonnerup* [1998]). In this case the algorithm finds a direction in space and a velocity (assumed constant) along this direction so that the variation in the tangential component of the electric field (the so called Faraday residue) is minimized. All the three single-spacecraft methods (i.e. MVAB, HT and MFR) will be used in our thesis and are presented in details in the Appendices A, F and G, respectively.

Later, another type of methods emerged, to be used in the case of multi-spacecraft missions. These are the so-called timing methods, where the differences in the position and time of the MP encounter by the satellites can be used to infer its orientation and velocity. In general, the timing methods assume also a planar MP and steady orientation in space for its normal.

The first such technique (called time of arrival method) designed for a four-satellites mission, was proposed by *Russell et al.* [1983] in order to infer the orientation of interplanetary shocks, considering a propagation with constant velocity. *Haaland et al.* [2004b] introduced another planar timing technique, assuming a constant thickness for the MP, to determine its orientation and its normal velocity, when the latter is described by a polynomial time dependence. A detailed description of these two approaches, termed Constant Velocity Approach (CVA) and Constant Thickness Approach (CTA), can be found in Section B.1.

Another line of approach in the effort to characterize the macroscopic properties (orientation and motion and, in case of non-planarity, the curvature) of a discontinuity when four points of measurements are available (like in case of Cluster) appear in the work of *Mottez and Chanteur* [1994] and *Dunlop and Woodward* [1998, 1999]. The method relies on combining the results provided by the single-spacecraft MVAB method applied on each satellite, with the information about the position and time of the MP encounter by all satellites. The main assumption in this case is that the individual normals, obtained from a planar technique, are not too much affected by the local curvature of a non-planar MP and by the motion of such a discontinuity during data sampling.

The present contributions to the study of MP geometry and dynamics
In the present thesis we propose a generalization of the planar timing method which assumes a constant thickness for the discontinuity (i.e. of the CTA method). The new technique is conceived for determining the crossing parameters (orientation, motion, thickness and curvature) of a 2-D, non-planar MP in a self-consistent way (i.e. all parameters are determined simultaneously and 'on equal footing').

Since a curvature in the MP (like a local bulge or indentation) as well as large amplitude travelling waves on this surface are phenomena relatively often encountered, the development of this new technique represents an important step. We shall illustrate our new technique with a particular MP crossing by Cluster.

1.2 The magnetic reconnection process

As we discussed above, when magnetized space plasmas of different origin come into contact, they will not mix but form a thin boundary layer inbetween. In the two adjacent regions, the magnetic fields frozen into the plasma may have different orientations, and therefore an electric current is also flowing in the separating layer. Under the influence of Maxwell stresses in the magnetic field, the intensity of this electric current may increase, together with the accumulated energy in the configuration. Magnetic reconnection is a fundamental process taking place at the boundary, whereby the energy in the magnetic configuration is converted into kinetic energy. It can be loosely described as follows: the situation of frozen - field breaks down locally and plasma elements from the two sides of the layer get connected, resulting in a change of magnetic topology. Because the newly reconnected field lines are highly bent, the magnetic tension force accelerates the plasma at high speed, providing in this way the energy conversion mechanism. A sketch of the different phases of the process is presented in Figure 1.3, adapted from *Paschmann* [2006].

The phenomenon of magnetic reconnection appears for the first time in the paper by *Giovanelli* [1946], where the author proposed a theory for solar flares. Initially, because of its low efficiency, the magnetic reconnection was contested as being an important process in the case of non-collisional plasmas. It was argued that the rate for conversion of magnetic to kinetic energy could not account for the explosive events observed in the solar atmosphere. This theoretical objection was solved by *Petschek* [1964] who proposed a model in which the necessary changes in plasma flow and magnetic field were accommodated by a structure of standing MHD slow-mode compressional waves attached to a small region (the so called *diffusion region*, where the 'frozen-in' condition breaks-down).

The concept of magnetic reconnection was introduced in the context of magnetospheric physics by *Dungey* [1961], at the time when the author advanced an explanation for the plasma convection inside the magnetosphere. In Figure 1.4 we present a sketch (taken from *Stern* [1995]) illustrating Dungey's scenario: the magnetic field lines 1, embedded in the solar wind and pointing southward, and $1'$, with both ends on the Earth surface, reconnect at the subsolar point N_1, which in this case is a X-type neutral point. The open magnetic lines 2 and $2'$ are formed, with one end on the Earth surface and the other in the solar wind, which are carried tailwards, over the polar caps, by the plasma motion in the magnetosheath. At a later time they reach the positions 3 and $3'$, when the field lines reconnect at a neutral point N_2 situated in the distant tail. Two lines are thus formed: a line completely decoupled from the Earth, transported further away by the solar-wind and a closed field line. Due to the magnetic tension, the latter field line will relax by moving sunward and around the Earth (in

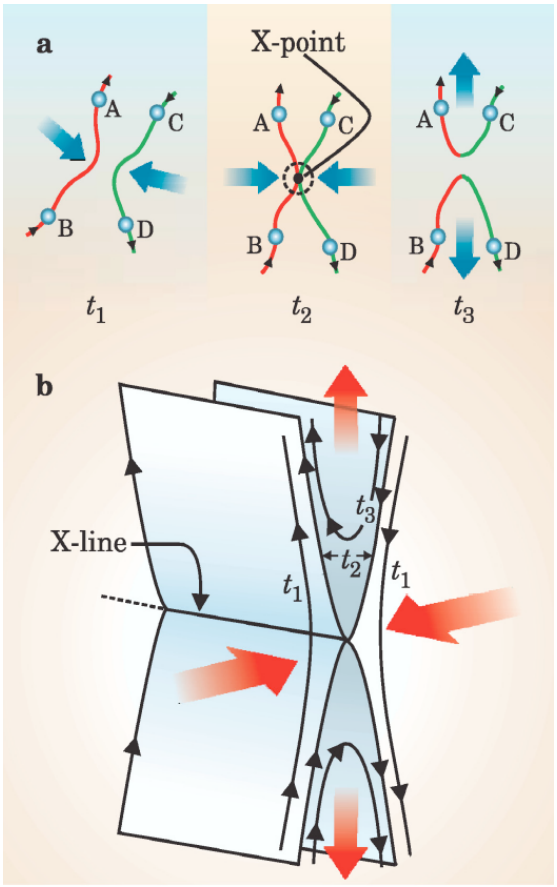

Upper part: In the MHD approximation, the plasma and the magnetic field are frozen together. Two particles initialy connected by a magnetic field line (like A and B, or C and D at the initial time t_1) will stay connected at any later time. However, when two oppositely magnetic field lines move towards each other and touch (at time t_2 in the figure), by the process of magnetic reconnection they break and reconnect at the so-called X-point. A change in the field topology occurs: at a later time t_3 the particles A and C will be on the same magnetic field line, different from the field line connecting the particles B and D. Because the newly reconnected lines are highly bent, the magnetic tension force accelerates the plasma at high speed, converting in this way the magnetic energy into plasma kinetic energy.

Lower part: A 3-D perspective of the reconnection process, taking place along an X-line, linking many X-points. Plasma flows into the configuration with relatively low velocity (indicated by the horizontal lines) and out of it with high-speed (vertical lines). The times t_1, t_2, and t_3 refer to the same phases of the process as in the upper part.

Figure 1.3: The geometry of magnetic reconnection (adapted from *Paschmann* [2006]).

the third dimension) and reaches again the position indicated by $1'$. A plasma flow pattern is thus established inside the magnetosphere.

The relevance of magnetic field reconnection in the magnetospheric physics is two-fold. On one hand, the open field lines enable a strong interaction between the solar-wind and the magnetosphere, stronger than in the case of a 'closed' magnetopause. The tailward convection above the polar cap is one consequence of this interaction. Also, plasma particles from the magnetosheath and from the magnetosphere may cross the magnetopause by moving along the open field lines. Then, because in a plasma the electric currents flow easily along the magnetic lines, the convection electric field associated with the solar-wind maps down to the polar cap ionosphere, producing an electric current oriented roughly from dawn to dusk. In this way part of the solar-wind dynamic energy is transported, via field aligned currents, and deposited in the ionosphere by Joule heating.

On the other hand by converting the magnetic energy into kinetic energy, the reconnection phenomenon accelerates particles. This aspect has a greater importance for the magnetic reconnection in the tail, being the primary explanation for the source of energy released during a magnetic substorm. In both cases, note that, although the reconnection takes place in small regions (indicated by points N_1 and N_2 in Figure 1.4) it has global consequences. That aspect differentiates this physical mechanism from the other candidates, discussed in Section 1.1, for the mass transport across the MP.

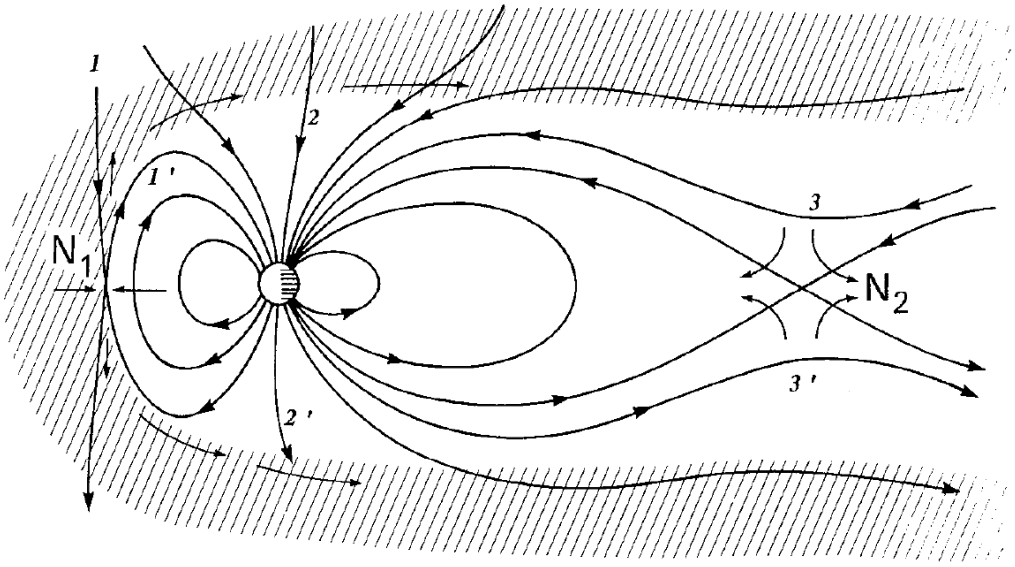

Figure 1.4: An illustration of Dungey's view of open magnetosphere. The southward oriented IMF reconnects with the terrestrial magnetic field at the subsolar point N_1 and the open field lines are carried tailward by the solar-wind. In the tail there is another reconnection point situated at N_2, producing an interplanetary field line and a closed field line. The latter flows sunward, around the Earth, to arrive again in the subsolar region (figure taken from *Stern* [1995]).

The Petschek model was derived for the case of symmetrical magnetic and plasma properties on the two sides of the interface. At the dayside magnetopause, where the magnetic field could have different intensities and arbitrary orientations in the magnetosheath and in the magnetosphere and where plasma densities are usually quite different on the two sides, a modification of wave geometry is needed. The necessary changes were proposed in *Levy et al.* [1964], where the authors concluded that the magnetopause should consist of an intermediate MHD standing wave (a large-amplitude Alfvén wave) followed by a slow-mode expansion fan (see also *Yang and Sonnerup* [1976, 1977]; *Vasyliunas* [1975]). The rotational discontinuity is necessary in order to provide the needed magnetic field twist. Indeed, with only a system of slow-mode waves, the magnetic fields in the up-stream and down-stream regions and the normal to the discontinuity should be in the same plane (coplanarity-theorem). It is precisely this large-amplitude Alfvén wave or rotational discontinuity that is considered characteristic for the magnetopause reconnection and the identification of which allows us to conclude whether such a process is occurring.

Observational evidence

A first class of such evidence consists of observations taken principally on ground (and later by low orbiting satellites) and therefore usually termed *indirect* or *remote evidence*. They refer to the strong correlation between the orientation of the interplanetary magnetic field and the geomagnetic activity. During the periods when the IMF is southward oriented it was observed that substorms are more frequent, the convection in the polar caps exhibits a well defined two-cell pattern and the field aligned currents are more intense. On the other hand, during periods when the IMF is northward oriented, the rate of substorms reduces, the convection becomes more irregular in the polar caps and their dawn-dusk potential drop diminishes. All these observations are in qualitative agreement with the predictions from Dungey's model.

Another effect related to the convection in the polar caps region and explained by the interconnection between the terrestrial magnetic field and IMF, refers to the detected asymmetry in the flow pattern according to the positive or negative orientation of solar-wind magnetic field GSE B_y component. The above mentioned interconnection was extensively proved also by the detection of energetic solar electrons on the polar cap field lines. This type of population is detected only in the polar cap connected magnetically to the Sun, and not in the one connected with the far distant heliosphere.

The second class of evidences refers to the *in-situ observations* of predictions imply by the reconnection mechanism. Detection of the normal magnetic component B_n at the MP would provide the most convincing evidence but this is usually difficult, although it was possible for few events. This is because B_n is much smaller than the tangential magnetic component and any minute uncertainty in the MP orientation would lead to errors in B_n bigger than its actual value. The same thing applies to the direct determination of the normal plasma velocity component V_n. Actually, in the latter case, the situation is even more complicated because the MP is always in motion, typically with normal velocity higher than V_n, and because the plasma velocity is usually measured with a lower accuracy.

The first unequivocal in-situ evidence that the process of magnetic reconnection is operating at the MP was provided by *Paschmann et al.* [1979] (see also *Sonnerup et al.* [1981]) using data measured by the ISEE spacecraft. By testing the tangential-stress balance equation across this discontinuity, the authors showed that, for some selected events, the MP behaved like a rotational discontinuity, i.e. as predicted by the magnetic reconnection models. Part of these events were analyzed for the direct topological connection between the magnetosphere and magnetosheath regions. In this respect strong evidence was provided for magnetospheric particles leaking out into the magnetosheath along the reconnected field lines (see also *Scholer et al.* [1981]). Since then, the tangential-stress balance test, called also the Walén test, established itself as the standard procedure for an RD identification at the MP. Thanks to this, the magnetic reconnection is the only process among the physical mechanisms proposed for explaining the plasma transfer across the magnetopause for which quantitative observational tests are well defined.

Another in-situ evidence of reconnection at the MP refers to how the distribution function is modified when particles streaming along reconnected (open) magnetic field lines, are reflected or transmitted at that boundary. The basic ideas of what we expect to happen was outlined by *Cowley* [1982]. The author analyzed qualitatively the reflection and refraction of individual particles in this region and predicted the shape of the velocity distribution function on either side of the MP by considering the typical populations encountered on the reconnected field lines (i.e the dense, relatively cold magnetosheath population, the high temperature ring current population and the cold magnetospheric population of ionospheric origin). These types of distributions, referred to as D-shape distributions, were later experimentally detected (see for example *Fuselier* [1995]).

By testing the Walén relation on low-latitude dayside MP crossings, *Phan et al.* [1996] found that this boundary behaves like a RD in 61% of the cases when the magnetic shear angle is large (larger than 45 °). It was also found that the orientation of the external magnetic field need not to be exactly antiparallel with the terrestrial magnetic field $\vec{B}_T$ for the occurrence of reconnection. In this respect, *Sonnerup et al.* [1981] proposed the idea that, at the point of reconnection, only an IMF component along the antiparallel direction of $\vec{B}_T$ is necessary. It was also proposed, and later experimentally confirmed, that reconnection may occur during times of northward orientation for the IMF in the regions tailward of the cusps (*Song and Russell* [1992]).

The above in-situ evidence was based on observations taken at the dayside MP, in the region of standing waves from the Petschek model, i.e. far from the reconnection point. The MHD approach is well justified in these region and is successful in catching the aspects related to the conservation of tangential momentum (acceleration or deceleration of the plasma) or (through topological consideration) to infer the position of the reconnection site relative to the measurement location. The effort to understand the microphysics that takes place in the *diffusion region* has been steadily increasing, both on the theoretical and on the simulation front, but there are still some open questions. A detailed experimental investigation of the processes taking place in the diffusion region would require a higher time resolution than the present satellite instrumentation can offer, in order to resolve spatial scales down to the electron inertial lengths. Nevertheles, at the scale of ion-inertial length there are some observations of this diffusion region based on single or multi-spacecraft measurements, consistent with the magnetic reconnection models (e.g. *Mozer et al.* [2002], *Vaivads et al.* [2004]).

Above we pointed out only some of the observational evidence supporing the magnetic reconnection process in the magnetosphere environment. Other experimental confirmations are reported in the literature (see for example the review articles by *Stern* [1996], *Haerendel* [2001] and *Scholer* [2003]).

The present contributions to the study of magnetic reconnection

In the Walén test we check whether the plasma flows at the local Alfvén velocity in the deHoffmann-Teller frame (i.e. the frame in which the flow becomes field aligned). The test proved very successful in establishing whether the MP has rotational character or not, but a long standing issue remains that the factor of proportionality between the plasma velocity in the deHoffmann-Teller frame and the Alfvén velocity is less than one, as required in the theory.

When performing a Walén test we rely on a simple one-dimensional, planar model for the MP. Also, we typically make two assumptions when computing the plasma moments entering in the analysis, namely we neglect the electrons' contribution (due to their much lower mass) and we consider all the ions as being protons (i.e. we neglect the influence of minor ion species, when present). In this thesis we shall study two MP events that allow us to asses experimentally the consequences of these simplifying assumptions. The knowledge of these consequences is important when we have to establish whether the MP behaves like a RD or not in a particular transition event.

We also quantitatively test a relation linking the evolution of plasma density and of the so-called plasma pressure anisotropy factor. This relation should hold for a rotational discontinuity, being based on the same conservation laws as the Walén relation. Using high resolution data and ruling out any other potential explanations, we proved for the first time that this relation is not experimentally supported.

The thesis is organized as follows:
Chapter 2 presents the Cluster mission and the instrumentation that provided the data used in this thesis.

Chapter 3 presents a case of magnetopause crossing by Cluster for which the analysis indicates a 2-D, non-planar geometry. The new timing based method, conceived for investigating such cases is introduced. For the sake of an easier reading, we put all the computational details related to the method in Appendix B.

In Chapter 4, the results of applying the new technique are presented and compared with the results provided by the standard methods. This chapter makes use of Appendix C containing tables and figures for all the solution we found, of Appendix D investigating the stability of the solutions and of Appendix E containing the details of comparing the results obtained in the 2-D case with the results from the planar MVAB method.

Chapter 5 deals with the aspects of reconnection process at the magnetopause discussed above. The details about the deHoffmann-Teller analysis and about obtaining centre-of-mass quantities from the measurements provided by the ion spectrometer on-board Cluster are presented in Appendix F and Appendix H, respectively.

The planar, single-spacecraft techniques of MVAB and MFR appear in Appendix A and Appendix G, respectively.

Chapter 6 contains the conclusions of the thesis.

CHAPTER 2

Satellite and instruments

2.1 The Cluster mission

The Cluster mission is one of the two missions constituting the first 'cornerstone' of the European Space Agency's Horizon 2000 program. Having been proposed in November 1982 by a group of scientists with strong participation from Max-Planck-Institut für extraterrestrische Physik (MPE), Garching, the mission was finally approved in 1986. In 1988 the 11 instruments that make up the science payload were selected from the competing proposals made in 1987, with MPE being heavily involved in two of the instruments. Ready for launch in 1995, the four spaceraft were destroyed when the Ariane 5 rocket exploded on its first test flight in June 1996. After a complete rebuild of the spaceraft and instruments, the four spaceraft were successfully launched in July and August 2000 on two Soyuz rockets from Baikonour, and put into an eccentric polar orbit, with apogee and perigee of about 20 R_E and 4 R_E, respectively. This sets the orbital period at around 57 hours. After an extensive commissioning phase of all instruments, routine science operations began in February 2001. The mission is expected to continue until at least 2009.

The four Cluster spaceraft carry identical instruments and are flying in close formation. Four is the minimum number of points needed to make measurements in three dimensions, necessary to resolve spatial from temporal variations in the measured time-series, a capability that was missing in all previous missions. For this purpose the four Cluster spacecraft are arranged in a tetrahedron configuration, with separation distances that have ranged between 100 and 20000 km in the course of the mission. The control of the inter-spacecraft separation is achieved by periodically (typically every 6 month) activating from ground the spacecraft's own propulsion systems, the basic goal being to revisit the key magnetospheric regions and obtain a picture of the important phenomena at different scales. These regions are predominately the solar wind and the bow shock, the magnetopause, the polar cusps, the magnetotail and the auroral zones. In Figure 2.1 we present the Cluster orbit in winter (when the apogee is situated in the magnetospheric tail) and in summer (when the satellite is able to cross the outer boundaries of the magnetosphere and reach the solar wind), together with the key magnetosphere regions encountered.

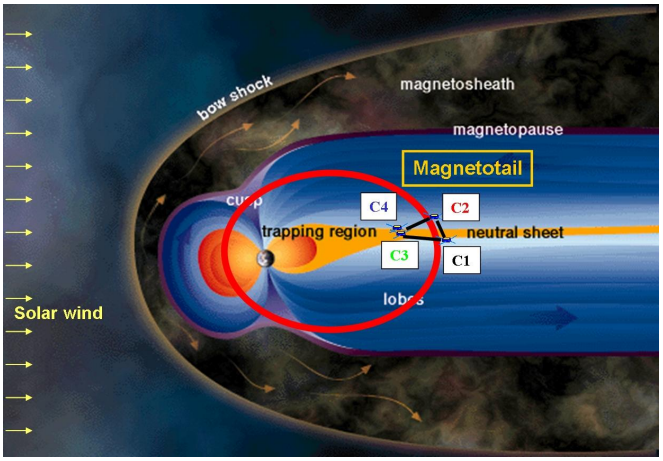

Cluster orbit (in red) with the apogee in the magnetotail. The spacecraft configuration is shown (not at scale), with C1, C2, C3 and C4 designating the four satellites. The key regions of the cusp and plasma sheet are encountered.

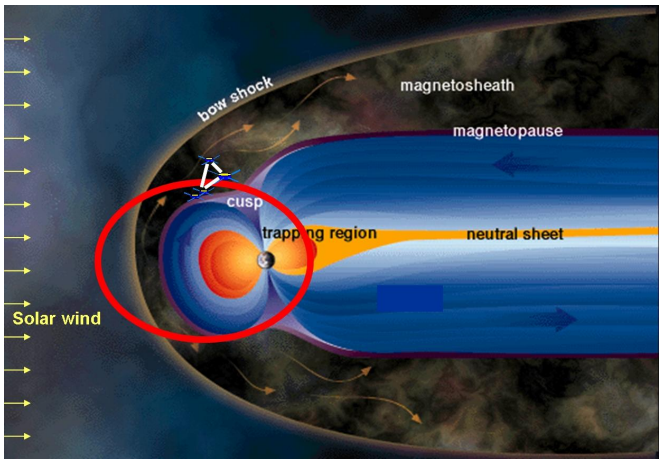

Cluster orbit with the apogee in the solar wind. The key regions of the cusp, magnetopause, bow-shock and solar wind are encountered.

Figure 2.1: Cluster orbit in winter (upper picture) and in summer (lower), together with the key magnetosphere regions encountered (credit to http://sci.esa.int/)

Data from the 11 instruments are stored on board and periodically transmitted to the ground. The data are processed by a network of eight national data centers, of which the German one is hosted by MPE, Garching. The final data products are kept on-line and made available to the scientific community.

2.2 The satellite payload

The CIS instrument

The objective of the Cluster Ion Spectrometry (CIS) experiment (*Rème et al.* [2001]) is to measure the three - dimensional velocity distribution function of ions. It consists of two separate sensors: the Hot Ion Analyser (HIA) and the COmposition and DIstribution Function (CODIF) analyser. In Figure 2.2 we present the schematic of CODIF and its operational principles. The figure applies also to HIA, the only difference between the two instruments being that the latter does not provide mass resolution.

The HIA instrument employs a 'top-hat', toroidal electrostatic analyser (EA) and a fast imaging detection system, based on micro-channel plate (MCP) technology. The ions incident

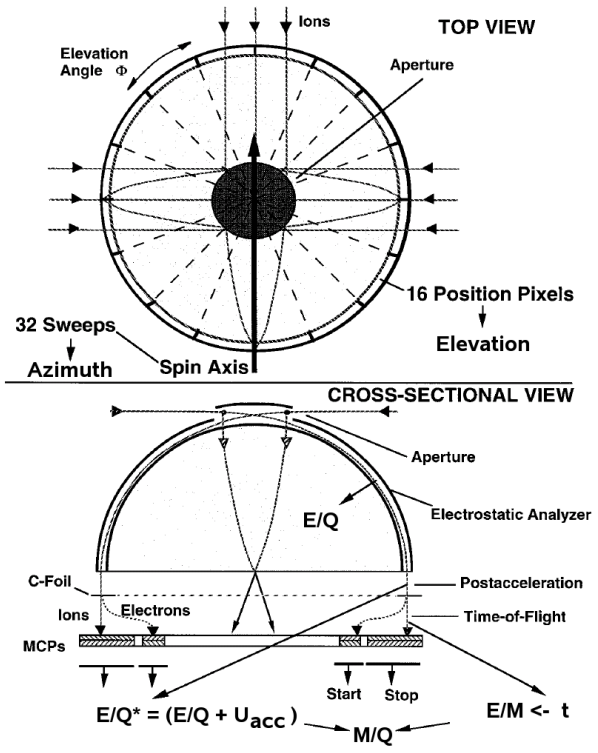

Upper part: Top view. The instrument axis of symmetry (out of the paper, at the center) is perpendicular to the spacecraft spin axis. The spin provides in this way the azimuthal coverage. Trajectories of ions are shown in order to ilustrate the focusing effect of such an analyser: after entering through the aperture, a parallel ion beam will be deflected 90 ° (as shown in the lower part of the figure) and focus at a certain location on the exit plane.

Lower part: Cross-sectional view. Behind the electrostatic analyser, which selects the particles acording to E/Q, the ions are post-accelerated and enter the time-of-flight section. Here, they first hit a semi-transparent Carbon foil, producing secondary electrons that are collected and thus provide the start time signal. The stop signal comes from the MCP at the end of the ions' flight path. Knowing E/Q, the energy gained in the post-accelerating section and the time-of-flight allows the determination of M/Q. Only one particle is analysed by the sensor at a time.

Figure 2.2: The schematic of the CIS/CODIF instrument and its operational principles (adapted from *Klumpar et al.* [2001]).

on the instrument entrance aperture, consisting of two narrow, 180 ° fans in polar angle (elevation angle ϕ in Figure 2.2) are deflected by the EA and instantaneously recorded on the exit plane by a system of position encoding discrete anodes. Ion energies from 5eV to 32 keV are sequentially measured by rapidly varying, in logarithmically spaced steps, the voltage across the hemispherical EA plates. Since EA's deflection selects particles based on energy/charge (E/Q), the HIA instrument cannot resolve different ion species that have the same E/Q. Coverage in azimuthal angle is achieved by utilizing the satellite spin. The spin rate of 15 rpm then sets the time-resolution of the measurements at 4 s. To accommodate the large dynamic range of ion fluxes that occur in different regions of the magnetosphere, the two 180 ° fans provided by the top-hat analyser have geometric factors that differ by a factor of ~ 25.

The CODIF instrument differs from HIA by an added time-of-flight section, following the E/Q selection by a 'top-hat' EA. In order to obtain the start-signal needed for the time-of-flight measurement, a thin, $\sim 3\mu g/cm^2$ Carbon foil is inserted into the particle's path. By hitting the foil, secondary electrons are produced and collected by a strongly focusing electron optics. To cross the Carbon foil, the particles need first to be accelerated by a voltage of about 15 kV after leaving the electrostatic analyser. The stop signal comes from the MCP at the end of the particle flight path. Knowledge of E/Q, of the post-accelerating voltage and of the time-of-flight allows the determination of the mass/charge (M/Q). In the magnetospheric environment, this actually means that CODIF is able to distinguish the presence of major species, namely H^+, He^{2+}, He^+ and O^+. As HIA, CODIF also has two largely different (by a factor of ~ 100) geometric factors for the two 180 ° polar angle sections. The energy range

for CODIF is from 20 eV to 40 keV. With an additional Retarding Potential Analyser device, mounted in the aperture system of the sensor, the lower limit of the energy range is extended to the spacecraft potential.

The two sensors, HIA and CODIF, complement each other in terms of sensitivity, mass resolution, and detection efficiencies. Both instruments involve extensive on-board data processing, including the computation of the moments of the velocity distribution functions (density, bulk velocity vector, pressure tensor, and heat flux vector). These moments are computed and transmitted to the ground every spin period (i.e., about 4 s), which is about the gyration period of the protons in a magnetic field of 16 nT. In the computation process the on-board processing software uses a table of efficiency coefficients. For CODIF, the efficiency depends on the energy and angular sector ϕ. However, because of limited memory resources, only an average (over ϕ) energy dependence is implemented. This results in inaccuracy of the CODIF on-board moment calculation, particularly in the later time of the mission, when asymmetric 'aging' of the angular sectors occur. For the HIA detector the efficiency is much larger, primarily because this sensor has no TOF section, and the on-board moments are not suffering from this problem.

The transmission to the ground of the complete 3-D distribution function (i.e. at full angular and energy resolution) is not possible due to the limited telemetry rates allocated to CIS. For example, in case of HIA it would require the transmission, every 4 seconds, of a matrix having `256 energy channels` × `16 elevation angles` × `32 azimuth angle` = `131072` elements, whereas in case of CODIF, four matrices (one for each ion species) of `128 energy channels` × `8 elevation angles` × `32 azimuth angle` = `32768` elements each. Therefore reduced distribution function (typically corresponding to `31 energy channels` × `88 angular directions` are computed on-board and transmitted to the ground with a time resolution of multiple spin periods.

Based on these reduced distribution functions, a set of ground computed moments are calculated. The efficiency coefficients used in this calculations are obtained after extensive inter-calibration (between satellites and also by using measurements provided by other experiments). Both the energy and the angular dependencies of the efficiency are considered in this process and therefore for CODIF the ground moments are usually more reliable than the on-board moments. In the thesis, both types of moments are being used.

For the CODIF instrument, each event is analyzed by first comparing the time-of-flight information with a set of thresholds: based on that the on-board software decides about the particle species. In the presence of large proton fluxes CODIF is affected by a 'spillover' effect, by which the sensor registers false counts in the He^+, He^{2+} and O^+ channels. The amount of this effect was measured in the pre-flight calibrations and has been quantitatively considered in the thesis.

Another issue with relevance to our thesis is the instrument saturation in plasma regions characterized by high proton fluxes (like in the magnetosheath). In case of CODIF, the more complex electronics sets a threshold for the particles counting rate: above roughly 100kHz significant dead-time effects occur, resulting in less reliable measurements. This threshold is much higher in case of HIA, which is thus practically unaffected in this respect.

The sensors were calibrated with particle beams in the laboratory before launch. The unavoidable degradation of the efficiencies of the channel-plate detectors with time (or accumulated charge) has required continued in-flight calibration.

MPE has provided the analog electronics, the MCP's, the post-acceleration and MCP's high voltage sections for the CODIF instrument, while the main responsibility was with Centre d'Etude Spatiale des Rayonnements in Toulouse.

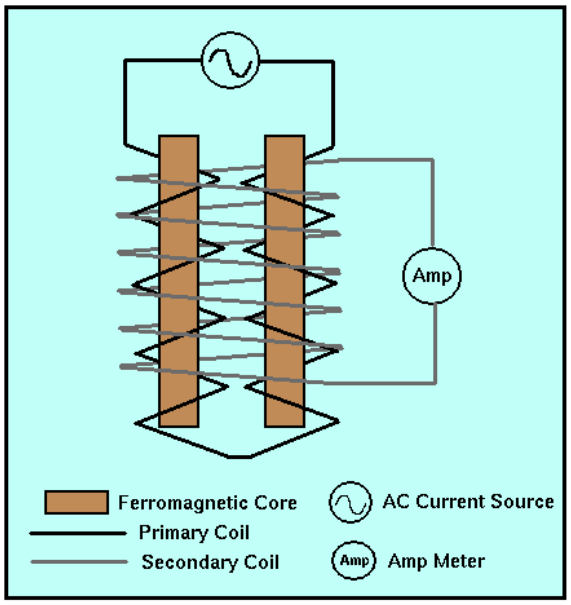

Figure 2.3: The schematic of a magnetic saturation circuit (taken from http://www.earthsci.unimelb.edu.au).

The FGM instrument

The flux-gate magnetometer FGM (*Balogh et al.* [1997]), provided by Imperial College London, with contributions from Technische Universität Braunschweig, measures the DC magnetic field vector with a tri-axial flux-gate sensor mounted at the end of a 5 m boom that was deployed after launch. Another sensor half-way down the boom helps identify spurious magnetic fields generated by unavoidable magnetic materials and currents on the spaceraft. FGM typically returns 22 samples per second.

Flux-gate magnetometers (also know as Förster-Sonde in German) determine the ambient magnetic field based on a so-called magnetic saturation circuit. A simplified schematic is presented in Figure 2.3. The primary coil is wrapped in opposite direction around two bars of ferromagnetic material. A periodic bipolar current is applied to the primary coil to drive each ferromagnetic core through an alternating cycle of magnetic saturation (i.e. magnetized - unmagnetized - inversely magnetized - unmagnetized - magnetized). When no external magnetic field along the cores direction is present, the induced magnetic fields in the cores have all the time the same strength but opposite orientation. Consequently, the voltage detected in the secondary coil would be zero. In the presence of an external field component, the induced field in one core will reach saturation at a different time from the other core. This difference will induce a voltage in the secondary coil, proportional to the strength of the external magnetic field.

In case of Cluster, a ring core configuration instead of the parallel core design is used, primarily because the latter requires high drive powers. There is one ring core to measure the field component along each of the three axes. As magnetic fields are small, ranging from a few nT in the solar wind to tens of nT at the magnetopause, careful calibration before launch and in flight is necessary. This is particularly important for identifying offsets in the component along the satellite spin axis, non-orthogonalities of the three sensors, miss-alignments of the boom, etc. An accuracy of about 0.2 nT has been achieved, helped by comparison with the electron gyro time measurements obtained with MPE's Electron Drift Instrument, EDI.

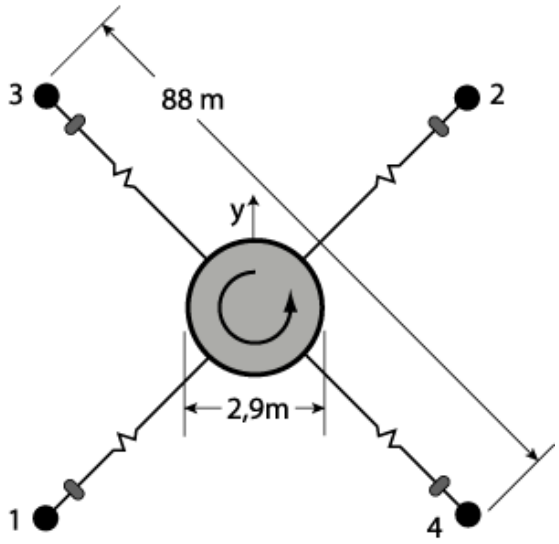

Figure 2.4: The schematic of the EFW experiment. The spherical probes are placed in the satellite spin plane on four wires booms, forming a cross with the spacecraft in the center (adapted from http://cluster.irfu.se/efw/)

The EFW instrument

The Electric Field and Wave instrument, EFW, (*Gustafsson et al.* [2001]) provided by a group under the responsibility of Swedish Institute of Space Physics, Uppsala, measures the ambient electric field using two pairs of spherical probes put at the end of four wire-booms. The booms were deployed in the spacecraft spin-plane after the spacecraft reached their final orbits. The voltage differences between the probes is determined and divided by the (effective) probe separation distance. Measurements of the spherical probes potential with respect to the spacecraft are also used as a measure of the ambient plasma density.

The distance from the satellite center to each boom tip is 44 m. Typical magnetospheric electric fields are of order 1 mV/m, the total voltage difference between two probes extended in opposite directions is only about 88 mV. Since Cluster carries no axial booms, the electric field component along the spacecraft spin axis is not measured and the instrument thus returns only a two-dimensional electric field vector in the spin-plane. Under favourable conditions the missing component can be inferred under the assumption that $\vec{E} \cdot \vec{B} = 0$.

In the magnetospheric environment there are two competitive processes that cause the probes to assume a potential different from the surrounding plasma potential. On one hand, under the influence of the sunlight, a conducting sphere will become positively charged due to the emission of photoelectrons. On the other hand, a conducting sphere placed in a plasma medium will be continuously struck by both electrons and ions. The electrons having a higher mobility, will hit the probe more often and cause the probe to become negatively charged. As soon as the above processes affect the probes to the same degrees, the potential difference between them will not be influenced. On the contrary, the measurement can be adversely affected from asymmetric photoelectron clouds, non-uniform surface properties of the probes or wake effects from cold plasma flows.

In the normal telemetry mode, the EFW instrument provides the two electric field components in the spin plane at 25 samples/s. The time resolution is increased to 450 samples/s in the burst telemetry mode.

Other Cluster instruments

The purpose of the Cluster instruments not used in this thesis are as follows:

ASPOC. When the spacecraft are in sunlight, photoelectrons from solar UV radiation hitting the spacecraft surfaces are able to leave the spaceraft until the spacecraft is charged sufficiently positive that no further electrons can leave. The resulting positive spacecraft potentials, which can reach up to hundreds of Volts, have obvious detrimental effects on the measurement of low-energy particles. ASPOC (for Active Spacecraft POtential Control) uses positive Indium ion beams, emitted along the spaceraft spin axis, to counter the effect of the photoelectrons and reduce spaceraft charging to just a few Volts.

EDI. The Electron Drift Instrument determines the ambient electric fields $\vec{E}$ by emitting two 1-keV electron beams and measuring the displacement of the beams that results from the $\vec{E} \times \vec{B}$ drift. When no electric field were to exist in the frame of the spacecraft, the electrons would return to their origin after one gyration in the ambient magnetic field. In the presence of an electric field, however, the electrons only return to the spacecraft when emitted in one of two specific directions that are determined by the instantaneous magnitude and direction of $\vec{E}$. To find those directions, the electron beams are swept in the plane perpendicular to the magnetic field (provided in real-time by the FGM instrument) until dedicated detectors indicate that the beams have been detected.

PEACE. This instrument, whose acronym means Plasma Electron And Current Experiment, measures the three-dimensional velocity distribution functions of electrons with energies selectable in the range between about 1 eV and 27 keV, using two top-hat electrostatic analyzers that include micro-channel plates as detectors. Full energy and angle coverage is obtained in a similar fashion to that of the ion instruments within CIS. The two PEACE sensors, mounted on opposite sides of the spacecraft, can either be operated with different energy ranges, or be combined to double the time resolution. Moments of the distribution functions are computed on board every spin period, much like on CIS. Three-dimensional distribution functions can be reduced on board to two-dimensional pitch-angle distributions.

RAPID. This instrument, whose acronym means Research with Adaptive Particle Imaging Detectors, measures energetic electrons from 20 to 400 keV and ions between about 40 keV and several MeV, depending on the ion species. To distinguish the different species, the instrument employs a time-of-flight section, with the start signal coming from an Aluminium covered Lexan foil, and the stop signal from a solid state detector that also records the particles' energy. Three sensor heads cover the 180 degrees polar angle range, whereas the azimuth angle range is covered by utilizing the spaceraft spin, much like for the CIS and PEACE plasma instruments.

DWP. The Digital Wave Processor controls the operation of the EFW, WHISPER, STAFF and WBD instruments. It also performs data compressions and includes a particle correlator.

STAFF. This instrument, whose name is taken from Spatio-Temporal Analysis of Field Fluctuations, is a boom-mounted three-axes search coil magnetometer, measuring magnetic field waveforms up to 10 Hz or 180 Hz depending on the chosen operational mode. It includes a digital spectrum analyser that also receives electric field data from the EFW instrument, and thus is able of computing in real-time cross-spectral matrix from three magnetic and two electric field components.

WBD. The Wide BanD instrument processes the signals from any one of four electric and magnetic field antennas, two of the probes of the EFW instrument, the other two from the STAFF instrument. It provides very high-time resolution measurements of plasma waves in the Earth's magnetosphere. The input frequency range can be shifted to any one of four ranges, starting at 0, 125, 250, or 500 kHz.

Table 2.1: Cluster instruments and the corresponding Principal Investigators.

Nr.	Acronym	Instrument description	Principal investigator
1	ASPOC	Active Spacecraft Potential Control experiment	**K. Torkar** (Space Research Institute, Austrian Academy of Sciences, Austria)
2	CIS	Cluster Ion Spectrometry experiment	**H. Rème** (Centre d'Etude Spatiale des Rayonnements, France)
3	EDI	Electron Drift Instrument	**G. Paschmann** (Max-Planck-Institut für extraterrestrische Physik, Germany)
4	FGM	Fluxgate Magnetometer	**A. Balogh** (Imperial College, UK)
5	PEACE	Plasma Electron And Current Experiment	**A. Fazakerley** (Mullard Space Science Laboratory, UK)
6	RAPID	Research with Adaptive Particle Imaging Detectors	**P. Daly** (Max-Planck-Institut für Aeronomie, Germany)
7	DWP	Digital Wave Processing experiment	**H. Alleyne** (University of Sheffield, UK)
8	EFW	Electric Field and Wave experiment	**M. André** (Swedish Institute of Space Physics, Sweden)
9	STAFF	Spatio-Temporal Analysis of Field Fluctuation experiment	**N. Cornilleau** (Centre d'Etudes des Environnements Terrestre et Planétaires, France)
10	WBD	Wide Band Data instrument	**D. Gurnett** (University of Iowa, USA)
11	WHISPER	Waves of High frequency and Sounder for Probing of Electron density by Relaxation experiment	**P. Décréau** (Laboratoire de Physique et de Chimie de l'Environnement, France)

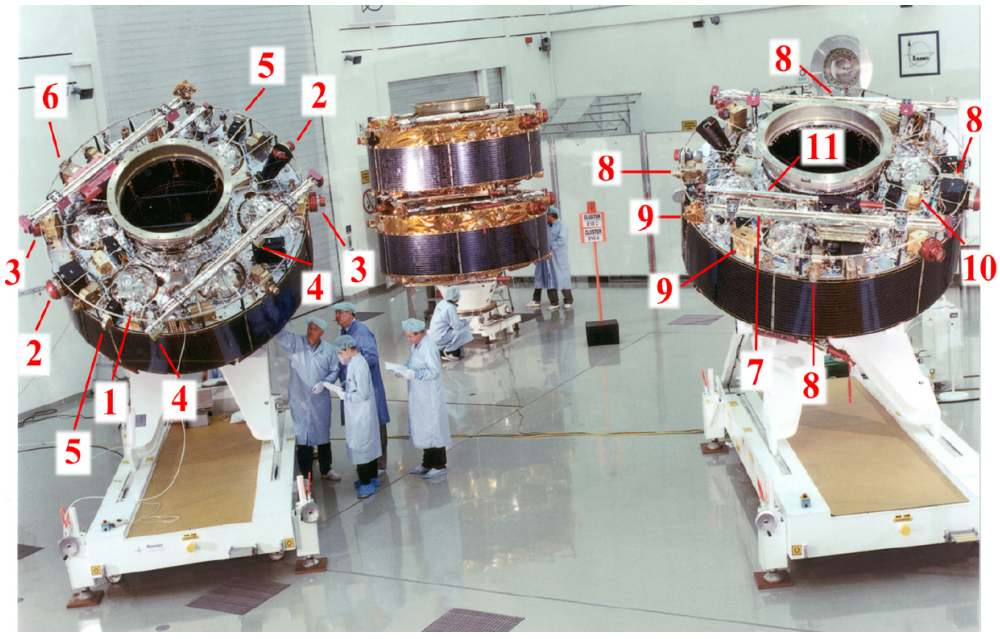

Figure 2.5: Cluster at the Industrieanlagen-Betriebsgesellschaft test facility in München (adapted from *Escoubet et al.* [2001]). The numbers indicating the position of instruments correspond to the left-most column in Table 2.1.

WHISPER. This instrument, whose acronym means Waves of HIgh frequency and Sounder for Probing of Electron density by Relaxation, serves two functions. First, it measures the AC electric fields up to a frequency of 80 kHz, which includes all the characteristic frequencies of the waves in the plasmas that Cluster encounters, utilizing the voltages recorded on the probes of the EFW instrument. Second, it periodically puts large voltage pulses on those probes in order to trigger wave emissions at the plasma frequency, from which the plasma density can be derived.

The teams responsable for the field and wave experiments on-board Cluster (i.e. DWP, EFW, STAFF, WBD and WHISPER) are forming the Wave Experiment Consortium, designed to coordinate their efforts in terms of experimental operation and in utilizing the limited spacecraft resources.

CHAPTER 3

A new technique for determining orientation and motion of a non-planar magnetopause

In this chapter we will present a case of magnetopause (MP) crossing by Cluster for which the analysis indicates a 2-D, non-planar geometry. Consequently, when determining the macroscopic properties of this discontinuity, viz. its orientation, motion and thickness, the existing single-satellite methods fail to provide the correct answer. The reason is that all these techniques are relying on the planar assumption for the MP. We are proposing a multi-satellite, timing based method that models the boundary between the magnetospheric and magnetosheath plasma as a 2-D, non-planar layer of constant thickness. This is a natural improvement of the standard, multi-satellite, timing technique that assumes a planar layer of constant thickness for the MP.

The content of the chapter is the following: in the first section, a brief review of the standard multi-satellite timing technique, build on the planar assumption for the MP, is provided. Then the newly developed methods, conceived for investigating 2-D, non-planar discontinuities, are introduced. This first two sections make strong use of Appendix B, where all the details of computation are presented. Starting with Section 3.3 we introduce the event from 24 June 2003, providing evidence in support of a 2-D, non-planar MP encounter by Cluster. The input parameters needed in applying the timing analysis are then extracted from the data.

3.1 The timing analysis procedure in the planar case

In a timing analysis, the instants of time when the four Cluster satellites encounter the MP are used. This information could in principle be obtained from any physical quantity that displays a significant change across the discontinuity. However, in our study we choose to use the magnetic field data because of its higher time resolution and smaller measurement uncertainties compared to other types of data.

The methods used so far in determining the MP orientation, motion and thickness that rely on timing information alone, assume a planar geometry. More specifically, we have the method which considers the MP is moving with a constant velocity across the four spacecraft (constant velocity approach or CVA technique), and the method which assumes it has a constant

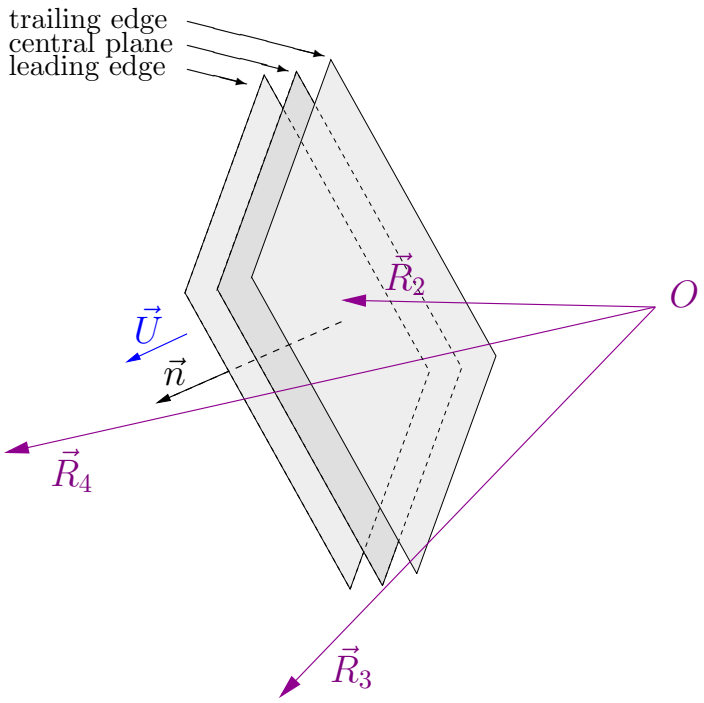

Figure 3.1: A sketch of a planar magnetopause moving past the Cluster satellites location. The first spacecraft detecting the MP is located at O, whereas the other three satellites have the relative positions indicated by $\vec{R}_2$, $\vec{R}_3$ and $\vec{R}_4$. The central plane, together with the leading and trailing MP edges are shown. The velocity $\vec{U}$ is oriented along the normal $\vec{n}$ in this model, being a constant vector in the CVA approach. In the standard implementation of CTA, the distance along $\vec{n}$ travelled by the central plane during each crossing time is constant, whereas in our variant of CTA the distance between the MP edges is constant.

thickness during the same interval (constant thickness approach or CTA technique). They are discussed in detail in *Haaland et al.* [2004b] and, since we will cite this work very often, we call it hereafter the *CTA paper*.

The planar methods of CVA and CTA are presented at length in Section B.1. Here we will only point out the underlaying ideas, using for illustration Figure 3.1, which is identical to Figure B.1. In this picture, the first satellite to encounter the MP is situated at O, whereas the other three satellites location are indicated by the relative position vectors $\vec{R}_2$, $\vec{R}_3$ and $\vec{R}_4$. The orientation of the MP surface is specified by the normal $\vec{n}$ and only the motion along this direction has a physical significance.

In the CVA method, first introduce by *Russell et al.* [1983] and called there the *time of arrival method*, one uses the central crossing times, i .e. the times when the central MP plane is detected by each satellite. We chose as origin of space the position of the first satellite to encounters that plane (O in Figure 3.1). The unitary vector $\vec{n}$ and the normal speed U, assumed constant, are the three unknowns that can be determined from a linear system of equations. These equations express the conditions that the relative positions of the other three satellites $\vec{R}_2$, $\vec{R}_3$ and $\vec{R}_4$ be situated on the central plane at the right time, i.e. in accordance with the timing information. Then, from the individual crossing durations we can compute the MP thickness at each satellite.

In the case of the CTA method, as introduced in the *CTA paper*, we determine the MP orientation and its normal velocity, assuming a polynomial time dependence for the latter.

This is achieved by imposing, apart from the conditions referring to the central plane, that the MP travels the same distance during the individual crossings. This makes a total of 7 equations from which one finds the MP thickness, the unitary vector $\vec{n}$ and 4 polynomial coefficients to describe the time evolution for the MP normal velocity.

In Section B.1 we proposed a variant of CTA that uses the times when each satellite detects the MP leading and trailing edges, i.e. not the central plane. The two CTA implementations do not necessarily give the same results (as will be seen for our test case); only when, for each individual crossing, the distance travelled by the MP in the first half-time is the same as in the second half the results will be identical. As will be seen, this way of using the timing information is proposed for the 2-D, non-planar techniques as well.

Procedure for obtaining the timing information

The times that enter in the timing method are obtained by the following procedure:

First, for each satellite the data interval corresponding to the magnetic field transition is selected, together with some small adjacent intervals of relatively constant magnetic levels in the magnetosheath and in the magnetosphere. Then a minimum variance analysis of the magnetic filed (MVAB) is performed (see Appendix A) and the magnetic data are transformed into the reference frame associated with the MVAB result (the one with the axes along the minimum, intermediate and maximum magnetic variance directions, respectively). According to the MVAB theory, the minimum variance direction is associated with the surface normal if the MP behaves locally (i.e. at the position and for the crossing duration corresponding to the satellite in question) as a planar, one-dimensional and time-stationary discontinuity.

For extracting the timing information, the components along the maximum-variance direction are used. After the first step, the data are most probable not in the same coordinate system because the MVAB analysis will not provide exactly the same direction in space for all satellites. This is either because the MP is not planar (judging at the scale of inter-spacecraft separation distance and for the time interval that includes all four crossings), because of the temporal changes in $\vec{n}$, or due to the inherently present fluctuations or measurement errors. In case of a 2-D MP assumption, where indications exist that non-planar effects are responsible for the different normal orientation, these maximum variance components will be used directly. On the other hand, in the case of planar assumption we have to proceed consistently and extract the timing information from the magnetic profiles in the same reference system for all the four satellites. Therefore we use the maximum-variance components in a coordinate system associated with an 'average' normal, obtained by some average procedure from the individual normals (for example by using the direction that corresponds to the vectorial sum of the four normals or by applying the minimum variance algorithm on these four individual normals).

The selected magnetic traces are then fitted assuming a certain time dependence for the magnetic profile at the MP. In the *CTA paper* a Harris sheet type profile was employed and we will use the same dependence when applying the new technique on a test case. More precisely, the following temporal dependence for the maximum-variance magnetic field component is used:

$$B(t) = B_0 + \frac{1}{2}\,\Delta B\; tanh\left[\frac{t - T_c}{\tau}\right] \tag{3.1}$$

Next a definition of the MP thickness is proposed. To give an example, we refer again to the *CTA paper* where for the profile described in equation (3.1) the MP thickness was defined as corresponding to the time-interval centred on T_c and of length 2τ. This, in turn, corresponds

to the region where the fitted magnetic component changes by the quantity

$$\Delta B \, \frac{e^2 - 1}{e^2 + 1}$$

i.e. approx. 76% of the total variation ΔB between the asymptotic levels in the chosen dependence.

In case of the standard planar methods the needed times are the central crossing times T_{ci} and the half-time crossing durations τ_i. For the variant of the planar CTA method that we developed and for the 2-D methods we will use the moments $M_{i1,2}$ corresponding to the MP edges encounter, namely

$$M_{i1} = T_{ci} - \tau_i \quad \text{and} \quad M_{i2} = T_{ci} + \tau_i, \qquad i = 1...4$$

Arguments for the constant thickness approach
Since the 2-D method to be developed in this chapter relies on the assumption that the MP has a constant thickness during the entire event and for the scale-length of inter-spacecraft separation distance, we would like to underline here the arguments in favour of such hypothesis as opposed to the arguments in favour of a constant velocity approach (from *CTA paper*):

- Due to its low mass per unitary cross-section, the magnetopause will experience big acceleration in case of a relatively small pressure imbalance. On the other hand, the compression in the same condition is relatively small (of the order of a few percent).
- Experimental evidence supports the idea of a MP having rapid changes in the normal velocity over time-periods comparable with the crossing duration by the Cluster formation, while the variation of its thickness remains relatively small (*Dunlop et al.* [2001], *Dunlop et al.* [2002a]).

The above arguments by no means exclude the possibility of large variations in the MP thickness during a crossing event. However, such a behaviour is expected to be caused not by a pressure imbalance but because of convecting phenomena at the MP surface or because of some internal processes. Also, the arguments could not be used to draw conclusions about thickness at points well apart on its surface (case of large inter-spacecraft separation).

Whether the constant thickness assumption is valid or not depends on the particular case. Nevertheless, when developing this method we have in mind the published experimental results (see for example *Haaland et al.* [2004b] and *Haaland et al.* [2004a]) and several events analyzed by us, where the planar CTA method proved successful. If the conditions are almost stationary and their spatial gradients are small enough we have no reason to believe that the MP thickness differs much from one point to another on its surface. As will be seen, the new technique is not restricted to cases when the inter-spacecraft separation distance is big (see the discussions on Section 4.5).

3.2 The timing method for a 2-D, non-planar magnetopause

We now extend the timing technique for determining the MP orientation, motion and thickness in cases when indications are present that this discontinuity could not be locally modeled as a simple planar layer but has a two-dimensional shape instead. This is the situation, for example, when in one MP traversal made by the four Cluster satellites, the minimum variance analysis of magnetic field data sampled by each spacecraft gives different normals to this discontinuity

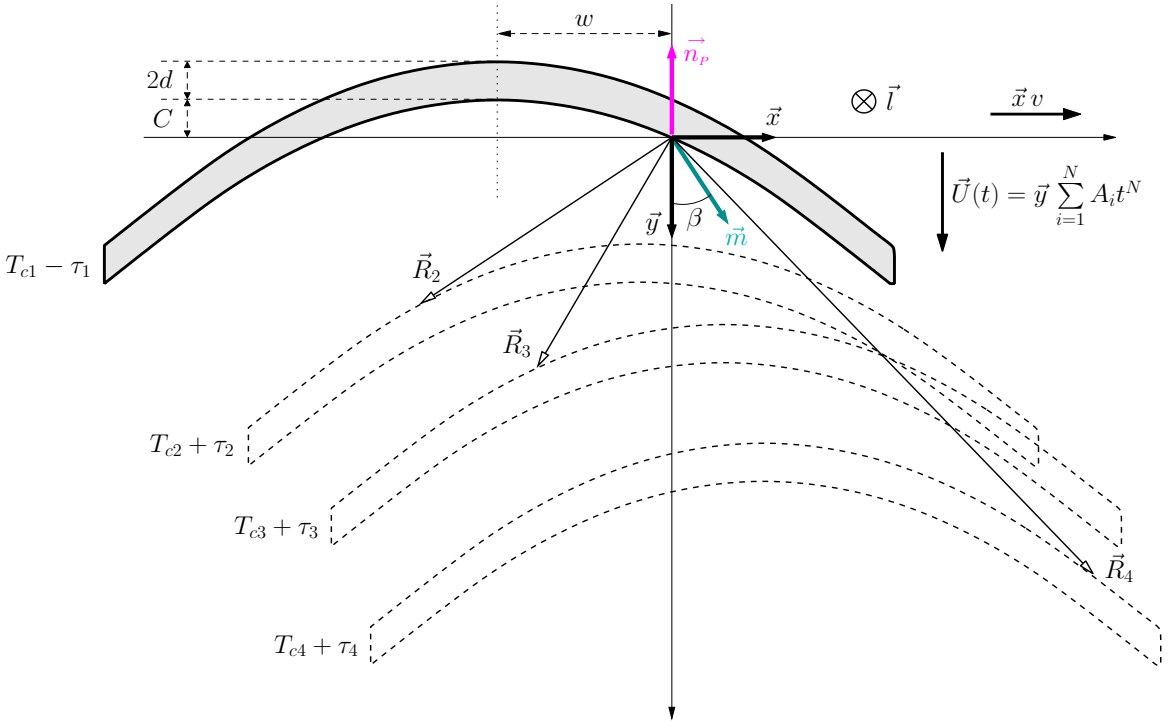

Figure 3.2: Magnetopause cross-sections in the plane normal to the invariant direction at successive moments. $\vec{y}$ designates the primary direction, along which the MP velocity is described by a polynomial time dependence and the layer has a constant thickness. The secondary movement, allowed in one variant of this model, takes place along $\vec{x}$. We depict here the situation when $\vec{n_P}$ (the unit vector along the parabolas axes pointing to exterior) is anti-parallel to $\vec{y}$. The Cluster satellites are located at $\vec{R}_i,\ i = 1...4$ with $\vec{R}_1 \equiv 0$. At the initial time $T_{c1} - \tau_1$, the MP leading edge encounters the first satellite at origin: in the other three configurations shown, the MP trailing edge is detected by satellites 2 to 4 at $T_{ci} + \tau_i,\ 2 = 1...4$. The initial coordinates (w, C) of the leading edge apex as well as the MP thickness $2d$ are indicated. Other quantities appearing in this figure are introduced in the text.

- the reason for that not being the inherently orientation errors resulting when working with experimental data - and, in addition, when all normals lye approximately in the same plane. The new method, to be introduced in this section, assumes that the direction perpendicular to this plane (designated by the unit vector $\vec{l}$) is an invariant direction for the MP. In such a case we have locally modeled the MP either as a parabolic layer of constant thickness or as a cylindrical layer, whose invariant axis lies along $\vec{l}$. We allowed for the layer to have either a simple movement along one direction in the plane perpendicular to $\vec{l}$, or a motion along two perpendicular directions in that plane.

In Section B.2 and Section B.3 all the details pertaining to the newly developed method are presented: here we will only outline their principal characteristics.

The parabolic layer model

In the first attempt to describe the orientation and motion for a 2-D, non-planar MP, we represent it as a parabolic layer of constant thickness, capable of moving in the plane perpendicular to the invariant direction $\vec{l}$. In Figure 3.2, which is a simplified version of Figure B.2 from Appendix B, we show the MP cross-section perpendicular to $\vec{l}$ (pointing into the paper) at different successive moments. The layer is allowed to move in the plane of the paper either

only along $\vec{y}$, i.e. parallel to the parabola's axis of symmetry, according to a polynomial time dependence for the velocity or it is allowed to have in addition a movement along $\vec{x}$ with constant velocity. By constant thickness we mean that the distance along $\vec{y}$ between the MP leading edge and trailing edge is the same (or, equivalently, that the MP trailing surface is obtained by a parallel displacement along $\vec{y}$ of the MP leading surface).

In this picture, the first satellite to encounter the MP is situated at the reference frame origin, whereas the location of the other three satellites are indicated by the relative position vectors $\vec{R}_2$, $\vec{R}_3$ and $\vec{R}_4$. The vector $\vec{n}_p$, lying parallel to the axis of symmetry but pointing to the exterior, is introduced for a simpler characterization of the MP topology, namely its orientation will tell us finally if the spacecraft encounter a bump or an indentation in the MP. We chose to represent the situation when it is anti-parallel to $\vec{y}$ and when also a tangential velocity is present. Whether $\vec{n}_p$ and $\vec{y}$ are parallel or anti-parallel and whether the tangential movement is along $+\vec{x}$ or along $-\vec{x}$, depends on the actual timing information and results directly from the algorithms to be described.

By proposing a parabolic shape we intent to describe two features of the actual MP: its nonplanarity and, by allowing for a second degree of freedom, the large scale waves that often travel along this surface. Indeed, in cases when the solution obtained by applying this method gives surface normals at each spacecraft level close to $\pm\,\vec{n}_p$ then the transversally moving parabolic shape (i.e. along $\pm\,\vec{x}$) is a good approximation for a travelling sine wave.

Using the procedure described in Section 3.1, with the particularities required when a 2-D MP is analyzed, we extract from the data the times when each spacecraft encounters the MP leading and trailing edges ($M_{i1} = T_{ci} - \tau_i$ and $M_{i2} = T_{ci} + \tau_i, \quad i = 1...4$). Then, knowing the relative positions of the satellites, we can impose a set of 8 conditions (corresponding to 2 conditions for each spacecraft) on the MP shape, thickness, direction of movement and velocity time dependence. Specifically, the unknown quantities to be found in this model are (see Figure 3.2; further explanations are given in Section B.2):

- ▷ the direction of the *primary* movement (i.e. along $\vec{y}$), specified by the angle β with respect to a reference direction in the plane perpendicular to $\vec{l}$. As reference direction we chose the vector $\vec{m} = \vec{R}_2 \times \vec{l}$
- ▷ the spatial scale of the structure, given by the quadratic coefficient a of the parabola
- ▷ the MP half-thickness d
- ▷ the initial position of the MP, specified by the coordinates w and C in the plane perpendicular to $\vec{l}$
- ▷ polynomial coefficients for describing the velocity time dependence (the remaining three unknowns). As is demonstrated in Section B.2, the model forces us to allow for a *secondary* movement (i.e. along $\vec{x}$) and therefore the primary motion will be described by a constant acceleration.

For this model of parabolic layer we were able to solve algebraically the required system of conditions. The steps we followed in finding the solution are presented in Section B.2. We also proved that for each set of timing parameters (each set of values $M_{i1,2}$) there is only one solution with physical significance.

The cylindrical layer model

A shortcoming of the parabolic model is that the layer thickness along the local normal is not constant; constant is only the distance between the parabolas defining its leading and trailing edges. As we shall see from the analysis of the test case, this could lead to solutions where the

actual thickness varies unreasonably from one satellite to the other or during the crossing time corresponding to one spacecraft. Therefore we also investigated the cylindrical model where by definition the layer has the same thickness along its normal.

The treatment is similar to the case of parabolic layer but now C and w will designate the coordinates of the cylindrical layer axis at initial moment. The other variables with geometrical meaning are R and d – the radius of the inner circle and the MP half-thickness – and the angle β, designating the direction of primary movement which in this model is radial. For a cylindrical layer we are not forced to allocate two degrees of freedom for the MP movement. Therefore one can cast the remaining three unknowns, describing the velocity time dependence, in two ways: either all of them for specifying the primary motion (i.e. along $\vec{y}$) or we can allow for a movement with constant velocity along the secondary direction (i.e. along $\vec{x}$) and a linear velocity dependence for the movement along $\vec{y}$.

In the cylindrical model we solved the system of timing conditions by using algorithms for finding a numerical solution. In order to apply the algorithms, we first reduced the number of equations by expressing some of the unknowns as a function of the others. Specifically, we arrived at a reduced set of equations having as unknowns the angle β and the parameters describing the MP velocity. The reason in keeping these variables was that we also have to provide an initial guess for the solution and these quantities seemed for us more suitable in this respect. For example the angle β has a limited range of variation (i.e from $-\pi$ to π) and we could search for the solutions in a loop that varies the initial estimate for β in this range in steps of a few degrees. All the details of the calculations are presented in Section B.3.

Another problem encountered refers to the number of solutions with physical significance satisfying the system of imposed conditions. It is difficult to answer this question in the general case and therefore when the numerical procedure is carried out one has to start the search from many initial points, sufficiently close to each other and covering a sufficiently broad range of values so that no solution is missing. What 'sufficient' means depends on the actual timing and position information. The strategy we followed in finding solutions for the cylindrical model is presented in Section 4.2.

Optimizing the timing procedure for a 2-D, non-planar discontinuity

The technique presented above relies (apart from the information about the invariant direction $\vec{l}$) only on the information about the times when the Cluster satellites encounter the MP edges. As we have seen, the main direction of the MP displacement (what was called *primary direction*), which lies in the plane perpendicular to $\vec{l}$ and therefore is fully specified by an angle in that plane, is an unknown quantity like any other unknowns (for example the half-MP thickness or the initial MP position) to be determined by the algorithm. In what follows, we shall refer to this method as ***plain timing analysis***.

Because the direction of the MP movement is fully described by an angle we can impose from outside different values for this parameter, like increasing it stepwise in the range $[-180\,^\circ, 180\,^\circ]$, and solve the timing problem with this condition. For each solution we find, we are in the position to compute the variance along the instantaneous (surface) normal or tangential direction for any quantities during the individual crossing time (in Section B.4 we deduced expressions for various average quantities characterizing the MP movement and orientation for a satellite traversal).

If a quantity obeys some conservation law at the MP, then its variance will have an extreme (minimum or maximum) across that boundary. Therefore, we can select that direction of $\vec{y}$ (i.e. that value for β) for which the global (over the 4 spacecraft) variance is extreme. Here by

'global' we mean a weighted sum of the individual variances (the details are given in Section B.5). The advantage of this procedure is twofold: firstly, a better characterization of the MP motion is achieved, because we can increase by one the degree of polynomial describing it. Then, the solution found in this way is optimized against the additional criterion employed, meaning a supplementary support from the physics involved.

We shall refer to this procedure, where the timing information together with results from other method(s) are used to infer the MP local geometrical and dynamical properties (thickness, orientation, velocity etc.), as the ***mixed*** or ***combined analysis***. In Section B.5 we will use MVAB technique as the additional method to be combined with the timing analysis. This is also the way we carry-out the investigations for our test case but in principle any other method could be used instead in the mixed-analysis (minimum Faraday residue, minimum variance of the current density etc. See *Sonnerup et al.* [2006] for a collection of possible methods).

3.3 Presentation of the test case

In this section we introduce the event from 24 June 2003, which constitutes the test case for the new 2-D, non-planar MP technique developed in the thesis. In Figure 3.3 the Cluster satellites orbit and configuration corresponding to the event are shown. The transition that will be analyzed occurred around 07:37:00 UT at the magnetopause dawn flank, near $[-7.7, -17.7, -1.4]\, R_E$ in GSM coordinate system. It is an inbound crossing from the magnetosheath plasma regime to the magnetosphere region (better seen on Figure 3.4). In the upper part of the figure showing the orbit (taken from Cluster Science Data System home page), a model MP and bow-shock are drawn and the distance between the satellites is scaled by a factor of 5. The four spacecraft are travelling in pairs, with C1 close to C3 (at approx. 350 km) and C2 close to C4 (at approx. 250 km). The distance between the pairs is around 7400 km.

On the bottom part of that figure two plane projections of this cigar-type configuration at the time of traversal are shown, both of them with C2 - the first satellite entering the MP - at the origin of the coordinate system. In the plot showing the projection on the so-called 'MP plane' - the plane perpendicular to the direction resulting from averaging the individual normals obtained from constrained minimum variance analysis of magnetic field (MVAB) - the $\vec{x}$ axis corresponds to the invariant direction (given by $\vec{l}$, introduced in the previous chapter and determined later in the analysis). The adjacent projection has the average MVAB normal direction as $\vec{x}$ axis and the same $\vec{y}$ axes. Because for an inbound transition a satellite is moving in the opposite direction of the MP normal, we can clearly see that the time-sequence of the satellites' crossings is C2, C4, C3 and C1. This sequence is indeed seen in the magnetic field data presented in Figure 3.6 and introduced later in the text.

In Figure 3.4 various physical quantities characterizing the conditions in the plasma around the time of the event (indicated with dashed vertical lines) are shown. The displayed measurements were taken by the Cluster3 (panels 1 - 6) and ACE (panels 7 and 8) satellites. From top to bottom we have:

- magnetic field components in GSE from Cluster FGM experiment
- plasma density, from HIA sensor of the CIS experiment. Both on-board (red) and ground (green) computed values are presented, demonstrating the agreement between them
- plasma velocity components in GSE calculated on-board from HIA measurements
- panels 4 and 5 present the plasma temperatures perpendicular (magenta) and parallel

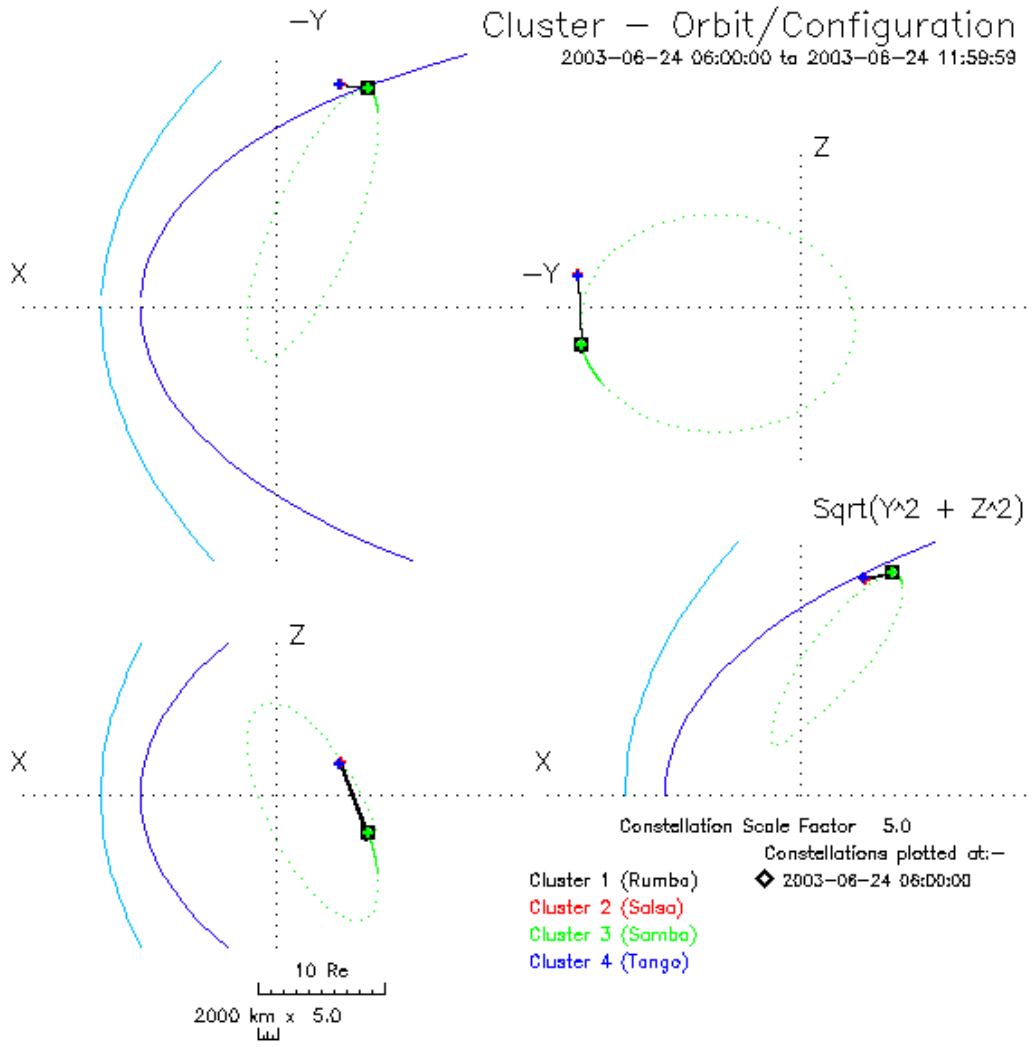

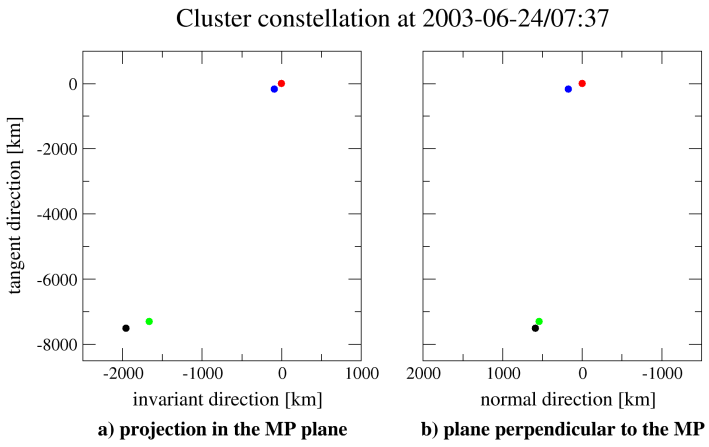

Figure 3.3: *Upper part:* Cluster orbit projections on the planes of GSE coordinate system for the time of event. The distance between the satellites was increased by a factor of 5. *Lower part:* Projection of Cluster configuration at the time of transition on the MP plane and on a plane containing the MP normal. See text for a detailed description.

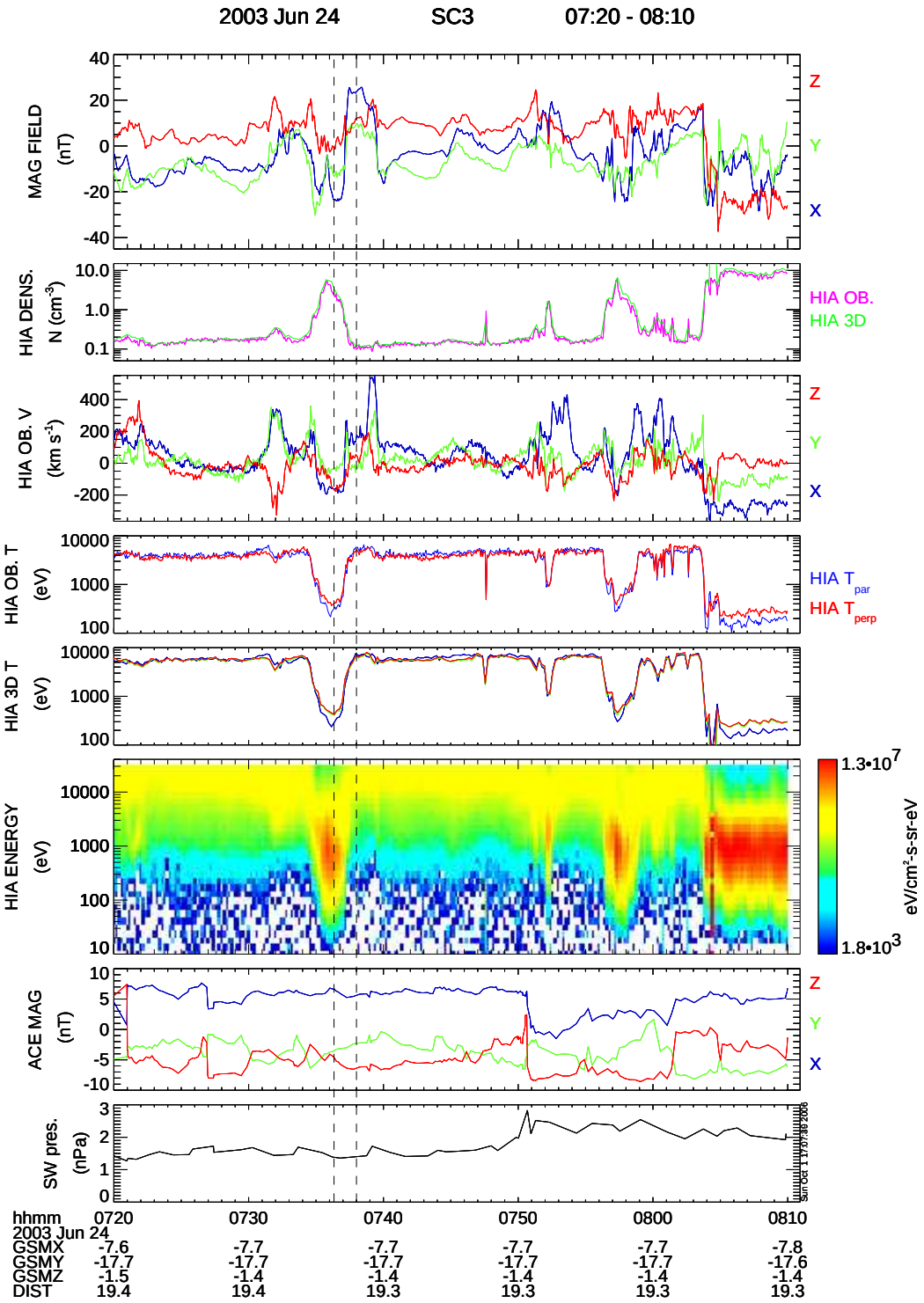

Figure 3.4: Magnetic field and ion measurements around the time of our event (indicated by the vertical dashed lines). From top to bottom, in the first six panels, we have magnetic field GSE components, ion density (computed on-board and at ground), components of ion velocity in GSE, ion parallel and perpendicular temperatures (computed on-board and at ground) and ion differential energy flux as measured by Cluster 3. The last two panels present the conditions in the solar wind, i.e. magnetic field GSE components and dynamic pressure, based on (shifted) ACE measurements. See text for further explanations.

(blue) to the magnetic field computed on-board and at ground

- HIA differential energy flux spectrogram for the total energy range of the sensor
- the last two panels show the conditions in the solar wind as seen by ACE satellite, located at the Lagrange point L1, about 1.5 million km sunward from Earth. The magnetic field components in GSE (MAG experiment) and solar wind dynamic pressure (calculated from SWEPAM measurements) are presented. When plotting them, we took into account the time-delay resulting from solar-wind plasma propagation between ACE and Cluster positions. This time-delay was first estimated by making use of the x-GSE component of the solar wind velocity. Then, a more precise correction was established by comparing the (shifted) ACE magnetic field measurements with the ones from Cluster when the latter was situated outside the magnetosphere.

During the period when Cluster was close to the magnetosphere's eastward flank, several MP transitions occurred between the hot, rarefied magnetospheric plasma environment and the much cooler, denser plasma with more stable flow, characteristic for the magnetosheath region. These transitions are clearly identifiable in the magnetic field change associated with the current system situated at the magnetospheric boundary. From Figure 3.4 it is evident that at 07:37 UT we have an inbound crossing. The solar wind parameters were relatively stable, with the interplanetary magnetic field southward oriented apart from some small intervals when it turned northward (like approx. 15 minutes before our event, when B_z was positive for a few minutes).

In order to investigate whether the MP behaves like a rotational or tangential discontinuity, the Walén test has been performed for each satellite where plasma data are available (i.e. we used HIA measurements for C1 and C3 and CODIF measurements in case of C4). The Walén test checks whether the plasma flows at the local Alfvén velocity in a coordinate system (the so-called deHoffmann-Teller frame) in which the flow is field aligned. The general description of this type of analysis is presented in Sections 5.1 and 5.2. In all cases a good deHoffmann-Teller (HT) frame was found (correlation coefficient $\gtrsim 0.95$) meaning that the necessary condition, although not a sufficient one, for a rotational discontinuity (RD) identification exists (see Appendix F for a presentation of HT analysis).

The Walén relation itself is poorly satisfied in case of C3 and C4, with the slope of the regression line being 0.40 and 0.43, respectively. In case of C1 we were able to identify a time interval for which apparently the test is successful. Figure 3.5, that shows in the left part the corresponding results from the HT and Walén analyses, indicates a slope $\simeq 0.83$ and correlation coefficient $\simeq 0.91$. However, for this satellite one should say that a careful observation of the lower right graphic indicates that the rotational character of the MP is not as certain as the mere value of the slope would suggest. In that part of the figure the plasma velocity components in the deHT frame (on ordinate) are plotted against the local Alfén velocity components $\vec{B}_i/(\mu_0\rho)^{1/2}$, $i = 1, 3$ (on abscissa). As we can see, the points corresponding to y and z components (represented in green and red, respectively) do not show a large spread along the regression line. The same would apply for the x components (in blue) if one would exclude the point near origin, corresponding to the x component of the last measurement taken in the chosen interval. This aspect of the plot, showing that there is no large dynamic variation in the components, means that the change in the velocity vector synchronous with the magnetic field rotation is not as conclusive. When the interval of analysis is increased, the values of the slope and of the correlation coefficient drop dramatically, being totally unacceptable for a RD. A higher time-resolution measurements would have helped us to establish the type of discontinuity in this case.

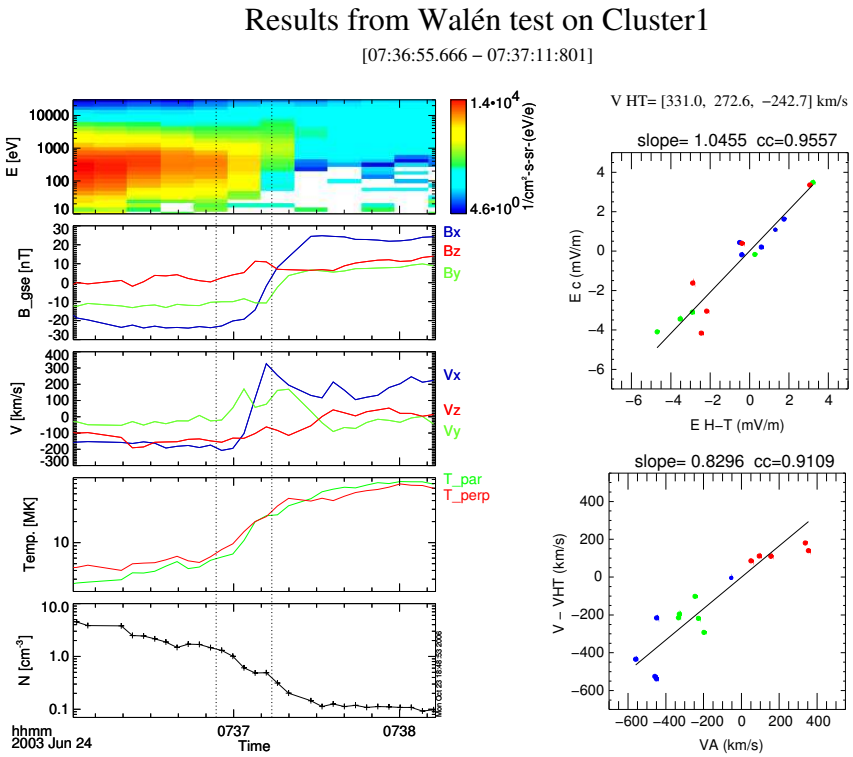

Figure 3.5: *Left side:* Cluster 1 magnetic field and plasma parameters (ions, from HIA measurements) around the time of MP crossing. The time-interval used to test the Walén relation is indicated by the vertical dotted lines. *Right side:* In the upper part, the result from deHoffmann-Teller analysis is shown. The plot presents the fit between the electric field $\vec{E}_c = -\vec{v} \times \vec{B}$ (on ordinate) and the convection electric field $\vec{E}_{HT} = -\vec{V}_{HT} \times \vec{B}$ associated with a time-stationary structure moving with the determined HT velocity (on abscissa). Different components are indicated by different colours. The lower part refers to the Walén test itself and shows the fit between the Alfvén velocity components and the plasma velocity components in the deHT frame. See text for more explanations.

The analysis presented above assumes an one-dimensional discontinuity for the MP and uses the proxy $\vec{E} = -\vec{v} \times \vec{B}$ for the electric field. The average proton gyro-radius for the analyzed interval, computed by using the perpendicular thermal velocity $v_T = \sqrt{2k_B T_{perp}/m_p}$ is approx. 133 km and the average proton inertial length $\lambda_p = 1/e\sqrt{m_p/\mu_0\rho}$ is approx. 270 km. These quantities have to be compared with the MP thickness, found later in this chapter to be around 800 km. As a conclusion, we can say that in this zero-order approximations for the MP, all satellites encounter a discontinuity for which a relatively good deHT frame was detected, where some correlation exists between magnetic field and velocity changes in the case of Cluster1.

In Figure 3.6 the magnetic field components in GSE reference frame and its magnitude as measured by each spacecraft are presented. Actually, one important criterion in selecting the test case was a 'clean' transition with a regular evolution of the magnetic field at each satellite. One can see that the asymptotic levels of the magnetic traces are clearly identifiable, the components on either side of the transition being almost constant for a relatively long period. This, and the smooth evolution in the transition region ensure a good fit of the measurements, necessary for a reliable timing analysis.

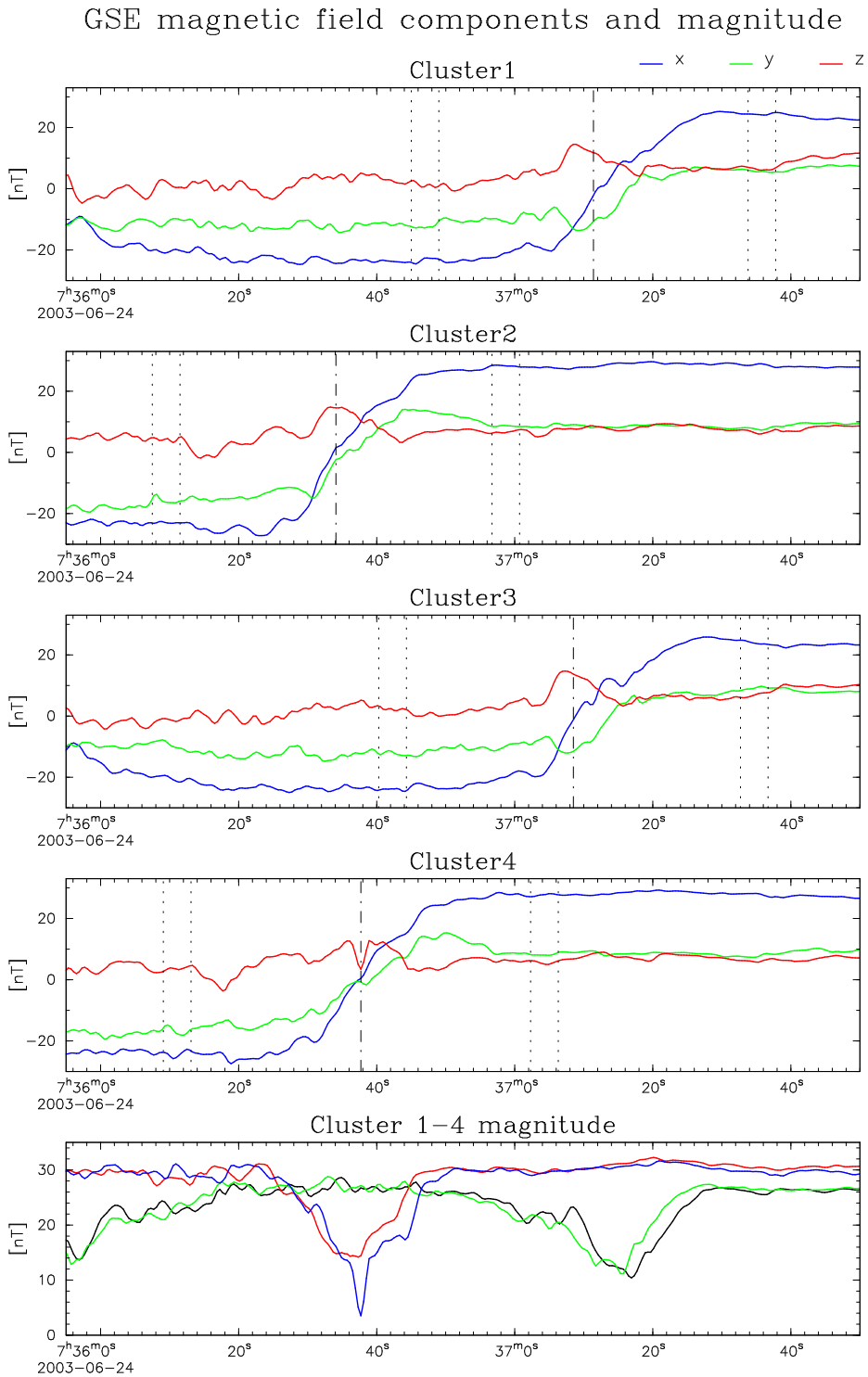

Figure 3.6: Magnetic field as measured by the Cluster satellites during the MP crossing. In the first four panels the x, y and z GSE components are indicated by blue, green and red lines respectively. The last panel shows the variations in the magnetic field magnitude, colour coded according to the mission convention, i.e. black, red, green and blue refers to Cluster1, Cluster2, Cluster3 and Cluster4 respectively. The minimum and maximum length intervals entering MVAB nested analysis (vertical dotted lines) together with their common central time (dot-dashed lines) are indicated for each satellite.

3.4 Obtaining the input parameters

The purpose of this section is twofold: to provide evidence that for the transition previously introduced the MP is behaving like a 2-D, non-planar discontinuity and to extract from the data the input parameters necessary for the various timing algorithms presented at the beginning of this chapter. These parameters are the timing information, i.e. the instances when the MP edges are detected by the four Cluster satellites and, in addition for the non-planar case, the unit vector $\vec{l}$, designating the invariant direction for the 2-D magnetopause.

A case of non-planar magnetopause. Finding the unit vector $\overrightarrow{\mathrm{l}}$

We will show that in our case the normals determined at each satellite by applying a minimum variance analysis (MVA) on the magnetic field data (also called individual or satellite normals) are contained approximately in the same plane; the perpendicular direction to this plane is then the invariant direction, indicated by the unit vector $\vec{l}$. In determining the individual normals we followed the procedure presented below:

- we started with data of 0.2 seconds time-resolution and then we 'boxcar-averaged' the measurements by using a boxcar of 1 second width, in the same time resampling the data to a resolution of 0.4 seconds. In this way we try to eliminate the finer small-scale structure which is of no interest in our study
- for each satellite a number of eleven symmetric nested intervals were chosen, centred on the same point approximately around the transition centre. The lengthes of the intervals are big enough to embrace the whole magnetic field change and a small part from the asymptotic regime on either side (but not to much, to avoid the effect of magnetic field fluctuation in these regions on MVAB result). The central times, the minimum and maximum length intervals are presented in Figure 3.6
- for each of these eleven intervals a constrained (to $\langle B_n \rangle = 0$) minimum variance analysis was performed (the general description of this method is presented in Appendix A). In other words, for each of the eleven intervals, containing the magnetic measurements $B_i, i = 1, n$, the direction in space perpendicular to the vector $\langle \vec{B} \rangle = \sum_{i=1}^{n} \vec{B}_i$ and for which the magnetic variance is minimum was identified. According to the theory of MVAB, this direction designates the MP normal
- from the eleven normals, an average direction was computed and associated with the MP normal at the spacecraft level in question. The averaging procedure is described in Appendix A.

At this point we would like to make a few comments. First, we choose to determine the individual normals from MVAB on eleven nested intervals in order to minimize the dependence of the result from the interval of analysis. This effect is relatively small in our case, with the normals corresponding to each interval being very close to one another. That is a consequence of the clean and smooth transitions seen on Figure 3.6 which results in case of Cluster 3 in eleven normals less than 1 degree apart from the (average) individual normal. For the other satellites the eleven normals are less than 2 degrees apart from the (average) individual normal.

Second, we used the results from constrained MVAB and not from standard, unconstrained technique, because the latter is often more prone to errors. This is due to the fact that almost in all situations small-scale magnetic field fluctuations are present that have their undesired influence on the magnetic variance computation. There are examples in the literature (see for example *Sonnerup et al.* [2006]; we will also provide three such cases in this thesis, namely the

present one and the ones introduced in Section 5.3 and Section 5.5) emphasizing this conclusion. Sometimes even for discontinuities having a small perpendicular magnetic component, the error in estimating their normal is most probable smaller when a constrained (to $\langle B_n \rangle = 0$) MVAB is being used rather than when no such constraint is imposed (in this respect, see the two examples from Section 5.3 and Section 5.5 when the magnetopause behaves as a RD). In our case the decision to use constrained normals gain support also from the Walén tests presented in Section 3.3. Other arguments are given below.

In general it is advisable to perform both types of analysis and to compare their results before deciding which are more reliable. Therefore we carry out also a standard (unconstrained) MVAB on our event in exactly the same manner described above and the results from both analysis are presented in Table 3.1. For each satellite the eigenvalues and the eigenvectors components in GSE of the magnetic variance matrix are presented, in case when the constraint $\langle \vec{B} \rangle \cdot \vec{n} = 0$ was imposed and without this condition. In the latter situation the value of $\langle \vec{B} \rangle \cdot \vec{n}$ is indicated in the right most column. The normal vectors provided by each technique are shown in bold face.

Figure 3.7 is a polar plot useful in visualizing the orientation in space of the various normals obtained in the analysis. The centre of this picture (the magenta square, symbol MVAB) designates a reference direction in space and we choose for that the average of the four individual normals provided by the constrained MVAB. Its components in GSE frame are indicated at the bottom. The vertical line is oriented along the cross product between the average MVAB normal and $\vec{X}_{GSE}$ (roughly pointing northward) and the horizontal line completes the cartesian frame. For each satellite, depicted in one particular colour, we plotted three normals: one from costrained analysis (MVABC1 symbol, represented with an error bar indicating the orientation uncertainty due to the statistical errors), one from plain analysis (MVABC0 symbol, accompanied by an error ellipsis for the same type of errors in orientation) and a normal provided by a MP model (*Roelof and Sibeck* [1993] in this case, but the particular model used is not so

Table 3.1: Results from the constrained and unconstrained minimum variance analysis of the magnetic field, performed on eleven nested intervals. For a detailed description of the procedures and of the parameters appearing in this table see the text. The normal components in GSE and the magnetic variance provided by each technique are shown in bold face.

	Constrained MVAB				Unconstrained MVAB				
	$\lambda\,[nT]^2$	n_x	n_y	n_z	$\lambda\,[nT]^2$	n_x	n_y	n_z	$\langle \vec{B}_n \rangle [nT]$
	0.00	0.1574	0.5228	−0.8377	**2.35**	**0.3054**	**−0.7163**	**−0.6272**	−1.42
Cluster1	**2.89**	**0.3327**	**−0.8270**	**−0.4535**	14.66	0.1712	−0.6067	0.7762	
	398.33	−0.9298	−0.2074	−0.3041	429.74	−0.9367	−0.3446	−0.0627	
	0.00	0.0567	0.3347	−0.9403	**4.07**	**0.4673**	**−0.8509**	**−0.2400**	0.22
Cluster2	**4.09**	**0.4649**	**−0.8423**	**−0.2717**	13.19	0.0608	−0.2399	0.9689	
	621.61	−0.8832	−0.4223	−0.2034	635.63	−0.8820	−0.4673	−0.0604	
	0.00	0.1602	0.5293	−0.8331	**2.05**	**0.3310**	**−0.7136**	**−0.6175**	−1.18
Cluster3	**2.58**	**0.3573**	**−0.8179**	**−0.4510**	15.77	0.1744	−0.5968	0.7832	
	427.32	−0.9201	−0.2254	−0.3201	462.86	−0.9274	−0.3669	−0.0731	
	0.00	−0.1192	0.2473	−0.9612	**4.33**	**0.4580**	**−0.8868**	**−0.0577**	1.34
Cluster4	**4.64**	**0.4471**	**−0.8510**	**−0.2744**	10.79	−0.0010	−0.0654	0.9976	
	624.44	−0.8865	−0.4627	−0.0091	624.76	−0.8889	−0.4571	−0.0309	

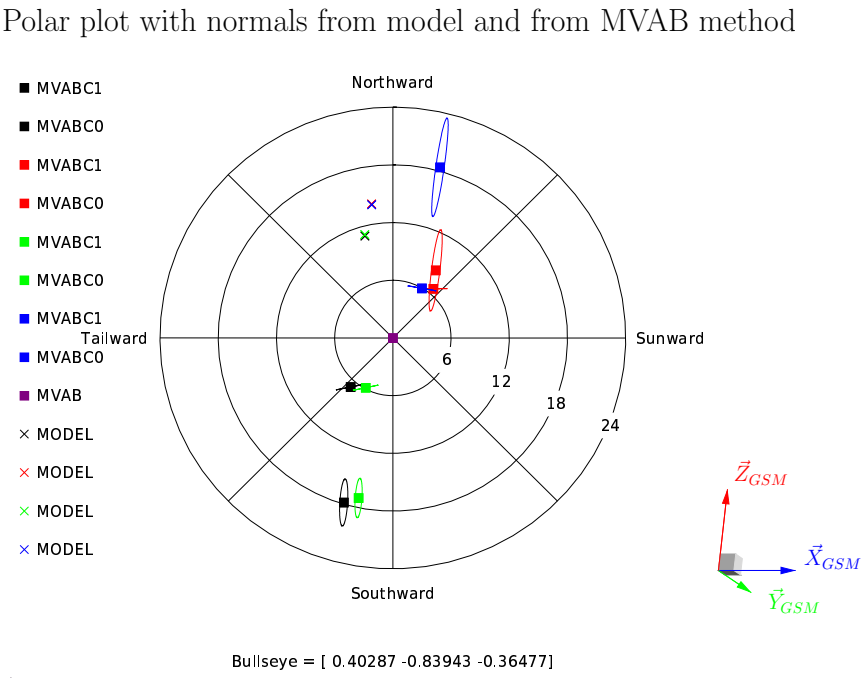

Figure 3.7: Polar plot with the orientation of various normals introduced in the text. The concentric circles designate directions in space situated at 6 °, 12 °, 18 ° and 24 ° from the origin. There are 12 individual normals in total, depicted in the mission colour code and referring to unconstrained normals (MVABC0), constrained normals (MVABC1) and model normals (MODEL). In addition, the average (MVAB) of the constrained normals, also chosen to be the reference direction, is presented. Its orientation with respect to the GSM reference frame could be judged by looking at the bottom right part of the figure. Further explanations are given in the text.

important for our discusion).

By looking at this picture and at Table 3.1 we can draw several conclusions. First, the constrained normals are very well defined, the ratio $\lambda_{max}/\lambda_{int}$ being ≥ 135. A rule of thumb requires a value greater than 15 for this ratio in order to have reliable normals. The same rule of thumb in the unconstrained analysis requires values for $\lambda_{int}/\lambda_{min}$ greater than 10 and this is not obeyed in our case (the values are 6.2, 3.2, 7.7 and 2.5 for Cluster 1, Cluster 2, Cluster 3, and Cluster 4 respectively). Therefore this latter normals are not qualified as reliable normals, the variance along the minimum and intermediate directions being too close to one another so that a clear distinction between them is not possible.

Then, in the same Figure 3.7 one can observe another fact that raises suspicions about the unconstrained results: the normals corresponding to satellites Cluster 2 and Cluster 4 are 11 degrees apart, which is strange considering the small separation distance between them and their regular and smooth magnetic field traces.

It is also interesting to observe the following detail: each unconstrained normal lies very close to the plane containing the corresponding $\langle\vec{B}\rangle = \sum_{i=1}^{n}\vec{B}_i$ vector and the constrained normal. This is easily seen considering that in accordance with the imposed constraint on MVAB, the error bars belonging to the constrained normals are perpendicular to the vectors $\langle\vec{B}\rangle$ (these error bars were drawn larger in the figure just to illustrate the present argument). The situation is consistent with the interpretation that small-scale surface waves are present on the MP. They induce normal (to the MP) variations which spoil the variance computation along that direction, explaining the bad outcome from the unconstrained MVAB. Indeed, these latter normals point approx. 12 degrees apart from the constrained ones (with the exception

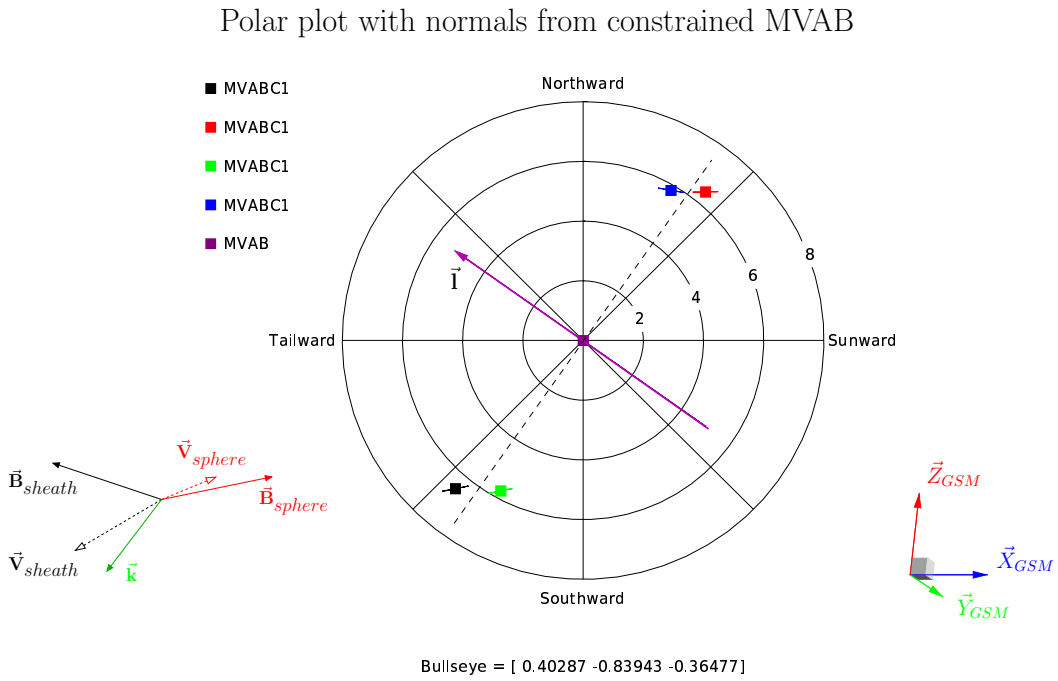

Figure 3.8: A zoom of the previous figure, when only the constrained (to $\langle B_n \rangle = 0$) normals are kept. The invariant direction obtained during the analysis is indicated by the unit vector $\vec{l}$. The lower left corner shows the tangential components of the magnetic field and velocity flow, as measured by Cluster 1, in the two regions adjacent to the MP interval: in the magnetosphere (red) and in the magnetosheath (black).

of Cluster 2 when the two normals are only 2 degrees apart) and the error ellipses are oriented with the major axis approximately in the $\langle \vec{B} \rangle$ direction. The interpretation offers also an explanation why the costrained alternative performed better in our case: in the MP case the magnetic field vector lies almost entirely in the discontinuity plane, the perpendicular component, if present, being very small compared to the tangential one. So much the more the vector $\sum_{i=1}^{n} \vec{B}_i$ will be in the same plane when small oscillations along the normal are present because their net effect will cancel when added. Therefore the constraint to search for a normal such that $\vec{n} \cdot \sum_{i=1}^{n} \vec{B}_i = 0$ is meaningfull.

The model normals were plotted to show what the difference in the individual MP orientation would be when this difference arises only from the curvature of the model MP at the scale of the interspacecraft separation distance. These normals are grouped in pairs, as expected, and are 3.3 ° apart. Based on that we can evaluate the local radius of curvature for a model MP and this turns out to be around 19.3 R_E.

Figure 3.8 is a zoom of the previous plot where only the constrained normals are shown. Here the error bars show their actual size. Between the normals detected by Cluster 1 and Cluster 2 the difference in orientation is about 13 °. Considering the fact that the pair of satellites Cluster 2 – Cluster 4 are well separated from the pair Cluster 1 – Cluster 3 and that the constrained MVAB normals are very reliable, we interpret the results in the figure as the effect of Cluster encountering a 2-D, non-planar MP. With the dashed line we show the closest (in a least square sense) plane situated between the individual normals. We shall refer to this plane as the *plane of the normals* later in the text. All four MVAB normals lie within 0.7 ° from it. The invariant direction which enters as input parameter in the 2-D timing technique is perpendicular to that plane and indicated by the unit vector $\vec{l}$. Quantitatively,

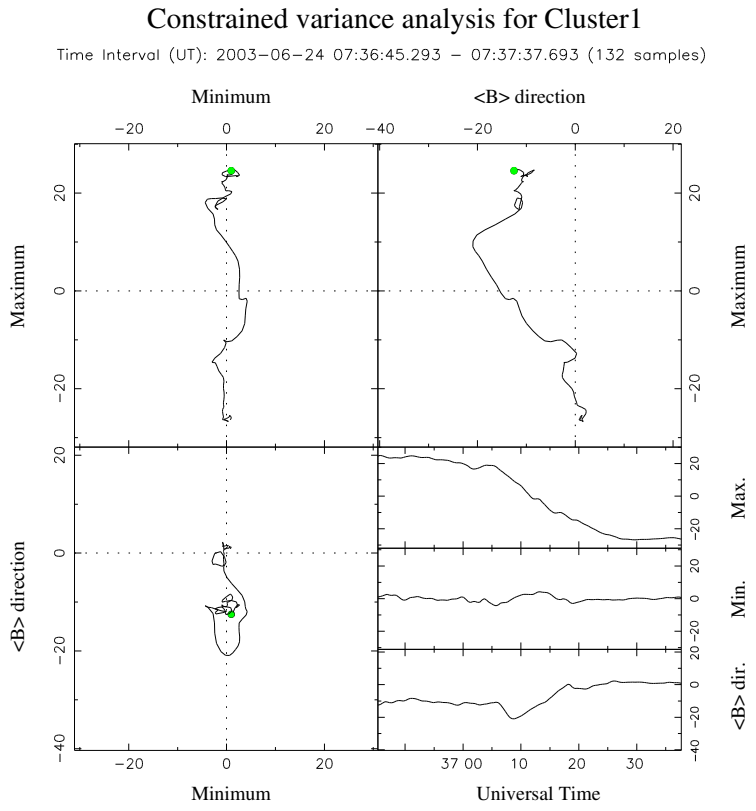

Figure 3.9: Evolution for the tip of the magnetic vector (the hodograph) in case of Cluster 1 transition. The projections on the planes determined by the minimum magnetic variance, maximum magnetic variance and $\langle B_n \rangle = 0$ directions are presented. The time interval corresponds to the largest interval from the nested analysis with the initial moment indicated by the green point.

the direction of the dashed line was computed by performing a variance analysis on the four individual normals, selecting the maximum variance direction. Then, the unit vector $\vec{l}$ along the invariant direction turned out to have the components $[-0.7478,\ -0.5317,\ 0.3976]$ in the GSE reference frame.

The lower left corner in Figure 3.8 depicts the tangential components of the magnetic field and velocity flow in the adjacent regions of the magnetosphere (in red) and the magnetosheath (in black), as measured by Cluster 1. Each of the vectors are averages over 5 data points, corresponding to the time interval [07:36:31 – 07:36:47] for the magnetosheath and [07:37:36 – 07:37:52] for the magnetosphere. The angle between the two flow directions is $\sim 172\,^\circ$ and the magnetic shear $\sim 150\,^\circ$. We will come back to this point in Section 4.4, when discussing the possible nature of this 2-D, non-planar MP feature. Now we only make an observation about our interpretation that small-scale fluctuations spoiled the unconstrained MVAB results. As we poited out when discussing Figure 3.7, each unconstrained MVAB normal (and the major axis of the ellipse that indicates its errors in orientation) lies roughly in the plane perpendicular to the error bar belonging to the corresponding constrained MVAB normal. From the lower left corner in Figure 3.8 we can see that surface oscillations along the same direction would be the most favourable from energetic point of view, being close to the perpendicular direction of the magnetic field (and therefore not requiring bending of the magnetic field lines).

In Figure 3.9 we show the hodograph of the magnetic vector for Cluster 1 and for the largest of the eleven nested analysis intervals. This type of picture is useful in visualizing how

the tip of $\vec{B}$ has moved during the transition. In the upper-right panel, which depicts the magnetic field change in the MP plane, the exterior normal points into the paper. Therefore during the transition a left-hand rotation occurs (i.e. opposite to the rotation associated with the MP normal) and this rotation is performed on the shorter path from the direction in the magnetosheath (green point) to the one in the magnetosphere. That is the typical behaviour we expect at the MP, reported previously in the literature (see for example *Sonnerup and Cahill* [1968] and *Berchem and Russell* [1982a]).

Obtaining the timing information

The procedure we adopted for determining the timing information was already described in Section 3.1. We resume it here and illustrate the results obtained for our test case:

- for each satellite the magnetic field data was transformed into the local MP reference frame, having the axis along the eigenvectors of the corresponding variance matrix (and shown in Table 3.1 in the columns referring to the constrained analysis). The three new magnetic field components will be then along the maximum variance direction, along the minimum variance direction and along the direction of $\langle\vec{B}\rangle$. Note that after this transformation the measurements from the 4 spacecraft are no longer represented in the same reference frame.
- the maximum variance component for each satellite was fitted with a hyperbolic tangent function

$$B(t) = B_m - \frac{1}{2}\,\Delta B \tanh\left[\frac{t - T_c}{\tau}\right] \tag{3.2}$$

  in order to determine the crossing times that characterize (in the global sense) that particular transition. The four parameters have the following meaning: B_m is the zero level of the tanh function, ΔB is the total magnetic jump between the asymptotic levels, T_c represents the central moment and τ describes the profile width.
- we define the magnetopause as being the region where the fit changes from

$$B_m - \frac{1}{2}\,\Delta B \tanh(-1) = B_m + \frac{1}{2}\,\Delta B\,\frac{e^2 - 1}{e^2 + 1} \tag{3.3}$$

  level to

$$B_m - \frac{1}{2}\,\Delta B \tanh(1) = B_m - \frac{1}{2}\,\Delta B\,\frac{e^2 - 1}{e^2 + 1} \tag{3.4}$$

  level. This corresponds to a fraction change of approx. 0.762 of the difference between the asymptotic levels ΔB.
- according to the proposed magnetopause definition, the leading edge encounter took place at $T_c - \tau$ and the trailing edge encounter at $T_c + \tau$

In Figure 3.10 the upper part presents Cluster 1 magnetic field components in the reference frame related to the MVAB normal. The vertical grey stripes mark the time span of the eleven nested intervals used in MVAB. By fitting the maximum variance component, the parameters T_c (indicated with the vertical dashed segment) and τ (the half-distance between the vertical dashed lines) were determined. The horizontal dashed lines represents the magnetic field levels associated with the MP boundaries. In the bottom part of that figure, the maximum variance

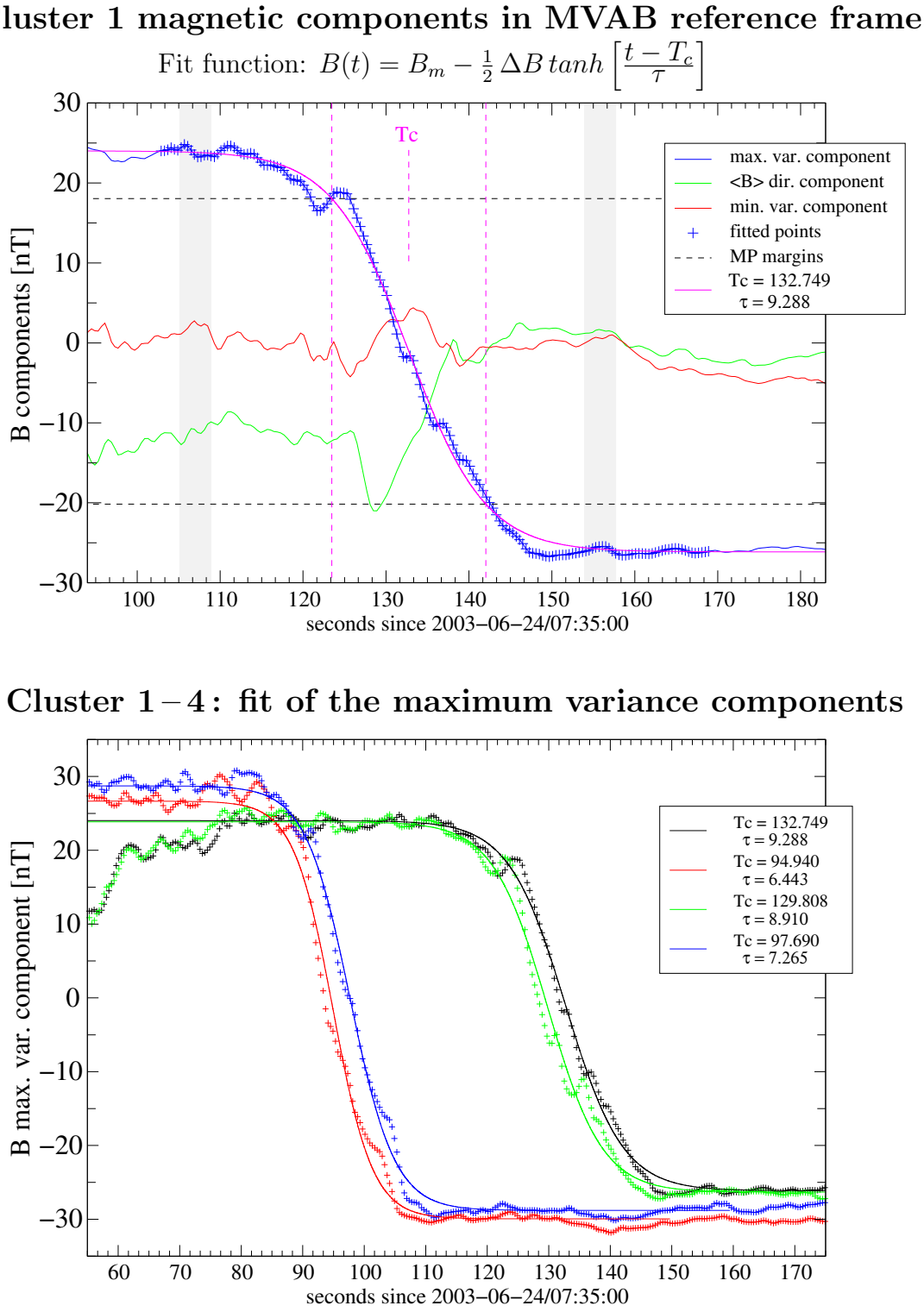

Figure 3.10: *Upper part:* Cluster 1 magnetic field components along the directions of minimum magnetic variance (in red), maximum magnetic variance (in blue) and $\langle B_n \rangle = 0$ (in green) are presented. The timing information is obtained by fitting the points corresponding to the maximum variance component (blue crosses) with a hyperbolic tangent function. *Lower part:* The (colour coded) maximum variance components together with their fits are shown for all four Cluster satellites. The timing information appears in the legend box.

components for all satellites, together with their corresponding fits are shown. The timing information determined by this analysis is provided in the insert.

The problem of setting the magnetic levels for the magnetopause borders will be addressed in the next chapter (see Section 4.3), when the various solutions obtained will be discussed and a comparison with the results obtained from the planar method will be presented. In addition, in the Appendix D we included also a study on how stable the 2-D MP solutions are with respect to the convention we adopt for the MP extent. Note that we choose the same levels for the MP boundaries and the same fitting function (hyperbolic tangent) as in the *CTA paper*. In principal, the fitting profile depends on the particular case under investigation. Our choice was not made assuming a model for the MP structure (despite the similarities between the magnetic traces shown in Figure 3.6 and that from a Harris type current structure). Nevertheless, this function provided also good results in other cases where the timing analysis was applied.

Implicitly, by using such a symmetric profile, we assume that, for the crossing duration, the MP has a symmetrical structure and its normal velocity is also symmetrical with respect to the central crossing time. This could be considered as a sort of zero-order approximation: strictly speaking the fitting profile should take into account the MP normal velocity, albeit this quantity is found a posteriori. One can imagine a possible development of the technique that takes into account this aspect by resorting to an iterative procedure for finding the timing information.

CHAPTER 4

Results for the 24 June 2003 magnetopause crossing: comparison of different methods

We will now present the results obtained when the planar and the 2-D, non-planar, timing techniques introduced in the previous chapter, are applied on the MP crossing made by Cluster on 24 June 2003. The outcome from the planar method will bring us once more to the conclusion that the non-planar aspect is playing a major role in this event. Afterwards, a comparison with the results provided by the planar, single-spacecraft methods (like minimum variance analysis of the magnetic field, minimum Faraday residue analysis and deHoffmann-Teller analysis) is carried-out. Several other issues will be addressed, among them the validity range and stability of the solutions and the nature of the 2-D, non-planar feature detected at the MP.

4.1 Results from the planar timing technique

In this section we will carry out the well-established timing analysis based on the planar assumption and, likewise, some variants of it developed by us, only for showing the poor results they provide and for later comparisons with the new 2-D method.

In the planar model, where a single normal direction characterizes the event, the timing information should be obtained from data represented in the same reference frame. That is the reason why the fits similar to those presented in Figure 3.10 were performed on the magnetic field components along the direction obtained by averaging the individual maximum variance eigenvectors. In our particular case this aspect has practically no significant influence on the result (we could equally well have used the timing information from the preceding section to obtain the same conclusions) but we decided to stay fully consistent with the planar assumption.

Figure 4.1 is a polar plot where normals from the planar timing analysis are shown. CTA designates the constant thickness assumption normal and CVA the constant velocity assumption normal. The constrained (to $\langle\vec{B}\rangle\cdot\vec{n}=0$) individual normals MVABC1, and their averaged direction MVAB (which, like in Figure 3.8, is the reference direction of the plot) are shown. As described in Section 3.1 (see also Section B.1), one can put the encounter conditions directly

on the MP edges (and not on its centre as in *CTA paper*) and then one obtains a slightly different normal (CTAE symbol in the polar plot).

Evaluating the outcome, one can see that the known planar techniques produce results that are not consistent with the MVAB method: the standard CTA and CVA normals are more then 32 ° away from the average MVAB direction and the CTAE normal, although it brings some improvement, results in a direction still more than 25 ° away. This does not seem acceptable considering the regular magnetic profiles seen by all satellites and the good quality of the fits, resulting in a trustworthy timing information. Together with the argument presented in the preceding section, namely that the constrained MVA normals are very reliable, the present unsuccessful result adds confidence to the assumption that, indeed, in our case we have a 2-D, non-planar MP. Further arguments, in the same line, will be given below.

One could ask the following question: why not assume a planar MP having a constant thickness, with the normal contained in the plane perpendicular to the invariant direction? This assumption would be simpler than the cylindrical or parabolic MP and, anyway, our new technique considers from the beginning that the MP normals are perpendicular to $\vec{l}$. We followed this line of reasoning and conducted a similar analysis to the one presented at the end of Section 3.1 but imposing in addition the condition that $\vec{n}_{planar} \cdot \vec{l} = 0$. The unknowns in this case are:

- the angle of the normal (which is also the direction of MP movement) with respect to some reference direction in the plane perpendicular to $\vec{l}$. This unknown corresponds to the angle β in the 2-D analysis.
- the MP half-thickness.
- the initial MP position along $\vec{n}$. If we choose as origin of time the moment when the first

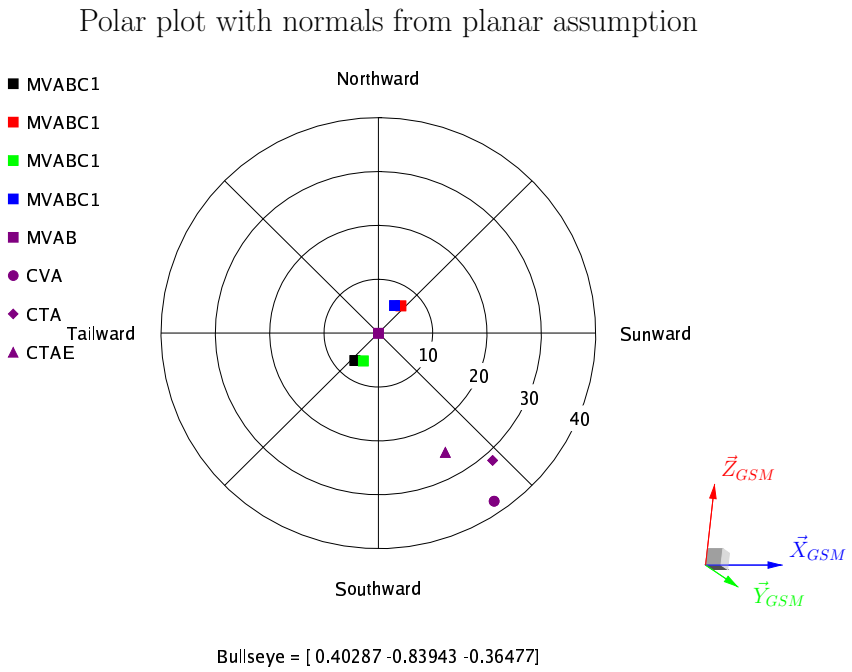

Figure 4.1: Polar plot similar to the one from Figure 3.8 but for a greater range in directions and with the timing normals obtained by assuming a planar MP added. The three timing normals correspond to the constant velocity approach (CVA), and to the two implementation for the constant thickness approach (CTA and CTAE). See the text for more explanations.

satellite meets the leading MP edge, this quantity becomes 0.

- $A_0, \cdots A_4$, five polynomial coefficients describing the MP normal velocity.

Solving one linear system of equations, similar to the equations (B.9), we obtain the solution shown in Figure 4.2. The evolution in time ($\vec{x}$ axis) of the MP displacement along the normal ($\vec{y}$ axis) is represented. The four horizontal continuous lines designate the satellites positions along the normal direction found in the analysis. Vertical dashed lines represent the moments $T_{ci} - \tau_i$ and $T_{ci} + \tau_i$ and we see that indeed the MP movement obeys the timing conditions (leading and trailing margins are at the intersection of the vertical dashed lines with the continuous horizontal lines). But one can observe that, for example, after the second satellite (i.e. Cluster 4) exits the MP, the solution we obtained implies a return of this satellite (and of Cluster 2 as well) to the MP interior. Therefore artificial transitions, not seen in the data, are introduced in order to accommodate the assumptions we made (planar discontinuity having the normal perpendicular to $\vec{l}$) with the timing information. We can count no less than 9 such artificial transitions (4 implying the leading edge and 5 for the trailing edge); also, after the end of our event ($T_{c4} + \tau_4$) there is a return into the magnetosheath. This behaviour makes the solution unacceptable.

In the lower part of the figure, with magenta, the evolution of the MP normal velocity is represented (with the scale on the right $\vec{y}$ axis). We observe that indeed the solution implies a

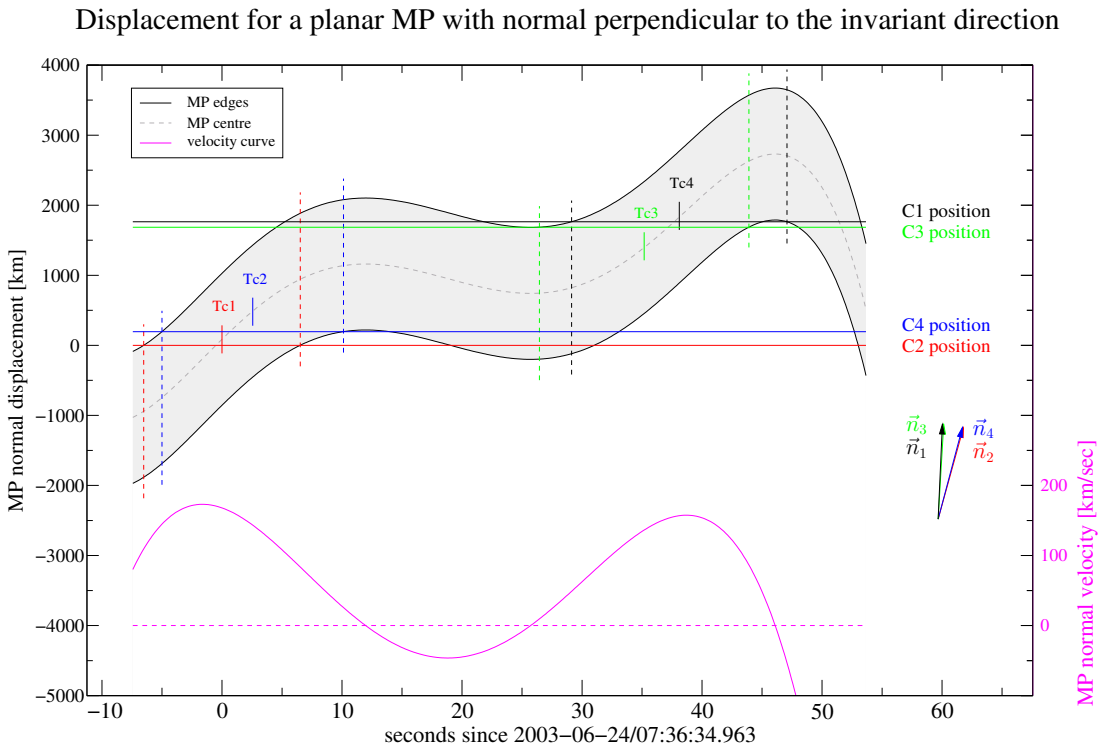

Figure 4.2: The displacement of a constant thickness MP along its normal direction (on ordinate) as a function of time (on abscissa) is presented in the case of a planar assumption. The MP boundary is shown in grey and the displacements of its margins (used in the timing conditions) are indicated by black lines. In the lower part, with magenta, the normal velocity variation is represented. The individual constrained MVAB normals are also shown. For a detailed description of the figure see the text.

change of sign in velocity after $T_{c2}+\tau_2$ and after $T_{c4}+\tau_4$, leading to the occurrence of artificial transitions. The individual nested MVAB normals are also shown: their angle with respect to the $\vec{y}$ axis, therefore with respect to the normal found in the present analysis, are 15.5°, 14.8°, 3.4° and 2.6° for Cluster 2, Cluster 4, Cluster 3 and Cluster 1 respectively.

The central times, represented by short vertical segments labelled T_{ci} are also indicated in the figure. We see that at these moments the position of the MP centre is not where the satellites are located, this being a consequence of the fact that the timing condition was imposed on MP edges. Conducting a similar analysis but working with the MP centre (as in *CTA paper*) one obtains essentially the same results.

In order to save the planar assumption one could argue that, perhaps, neither the constant thickness approach nor the constant velocity approach are valid for this event but, instead, there is a variable normal velocity and the MP has different thickness at different points on its surface. We investigated this possibility too, by imposing different orientations for the (planar) MP, around the direction of MVAB normal (central normal in Figure 4.2). Then, the central crossing moments and the relative positions of the satellites allow us to determine the evolution of the MP normal velocity. In the mathematical form, let S_1, S_2 and S_3 be the distances travelled by the MP on the (imposed) normal direction after the first satellite encounters the MP central plane. Then, using the notations from Appendix B we have:

$$\begin{aligned} S_2 &= A_0 t_2 + A_1 t_2^2/2 + A_2 t_2^3/3 \\ S_3 &= A_0 t_3 + A_1 t_3^2/2 + A_2 t_3^3/3 \\ S_4 &= A_0 t_4 + A_1 t_4^2/2 + A_2 t_4^3/3 \end{aligned} \tag{4.1}$$

where A_0, A_1 and A_2 are the polynomial coefficients describing the time-dependence of the normal velocity $U(t) = A_0 t + A_1 t^2 + A_2 t^3$ and t_i represents the central crossing moment for the satellite i, with t_1 as origin of time. The system of equations (4.1) can readily be solved and, by using the crossing durations $2\tau_i$ we can compute afterwards the MP thickness at each satellite location (note that by taking this path we made no assumptions about the MP thickness or normal velocity).

By proceeding in this way, when imposing for example the average MVAB direction as normal for the MP we obtain a MP thickness of approx. 999 km, 930 km, 254 km and 437 km at Cluster 2, Cluster 4, Cluster 3 and Cluster 1 position, respectively. Considering that the inter-spacecraft separation between Cluster 3 and Cluster 1 in the plane tangential to the MP is only 202 km and that the two satellites cross the discontinuity practically simultaneously, the variation in the MP thickness between their locations (i.e. 183 km) seems unreasonably large. A similar behaviour was noticed for other directions close to the average MVAB normal.

One more observation related to Figure 4.1: because the technique we employed in this section relies only on the satellites position and on the timing data, but not directly on the measurements (like MVAB for example), a 2-D MP will not produce, in general, normals in the plane perpendicular to $\vec{l}$. In other words, the situation is as follows: when the MVAB technique (that assumes a planar discontinuity) is applied on a 2-D MP, the orientation of the normal will be corrupted by the non-planar effects but still, the information about the 2-D symmetry contained in the magnetic measurements is reflected in the outcome, i.e. the obtained normal will lie in the plane perpendicular to the invariant direction. When extracting the timing data from the magnetic profile by the procedure described in the preceding chapter, the information about the symmetry is lost. Then, when performing a timing analysis and trying to accommodate a planar model with the spacecraft relative positions and with the timing data corresponding to a 2-D MP one will obtain, in general, normals not perpendicular to the invariant direction.

In conclusion to this section, we can say that the planar assumption produced unphysical results, which strengthen the argument that the 2-D, non-planar aspect is playing a major role in this event.

4.2 Solutions from the 2-D timing technique

For the case of 24 June 2003 event, we applied the various implementations of the timing method introduced in Chapter 3 and designed for a 2-D, non-planar MP. A comprehensive presentation of these solution is provided in Appendix C. There, for each solution a table with the values of several parameters characterizing the MP geometry, orientation and motion, and parameters usefull in comparing the planar and 2-D, non-planar method can be found. Also, an associated figure to visualize the corresponding MP configuration and movement is presented. A detailed description of the tables and figures can be found at the beginning of that appendix (pages 163 to 165).

In what follows, for simplicity, we will use a certain nomenclature to name a particular solution appearing in this study. Each name will indicate the model adopted for the MP ('Prbl' for parabolic and 'Cyl' for cylindrical), the number of degrees of freedom allowed for the MP movement in the plane perpendicular to the invariant direction ('1deg' or '2deg') and the implementation of the method ('TA' for the plain timing analysis and 'OpTA' for the optimized method, combining timing analysis and MVAB techniques). In case of the cylindrical model, when we allowed for 2 degrees of freedom for the MP, we found two solutions in the case of combined timing-MVAB technique. We will designate these two solutions by the suffix 'solA' and 'solB' respectively.

The following is a list of all solutions, with the locations in Appendix C where their corresponding detailed presentation can be found:

Prbl_2deg_TA	Table A and Figure A	pages 166 and 167
Prbl_1deg_OpTA	Table B and Figure B	pages 168 and 169
Prbl_2deg_OpTA	Table C and Figure C	pages 170 and 171
Cyl_1deg_TA	Table D and Figure D	pages 172 and 173
Cyl_2deg_TA	Table E and Figure E	pages 174 and 175
Cyl_1deg_OpTA	Table F and Figure F	pages 176 and 177
Cyl_2deg_OpTA_solA	Table G and Figure G	pages 178 and 179
Cyl_2deg_OpTA_solB	Table H and Figure H	pages 180 and 181

Finding solutions in the cylindrical model

In the case of the parabolic model, the process of finding a solution is straightforward because there is an analytic expression for it. This is not the case for the cylindrical model where we have to resort to numerical algorithms and where the important question is whether we found all possible solutions. We based our search on the following considerations:

- it is sufficient to look for solutions having β (the angle of the principal direction) in the range $[0, 180]$ because for each solution described by β, V, A_i there is another one with the parameters $-\beta, -V, -A_i$.
- in case of combined timing - MVAB method, if we find one solution for a particular inclination of the primary direction, we can easily trace it to other inclinations. This is done by changing the angle β in steps sufficiently small, using as initial guess for the new

solution the results obtained in the previous calculation. That is one procedure we used to find solutions for the optimized timing technique, where the starting point was the result from the plain timing method.

- for some chosen directions $\beta \in [0, 180]$ we search carefully (i.e. many initial starting points, covering a large range, for V and, say A_0, A_1, A_2) for a possible solution of the optimized problem. Then we traced its evolutions to see whether there is one inclination for which $A_2 = 0$: this would satisfy the plain timing analysis problem. In this way, for example, we found that the solution Cyl_2deg_OpTA_solB has no correspondence in the plain timing analysis because A_2 remains always negative.

Stability of the solutions

In Appendix D we present a study about the stability of one solution obtained in the 2-D, non-planar case, when the magnetic levels used to set the timing conditions are changed. We recall that in Section 3.4 the timing information was determined as the times when each satellite encounters certain magnetic levels, namely the ones encompassing a fraction of $\texttt{tanh}(1) \approx 76.2\%$ of the total MP magnetic jump. In order to see how much the results depend on this choice, we took the Cyl_2deg_OpTA_solA solution and studied how the MP macroscopic parameters (orientation, velocity, geometry) change when we used other magnetic levels for setting the timing conditions. That particular solution involves one of the highest dynamical behaviours for the MP. Indeed, it implies a small radius of curvature, high variations in instantaneous normal velocity (see in this respect Figure 4.5, to be introduced later in text) and relative high variations in the orientation of the instantaneous geometrical normal (parameter $\Delta\vec{n}_{GEO}$ in the tables from Appendix C). Therefore one can presume that the characteristics of this solution depend more on the timing information than in other cases.

The stability of the results was tested by using other three choices when determining the timing information, namely when the satellites detect the magnetic levels encompassing $\texttt{tanh}(1.1) \approx 80.0\%$, $\texttt{tanh}(1.2) \approx 83.4\%$ and $\texttt{tanh}(1.3) \approx 86.2\%$ of the MP total magnetic jump. We found that, as far as the geometrical parameters are concerned, the solution is very stable. For example, the direction of the primary MP movement changed by only 1.5 degrees and the values of the angles $\sphericalangle(\vec{n}_{GEO}^{\,ave}, \vec{n}_{MVAB})$ (between the average geometrical normal and the normal from the planar nested MVAB) and $\Delta\vec{n}_{GEO}$ (indicating the variation of the geometrical normal during one transition) vary approximately within the same range.

The dynamical parameters have a somewhat larger variation, with the average normal velocity varying by $\approx 3.2\%$, $\approx 6.8\%$ and $\approx 10.3\%$ when the timing information was set at $\texttt{tanh}(1.1)$, $\texttt{tanh}(1.3)$ and $\texttt{tanh}(1.3)$ MP magnetic extension, respectively. A similar behaviour is noticed for the MP thickness. We believe that this has to do with the relative large variation in the normal velocity at each spacecraft (see in Figure 4.5, the evolution of the blue line), which is in conflict with our initial use of a symmetrical profile to fit the magnetic traces. Indeed, we carry-out a similar investigation for a solution implying less variation in the normal velocity namely the solution Cyl_2deg_OpTA_solB. In Figure 4.5 that solution appears in yellow trace. In this case, the analysis indicates that the variations in the average normal velocity are only $\approx 1.0\%$, $\approx 2.2\%$ and $\approx 3.6\%$ respectively.

4.3 Comparison with planar, single spacecraft techniques

In this section we shall compare the results obtained in the various implementations of the timing-technique designed for a 2-D, non-planar MP, with the results provided by the planar,

single-spacecraft methods (like minimum variance analysis of the magnetic field, minimum Faraday residue analysis and deHoffmann-Teller analysis).

There are two common problems that make such a comparison difficult. In the first place, the planar methods and the 2-D method rely on different data intervals, with the latter technique using only the smaller central intervals $[\,T_{ci}-\tau_i,\ T_{ci}+\tau_i\,]$. And, in the second place, the single-spacecraft methods offer per definition parameters of the crossings (normals, velocities etc) not correlated over the four satellites whereas the 2-D method is a multi-spacecraft technique, providing in each moment parameters linked through the MP geometry and dynamics. In the next subsections we will discuss these aspects in detail.

4.3.1 Comparison with minimum variance analysis of the magnetic field

As mentioned in Section 3.2 we developed a criterion to optimize the results obtained in the plain timing analysis for the problem of a 2-D, non-planar MP (see also Section B.5). For this purpose we define a global (i.e. over the four Cluster satellites) normal magnetic variance as a weighted sum of the individual variances along the instantaneous (i.e. geometrical) normals. Then, by imposing different orientations for the direction of principal MP movement in the plane perpendicular to $\vec{l}$, we solve the timing problem and select at the end that solution for which the global normal magnetic variance is minimum.

This criterion appears to us natural and well-grounded and offers the possibility to compare different solutions describing the movement and configuration of a 2-D MP. When it comes to the problem of comparing the results obtained in the planar assumption with the ones from the non-planar method it is difficult to decide which of the two approaches performs better from the point of view of magnetic variance analysis. At the heart of this difficulty lies the different data interval used by each method: planar MVAB requires an interval large enough to encompass the whole magnetic field rotation whereas in our method we use only the central interval, between $B_m + (1/2)\,\Delta B\,\texttt{tanh}(-1)$ and $B_m + (1/2)\Delta B\,\texttt{tanh}(1)$, according to our convention for extracting the timing information. In this respect, compare for example in the upper part of Figure 3.10 the intervals between the vertical grey stripes (marking the extent of the eleven nested intervals used in the planar MVAB) with the interval between the vertical magenta dashed lines (used for establishing the timing information).

Where to set the magnetic levels used in extracting the timing information in the 2-D, non-planar case, is a trade-off between the following considerations. On one hand, the solutions to be found for the MP movement and geometry are valid, strictly speaking, only for the transition intervals $[T_{ci}-\tau_i, T_{ci}+\tau_i]$. Therefore we would like to have values for τ_i as large as possible to embrace the whole field transition seen at the magnetopause. A large interval would also reduce the influence of possible local variations in the MP structure (like, for example, magnetic islands or noise) and would provide a better comparison of the 2-D geometric normals with the individual (planar) MVAB normals, determined by using greater intervals.

On the other hand, as we know, the MP is in general not moving uniformly during the crossing interval: often relatively big changes in the normal velocity take place, sometimes even a reverse motion, and this behaviour is very hard or even impossible to be noticed in the data when the spacecraft is closer to the adjacent asymptotic regimes. Also, in following the procedure for extracting the timing information, we actually make an assumption about the normal velocity variation and magnetic profile of the MP. For example by using a Harris type dependence as fitting function we make the approximation that the net effect of the MP movement and structure is a symmetric magnetic trace (as pointed out in Section 3.4, the magnetic profile used to extract the timing information should be consistent with the

normal velocity variation, but this is not know at the beginning). Therefore, considering the last arguments, it is more advisable to use small central intervals, corresponding to the region where the magnetic field gradient is high. There the possible irregularities in the MP movement are easily seen and from the quality of the fit one can establish whether our model for the magnetic profile takes them correctly into account.

Coming back to the point of comparing the two techniques (planar and 2-D) we stress that extending the 2-D solutions beyond the intervals used in the timing conditions should be done with care. There is no reason to believe that the MP will keep its dynamic regime for a long time outside these central interval. On the other hand, using for comparison the results obtained from planar MVAB when this technique is applied on the central intervals $[Tc_i - \tau_i,\, Tc_i + \tau_i]$ involves the risk of a big influence from the local internal irregularities.

For analysing this issue, we have chosen all the solutions obtained from the optimized timing-MVAB method in the 2-D problem and, by using different central intervals of increasing width, we studied how the corresponding normal magnetic variance and normal magnetic component $\langle B_n \rangle$ compare with the similar quantities obtained from the single-spacecraft, planar MVAB technique. More precisely, for the above mentioned time-intervals, we computed the global and the individual (i.e. for each satellite) quantities of normal magnetic variance and $\langle B_n \rangle$ using the following normals:

- the instantaneous, geometrical normals implied by the 2-D, non-planar MP. Clearly, the direction of these normals are changing in time, according to the MP movement. Because in the analysis we used also time intervals different than $[T_{ci} - \tau_i, T_{ci} + \tau_i]$, we have to extend the validity range of the 2-D solutions.
- the normals that appear in Table 3.1, i.e. provided by the (constrained to $\langle B_n \rangle = 0$) MVAB on the eleven nested intervals. The direction of these normals are fixed in space.
- the normals obtained when, for each satellite and for the time-interval in question, a constrained MVAB is performed. By 'constrained' we meant here perpendicular to the invariant direction $\vec{l}$. As a consequence, in this case the direction of the normals is changing with the interval of analysis according to the planar MVAB theory. We will refer to these normals as the *planar, interval-specific MVAB* normals.

The results obtained in this study are presented in Appendix E, Figures E.1, E.2 and E.3. At that location, a detailed comparison between the planar and Cyl_2deg_OpTA_solA solutions is provided. Specifically, in this case we found that:

- for all satellites and for most of the intervals with a half-width smaller than $2\tau_i$, the average normal magnetic component $\langle B_n \rangle$ computed with the 2-D, instantaneous normals are smaller than the similar quantities obtained from the *planar, interval-specific MVAB* normals. This is an indication that no undesired and non-realistic offset in the values of $\langle B_n \rangle$ are introduced by the timing problem for the particular solution we discuss.
- for intervals having the half-width $\upsilon_i < \tau_i + 5$ seconds the 2-D, instantaneous normals offer a smaller global variance than the *planar, interval-specific* normals, which are the best possible planar MVAB normals for each interval.

Considering the above arguments, one can definitely endorse the assertion that, for the specified intervals, the Cyl_2deg_OpTA_solA MP solution performs better than the planar one from MVAB point of view. A similar behaviour was seen for the Prbl_2deg_OpTA solution but for the other 2-D solutions the global magnetic variance based on the instantaneous, geometrical normals started to raise monotonically when the interval of analysis increases.

Nevertheless, when comparing one particular 2-D solution and the MVAB planar results, it

is not necessary to adopt a too strict criterion, namely that the global magnetic variance based on the 2-D, instantaneous normal to be smaller than the similar quantity based on the *planar, interval-specific MVAB* normals. As mentioned at the beginning of this section, the individual *planar, interval-specific MVAB* normals are decoupled, whereas in the 2-D method they are linked in each moment through the chosen geometry and the resulting dynamics, giving a more realistic description of the MP.

Another interesting aspect revealed by the study refers to Cluster 2. For this spacecraft and for the central interval $[T_{c2} - \tau_2, T_{c2} + \tau_2]$, used in determining the timing information, we found out that the magnetic local, internal irregularities (magnetic islands, noise etc.) are playing an important role, making the comparison of the 2-D and planar, interval-dependent MVAB results irrelevant. This is the reason why, in Table 4.4 from Section 4.4, and in tables A to H from Appendix C, when we make a comparison of the 2-D, non-planar solution with the results from the planar MVAB method, we compared the global magnetic variance using data from all satellites (black numbers) and data only from Cluster 1, Cluster 3 and Cluster 4 (the blue numbers).

On the other hand, in case of Cluster 3 and Cluster 1 for the intervals having τ_i as half-width, we found that basically for all the central intervals participating in the analysis the *planar, interval-specific MVAB* normals lie in the angular range of evolution for the 2-D, instantaneous normals. That is exactly what one would expect from the results of a planar MVAB technique applied on an ideal 2-D discontinuity (see *Dunlop and Woodward* [1998]). This result is remarkable considering the fact that the 2-D solution which we currently analyse is practically the same as one obtained from the plain timing analysis (solution Cyl_2deg_TA, from pages 174 and 175).

In Table 4.4 from Section 4.4 we present a comparison between the results obtained from three single-spacecraft planar techniques and from the various solutions provided by the 2-D method. The planar techniques, appearing in the upper part of the table, are MVAB, Minimum Faraday residue (MFR) and deHoffmann-Teller (HT) analysis. The results related to this subsection are shown in the leftmost column, concerned with the global normal magnetic variance. In the planar case, we present the value of this quantity as resulted from the MVAB nested technique and the value obtained when the *planar, interval-specific MVAB* normals corresponding to $[T_{ci} - \tau_i, T_{ci} + \tau_i]$ intervals were used. In the lower part of the table, for each 2-D MP solution we showed the global magnetic variance computed along the instantaneous, geometrical normals. Two sets of numbers are displayed: the black ones are based on data provided by all 4 satellites, whereas the smaller, blue numbers are based on data provided only by Cluster 1, Cluster 3 and Cluster 4.

In Table A to H from Appendix C, under the 'MVAB results' section we give a more detailed comparison. On one hand, we provide also the individual values of the normal magnetic variance and of the average normal magnetic component. On the other hand, we strive to take into account the small 3-D effects present in this event, responsible for the fact that the individual, nested MVAB normals are not exactly contained in one plane (see Figure 3.8). It turned-out that this aspect is not important in the comparison (see Section 4.4 and the description of the tables from Appendix C).

In Section 4.4 we will comment different solutions provided by the 2-D, non-planar method and we will compare the results provided by the planar and non-planar techniques. On that occasion, two solutions turned out to be unsatisfactory, namely Prbl_2deg_TA and Cyl_1deg_TA. They appear on gray background in Table 4.4.

4.3.2 Comparison with minimum Faraday residue method

The results from the timing technique introduced in Chapter 3 could be compared with the results from another single-spacecraft method, relying on a planar assumption for the MP, called Minimum Faraday Residue (MFR) and presented in Appendix G. It infers the normal direction and the velocity along that normal (considered constant) based on the conservation of the magnetic flux across a discontinuity.

For this method we need, apart from magnetic field data, the electric field information as well. In many cases one could use the plasma velocity measurements $\vec{v}$ and the electric field approximation $\vec{E} = -\vec{v} \times \vec{B}$ with good results (see for example *Khrabrov and Sonnerup* [1998], *Haaland et al.* [2004a], *Sonnerup et al.* [2006]). However, in our particular case, due to the 4 second time-resolution of the CIS plasma instrument on-board Cluster, one would obtain only few points of data contained in the central intervals used for setting the timing conditions.

Unfortunately, in our test case the use of high resolution measurements provided by the electric field experiment EFW on-board Cluster entails significant problems, besides the problem of sunward field offsets (see the paragraph presenting this instrument in Section 2.2). Under these circumstances, to be addressed below, we could not fully incorporate this technique in our analysis and therefore we choose it for comparison only. Indeed, without these problems we could have combined the timing analysis with the MFR analysis in the same way as we have done with MVAB technique. In the words of Section B.5, the optimum orientation of the primary direction (the value of angle β) would then be one for which the corresponding solution offers a minimum (global) Faraday residue. Also, as another possibility, a set of reliable electric field data could have been used simultaneously with the magnetic field data by adding the variances provided by MFR and MVAB techniques and using the minimum of this quantity to identify the optimum solution (see the last paragraph of Section B.5).

Determining the electric field vector

As was described in Section 2.2, the EFW experiment provides only the projection of the electric field vector on the spacecraft equatorial plane (spin plane). This is done by measuring the potential difference between two pairs of probes disposed along perpendicular directions in that plane. But for Cluster 1 ad Cluster 3 satellites, one probe (the probe number 1) is not working and therefore the measurements provided by the remaining functional pair of probes (probes 3 and 4) are not sufficient for obtaining the electric field vector in the spin plane with high time resolution. In principle one can use for this the additional information provided by the potential difference between probe 1 and one probe from the remaining pair (say probe 3). But there is an asymmetric contamination with photoelectrons for different booms and probes which raises the level of uncertainties.

Another problem refers to the procedure used for inferring the third (i.e. out of the plane of measurements) electric field component. This relies on the assumption $\vec{E} \cdot \vec{B} = 0$ from which the needed component is obtained by applying the formula

$$E_z = -\frac{E_x B_x + E_y B_y}{B_z} \tag{4.2}$$

in the so-called ISR2 reference frame (a fix, i.e. despun, reference frame with the xy plane, containing the electric field sensors, that slightly differs from the GSE xy plane). In our case it turned out that, for a significant part of the MP region, the magnetic field vector is close to this plane (B_z small) which results in high errors for E_z. As a rule of thumb, an angle of minimum 15° between $\vec{B}$ and the spin plane is considered appropriate for applying formula

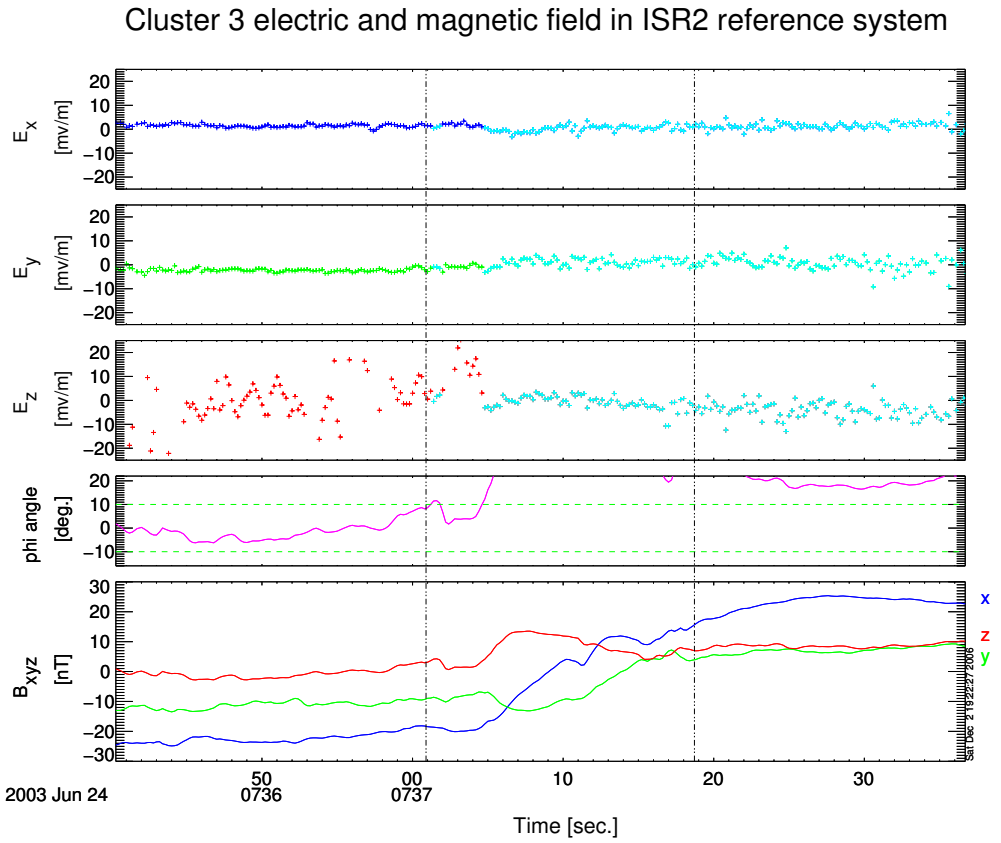

Figure 4.3: From top to bottom we have: the measured E_x (in blue) and E_y (in green) electric field components, the computed E_z (in red) component, obtained by applying formula (4.2), the angle ϕ of $\vec{B}$ with the spin, equatorial plane and the magnetic field components. All the quantities refer to Cluster 3 satellite and are presented in the ISR2 reference frame. We showed in cyan the electric field values for the times when $\phi \geq 10\,^\circ$. The vertical dashed lines indicate the central crossing region entering in the timing analysis.

(4.2). However, when we compute the electric field third component in case of Cluster 1 and Cluster 3 we decided to lower this limit to only $10\,^\circ$ in order to obtain more data points within the crossing intervals[1]. For this threshold the values of E_z are still reasonable on both satellites.

For illustrating this procedure, we present in Figure 4.3 the Cluster 3 electric and magnetic field measurements in ISR2 reference frame. The displayed time interval corresponds to the largest interval from the nested MVAB analysis and the vertical dashed lines indicate the central crossing region. In the first two panels the primary data is shown, i.e. the measured E_x, respectively E_y electric field component. The third panel contains the E_z component obtained by applying formula (4.2). From the forth panel, representing the angle of $\vec{B}$ with the equatorial (spin) plane (ϕ angle in degrees, only in the range $[-16, 22]$), one can see that, for a significant part of the crossing, it has a relatively small value. Consequently, the corresponding points in the third panel are more spread and take unreasonable high values.

[1]Electric field data for Cluster 2 and Cluster 4 was provided directly as full 3-D vector in GSE (0.04 sec. time resolution) by Bjørn Lybekk and Arne Dahlback from University of Oslo. For Cluster 1 and Cluster 3, which needed special treatment due to the lack of measurements from probe 1, the data was provided by Per-Arne Lindqvist and Tomas Karlsson from Alfvén Laboratory, Stockholm as x and y components in ISR2 reference system (0.2 sec. time resolution). Therefore, in this case, the procedure for finding the third component was applied by ourselves.

Table 4.1: Results from constrained Minimum Faraday Residue technique. The columns appearing in this table are for the eigenvalues, for the three GSE components of the eigenvectors resulting in the analysis, for the MP normal velocity and for the angle between the predicted normals (shown in bold faces) and the plane perpendicular to the invariant direction.

	$\lambda \cdot 10^6$ $[mV/m]^2$	n_x	n_y	n_z	u_n $[km/s]$	Ω $[deg.]$
	0.0	0.0669	0.4928	−0.8675		
Cluster1	**4.188**	**0.3610**	**−0.8226**	**−0.4394**	167.05	−0.42
	11.803	−0.9302	−0.2838	−0.2329		
	0.0	−0.0397	0.1493	−0.9880		
Cluster2	**1.278**	**0.5725**	**−0.8070**	**−0.1449**	138.77	−3.25
	15.011	−0.8189	−0.5714	−0.0534		
	0.0	−0.1100	0.4701	−0.8757		
Cluster3	**2.282**	**0.4171**	**−0.7779**	**−0.4700**	56.09	−4.89
	4.494	−0.9022	−0.4169	−0.1105		
	0.0	−0.1401	0.0292	−0.9897		
Cluster4	**6.185**	**0.5813**	**−0.8068**	**−0.1061**	182.22	−2.75
	17.637	−0.8016	−0.5901	0.0960		

In the first three panels we overplotted in cyan the same data points when $\phi \geq 10\,^\circ$; these are considered as valid points, from which we selected the points taking part in the MFR analysis.

Results from the planar MFR technique

In Figure 4.4 we show the GSE electric field components for all satellites and a polar plot with the normals obtained from the MFR method. In the upper part the plotted time range for each spacecraft has the same extension as the largest time interval from nested MVAB analysis. The central regions, used for setting the timing conditions, are indicated by vertical continuous lines. In applying the MFR analysis we used the symmetrical (with respect to the central crossing times) intervals between the vertical dotted lines. We computed each normal by imposing the constraint that the average normal magnetic component $\langle B_n \rangle$ is zero for the interval of analysis. In order to minimize the influence of small-scale fluctuations we 'boxcar-averaged' the measurements by using a boxcar window of 2 seconds width, in the same time resampling the data to a resolution of 0.5 seconds.

In the polar plot at the lower part of the figure, the origin is the same reference direction as in Figure 3.7 and Figure 3.8, namely the direction obtained by averaging the normals provided by the constrained (to $\langle B_n \rangle = 0$) nested MVAB analysis. These normals are also shown for comparison and the invariant direction $\vec{l}$ is indicated by the magenta arrow. The MFR normals are shown as crosses, together with their corresponding error bars, calculated by taking into account the statistical fluctuations.

Without the constraint $\langle B_n \rangle = 0$, the resulting MFR normals (not shown) are more scattered and, with the exception of Cluster 2, none of them fit in the range we choose for the polar plot. Also, they are oriented well out of the plane perpendicular to the invariant direction $\vec{l}$, the angle being 27.8 ° for Cluster 1, 10.7 ° for Cluster 2, 22.7 ° for Cluster 3 and 21.2 ° for Cluster 4

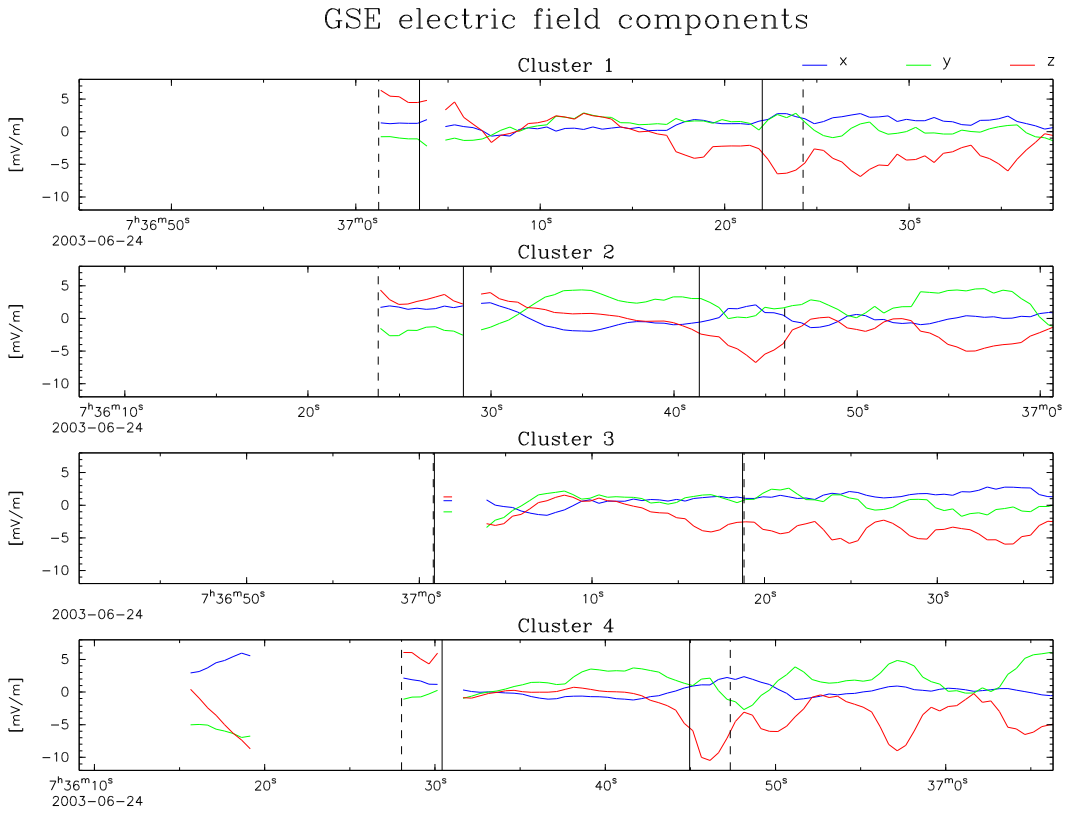

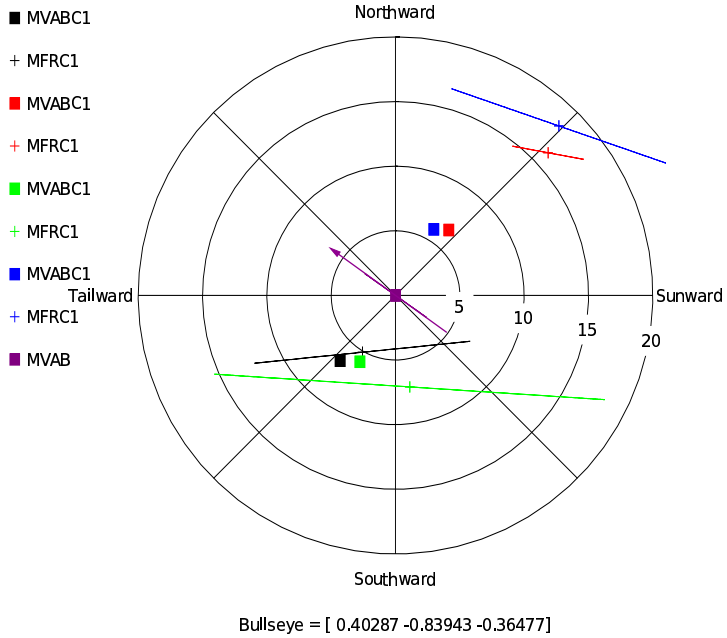

Figure 4.4: *Upper part:* Cluster 1 – 4 electric field components in the GSE for the moments when the data are considered valid to take part in a MFR analysis. The significance of the plotted interval range and of the vertical lines is explained in the text. *Lower part:* Polar plot with the normals obtained from the nested, constrained MVAB analysis described in Section 3.4 and with the normals obtained from the constrained MFR analysis.

By looking at Table 4.1, where the parameters from constrained MFR technique are presented, we can make the following observations:

- the normals provided by this technique (appearing in bold faces) are not so well defined, except, perhaps, in the case of Cluster 2 where the ratio between the maximum and intermediate variance $\lambda_{max}/\lambda_{interm}$ is around 11.7. For the other satellites this quantity is 2.82 (Cluster 1), 1.97 (Cluster 3) and 2.85 (Cluster 4). One possible explanation, apart from the already discussed sources of errors, could be that, due to the lack of data points, our intervals of analysis do not embrace the whole MP transition. Indeed, in case of Cluster 2 approx. 93.7% of the magnetic field rotation takes place during the interval chosen for the MFR analysis (the largest) whereas for Cluster 3 only 76.2% (the smallest).
- the values obtained for the normal velocity (parameter u in the table) are much higher when compared with the average normal velocities obtained from the timing analysis (see Table A to Table H from Appendix C), except in the case of Cluster 3. Also, for Cluster 2 and Cluster 4 (but not so much for Cluster 1 and Cluster 3) the angles between the corresponding MFR normals and nested MVAB normals are relatively big ($\approx 10\,^\circ$ and $\approx 13\,^\circ$). We will discuss these issues further down.

Because of these reasons we decided to use the MFR normals for comparison only (i.e. we did not optimize the timing technique against the MFR method, as we did for MVAB case), illustrating how such a comparison could be done. And yet, it is remarkable that, despite all mentioned sources of errors, the constrained MFR normals lye very close to the plane perpendicular to the invariant direction $\vec{l}$ (see parameter Ω in the table). This supports our initial assumption about a 2-D MP in this case and indicates that such a comparison is valuable. Note that, as in the case of the MVAB method, for an ideal 2-D MP the normals provided by the MFR technique will lie in the plane perpendicular to $\vec{l}$, although their orientation will be influenced by the non-planar effects.

Faraday residues in the planar and 2-D, non-planar method
We would like to give an indication of how sensitive the MFR technique is when applied to a 2-D, non-planar structure. We refer to the expression (G.3), presented in Appendix G for the quantity to be minimized (from *Khrabrov and Sonnerup* [1998])

$$I_F = \left\langle |\delta \vec{E}_\perp{}'|^2 \right\rangle + u_n^2 \left\langle (\vec{n} \cdot \delta \vec{B})^2 \right\rangle \qquad \text{where} \quad \vec{E}\,' = \vec{E} + u_n(\vec{n} \times \vec{B}) \tag{4.3}$$

Here $\langle\ \rangle$ designates the average of a given quantity over the data set corresponding to the transition and the symbol δ denotes the variation of a given quantity from its mean value. $\vec{E}\,' = \vec{E} + u_n(\vec{n} \times \vec{B})$ is the electric field as measured in the frame of reference moving with the layer (at a velocity $u_n\vec{n}$ with respect to the point of observation) and the symbol $\perp$ indicates the transversal component.

From this expression we see that in the MFR method the parameters u_n and $\vec{n}$ are found by minimizing the variance of $(\vec{E} + u_n\vec{n} \times \vec{B})_\perp$ plus u_n^2 times the variance of B_n. Commonly at the MP (and in our case in particular) $\vec{E}$ has the largest component in the normal direction and $\vec{B}$ is much larger in the tangential plane. Therefore this method is very sensitive to the planar character of the MP: even small 2-D, non-planar effects may be sufficient to destroy the ability to find accurate values for the normal direction and the velocity along this normal. From this perspective we think that the MFR normals obtained in our case are reasonable good. As for the high u_n values in Table 4.1 (when comparing with the average normal velocities provided

by the timing analysis) we have no particular explanation, except, probably, the drop in the magnitude of $\vec{B}$ observed at the central part of each transition (see Figure 3.6). A more detailed investigation, like using simulated data to study how the (planar) MFR method performs on a 2-D discontinuity, as done by *Dunlop and Woodward* [1998] for the case of MVAB technique, would be useful.

In order to compare the results from the MFR method and the timing technique introduced in Chapter 3, for each satellite we computed in the first place the Faraday residue on the central crossing intervals based on the parameters $\vec{n}$ and u_n from Table 4.1 (note that these parameters are obtained from larger intervals, indicated by vertical dotted lines in Figure 4.4). For this we used the formula (4.3). Then, we calculated similar quantities based on the instantaneous normals $\vec{n}_{GEO}$ and normal velocities u_{GEO} provided by the timing technique. More precisely we used the formula

$$I_F = \left\langle |\delta\vec{E}_\perp{}'|^2 \right\rangle + u_{GEO}^2 \left\langle (\vec{n}_{GEO} \cdot \delta\vec{B})^2 \right\rangle \qquad \text{where} \quad \vec{E}\,' = \vec{E} + u_{GEO}(\vec{n}_{GEO} \times \vec{B})$$

We took this line of action because we wanted to compare the same time-intervals and, as discussed in Subsection 4.3.1, the solutions from the timing analysis are valid, strictly speaking, only for the central crossing intervals. Global quantities were computed by summing the Faraday residues from all four spacecraft using weighting coefficients defined in a similar way as for the MVAB technique:

$$w_i = \mathbf{Tr}_{c,i}^{-1}(\lambda) \Big/ \sum_{k=1}^{k=4} \mathbf{Tr}_{c,k}^{-1}(\lambda) \tag{4.4}$$

where $\mathbf{Tr}_{c,i}$ is the trace from the constrained MFR analysis performed with satellite i data, on the corresponding central crossing interval.

The result of the comparison appears in the middle column of Table 4.4 and in each table from Appendix C, under the 'MFR results' section. In all the places, two set of numbers are displayed: the black ones are based on data provided by all 4 satellites, whereas the smaller, red numbers are based on data provided only by Cluster 3 and Cluster 1. As will be explained in Section 4.4, Cluster 2 and Cluster 4 provide a somehow contradictory MFR results and therefore we prefer to have this additional way of comparison.

4.3.3 Comparison with deHoffmann-Teller analysis

The deHoffmann-Teller (HT) technique is presented in Appendix F. It is used to determine a moving reference system in which the electric field vanishes, or nearly vanishes in the context of experimental data. More precisely, starting from the set of measured values for the magnetic field and electric field, the method searches for the necessary velocity $\vec{V}_{HT}$ of such a frame that transforms away the electric field. The existence of a HT frame implies that the measurements are compatible with the steady movement, relative to the instrument frame, of a quasi stationary structure with no internal electric field.

In our test case we were able to identify 'good' HT frames (i.e. with correlation coefficients $\gtrsim 0.95$) associated to the crossing intervals for all four Cluster satellites. Table 4.2 presents the results obtained from this analysis, and the meaning of the parameters appearing in it (explained also in Appendix F). We used plasma measurements in case of Cluster 1, Cluster 3 (HIA sensor) and Cluster 4 (CODIF sensor) together with the approximation $\vec{E} = -\vec{v} \times \vec{B}$ for the electric field. When using directly the electric field measurements provided by the EFW instrument, the method did not provide reasonably good HT frames for these satellites,

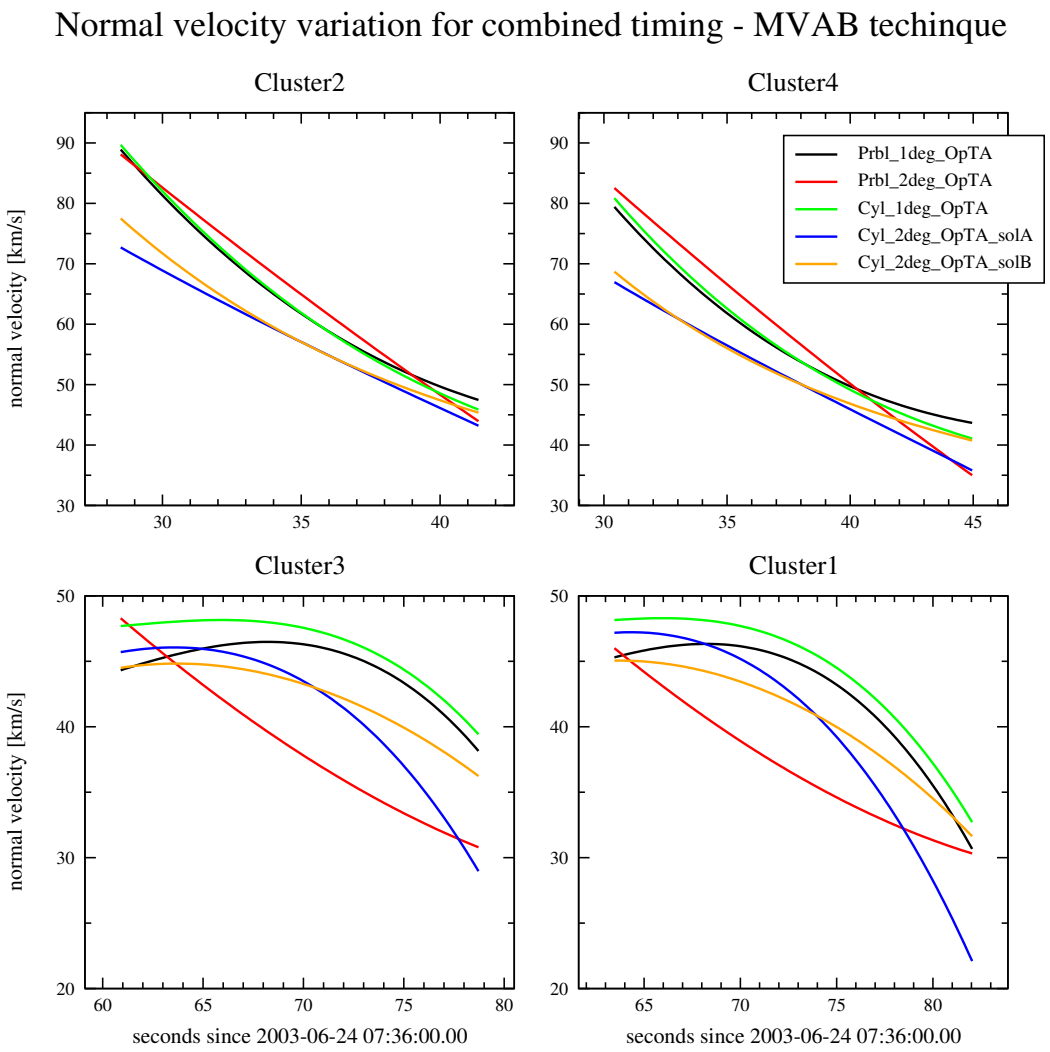

Figure 4.5: Time dependence of the MP normal velocities according to the different implementations (represented in different colours as indicated in the legend box) of the timing – MVAB technique. For each satellite the time range corresponds to the central crossing interval.

Table 4.2: Results from the deHoffmann-Teller analysis. For each satellite the following parameters are shown: the interval of analysis, the number of data samples, the central interval used to set the timing conditions, the correlation coefficient and the slope of the fit between the electric field $\vec{E}_c = -\vec{v} \times \vec{B}$ and the convection electric field $\vec{E}_{HT} = -\vec{V}_{HT} \times \vec{B}$ (like in Figure 3.5), the ratio between the convection electric field in the starting reference frame and in the deHoffmann-Teller frame and the three components of V_{HT} velocity in GSE.

	HT interval	samples	central int.	correl.	slope	D/D_0	$V_{HT}\,[km/s]$
Cluster2	[28.50−41.38]	24	[28.50−41.38]	0.944	1.030	0.109	[231.7 57.9 −102.0]
Cluster4	[27.44−47.33]	5	[30.42−44.96]	0.990	0.997	0.019	[199.9 177.2 −202.7]
Cluster3	[58.88−78.90]	5	[60.60−78.72]	0.990	1.000	0.020	[77.2 151.4 −181.4]
Cluster1	[65.77−81.87]	4	[63.46−82.04]	0.955	0.981	0.088	[250.8 155.6 −149.5]

the correlation coefficients corresponding to the central crossing intervals being 0.71, 0.43 and 0.86 in case of Cluster 1, Cluster 3 and Cluster 4 respectively. But fortunately, in case of Cluster 2, where no plasma data are available, the identification proved successful, with the corresponding correlation coefficient of 0.944 (see column 5 of Table 4.2). The time intervals for the analysis (appearing in column 2) was chosen as close as possible to the central crossing intervals used for the timing conditions (appearing in column 4).

In evaluating the results of HT analysis, the projection of $\vec{V}_{HT}$ along the discontinuity normal (which is not found in the HT analysis but inferred in a different way) is compared with the normal velocity provided by other method. We will do so by computing the projection of $\vec{V}_{HT}$ along the normals provided by the nested MVAB analysis $\langle\vec{n}\rangle_{MVAB}$ (i.e. the ones shown in Table 3.1) and along the average geometrical normals resulting from different implementations of our timing technique. These values are to be compared with the normal velocities predicted by the timing analysis in that particular case.

The result of the comparison appears in tables A to H from Appendix C, under the 'deHoffmann-Teller results' section and will be discussed in Section 4.4. Also, a synthesis of the information contained in these tables, comparing the projection of $\vec{V}_{HT}$ along the $\langle\vec{n}\rangle_{MVAB}$ normals with the normal velocities from the 2-D solutions can be found in the four rightmost columns of Table 4.4 from Section 4.4.

When making the comparison one has to consider the following aspects: in the implementation we used for finding a HT frame, we assumed a constant velocity for it both in direction and magnitude. In general for a 2-D, non-planar MP having 2 degrees of freedom the first condition is not obeyed. As for the second part, this is also in general not the case. To see this more clearly, we present in Figure 4.5 how the normal velocity varies according to the solutions found in the various combined timing - MVAB implementations.

4.4 Comments and discussions

Discussions of the solutions

In Table 4.3, compiled from the tables A to H in Appendix C, for each solution found with the 2-D, non-planar method we present the global parameters referring to the MP orientation, radius of curvature, normal velocity and thickness. From left to right we have:

- the angle between $\vec{n}_{ext}$ and $\langle\vec{n}\rangle_{MVAB}$. The first unit vector is along the average (over the 4 satellites) direction of the individual average (over the crossing duration) geometrical normals. It points towards the exterior of the boundary (in the geometrical sense). $\langle\vec{n}\rangle_{MVAB}$ represents the average of MVAB normals obtained in the nested analysis. We recall that $\langle\vec{n}\rangle_{MVAB}$ was also chosen as reference direction in the polar plots 3.7, 4.1 and 4.4.
- in the third, fourth and fifth columns we show the global radius of curvature, normal velocity and thickness, respectively. By global we mean the geometrical mean (radius of curvature) or the arithmetical mean (normal velocity and thickness) of the corresponding individual quantities detected by each Cluster satellite.
- the sixth column presents the angle between the MP primary direction of motion (along $\vec{y}$ axes in all figures from A to H) and $\langle\vec{n}\rangle_{MVAB}$
- in the last column, useful for the discussions at the end of this subsection, we show how different the normals obtained from 2-D method and the normals from the planar MVAB technique corresponding to the crossing intervals are. More precisely, we computed for

each satellite the angle between the average geometrical normal $\vec{n}_{GEO}^{\,ave}$ and the constrained (i.e. perpendicular to $\vec{l}$) planar normal $\vec{n}_{MVAB,\perp\vec{l}}^{\,central}$ obtained when MVAB is applied on the central points of the transition. We took the absolute values of these quantities and show in the last column, for each 2-D solution, the arithmetical mean of these values considering all four satellites (black numbers) or only Cluster 1, Cluster 3 and Cluster 4 (blue numbers).

When comparing different solutions obtained in our analysis, we have to drop right away the one provided by the parabolic model, with the plain timing analysis (i.e. Prbl_2deg_TA, see pages 166 and 167). The distance between the MP leading and trailing edges, although fixed in the model along the the primary direction, varies during the crossings along the normal direction at each satellite location. Therefore the differences between the MP thickness at the beginning and at the end of transition seems to us artificial, resulting in a relative variation (parameter δT_i from equation (B.76)) up to 71% for Cluster 2 and 72% for Cluster 4. In the same time, the values for the average normal magnetic field (2.85 nT for Cluster 2 and 3.54 nT for Cluster 4) and magnetic variance (for example 13.409 nT^2 in case of Cluster 2) are very high as well. Besides, based on this test-case and on another event not presented in the thesis, we found that this particular implementation of the 2-D, non-planar timing analysis gives unstable results: small changes in the satellites relative positions or in the timing information lead to big variations in the parameters of the solution.

By proposing a parabolic shape for the MP, the underlying idea was to model travelling waves on this boundary. Therefore we hoped for a solution with the primary direction (along $\vec{y}$ in Figure A) close to the average of MP normals (indicated by $\vec{n}_{ext}$): when the angle between the two directions is less than 30 ° a wave form is well approximated (within 0.5% relative error) by a parabolic curve. It turned out that, although mathematically valid, the above mentioned solution do not fulfil this expectation. The satellites transitions take place far away from the

Table 4.3: Characteristics of the 2-D, non-planar MP, as obtained from the various implementation of the method. Global values of orientation, curvature, normal velocity and thickness are presented in the second to fifth columns. In the sixth column we show the angle between the direction of MP primary motion and the average direction of MVAB normals obtained in the nested analysis. The last column show how different are the normals obtained from 2-D method and the normals from the planar MVAB technique corresponding to the crossing intervals. The meaning of the background colours attached to each solution is explained in the last paragraph of this section.

	$\sphericalangle(\vec{n}_{ext}, \langle\vec{n}\rangle_{MVAB})$ [deg]	radius [R_E]	velocity [km/s]	thickness [km]	$\sphericalangle(\vec{y}, \langle\vec{n}\rangle_{MVAB})$ [deg]	$\sphericalangle(\vec{n}_{GEO}^{\,ave}, \vec{n}_{MVAB,\perp\vec{l}}^{\,central})$ [deg]	
Prbl_2deg_TA	172.1	-784.7	50.58	704.5	−88.8	18.9	15.8
Prbl_1deg_OpTA	9.0	2.87	52.04	809.8	−3.9	4.6	2.1
Prbl_2deg_OpTA	7.1	1.81	49.74	764.9	16.8	3.1	1.0
Cyl_1deg_TA	11.0	4.82	55.19	861.1	−122.9	6.4	3.7
Cyl_2deg_TA	3.9	1.85	47.45	740.3	−105.3	2.9	2.4
Cyl_1deg_OpTA	9.8	2.09	52.84	824.4	−37.1	5.2	3.2
Cyl_2deg_OpTA_solA	3.9	1.85	47.45	740.3	−105.2	2.9	2.4
Cyl_2deg_OpTA_solB	6.7	2.39	48.40	755.1	−95.0	3.0	1.6

parabola's peak, where its branches form almost a plane surface; consequently, the radius of curvature, expressed in Earth radii takes very large value. Despite its unrealistic behaviour, we decided to present this case for comparison: one can see below that the optimization through magnetic variance analysis brings significant improvements.

Indeed, the other two solutions corresponding to the parabolic MP provided by the combined timing-MVAB technique (i.e Prbl_1deg_OpTA and Prbl_2deg_OpTA), look much better from this respect. For example the implementation which allows for MP displacements only in one direction gives a solution in which this direction of movement is very close (namely 3.9 °) to the averaged (over the four spacecraft) nested MVAB normal $\langle \vec{n} \rangle_{MVAB}$. Taking into account that we have for this event an in-bound transition (see Figure 3.4) the result implies a local, stationary bulge (i.e. not moving along the MP surface but with this boundary as a whole) having approximately 2.9 R_E as radius of curvature. Actually in all implementations, with the exception of the one we dropped from the beginning, we obtained positive values for the radius of curvature, implying a convex shape for the MP. The different scale-length (i.e. local radius of curvature) provided by different solutions have to be compared with the radius of curvature of a model MP at the position of the event, computed in Section 3.4 to be around 19.3 R_E.

The Prbl_2deg_OpTA solution (pages 170 and 171) has its principal direction 16.8 ° from $\langle \vec{n} \rangle_{MVAB}$. It implies a smaller average radius of curvature (1.81 R_E) which was somehow expected because now also a secondary movement, perpendicular to the primary direction and with constant velocity, is present. The MP thickness varies during the crossing intervals up to 9% in case of the trailing spacecraft (Cluster 1) and only 2% for the leading one (Cluster 2). We stress again that this variation is not due to a compression or expansion of the boundary surface but is a perception effect of a moving MP relative to the (allmost) fixed satellites.

The Prbl_2deg_OpTA solution, as well as the cylindrical solutions Cyl_2deg_TA (pages 174 and 175) and Cyl_2deg_OpTA_solA (pages 178 and 179), imply a return to the MP of the first pair of satellites (Cluster 2 and Cluster 4) at the end of the event, i.e. around the time when the second pair of satellites (Cluster 3 and Cluster 1) finish their transitions. This return is not seen in the data and therefore means a disagreement with the physical situation.

This aspect could be reconciled if we limit in an appropriate way their range of validity. In general, a limitation in the validity of any solution found in this chapter is obvious: all of them describe the MP boundary only locally. Also, we expect that, for a solution involving a smaller radius of curvature the range of validity to be smaller as well. In Figure C, presenting the MP configuration in the Prbl_2deg_OpTA implementation, we draw only a portion of the MP layer that extends to the left (positive $\vec{x}$ direction) from the parabola's peak. Judging from the satellites transitions alone, the MP layer could extend infinitely to the left but we showed only a portion of 8000 km of it. As for the right margin we have to cut the layer around the parabola's peak (where the local radius of curvature is only 1.24 R_E) in order to avoid the mentioned 'artificial' transitions. Therefore, the solution obtained in this implementation demands a change in the MP geometry, to the right from this point. Another possibility would be to consider the MP as a steady-state structure only for a limited spatial-temporal neighbourhood around the individual transitions and therefore to argue that after the first pair of satellites crossed the layer, it changed its shape.

As just mentioned, a similar limitation in the validity range is necessary for the solutions Cyl_2deg_TA and Cyl_2deg_OpTA_solA. In the corresponding figures describing the MP configuration and movement, we have drawn the MP as a cylindrical sector that has an upper angular limit of approx. 29 ° from the $\vec{x}$ axis.

The fact that in the two parabolic cases the primary directions are close to $\langle \vec{n} \rangle_{MVAB}$ makes them interesting because in this case we can ascribe naturally a physical interpretation to

the parameters $A_0, A_1, ...$ and V (see the discussion at the end of Section B.4). The first parameters represent the initial normal velocity, normal acceleration and so on, that globally characterize the MP movement, whereas V is the tangential (to the MP) velocity. Near all the solutions in the cylindrical case the primary direction $\vec{y}$ makes a larger angle with $\langle \vec{n} \rangle_{MVAB}$, sometimes close to 90 °. In these situations the notions 'MP tangential movement' and 'MP normal movement' are linked with the primary direction and secondary direction respectively (the reverse situation from what we had in mind when introducing the techniques).

We illustrate this aspect in Figure 4.6, which presents a sequence of 12 MP positions, corresponding to the solution Cyl_2deg_OpTA_solB from pages 180 and 181. In this case the angle between the principal direction (along $\vec{y}$) and the direction of averaged nested MVAB normals $\langle \vec{n} \rangle_{MVAB}$ is 95 °. Therefore the 'normal' MP movement is due to the constant velocity along the secondary direction whereas the 'tangential' velocity is described by A_0, A_1 and A_2. The markers on the MP helps in tracing this tangential movement: first there is a relatively fast displacement in the upward direction (as seen from the central marker on the MP) in the figure followed by an almost still period (panels 4 to 7) and then a small recoil (starting with panel 8). This back-and-forth movement is also encountered in the other two solutions corresponding to the cylindrical model with 2 degree of freedom (i.e. Cyl_2deg_TA and Cyl_2deg_OpTA_solA).

A similar situation occurred in the case of Cyl_1deg_TA implementation (pages 172 and 173), but here the solution deserve a special attention. In this case we have no displacement along $\vec{x}$ (oriented relatively close to the MP normal direction) and the crossings are produced by a tangential (to the MP) movement of a wave-like structure. It is therefore no surprise that after approx. 9 seconds from the end of the event the solution implies a return of the satellites to the magnetosheath, beginning with Cluster1. That solution has also a systematically higher value for the normal magnetic field variance when compared with other 2-D solutions or with the planar analysis (see Table 4.3 for the global value of this quantity and tables A to H for the individual ones). We therefore conclude that our event is not well described by this implementation.

Actually, in case of a cylindrical MP, only the solution Cyl_1deg_OpTA (presented on pages 176 and 177), which is the optimized version of the solution we just dropped as inadequate, seems to be oriented according to the situation we had in mind when the model was proposed. This is similar to what happened in the parabolic case (discussed at the beginning of this subsection) where the optimization lead to a change in orientation. The decrease in the global magnetic variance from 4.191 to 3.220 is associated with a change of ~ 86 ° in the orientation of the primary MP motion, with the new direction closer to the average nested MVAB normals.

We would like to add some additional observations at the end of this subsection

- the parameters $A_0, A_1, ...$ and V take reasonable values in all the implementations we considered valid (see tables A to H from Appendix C).
- the transition parameters obtained in each case (orientation, normal velocity, thickness and radius of curvature) are not very different. For example, the global MP orientation, as expressed by $\vec{n}_{ext}$, change within approx. 6 ° across different implementations. In the same time, the global values of the normal velocities vary from 47.45 to 52.84, i.e. approx. 10%. Of course, the same applies to the global values of MP thickness because the crossing durations are the same. In case of radius of curvature, the variation is between 1.85 and 2.87 R_E, i.e. approx. 45%.
- the average geometrical normals and the constrained (i.e. perpendicular to $\vec{l}$) planar MVAB normals corresponding to the central intervals (rightmost column in Table 4.3) are remarkably close to one another. Neglecting the Cluster 2 situation, for the reason

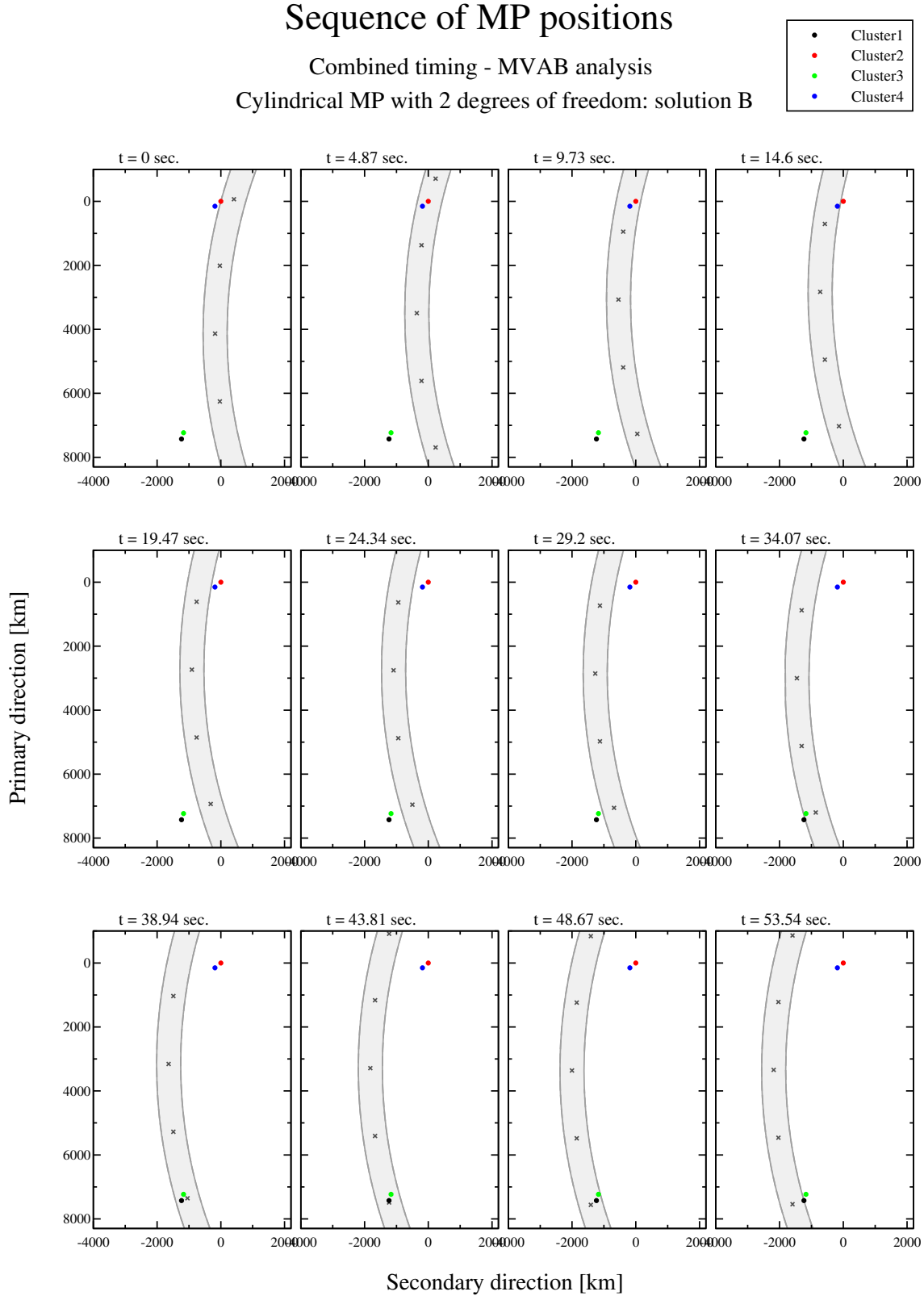

Figure 4.6: MP positions at successive, equally spaced moments for the solution presented on pages 180 and 181. The first and the last panel correspond to the moment when the leading satellite (Cluster 2) enters the boundary and, respectively, to the moment when the trailing satellite (Cluster 1) leaves it. In order to follow easier the MP displacement we showed some markers on its body.

discussed in Subsection 4.3.1 and in Appendix E, we obtained agreement within few degrees (i.e. less than 5 ° for the individual crossings and less then 3.5 ° in terms of global averages).

Comparison with the planar methods

In discussing how the planar MVAB method and the 2-D solutions compare from the magnetic variance point of view, we will often make use of the results and concepts from Appendix E. There, such type of study was given for the Cyl_2deg_OpTA_solA solution, the conclusion being that in this case the normals from the 2-D solution provide better results than the best possible planar normals (i.e what we called there the *planar, interval-specific MVAB* normals). Looking at Figure E.2 from the same appendix, one can make a similar statement for the solution Prbl_2deg_OpTA (presented in the panels on the right). Indeed, for the central intervals and the adjacent larger ones, the average normal magnetic field components computed by using the 2-D, instantaneous normals have roughly the same values or lower than the same quantities computed with *planar, interval-specific MVAB* normals. In the same time, the global normal variance curve for the 2-D solution (with magenta, in the right lower panel) is below the similar curve corresponding to the *planar, interval-specific MVAB* normals (with orange) for the same intervals.

It is interesting to compare these results with the ones from the left column of the same figure, corresponding to the Prbl_1deg_OpTA solution. In the last case, like in other solutions where the boundary moves only in one direction, essentially the geometry alone influences the evolution of various curves. When we allow for a second degree of freedom we see the combined effect of geometry and dynamics. One would like to stress again that the magenta curves in the last panels designate global magnetic variances corresponding to normals coupled in each moment by the chosen geometry and from one moment to another by the MP dynamics. In contrast, the orange curves refer the same quantity computed with individual normals, resulting from the *planar, interval-specific MVAB* analysis and therefore decoupled from one another or from one moment to another. In this case, the fact that the orange curve is below the magenta curve does not mean that the 2-D solution 'performs' poorer than in the planar assumption.

Table 4.4 presents the MP global parameters obtained in the 2-D and in the planar methods. It was introduced in Subsections 4.3.1, 4.3.2 and 4.3.3. By looking at the leftmost column we note that, with the exceptions of the two solutions already excluded, the global magnetic variance along the 2-D, instantaneous normals provides better results than the planar, nested MVAB analysis. The two variances are computed on different data intervals, but making a comparison between the two is reasonable because this quantity is an arithmetical mean. When the comparison is done with the variance along the *planar, interval-specific MVAB* normals, based on measurements from $[T_{ci} - \tau_i, T_{ci} + \tau_i]$, one still can say that the 2-D solutions offer similar or even lower values. This is better seen by looking on the blue numbers, obtained when the Cluster 3 data were not considered. The reason for this exclusion was discussed in Appendix E. We will resume this discussion below from a slightly different perspective.

In Figures A to H (see Appendix C) we showed for each satellite the geometrical normals corresponding to the MP leading edge (gray arrow) and trailing edge (black arrow) encounter, together with the normal obtained from the nested MVAB method (green arrow). In this way we can visualize the results obtained in the planar and 2-D, non-planar technique. As a general behaviour, we notice that in all solutions the geometrical normals referring to satellites 3 and 1 have a systematic preference for larger angles (negative values, in the approximate range $[-17, -11]$ for the quantity $\sphericalangle \left(\vec{n}_{GEO}^{\,ave}\,,\, \vec{n}_{MVAB}^{\,nested}\right)_{\perp \vec{l}}$ appearing in the Tables A to H). One could think that this is an offset induced by the chosen 2-D geometry but actually this is not

Table 4.4: Comparison between the single-spacecraft planar methods and the solutions provided by the 2-D method. *Upper part:* Results from the MVAB, MFR and HT techniques are shown. From left to right we have: the global magnetic variance along two set of planar normals, i.e. those provided by the MVAB nested technique and by applying the planar MVAB on the central intervals (see the description from Subsection 4.3.1), the global Faraday residue along the MFR normals (see Subsection 4.3.2) and the individual deHoffmann-Teller velocity along the normals provided by the MVAB nested technique (see Subsection 4.3.2). *Lower part:* For each solution obtained from the 2-D, non-planar method, we present the global magnetic variance along the instantaneous normals $\vec{n}_{GEO}$ (left column), the global Faraday residue using the instantaneous normals and normal velocities u_{GEO}(middle column) and the average normal velocity corresponding to each satellite (the group of 4 columns at the right). The meaning of the background colours attached to each solution is explained in the last paragraph of this section.

Planar methods

mag. variance $[nT]^2$				Faraday residue $[mV/m]^2$		$\vec{V}_{HT} \cdot \vec{n}_{MVAB}^{\,nested}$ [km/s]			
$\vec{n}_{MVAB}^{\,nested}$		$\vec{n}_{MVAB,\perp\vec{l}}^{\,central}$		$\vec{n}_{MFR}$ and u_{MFR}		$C2$	$C4$	$C3$	$C1$
3.587	3.448	2.724	2.697	2.649	2.847	86.64	−5.78	−14.44	22.56

2-D, non-planar method

	mag. variance $[nT]^2$		Faraday residue $[mV/m]^2$		normal velocity $[km/s]$			
	$\vec{n}_{GEO}$		$\vec{n}_{GEO}$ and u_{GEO}		$C2$	$C4$	$C3$	$C1$
Prbl_2deg_TA	7.505	5.811	2.077	3.737	86.79	75.73	20.86	18.96
Prbl_1deg_OpTA	3.276	2.758	1.706	2.672	64.02	56.84	44.63	42.68
Prbl_2deg_OpTA	2.764	2.518	1.762	2.751	65.44	58.00	38.51	37.00
Cyl_1deg_TA	4.191	3.527	1.687	2.617	66.82	59.26	48.32	46.35
Cyl_2deg_TA	2.497	2.261	1.783	2.867	57.45	50.95	41.54	39.85
Cyl_1deg_OpTA	3.220	2.852	1.684	2.581	63.97	56.73	42.26	44.38
Cyl_2deg_OpTA_solA	2.497	2.260	1.784	2.868	57.44	50.94	41.54	39.85
Cyl_2deg_OpTA_solB	3.014	2.712	1.714	2.708	58.60	51.97	42.37	40.65

the case. As shown in Appendix E, it has to do with the fact that the planar, nested MVAB normals and the geometrical normals correspond to different data sets, i.e. for the latter only the central transition points were used.

In Figure G presenting the Cyl_2deg_OpTA_solA solution, we plotted with orange arrows the normals $\vec{n}_{MVAB,\perp\vec{l}}^{\,central}$ obtained from the constrained (i.e. perpendicular to $\vec{l}$) planar MVAB normals corresponding to the central intervals. We have done this only for that particular solution in order to avoid unnecessary overload of the figures and because the angles between green and orange arrows will be the same in all implementations. As one can notice, for Cluster 3 and 1 the directions of $\vec{n}_{MVAB,\perp\vec{l}}^{\,central}$ lye inside the openings formed by the leading and trailing normals. That is exactly what one would expect from a planar analysis on an ideal 2-D, non-planar MP (see *Dunlop and Woodward* [1998] section 11.5.2). This fact is remarkable, also, when we take into account that practically the same solution was obtained

from the plain timing analysis (i.e. the solution Cyl_2deg_TA presented on pages 174 and 175) or, more general, that all plain timing-analysis suggest such an 'offset'. In the Tables A to G, as well as in Table 4.3, we presented also the quantity $\sphericalangle\,(\vec{n}_{GEO}^{\,ave}\,,\ \vec{n}_{MVAB,\,\perp\vec{l}}^{\,central}\,)$, which is the angle between the mean geometrical normal and the normal from constrained (i.e. perpendicular to $\vec{l}$) MVAB, performed on the central intervals. Now there is no sign of an 'offset' in orientation, except perhaps in the case of Cluster 2 (seen only in Tables A to H). The deeper analysis from Appendix E suggests that in this case the internal MP structure starts to play an important role in the MVAB technique when we limit the points to the central ones (the approximation of an ideal 2-D MP fails).

We consider the magnetic variance that takes into account also the small 3-D effects present in this event, responsible for the fact that the individual, nested MVAB normals are not exactly contained in one plane (see Figure 3.8). For this we constructed individual normals having at any moment the same inclination with respect to the plane perpendicular to the invariant direction as the nested planar MVAB normals and the projection on that plane along the instantaneous 2-D geometrical normals. In general, this brings a slight improvement in the global magnetic variance (see in the Tables A to H the line entitled 'variance using $\vec{n}_{GEO,\,3D}$') but this is mainly due to Cluster 2, for which this behaviour is systematic. This fact allows us to speculate that, perhaps, the internal structure having a noticeable effect on the MVAB results for Cluster 2, is of 3-D nature.

In the middle column from Table 4.4 we compare the global Faraday residue in the planar method (upper section) and the global Faraday residue implied by each 2-D, non-planar solution. In all cases the intervals of comparison are the central crossing ones, i.e $[T_{ci}-\tau_i, T_{ci}+\tau_i]$. In the planar case, we used the normals $\vec{n}_{MFR}$ and the normal velocities $\vec{v}_{MFR}$ obtained in Subsection 4.3.2 and shown in Table 4.1, whereas in the 2-D section we used the 2-D, instantaneous normals $\vec{n}_{GEO}$ and normal velocities $\vec{v}_{GEO}$.

In Tables A to H from Appendix C, under the section 'MFR results' we present a more detailed comparison. On the one hand we show the individual, i.e. referring to each satellite, not just the global Faraday residues. Then, because the $\vec{n}_{MFR}$ normals and the normal velocities $\vec{v}_{MFR}$ are not exactly in the plane perpendicular to the invariant direction, and therefore some 3-D effects might play a role in the comparison, we decided to present the Faraday residues computed in four ways. The two lines on the gray background show this quantity calculated as described above, i.e. when presenting the Table 4.4. For the other two lines we used the projection on the plane perpendicular to the invariant direction of $\vec{n}_{MFR}$ and $\vec{v}_{MFR}$ (first line) and the vectors $\vec{n}_{GEO,\,3D}$ and $\vec{v}_{GEO,\,3D}$ (second line). The last group of vectors are artificial, constructed as follows: for each satellite, $\vec{n}_{GEO,\,3D}$ and $\vec{v}_{GEO,\,3D}$ have the same orientation with respect to the plane perpendicular to the invariant direction as the corresponding $\vec{n}_{MFR}$, and the projection on that plane is given by $\vec{n}_{GEO}$ and $\vec{v}_{GEO}$ respectively.

Due to the limited accuracy of the electric field data for this event (see the discussion in Subsection 4.3.2) we have to take with cautions the results obtained in the MFR analysis. For example, if one looks at the leading pair of satellites (Cluster 2 and 4), they give somehow contradictory results, despite being relatively close to one another: the planar MFR analysis yields big differences in the Faraday residues (0.464 $[mV/m]^2$ as compared to 4.206 $[mV/m]^2$). At the same time the Faraday residue obtained from the instantaneous normals and normal velocities are in general smaller for Cluster 4 that in case of Cluster 2. This is the reason why, in all tables, we indicated in addition the global Faraday residues based only on the trailing pair of satellites (smaller numbers, appearing in red).

By looking at the global Faraday residues presented in Table 4.4, one notices that the black numbers, based on all four satellites, are systematically lower for the 2-D solutions than

in the planar case, the reduction being around 34% (we are not considering, as mentioned above, the Prbl_2deg_TA and Cyl_1deg_TA solutions). A more conservative comparison, by using the red numbers, indicates that the Faraday residues in the 2-D case are smaller or slightly bigger (below 1%) than in the planar case. On the other hand, the same observation made when investigating the magnetic variance also applies here, namely that the individual normals resulting from the planar MFR technique are decoupled from one another whereas $\vec{n}_{GEO}$ and $\vec{v}_{GEO}$ quantities are linked in each moment by the chosen geometry and from one moment to another by the dynamics of the MP. All these aspect taken into account allows us to conclude that the solutions obtained in the various implementations of the 2-D, non-planar method, perform better than the planar technique from the Faraday residue perspective.

From Table A to H, by looking at the global Faraday residues based on the projection of $\vec{n}_{MFR}$ and $\vec{v}_{MFR}$ on the plane perpendicular to the invariant direction, and on the same quantity based on $\vec{n}_{GEO,\,3D}$ and $\vec{v}_{GEO,\,3D}$, one notices that the 3-D effects do not play an important role in the analysis. The values we obtained with this modified vectors are approximately the same (in the range of a few percent) as the ones obtained from the corresponding starting vectors.

In the last four columns of Table 4.4 we compare, for each spacecraft, the deHoffmann - Teller velocity (V_{HT}) projected on the normal obtained in the planar, nested MVAB analysis, $\vec{n}_{MVAB}^{\,nested}$, with the average normal velocity prescribed by the 2-D, non-planar MP solutions. Also, under the 'deHoffmann-Teller results' section from Table A to H, we show, in addition the deHoffmann - Teller velocities (V_{HT}) projected on the average geometrical normals $\vec{n}_{GEO}^{\,ave}$ provided by the 2-D method.

One notices immediately that the planar method gives (in case of Cluster 4 and Cluster 3) negative values for the MP velocity, which is inconsistent with an inbound crossing. The situation improves a little when the $\vec{n}_{GEO}^{\,ave}$ normals are used, with the normal MP velocity becoming positive for Cluster 3 but still remaining negative or taking small positive values for Cluster 4. At the end of Subsection 4.3.3 we gave a possible explanation why the normal components of V_{HT} are so different from the average normal velocities obtained in the 2-D method, namely that the former assumes a constant velocity vector for the MP. On top of that, for Cluster 4 we used CODIF measurements for the plasma velocity because the HIA sensor,providing more accurate plasma moments in the MP region, is not available for that satellite.

Considering the fact that, for the event we analyse, the various implementations of the 2-D timing technique ascribe values for the MP normal velocity not very different from one another, one may think at this method as providing a diagnostic tool for the performance of the HT analysis. Therefore, when looking at Table 4.2 from Subsection 4.3.3, presenting the HT results, it is surprising to note the discrepancy between the high correlation coefficient in case of the Cluster 4 transition - i.e. 0.99, indicating a good identification of HT frame - and the very poor predictions of MP normal velocity based on V_{HT}. Also, in the same table one can see that for Cluster 2 the electric field residues in the HT frame are relatively high ($D/D_0 = 0.109$) but still, the predictions for the MP normal velocity are rather better than in case of Cluster 4 and Cluster 3, where reliable HT frames were identified ($D/D_0 = 0.019$ and $D/D_0 = 0.020$, respectively).

The nature of the 2-D MP feature

In Figure 3.8 from section Section 3.4 we plotted the tangential components of the magnetic field and velocity flow in the magnetosphere (in red) and magnetosheath (in black), as measured by Cluster 1. The angle between the two flow directions is around 172 ° and the magnetic shear around 150 °. The large flow shear across the MP (around 350 km/sec.) makes us consider

the Kelvin - Helmholtz mechanism as possible explanation for the 2-D feature encountered by Cluster in this event. The vector $\vec{k}$ (shown in green), perpendicular to the invariant direction, would then correspond to the wave vector. It is noticeable that the wave vector has an orientation in between the direction perpendicular on B_{sheath} and the direction of V_{sheath}. With these two direction it makes an angle of around 19 ° and 22 °, respectively. This is consistent with the interpretation that we have a wave driven by the magnetosheath flow, propagating on the MP surface almost perpendicular to the magnetic field, which, from energy considerations, is the most favoured direction.

If this is the case then one could easily estimate the wavelength and the periodicity of such a structure. The most appropriate way to model the physical situation would be that of a the parabolic MP having 2 degrees of freedom (i.e. Prbl_2deg_OpTA) which gave us (see Table C) a radius of curvature at the parabola's nose of approx. 1.24 R_E and a MP tangential velocity of approx. 78 km/sec. This leads to a wavelength of ~ 7.8 R_E and a period of ~ 10.5 minutes. Of course, as we discussed at the beginning of this section, we found that the corresponding solution is not valid on both sides of the parabola's peak but we can still estimate quantities involved.

Using the parameters from the magnetosheath and magnetosphere, we checked on the Kelvin - Helmholtz instability criterion, deduced in the case of a planar interface between two incompressible fluids having no viscosity:

$$\frac{\rho_1\rho_2}{\rho_1+\rho_2}\left[\vec{k}\cdot\left(\vec{V}_{sheath}-\vec{V}_{sphere}\right)\right]^2 > \frac{1}{\mu_0}\left[(\vec{k}\cdot\vec{B}_{sheath})^2+(\vec{k}\cdot\vec{B}_{sphere})\right]^2$$

(see *Chandrasekhar* [1961]) and we found that for all directions $\vec{k}$ in the plane perpendicular to the invariant direction, this is not satisfied. The stabilizing factor due to the magnetic tension (right part) is always greater by at least one order of magnitude than the left term which accounts for the driving, instability force. Therefore, although one could interpret the 2-D feature as a large amplitude wave produced by the velocity shear across the MP, the data suggest that this wave will not grow into the nonlinear regime.

What is the best 2-D solution?

In this paragraph we draw some final conclusions about the various 2-D MP solutions, corresponding to the event from 24 June 2003. As shown, two solutions (namely Prbl_1deg_TA and Cyl_1deg_TA) were dropped because they do not represent realistically the evolution of the MP in this test case. In Table 4.3 and Table 4.4 they appear on a gray background. The remaining six solutions may be classified in three groups, as follow:

- the global parameters corresponding to the solutions Prbl_2deg_OpTA, Cyl_2deg_TA and Cyl_2deg_OpTA_solA (represented in Figures C, E and G, respectively), suggest that they belong to the same family, describing a MP having two degrees of freedom in the parabolic or cylindrical geometry. In terms of radius of curvature, velocity and thickness the variations are only around 2% across different implementations. These are also the solutions for which the global normal magnetic variance was minimum and for which we need to limit their range of validity in order to avoid an artificial return in the MP of the first pairs of satellites. The last two solutions are practically identical, meaning that the plain timing analysis performed very well in this implementation (the optimization procedure brought practically no modifications). In Table 4.3 and Table 4.4 they appear on a violet background.

- the solutions Prbl_1deg_OpTA and Cyl_1deg_OpTA, presented in the Figures B and F of Appendix C are similar but obtained with the assumption of a parabolic or cylindrical MP, respectively. They imply a unidirectional displacement for the MP and the resulting global crossing parameters are very similar (i.e. 1.5% relative variation for the velocity and thickness and 35% for the radius of curvature). If we consider only Cluster 4, Cluster 3 and Cluster 1 and look at the differences between the average geometrical normals and the planar MVAB normals corresponding to central intervals (last column in Table 4.3) and at the global normal magnetic variance (first column in Table 4.4), we may conclude that the parabolic model provides slightly better results. In Table 4.3 and Table 4.4 they appear on a green background.
- the solution Cyl_2deg_OpTA_solB presented in Figure H has no correspondence in the parabolic model. It implies a back and forth tangential MP movement whereas the movement along the 'normal' (i.e radial) direction is with constant velocity. In terms of global magnetic variance, it implies a lower value than the second group of solutions. In Table 4.3 and Table 4.4 it appears on a blue background.

4.5 Relation between the current work and previous approaches

In this section we would like to show the relation of the present work with respect to the previous efforts along the same line.

The first timing technique (called time of arrival method) using 4 satellites was proposed by *Russell et al.* [1983] in order to infer the orientation of an interplanetary shock, assuming a propagation with constant velocity. The method, which according to our terminology is a plain timing technique, appears in *Haaland et al.* [2004b] under the name of Constant Velocity Approach. In the same paper the Constant Thickness Approach was introduced and applied to a magnetopause crossing; both of them are planar methods and are described in Section B.1.

The present timing-techniques are natural generalizations of the planar timing method which assumes a constant thickness for the discontinuity. For describing the shape of a 2-D MP we proposed two simple, constant thickness geometries (i.e parabolic and cylindrical) and a polynomial time dependence in the velocity. We allowed for one or two degrees of freedom in the displacement of the discontinuity. This assumptions led us to a set of 8 conditions for motion, corresponding to the encounter of spacecraft positions by the MP's edges, and, by solving them, we found the individual crossing parameters at each satellite level.

There is another line of approach in the effort to characterize the macroscopic surface properties (orientation and planarity or, in case of non-planarity, the curvature) of a discontinuity and its motion when 4 points of measurements are available, like in case of Cluster (*Mottez and Chanteur* [1994]; *Dunlop and Woodward* [1998, 1999]). This relies on combining the information obtained by each spacecraft separately (via MVA of the magnetic field) with the information obtained from the differences across satellites, i.e. the time differences in detecting the discontinuity and the relative positions of the satellites at these moments. In the above papers, the authors assumed that, for a non-planar structure, the boundary in question is thin (when compared with radius of curvature) so that the individual normals, obtained with MVAB, are not too much affected by the local curvature of the field or by the discontinuity motion during data sampling.

Mottez and Chanteur [1994] described a method to analyze the local geometry of a 3-D surface crossed by a group of 4 satellites, when its geometry is regular at a scale of the inter-

spacecraft separation distance (and therefore characterized at each point by the same two principal radii of curvature) and the velocity of the structure convecting past the spacecraft is constant. *Dunlop and Woodward* [1998] showed that the latter condition could be relaxed by allowing an acceleration.

In the work of *Dunlop and Woodward* [1998, 1999] (termed discontinuity analysis) the authors presented in a detailed manner the problem of combining the results from the planar, single - spacecraft method of MVAB across a number of satellites (up to 4) in order to infer the motion and shape of a non-planar discontinuity. In a 2-D situation, they consider the cylindrical shape and presented the procedure of finding the radius of curvature and the parameters of motion (in terms of velocity and acceleration vectors in the plane perpendicular to the invariant direction). In that respect, the differences in the central crossing times, relative positions of the satellites and the differences between individual normals detected by each satellites were used.

The authors used simulated data to show how the calculation of the normal, using planar MVAB method, is influenced, in case of a curved boundary, by various effects like data interval length and spacecraft trajectory. The study indicated that for trajectories implying big variations, during the traversal, in the local radial direction and for large data intervals participating to MVAB the influences are greater. If one wants to limit these effects, the analyzed discontinuity should be characterized by a large radius of curvature (relative to the thickness) and only points from a thin interval around its centre should be used for the MVAB. The latter condition, as we discussed in our case, could be problematic in a real event as the measurements in that region may be affected by the internal structure of the discontinuity, by noise, waves etc.

At this point we note that our method is not affected by this type of problems. For a 2-D MP, the MVAB method applied to each satellite will not fail to indicate the plane containing all individual normals and we used only this information later on. Therefore, we are not so strict in imposing the small curvature condition for the boundary. For other considerations, discussed in Subsection 4.3.1 we do use points from central intervals only, embracing $\sim 76\%$ of the total magnetic change.

Dunlop and Woodward [1998] pointed out the need to find a method that determines self-consistently the parameters characterizing the curvature of a discontinuity and its non-constant motion. In this respect they formulated the general problem and proposed a criterion for optimization that involves magnetic variation along the instantaneous, local normal (their equation from page 299). This is actually what we have implemented in our combined timing - MVAB method with the help of equation (B.87), used in the optimization procedure (see Section B.5). We recall here in brief how we arrived at that point.

One of the necessary parameters in describing the MP movement is the direction of displacement. Because in a 2-D case this is completely specified by an angle in the plane perpendicular to the invariant direction, we proposed to solve the 8 motional conditions when imposing from the beginning different orientations for the MP movement and to select that solution which satisfies the criterion of minimum magnetic variance along the instantaneous MP normal. As pointed out in Section B.5, we can base the optimization not only on the variance of the normal magnetic component but on any other quantity that obeys a conservation law across the discontinuity. We can also combine different quantities and use them simultaneously by summing up their variance (with appropriated weighting factors) following the same procedure developed by *Sonnerup et al.* [2006] in case of the planar assumption.

The important assumption we adopted for the MP, namely that it has a constant thickness, resulted in a significant simplification of the task to infer its curvature and motion. In the paper

by *Haaland et al.* [2004b], where the planar constant thickness approach was introduced, the authors brought arguments in favour of this assumption as opposed to the constant velocity assumption (see the discussion in Section 3.1).

Clearly, not all MP events will comply with this approximation, especially when the crossing points are well separated along the surface. Nevertheless, we think that this study can be applied on an event basis and could be used as a starting point for further development. One potential development would be to relax the constant thickness condition. For example, if the Cluster formation is such that the satellites are making the transitions in pairs (like in our example, where the distance between Cluster 2 and 4 is around 250 km), we can consider to introduce a new parameter, allowing for a linear increase in the MP thickness in the plane perpendicular to the invariant direction. Then one can perform the timing analysis for different values of this parameter and select the one for which the global magnetic variance takes the minimum value. Now the optimization procedure is performed with respect to the new parameter and not with respect to the angle specifying the (primary) direction of MP movement.

CHAPTER 5

Observation of magnetic reconnection at the magnetopause

In order to establish from the satellite measurements whether the MP behaves like a rotational discontinuity we perform the so called Walén test. The test compares the plasma velocity in the deHoffmann-Teller (HT) frame (a system of reference where the plasma flow becomes field aligned) with the local Alfvén velocity. We expect a good agreement between the two quantities in case of a RD.

The Walén test proved very successful in establishing whether a discontinuity has a rotational character or not but a long standing issue remains that, for a RD, the factor of proportionality between the plasma velocity and the Alfvén velocity is less than the ideal value of one required by the theory. This aspect could have an explanation in the fact that the Walén analysis relies on some simplifying assumptions when testing the RD model (to be discussed in Section 5.2).

It is the purpose of this chapter to experimentally investigate two such assumptions. One of these, to be address in Section 5.4, refers to the electrons' role in the analysis, which is usually neglected. A second assumption is to consider all the ions as being protons, therefore neglecting the influence of minor ion species, an approximation justified by the protons relative abundance in the MP environment. This issue will be analyzed on Section 5.6.

A puzzling aspect of RD identification at the MP concerns the experimental proof of the relation $\rho(1-\alpha) = const.$, with ρ being the plasma density and α the plasma pressure anisotropy factor (see the next section). This relation should hold for such a discontinuity and could be incorporated in the Walén test. Typically, from the latter variant of the test one obtains better results than in the situation when $\rho(1-\alpha) = const.$ is not considered. However, in general the equation is not supported by experimental evidence, as will be shown (Section 5.4).

In the last section, we will present some experimental observation referring to the Oxygen ions, existing in a relatively high abundance in one of the event analyzed in this chapter.

5.1 Jump relations for a rotational discontinuity

In this section we will present the main features of the RD model, deducing the relations between the plasma properties on either side of it. The intention is to illustrate in this way

the basis of an RD identification in experimental data. The analysis is made in the following circumstances (*Hudson* [1970]):

- We will not consider the detailed structure of the discontinuity, but the implications of various conservation laws across it (the Rankine-Hugoniot relations, linking plasma parameters of the adjacent asymptotic regimes).
- We treat the plasma as a singe fluid, i.e. we make no distinction between different ion species and electrons, working only with the centre-of-mass quantities.
- We assume that the discontinuity surface is planar, with all the parameters varying only along the normal direction. In addition, we assume time-stationarity.
- In the asymptotic regions, we assume that the only electric field arises from the plasma moving across the magnetic field.
- The plasma is considered anisotropic, therefore being characterized by a parallel and a perpendicular (to the magnetic field) temperatures.

An one-dimensional RD is defined by the conditions

$$B_n \neq 0, \qquad \rho v_n \neq 0 \qquad and \qquad \vec{v}_1 = \vec{V}_{A1}, \qquad \vec{v}_2 = \vec{V}_{A2} \tag{5.1}$$

Here the subscripts 1 and 2 refer to the conditions in the asymptotic regions on the sides of the discontinuity. $\vec{v}_{1,2}$ designate the plasma bulk velocities in the deHoffmann-Teller frame (to be introduced later in the text) and $\vec{V}_{A1,2}$ refer to the Alfvén velocities, considered as vectors of magnitude $V_{A1,2}$ oriented along the local magnetic field direction. B_n and ρV_n are the magnetic field component and the mass flux along the normal direction. As opposed to a *tangential discontinuity* (TD), which is a boundary that does not connect the adjacent plasma regimes (no magnetic flux or mass flux along the normal direction) and for which the velocity, density or the magnetic field can change in any way across it, for a RD we do have such a coupling in both physical quantities.

We will now show how the relations (5.1) appear (*Hudson* [1970]; *Sonnerup et al.* [1981]; *Paschmann et al.* [1986]). From the Faraday equation $\nabla \times \vec{E} = -\partial \vec{B}/\partial t$ applied to a 1-D, time-stationary discontinuity we obtain that the tangential component of the electric field is constant

$$\vec{E}_t = -(\vec{v} \times \vec{B})_t = const. \tag{5.2}$$

In the same conditions, the equation $\nabla \cdot \vec{B} = 0$ gives us

$$B_n = const. \tag{5.3}$$

Writing the MHD momentum equation for an anisotropic plasma in the form of a conservation law (see for example *Landau and Lifshitz* [1960] §**51** and *Clemmow and Dougherty* [1969] §**11.3.2**)

$$\frac{\partial(\rho v_i)}{\partial t} = -\frac{\partial \Pi_{ik}}{\partial x_k} \tag{5.4}$$

with

$$\Pi_{ik} = \rho v_i v_k + \left(p_\perp + \frac{B^2}{2\mu_0}\right)\delta_{ik} - B_i B_k \left(\frac{1}{\mu_0} - \frac{p_\parallel - p_\perp}{B^2}\right) \tag{5.5}$$

(i, j, k indicating the components in a cartesian reference system) and applying this to our model (variation only along normal direction and $\partial/\partial t \equiv 0$) we obtain the conservation of the tangential momentum

$$G\vec{v}_t - \frac{B_n}{\mu_0}\vec{B}_t(1-\alpha) = const. \tag{5.6}$$

and the conservation of the normal momentum

$$Gv_n + \left(p_\perp + \frac{B^2}{2\mu_0}\right) - \frac{B_n^2}{\mu_0}(1-\alpha) = const. \tag{5.7}$$

where $\alpha \equiv (p_\parallel - p_\perp)\mu_0/B^2$ is the plasma pressure anisotropy factor, with $p_\parallel$ and $p_\perp$ being the plasma pressure parallel and perpendicular to $\vec{B}$.

The conservation of the normal mass flux

$$G = \rho v_n = const. \tag{5.8}$$

together with the equation (5.2) leads us to

$$B_n(\vec{v}_{2t} - \vec{v}_{1t}) = G(\vec{B}_{2t}/\rho_2 - \vec{B}_{1t}/\rho_1) \tag{5.9}$$

where subscripts 1 and 2 designate plasma parameters in the two asymptotic states. From here and when $B_n \neq 0$ (as we assumed), we find an expression for $\vec{v}_{2t} - \vec{v}_{1t}$. This we introduce in the relation

$$G(\vec{v}_{2t} - \vec{v}_{1t}) = \frac{B_n}{\mu_0}[\vec{B}_{2t}(1-\alpha_2) - \vec{B}_{1t}(1-\alpha_1)] \tag{5.10}$$

which is another way to write the equation (5.6). We arrive at the result

$$v_{n1,2} = \pm\frac{(1-\alpha_{1,2})^{1/2}B_n}{(\mu_0\rho_{1,2})^{1/2}} \tag{5.11}$$

saying that the normal bulk velocity on either side of the discontinuity is equal to the local Alfvén velocity corrected for the pressure anisotropy, based on the normal magnetic field component. In addition, by changing the reference frame to a suitable one, moving along the discontinuity (the so called deHoffmann-Teller frame), we will obtain the same type of relation between the tangential components of the plasma bulk velocity and magnetic field on both sides of the layer (i.e. the relation (5.1)). Therefore we can write

$$\vec{v}_{1,2} = \pm\sqrt{\frac{1-\alpha_{1,2}}{\mu_0\rho_{1,2}}}\ \vec{B}_{1,2} \tag{5.12}$$

The above relation, identical with (5.1), represents the so called Walén relation. The variant with + corresponds to the situation when v_n and B_n have the same sign whereas the one with − applies in the opposite case. In the magnetopause context, the density in plasmasheath being higher then in the magnetosphere, v_n has allways a negative value (opposing the exterior normal vector). From here and from the topology of the magnetic field lines inside the magnetospheric cavity, we can draw conclusions about where the reconnection point is situated relative to the point of observation. For example, in case of a day-side reconnection, the + situation appears when the satellite collected data north of the reconnection location (when B_n is also negative).

From equation (5.11) and taking into account (5.3) and (5.8) we arrive directly at

$$\rho_1(1-\alpha_1) = \rho_2(1-\alpha_2) \tag{5.13}$$

that should be verified for an RD. Also, the conservation of normal momentum leads to

$$p_\perp + \frac{B^2}{2\mu_0} = const. \tag{5.14}$$

expressing the normal pressure balance (we recall here that at the MP, the magnetic field vector is almost tangent to the surface, B_n being relatively small, around $1/10^{th}$ of its magnitude).

The deHoffmann-Teller (HT) reference system, particularly useful in theoretical analysis and data interpretation pertaining to a discontinuity like the magnetopause, was introduced in the context of MHD theory of shock waves [*deHoffmann and Teller*, 1950]. Because when speaking about the velocity of a planar discontinuity, only its normal component has a physical significance, the authors made the observation that in a properly chosen reference system, moving along the discontinuity with constant speed, the jump conditions across the shocks simplify. In such a frame the magnetic field and plasma bulk velocity vectors have the same orientation on either sides of it or, equivalently, since then $\vec{E} = -\vec{V} \times \vec{B} = 0$ we can say that the convection electric field in the adjacent asymptotic regimes vanishes in that particular reference frame.

Such a definition allows the existence of a HT frame not only in the RD case: *Paschmann* [1985] has shown that it exists, in general, for a TD as well. Actually, with the exception of few particular cases (like the case for a TD when the magnetic fields on the sides are parallel and the velocities perpendicular to these fields are different) all one-dimensional discontinuities posses such a frame (see *Khrabrov and Sonnerup* [1998]). We will see in the next section how this concept is changed when it comes to experimental identification of RD in satellite data.

5.2 Practical issues in the identification of a rotational discontinuity

For determining whether or not the MP behaves like a RD, usually we do not check the Walén relation using measurements taken only in the asymptotic regions. The reason for that is our inability to establish from the data, with a precision sufficiently high to rule-out ambiguity, the two sets of parameters defining such states. In the real events there are allways present fluctuations in the plasma and field parameters.

Connected to this issue, it is worth mentioning that the MHD treatment of the region situated away from the reconnection site (i.e away from the diffusion region, where the data samples are collected) predicts a complex structure of the reconnection layer that includes not only standing Alfvén (intermediate) waves. For example, according to *Biernat et al.* [1989], who used an MHD isotropic plasma model in order to match the asymmetric parameter values in the magnetosheath and magnetosphere, we need a standing nested pair of Alfvén waves (providing the needed magnetic field rotation) and slow-mode waves (responsible for matching the field intensities) surrounding a contact discontinuity (taking care of asymmetries in plasma parameters). Probably this description of plasma behaviour is too simple but nevertheles we expect a slow-mode expansion fan region, earthward of the rotational discontinuity; the RD remain the dominant magnetic feature of the MP at the high density side which is usually the magnetosheath side (see *Sonnerup et al.* [1995])

In the papers from *Paschmann et al.* [1979] and *Sonnerup et al.* [1981], providing the first in-situ evidence for reconnection at the MP, the Walén relation (5.12) was tested between a reference point in the magnetosheath and points within the MP structure, as well as on its magnetospheric side (see also *Paschmann et al.* [1986]). This form of checking the tangential-stress balance equation - which established itself as the standard procedure in RD identification - relies on the assumption that the discontinuity is sufficiently thick when compared with the local ion inertial length and ion gyro-radius. In this respect, the authors provided experimental proofs for their analyzed events. Note that by proceeding in this way one actually overchecked the tangential stress balance equation, ruling-out a fortuitous success of the test.

In order to see the underlying arguments for the assumption made in the preceding paragraph we consider the generalized Ohm's law for a two-component, collisionless plasma (see *Rossi and Olbert* [1970], Chap. 12)

$$\vec{E} + \vec{v} \times \vec{B} = \frac{m_e}{ne^2} \left[\frac{\partial \vec{J}}{\partial t} + \nabla \cdot (\vec{J}\vec{V} + \vec{V}\vec{J}) \right] - \frac{1}{ne} \nabla \cdot \mathbf{P}^e + \frac{1}{ne} \vec{J} \times \vec{B} \tag{5.15}$$

where e stands for the elementary charge, m_e for the electron mass, $\vec{J}$ for the electric current density and $\mathbf{P}^e$ for the electron pressure tensor. In obtaining the above relation, the only approximations made were that the electron's mass is much less than the ion's mass ($m_i \gg m_e$) and that the thermal energies of the electrons and ions do not differ by a large factor.

Vasyliunas [1975] compared the order of magnitude of the various terms in (5.15) for typical values of the physical quantities appearing there. He concluded that the first term on the right, taking into account the inertial effects, has a characteristic scale length of electron inertial length (or skin depth) $\lambda_e = \sqrt{m_e/\mu_0 ne^2}$ whereas the scale length for the second and last term in RHS, expressing the effects of pressure gradient and of the Hall effect is the ion inertial length $\lambda_i = \sqrt{m_i/\mu_0 ne^2}$. For the first event to be presented in this chapter, the ion gyro-radius $\rho_i \simeq 49$ km and the ion inertial length $\lambda_i \simeq 82$ km, values much greater then the typical values of $\simeq 1$ km for λ_e at the MP. Therefore one can safely neglect the first term on the RHS of (5.15). When the discontinuity characteristic length (i.e. its thickness) is much greater than ρ_i and λ_i, the contribution from the other two terms can be neglected as well, allowing to test the Walén relation by using points from inside the RD.

As for the deHoffmann-Teller analysis, the procedure is performed in a consistent manner, namely by using also the measurements inside the structure when searching for the existence of HT frame[1]. In this way the chance of wrongly attributing a rotational character to a tangential discontinuity decreases even more. Indeed, if only data points from the asymptotic states would be allowed to participate in the test, then, in general, also for a tangential discontinuity the result will be successful. For a TD *Paschmann* [1985] has shown that, with the exception of the situation when the magnetic field in the asymptotic regimes are aligned and the velocities transverse to these fields are different, it is possible to find a reference frame in which the electric field outside the layer vanishes. Nevertheless, in this case an intrinsic electric field component along the normal will, in general, remain in the interior of the layer because the required rotation of the magnetic field and velocity vectors, needed to accommodate the plasma regimes on the sides (both having only a tangential component in this situation) are independent.

On the contrary, in the case of a RD, we expect that by transforming in the HT frame also the electric field in the interior of the structure will be resolved. According to *Paschmann*

[1]The exact treatment of the data is presented in Appendix F. There, a procedure will be indicated (*Khrabrov and Sonnerup* [1998]) that seeks a reference frame in which the electric field becomes as small as possible - in the mean square sense - for the given set of measurements

[1985], the needed transformation consists in removing firstly the electric field associated with motion of the layer normal to itself, followed by the velocity transformation $\vec{V_0} = \vec{E_t} \times \vec{B_n}/B_n^2$ where $\vec{E_t}$ and $\vec{B_n}$ are the tangential electric field component and the normal magnetic field component. Note that, due to the conservation relations referring to $\vec{E_t}$ and $\vec{B_n}$, $\vec{V_0}$ has the same value everywhere for a one-dimensional, time-stationary discontinuity. By applying this transformations the tangential component of the electric field inside and outside the discontinuity vanishes and in MHD approximation a RD has no internal electric field along the normal direction (because in this model there is no electric field component along $\vec{B}$). As pointed by *Khrabrov and Sonnerup* [1998], such an intrinsic normal electric field comes exclusively from the $\nabla \cdot \mathbf{P}^{\,e}$ term of equation (5.15) which could be neglected when the discontinuity is sufficiently thick.

Nevertheless, it should be stressed that a good identification of HT frame is only a sufficient condition for the existence of a RD, even when points from inside the discontinuity were used in the analysis. There are cases of TDs that pass this test but for which the Walén relation is not satisfied.

Another important experimental aspect in RD identification refers to the plasma moments used in the HT and Walén tests. In Section 5.1 all the plasma quantities (density, velocity, temperature and pressure) refer to the centre of mass (COM) moments. The contributions from each ion species and from electrons are in this way properly weighted. But in practice, it is difficult to obtain reliable moments for electrons and for minor ion species (in case these are present) and therefore, in the usual case, we work with the proton moments.

In principle, trustworthy electron moments would have two important advantages as indicated in *Scudder et al.* [1999]. In that paper, the authors formulated the Walén relation based only on electrons (and magnetic field) quantities and provided arguments that testing for a RD with the new relation is more appropriate because these particles better follow the magnetic field lines as compared with the ions. In this way one can apply the test using points from inside the structure, even when the discontinuity's thickness is not large compared with λ_i and ρ_i, and therefore the last two terms in equation (5.15) become important. The second benefit of an electron based Walén relation relies on the fact that they are the only negative particles, and therefore the problem of separating between different species disappears. In case of positive ions when, in principle, we have to asses the contributions from each ion species in the tangential-stress balance equation, such a separation is always a problem as will be discussed later on.

However, obtaining reliable electron moments from measurements taken on-board satellites is a challenge because there is always a population of photoelectrons present, created by the solar radiation incident on the spacecraft surface, and whose influence on the detectors corrupts the signal from 'true', ambient electrons. In addition, in the MP region the electrons are highly subsonic, i.e. their thermal velocity greatly exceeds the bulk velocity, making the experimental determination of the latter difficult (see *Paschmann et al.* [1998]). In the paper from *Scudder et al.* [1999], presenting results of RD identification at the magnetopause by using electron data from the Polar, Hydra instrument, the authors reported a procedure to clean the influence of photoelectrons on their detector. No such study was reported, to our knowledge, with the Cluster, PEACE electron detector even though the mission was equipped with an active spacecraft potential control device (ASPOC) which limits the role of photoelectons in the measurements.

In the MP region we expect, besides protons, the presence of some minor ion species, particularly He^{2+} particles of magnetosheath origin and He^{+} and O^{+} ions of ionospheric origin, whose contributions in the Walén relation have to be taken into account properly. Ideally, one

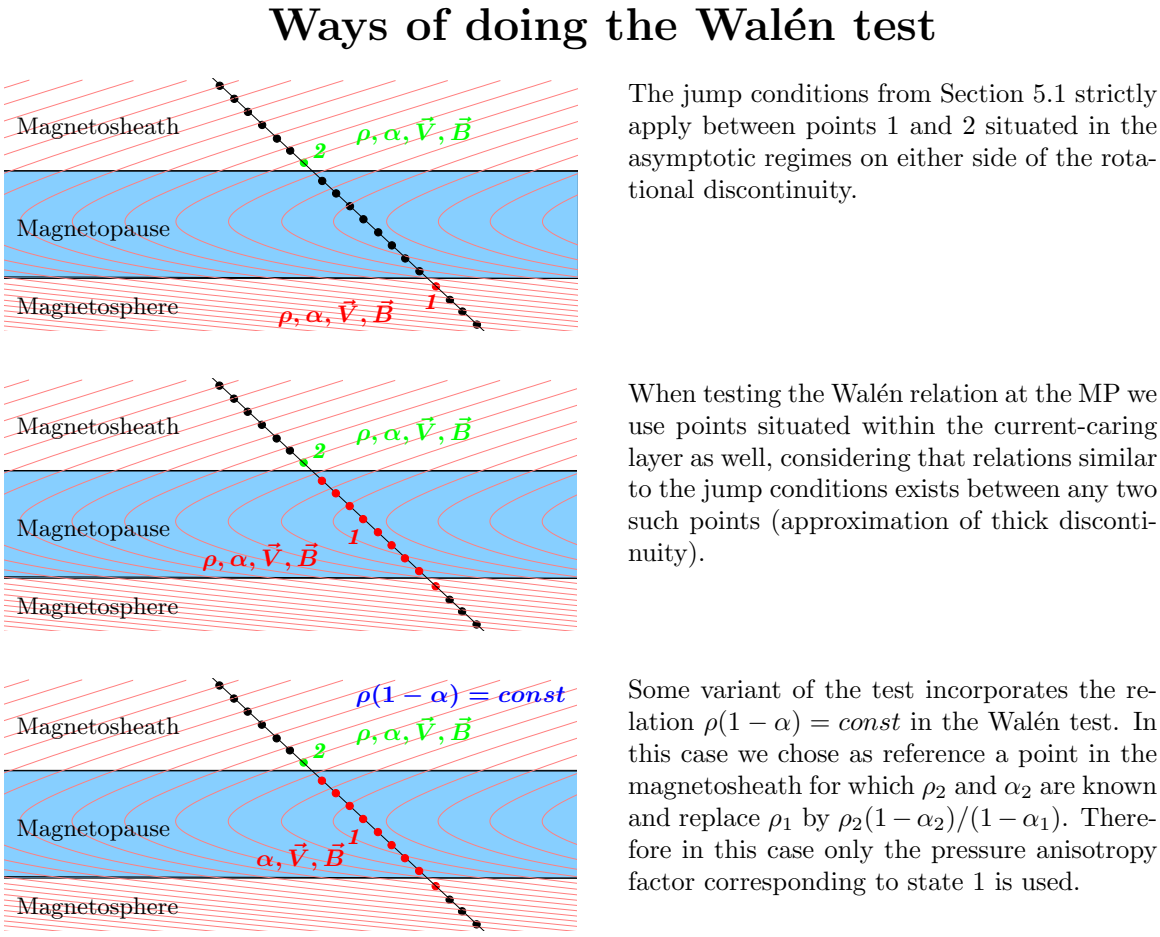

The jump conditions from Section 5.1 strictly apply between points 1 and 2 situated in the asymptotic regimes on either side of the rotational discontinuity.

When testing the Walén relation at the MP we use points situated within the current-caring layer as well, considering that relations similar to the jump conditions exists between any two such points (approximation of thick discontinuity).

Some variant of the test incorporates the relation $\rho(1-\alpha) = const$ in the Walén test. In this case we chose as reference a point in the magnetosheath for which ρ_2 and α_2 are known and replace ρ_1 by $\rho_2(1-\alpha_2)/(1-\alpha_1)$. Therefore in this case only the pressure anisotropy factor corresponding to state 1 is used.

Figure 5.1: Variants of the Walén test. In the above pictures we sketch a satellite trajectory as it crosses a planar MP behaving like a rotational discontinuity. The dots along the trajectory indicate the points where plasma as well as magnetic field measurements are taken. In the right column the three possible ways of performing a Walén test is described.

would need precise measurements, and with enough time resolution, of their moments in terms of density, velocity and temperatures, but that proves to be a difficult goal to achieve. For example, in case of Cluster mission, the CODIF sensor, (the ion mass spectrometer, part of the CIS experiment) is often saturated in the magnetosheath region, an effect difficult to be assessed with enough accuracy. Another issue that should be considered with CODIF is the spillover effect, by which the sensor registers false counts in the He^+, He^{2+} and O^+ channels produced in the presence of large proton fluxes. Therefore one prefers to work with the measurements provided by HIA sensor, the part of the CIS experiment than does not separate between different ion species and, consequently, where in the computation of the moments all particles are considered as protons. For this detector, the saturation is not an issue and the plasma moments are in general computed based on measurements acquired with higher spatial, energy and temporal resolution than for CODIF.

In the papers of *Paschmann et al.* [1979] and *Sonnerup et al.* [1981], reporting about the first direct evidence of magnetic reconnection at the MP, a certain percentage of He^{2+} particles was assumed (typical values or values based on fortuitous simultaneous measurements in the solar wind, provided by another satellite) in order to take their influence into account. In *Paschmann*

et al. [1986] another manner for assessing the contribution of He^{2+} was proposed, relying on the equation (5.13), namely that the quantity $\rho(1-\alpha)$ is constant for a RD. The authors used measurements from an energy/charge plasma instrument unable to resolve different ion species and showed that, for some typical plasma parameters at the MP and when a minor population of heavier ions is present, the errors in assessing the plasma pressure anisotropy factor α from this type of instrument are smaller than the errors in density. Consequently, when performing the Walén test, they proceed in the following manner: first, a reference point in the magnetosheath is chosen for which the quantities, say α_2 and ρ_2 are known (or, alternatively, the used average values on certain number of data points from that region). Then, for the points inside the discontinuity, the values of α provided by the instrument are considered whereas for the density the values $\rho_2(1-\alpha_2)/(1-\alpha)$ are used.

The three ways of performing the Walén test at the MP, described in this section, are shown in Figure 5.1

It is worth mentioning that the background of the practical aspects presented in this section is the goal to experimentally verify the Walén relation (5.12). While the required vectorial parallelism of (5.12) is confirmed with high accuracy, the recovery of the proportionality constant was less satisfactory, the observed values being typically around $60\% \div 80\%$ of the one theoretically predicted (see for example *Sonnerup et al.* [1981], *Phan and Paschmann* [1996] and *Phan et al.* [1996]). In the line to explain this discrepancy, one would also like to mention the work from *Sonnerup et al.* [1990], where the interpretation was proposed that a possible acceleration of the discontinuity is the responsible cause. Therefore an improvement of the HT technique was introduced which allows for an accelerating movement of this reference frame (see Appendix F).

Related to the success of a RD identification in the experimental data, an important aspect to be considered is that the Walén test is based on the one-dimensional model (i.e. the physical quantities vary only along the normal direction). In the real situation, we compare the change in plasma velocity with the magnetic field change, all measurements being taken along the satellite trajectory. But the plasma sampled on the earthward side of the discontinuity crossed the MP far away from the satellite location, closer to the diffusion region, and did not experienced the MP magnetic structure at the point of observation (see *Sonnerup et al.* [1981]).

5.3 Overview on the 14 March 2002 event

General conditions.
In Figure 5.2 the Cluster satellites orbit and configuration corresponding to the first event to be discussed in this chapter are shown. The transition occurred around 01:06:00 on 14^{th} of March 2002 at the dayside MP, near $[7.9, -3.0, 8.0]\, R_E$ in GSM coordinate system. It is an inbound crossing from the magnetosheath plasma regime to the magnetosphere region (better seen on Figure 5.3, to be presented later in the text). In the upper part of the figure showing the orbit (taken from Cluster Science Data System home page), a model MP and bow-shock are drawn and the distance between the satellites is scaled by a factor of 175. The four spacecraft are in a tetrahedral configuration, the separation distance being around 100 km.

On the bottom part of that figure two plane projections of the Cluster configuration at the time of traversal are shown, both of them with C3 - the first satellite entering the MP - at the origin of the coordinate system. In the plot showing the projection on the MP plane - the plane perpendicular to the direction obtained by averaging the individual normals from constrained MVAB method - the $\vec{x}$ axis corresponds to the direction along which the magnetic

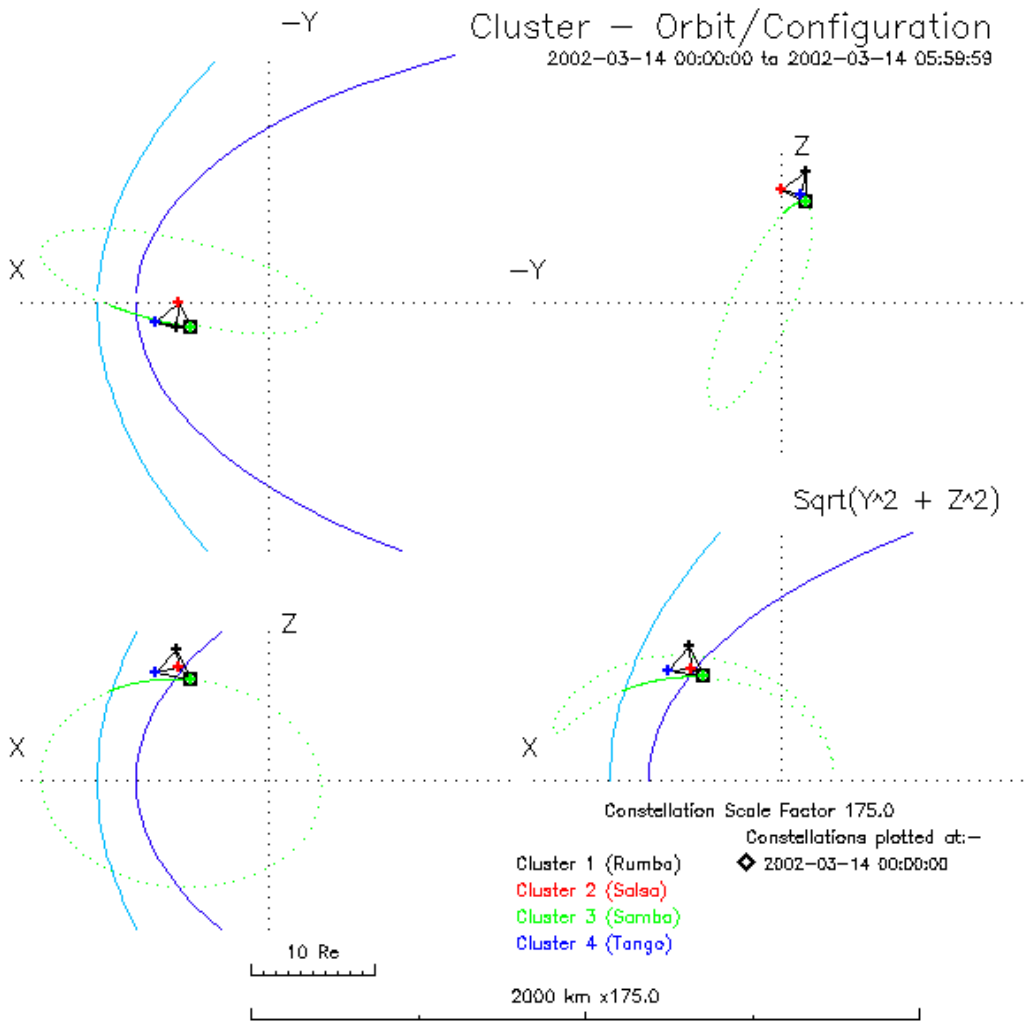

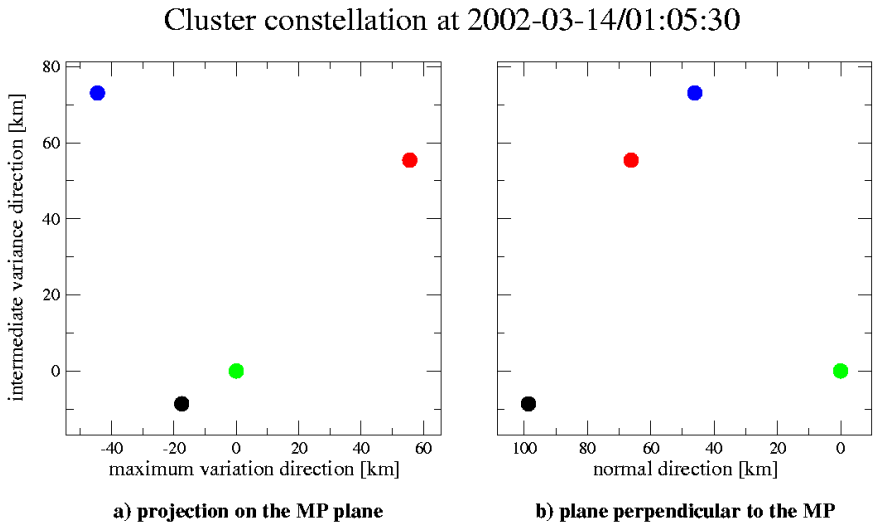

Figure 5.2: *Upper part:* Cluster orbit projections on the planes of the GSE coordinate system for the time of event. The distance between the satellites was increased by a factor of 175 in the plot. *Lower part:* Projection of Cluster configuration at the time of transition on the MP plane and on a plane containing the MP normal. See text for a detailed explanation.

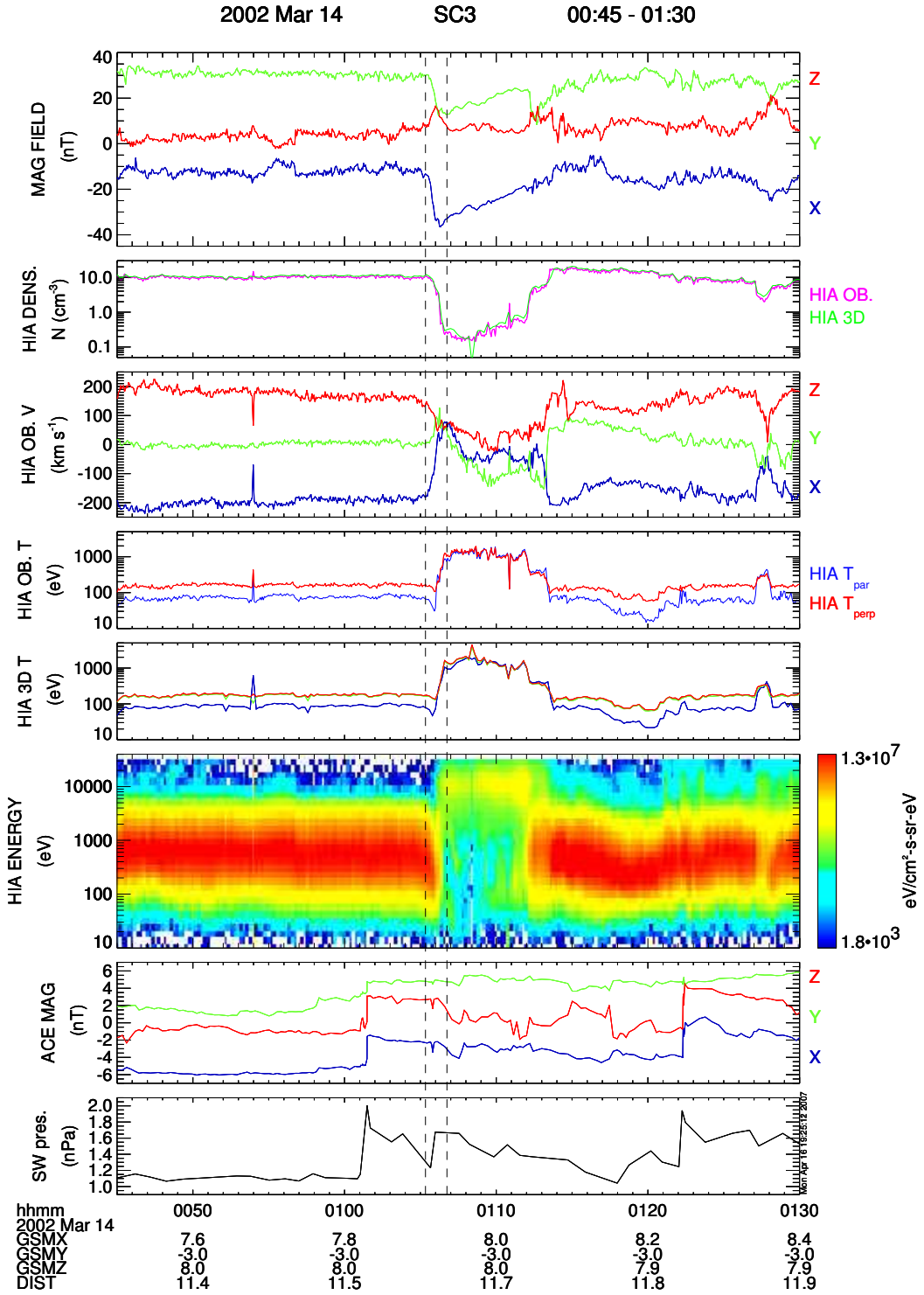

Figure 5.3: Magnetic field and ion measurements around the time of our event (indicated by the vertical dashed lines). From top to bottom, in the first six panels, we have magnetic field GSE components, ion density (computed on-board and at ground), components of ion velocity in GSE, ion parallel and perpendicular temperatures (computed on-board and at ground) and ion differential energy flux as measured by Cluster 3. The last two panels present the conditions in the solar wind, i.e. magnetic field GSE components and dynamic pressure, based on (shifted) ACE measurements. See text for further explanations.

field exhibits the maximum variance whereas the $\vec{y}$ axis indicates the magnetic intermediate - variance direction. The adjacent projection has the average MVAB normal direction as $\vec{x}$ axis and the same $\vec{y}$ axis. Because for a inbound transition a satellite is moving in the direction opposite to the MP normal, we can clearly observe that the time-sequence of the satellites' crossings is C3, C4, C2 and C1. This sequence is indeed obtained from the timing analysis (see the upper part of Figure 5.6, introduced later in the text).

In Figure 5.3, we present the same physical quantities as in Figure 3.4 namely GSE magnetic field components, HIA plasma moments (density, GSE velocity components, parallel and perpendicular temperatures), HIA differential energy flux and the parameters of the solar wind. The time interval for our event is indicated with dashed vertical lines. Again, the displayed measurements were taken by Cluster 3 (panels 1 - 6) and ACE (panels 7 and 8) satellites. When plotting ACE measurements, we took the time-delay into account resulting from solar-wind plasma propagation. A retardation of around 51 minutes, needed for the solar wind to reach the $[10, 0, 0]\, R_E$ point in GSE coordinates was estimated by using the Weimer method (*Weimer et al.* [2002]; *Haaland et al.* [2006]). More precisely, the solar wind phase front orientation was computed using the constrained MVA of the interplanetary magnetic field (IMF) data and then the solar wind velocity along that direction was considered[2]. A less precise method, that takes only the x GSE component of the solar-wind into account produced a similar result (i.e. 53 minutes), leading practically to the same conclusions.

In Figure 5.4 the first four panels present the magnetic field components in the GSE reference frame. For each satellite one can identify a 'clean' MP transition by the smooth rotation of the magnetic field vector between the roughly constant levels of magnetosheath (to the left) and magnetosphere (to the right). Owing to that behaviour, this event qualifies for a reliable investigation with the timing method. The significance of the vertical lines is related to the computation of the MP normal by the MVAB method and will be explained below.

Because the separation distance between the satellites was only 100 km, and taking into account that the computed MP thickness for this event is around 1060 km (as will be shown later in this sections), the conditions for applying the curlometer technique are fulfilled.[3] We show in the last two panels the current density obtained from this method (the three components in GSE reference frame) and a comparison between the magnitude of $\nabla \times \vec{B}$ (in violet) and of $\nabla \cdot \vec{B}$ (in yellow). Since $\nabla \cdot \vec{B}$ should be ideally zero, this comparison is an indicator of the errors in assessing the current density by the curlometer method, the rule of thumb being that the values of $|\nabla \cdot \vec{B}|$ should be smaller than those corresponding to $|\nabla \times \vec{B}|$. As one can see, this criterion is fullfiled when all the spacecraft are inside the MP structure (time interval between the vertical dotted lines in the last two panels) with the exception of a single point, where $|\nabla \times \vec{B}| \simeq 0$. In establishing the positions of these vertical lines, we used the information from the timing analysis (upper part of Figure 5.6): the first line indicates the time when the trailing satellite (Cluster 1) reaches the MP leading edge whereas the second line indicates the time when the leading spacecraft (Cluster 3) exits the MP interior.

[2]We thank Dr. Stein Haaland for applying the Weimar method for this event

[3]The curlometer technique (see for example *Dunlop et al.* [2002b] and the references therein) makes use of the Cluster 3-D multi-point capability. It refers to the direct estimation, via Ampère's law, $\nabla \times \vec{B} = \vec{J}$, of the electric current density $\vec{J}$ by using the magnetic field measurements $\vec{B}$ taken simultaneously at the four satellites. Linear spatial variation between the points of measurements, meaning the constancy of $\vec{J}$ over the satellite configuration, is assumed. Therefore, the method is applicable when the inter-spacecraft separation distance is much less than the scale length of the current density variation. Another assumption made is time-stationarity. In practice, an indication of the linearity of the spatial magnetic variation is obtained by checking the $\nabla \cdot \vec{B} = 0$ relation, but there are other effects that may cause non-zero values for this quantity (like non-stationarity, error measurements or big distortions from the spacecraft tetrahedronal configuration).

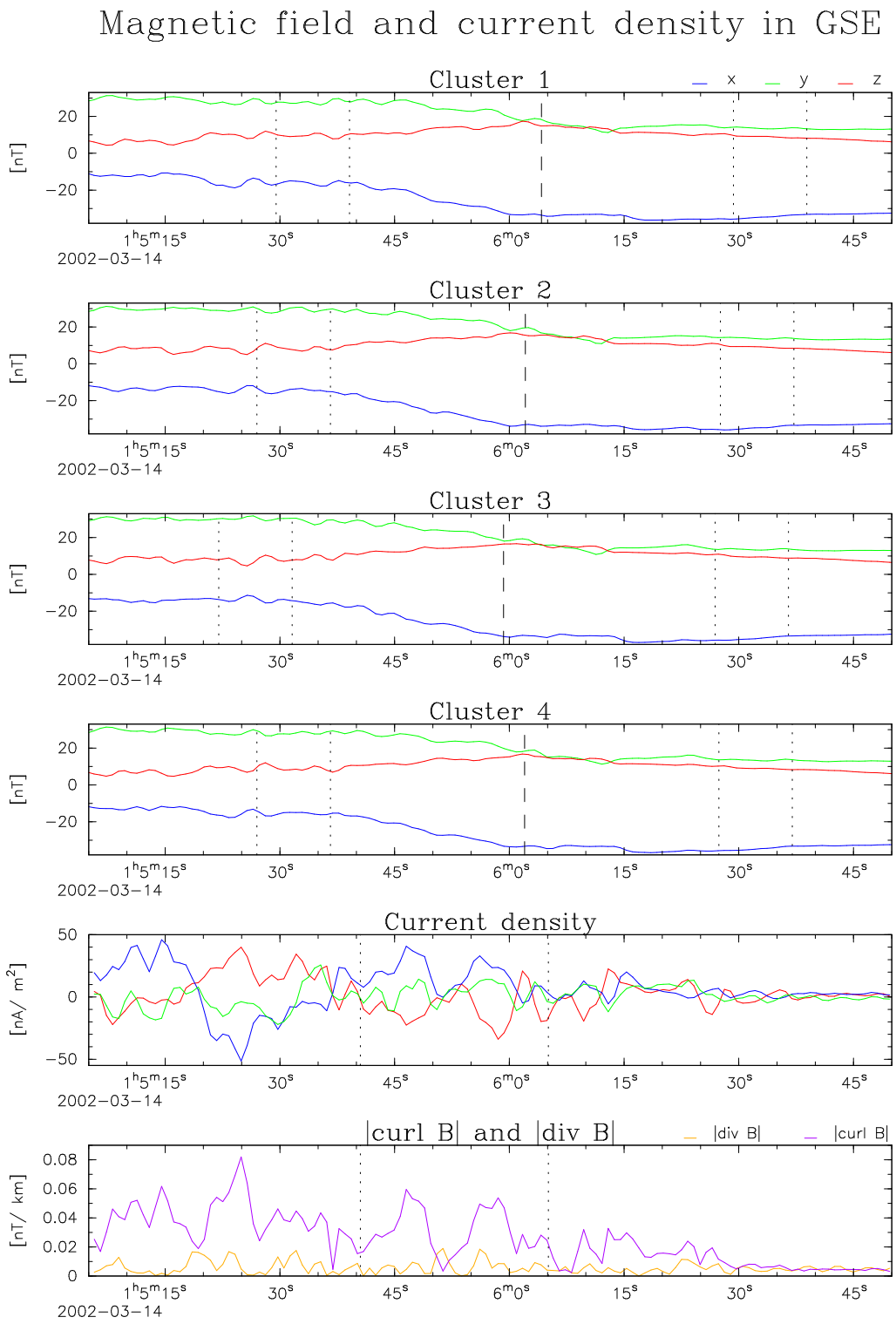

Figure 5.4: *First four panels:* Magnetic field as measured by the Cluster satellites during the MP crossing. The x, y and z GSE components are shown in blue, green and red lines respectively. The minimum and maximum length intervals entering the MVAB nested analysis (vertical dotted lines) together with their common central time (dot-dashed lines) are indicated for each satellite. *Last two panels:* Current density components in GSE, obtained from the curlometer technique and a comparison between the absolute values of $\nabla \times \vec{B}$ (violet trace) and of $\nabla \cdot \vec{B}$ (yellow trace). The time interval when all four satellites are inside the MP structure is indicated.

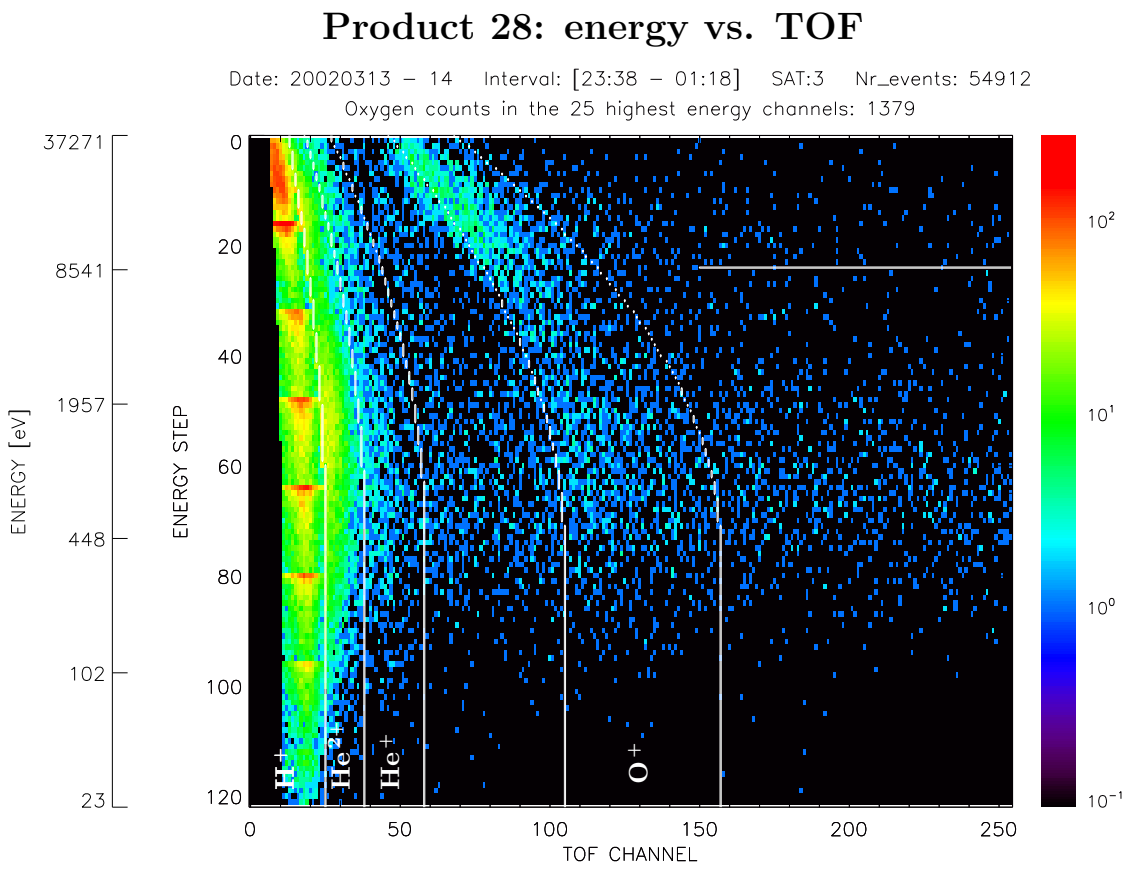

Figure 5.5: The distribution of events registered by the product P28 during a 100 minutes period that includes the analyzed transition, according to the TOF channel (on the abscissa) and energy channel (on the ordinate). The white vertical lines indicate the thresholds used by the on-board software to discriminate the particles according to their species. The Oxygen ions are seen at higher energies; see the text for more explanations.

Due to the already mentioned spill-over effect (see Section 5.2), when assessing the presence of minor ion species at the MP it is advisable not to fully rely on the plasma moments provided by CODIF. Still, one can qualitatively evaluate the presence of minor ions by using the so-called P28 data product provided by the instrument. This product is collected with a poor time resolution and poor statistic (an average of around 10 counts per second) but has the advantage of transmitting to the ground the full information on time-of-flight (TOF), energy and direction for each registered event.

In Figure 5.5 we present a 2D histogram of the number of events recorded on-board Cluster 3 with the P28 product, according to the TOF channel (on the abscissa) and energy channel (on the ordinate). The plot corresponds to a time interval of 100 minutes that includes the analyzed MP transition. During this period the satellite spends about the same amount of time inside and outside the magnetosphere. The over-plotted vertical parabolic white lines designate regions in the TOF - energy plane assigned by the instrument to different ion species. Consequently, we have, starting from the low TOF channels, the areas corresponding to protons, He^{2+}, He^{+} and O^{+} particles (the zone between He^{+} and O^{+} is not associated with any type of particles).

In interpreting Figure 5.5 we have to consider that protons are suppressed by a factor of 10 in the P28 product in order to improve on the statistics of minor ions. Therefore, in

reality, the number of counts in the proton area is 10 times higher. The manifestation of the spillover effect is visible by the relative high numbers of counts, adjacent to the H^+ region. Therefore, most of the events in the He^{2+} band are not caused by Alphas but by protons that give a false signal in that region. We notice the presence of a 'genuine' (i.e. not produced by the spillover effect) O^+ population. This population is faint and we do not think it has a significant influence on the Walén relation. Later on in this chapter we will consider another event with a considerably higher O^+ presence (see Figure 5.14) for which this type of influence is examined. A comparison between the two events is facilitated by the number of O^+ counts in the highest 25 elementary energy channels (approximately between 8.5 keV and 40 keV; above the horizontal white line indicated in the plot) that roughly contains this population in both events.

Inferring the magnetopause thickness.
In determining the individual MP normals we used the magnetic variance analysis and followed a similar procedure presented in Section B.4:

- we started with data of 0.2 seconds time-resolution and then we averaged the measurements by using a boxcar window of 1.6 second width, in the same time resampling the data to a resolution of 0.8 seconds, with the intention to eliminate the finer small-scale structure which is of no interest in our study.
- for each satellite a number of thirteen symmetric nested intervals were chosen, centred on the same point approximately around the transition centre. These central times, the minimum and maximum length intervals are indicated for each satellite by the vertical lines in the first four panels of Figure 5.4.
- for each of these thirteen intervals a constrained (to $\langle B_n \rangle = 0$) minimum variance analysis was performed (see Appendix A for a method description) and the directions in space identified in this way were associated with the MP normal for the satellite in question and for that particular data interval.
- from the thirteen normals, an average direction was computed and associated with the individual MP normal for that specific spacecraft. By using the nested intervals, we minimize the dependence of the result from the interval of analysis.

We carry out also a plain (unconstrained) MVAB on our event in exactly the same manner and the results from both analysis are presented in Table 5.1. For each satellite the eigenvalues and the components of the eigenvectors in the GSE reference frame of the magnetic variance matrix are presented in case when the constraint $\langle \vec{B} \rangle \cdot \vec{n} = 0$ was imposed and without this condition. In the latter situation the value of $\langle \vec{B} \rangle \cdot \vec{n}$ is indicated in the rightmost column. The normal vectors provided by each technique appears in bold face. One can notice that the constrained normals are very well defined, the ratio $\lambda_{max}/\lambda_{int}$ being ≥ 21 whereas in case of the unconstrained analysis the ration $\lambda_{int}/\lambda_{min}$ is around 3, which makes these normals unreliable. Another argument to reject the unconstrained normals takes into account the high normal magnetic component which they imply (between 22.8 and 25.3 nT), values that are unreasonable large. This is another example when the plain MVAB method gives erroneous results (see the discussion from Section B.4).

In the upper part of Figure 5.6 the procedure of extracting the timing information from the magnetic field data is illustrated. We follow the same steps as in Section B.4, the only difference being that now the MP was considered as planar. This assumption is supported by the orientation of the individual constrained MVAB normals, represented with coloured squares

Table 5.1: Results from the constrained and unconstrained minimum variance analysis of the magnetic field, performed on the thirteen nested intervals. For a detailed descriptions of the procedures and of the parameters appearing in this table see the text. The normal components in GSE and the magnetic variance provided by each technique is shown with bold faces.

	Constrained MVAB				Unconstrained MVAB				
	$\lambda\,[nT]^2$	n_x	n_y	n_z	$\lambda\,[nT]^2$	n_x	n_y	n_z	$\langle\vec{B}\rangle\,[nT]$
	0.00	0.7871	−0.5262	−0.3219	**1.93**	**0.5792**	**−0.6593**	**0.4784**	−24.3
Cluster1	**3.55**	**0.2353**	**−0.2261**	**0.9452**	5.51	−0.2768	0.3926	0.8766	
	74.65	−0.5701	−0.8197	−0.0542	80.73	−0.7664	−0.6406	−0.0445	
	0.00	0.7746	−0.5418	−0.3261	**1.86**	**0.5808**	**−0.6403**	**0.5021**	−23.5
Cluster2	**3.87**	**0.2545**	**−0.2049**	**0.9451**	6.45	−0.2708	0.4294	0.8611	
	82.61	−0.5789	−0.8151	−0.0209	89.03	−0.7672	−0.6365	0.0765	
	0.00	0.7616	−0.5550	−0.3344	**2.01**	**0.5972**	**−0.6723**	**0.4361**	−25.3
Cluster3	**4.04**	**0.2871**	**−0.1736**	**0.9**420	5.91	−0.1765	0.4202	0.8894	
	93.72	−0.5809	−0.8135	0.0270	102.72	−0.7821	−0.6089	0.1326	
	0.00	0.7799	−0.5357	−0.3236	**1.96**	**0.5630**	**−0.6379**	**0.5252**	−22.8
Cluster4	**3.38**	**0.2537**	**−0.2020**	**0.9459**	5.40	−0.2722	0.4568	0.8468	
	78.91	−0.5720	−0.8199	−0.0217	86.54	−0.7802	−0.6198	0.0837	

and MVABC1 symbols in the polar plot (the bottom part of the same figure). One notices that these normals are contained in a cone having approximately 2 ° half-width and with the axis oriented along the average (over the four satellites) MP normal direction (magenta square, symbol MVAB).

The magnetic profiles used in extracting the timing information correspond to an average (over the four satellites) maximum variance direction. The magnetic levels in the magnetosheath and in the magnetosphere are approximately the same for all satellites, as it should be for a planar discontinuity. Therefore, when fitting the data, we impose common values of the asymptotic levels for all four traces. We also excluded a few points on the magnetosheath side of the discontinuity from the fitting process, representing some local, smaller scale irregularities. Like in Section B.4, a hyperbolic tangent profile has been assumed for the magnetic variation at the MP and the same convention about the MP extent was adopted (i.e. a fraction of $tanh(1) \approx 76\%$ of the total magnetic jump - between the horizontal dashed magenta lines).

The timing normals (symbols CTA and CVA refer to the constant thickness approach and, respectively, constant velocity approach; see Section B.1 for a short presentation of these techniques) are also close to MVAB direction (approximately 4 °). The result implies an independent confirmation of the MP planarity for this event. The average MP thickness obtained from CVA was around 1200 km, whereas the CTA technique gives a value of 915 km for this parameter. If we consider the average direction obtained from the two timing procedures (vectorial sum of the CTA and CVA normals) we obtain a MP thickness of around 1060 km.

5.4 Analysis of the event from 14 March 2002

In case of the transition presented in Section 5.3, there is convincing evidence that the MP behaves like a rotational discontinuity. In Figure 5.7 we show the evolution of various physical

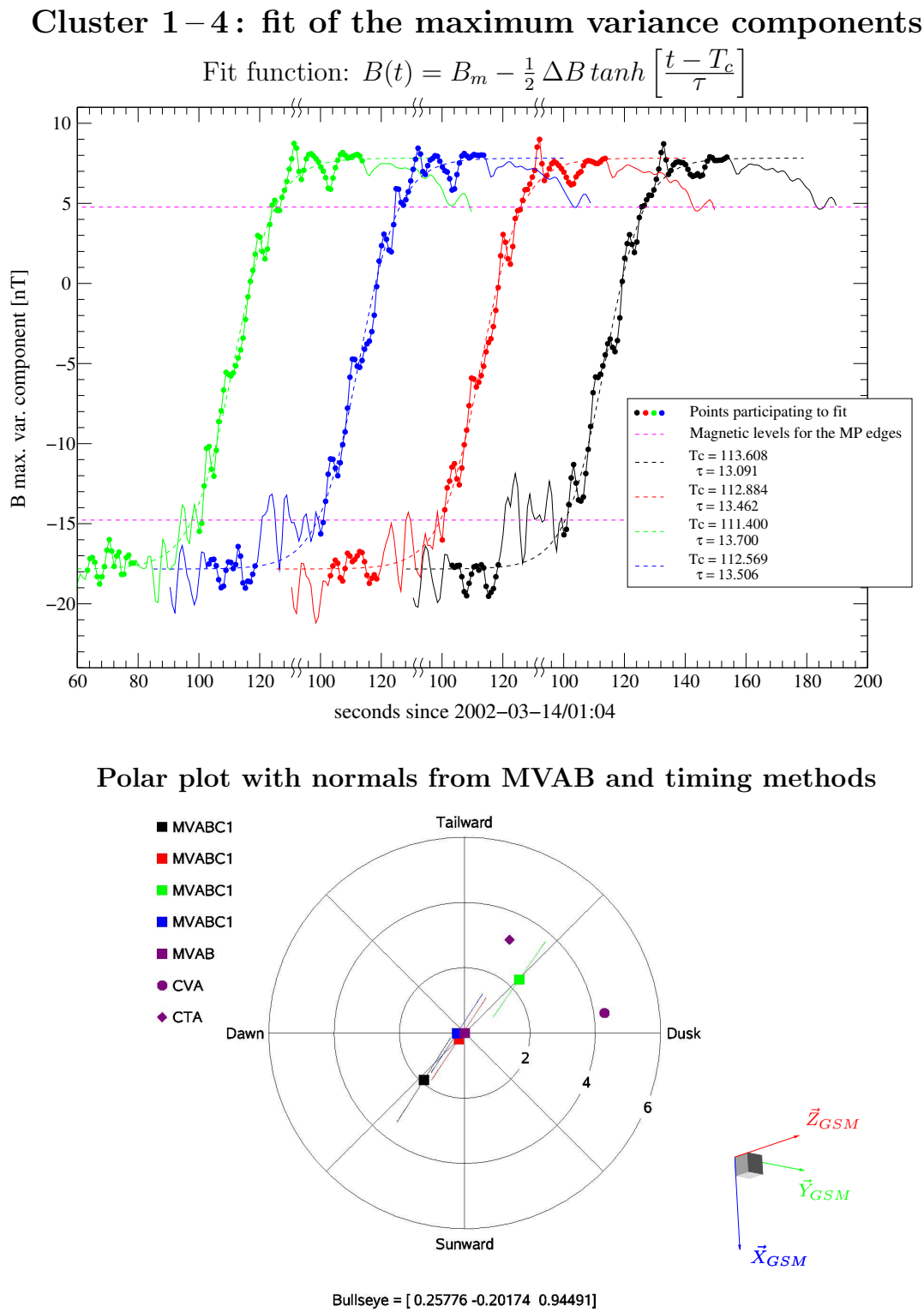

Figure 5.6: *Upper part:* The magnetic maximum variance components together with their fits are shown for all four Cluster satellites according to the mission colour code. Note that the traces are displaced for a better visualization. The magnetic levels corresponding to the MP boundaries are indicated by horizontal dashed lines. Timing information appears in the legend box. *Lower part:* Polar plot with the normals obtained from the constrained MVAB of the magnetic field and by using the planar timing techniques of CVA and CTA. In the lower right corner the orientation of GSM unit vectors in the MP reference frame is shown.

parameters, as measured by Cluster 3, around the time of the MP encounter. Starting from top to bottom we have:

- HIA differential energy flux - time spectrogram for the whole energy range of the sensor
- magnetic field components in GSE, with B_x in blue, B_y in green and B_z in red
- plasma bulk velocity components in GSE, with the same colour code. All the moments in this plot are calculated on-board from HIA measurements
- the magnitude of the plasma bulk velocity
- plasma pressure perpendicular to $\vec{B}$ (in red), magnetic pressure $B^2/2\mu_0$ (in black) and their sum (in cyan)
- plasma parallel (in green) and perpendicular (in red) temperatures
- plasma pressure anisotropy factor $\alpha \equiv \mu_0(p_\parallel - p_\perp)/B^2$ computed in two ways: by diagonalization of the plasma pressure tensor (in black) and by directly using the information about the orientation of $\vec{B}$ (in blue)
- the quantity $N(1-\alpha)$, which for a rotational discontinuity should be constant if we neglect the electrons contribution. In this panel there are actually two traces, corresponding to the two different ways of computing α, but they indicate practically the same evolution.
- plasma ion density (in black) and electron density from WHISPER instrument (in green). For the ions density we indicated the central time of the measurements taken with the HIA detector.

In Figure 5.8 we show the results from deHoffmann-Teller and Walén tests corresponding to the time interval indicated by the black dotted vertical lines. The interval is located on the magnetosheath side of the transition and starts around the time when the change in the plasma velocity is noticed (better seen in the panel presenting its magnitude). In the left plot, we present the fit between the measured convection electric field $\vec{E}_c = -\vec{V} \times \vec{B}$ (on ordinate) and the convection electric field $\vec{E}_{HT} = -\vec{V}_{HT} \times \vec{B}$ associated with a time-stationary structure moving with the determined HT velocity (on abscissa). Different components are indicated by different colours. The slope of the fit line (1.01), the correlation coefficient (0.99) and the ratio D/D_0 between the electric field intensities in the starting and HT frames (0.01) demonstrate a very good identification of the HT frame. The right plot, with the outcome of the Walén test, shows the fit between the plasma velocity components in the HT frame (on ordinate) and the local Alfvén velocity components $\vec{B}_i/(\mu_0\rho)^{1/2},\ i = 1, 3$ (on abscissa). The correlation coefficient of -0.99 is close to the ideal values of ± 1 whereas the value of the slope (-0.68) is different from the values predicted for a model RD (i.e. ± 1) but well convincing for a successful Walén test at the MP (see e.g. *Paschmann et al.* [2005a]). Notice also the relative large dynamic range in the x and z components (blue and red points) and the fact that all points lye close to the regression line, findings in support of a RD.

The negative values obtained when testing the tangential stress balance indicate that the normal components of the magnetic field B_n and bulk velocity V_n have different signs. Because V_n is oriented opposite to the MP normal (the magnetosheath plasma density being higher than the plasma density inside the magnetosphere) it means that B_n is positive (i.e pointing along the MP normal). Considering the topology of the magnetic field lines inside the magnetosphere for its northern hemisphere, we conclude that the measurements were made southward to the reconnection line. This is a typical case of tailward of the cusp reconnection, favoured by the northward orientation of IMF B_z component. Due to the precise computation of the time necessary for the plasma conditions measured by ACE to propagate at the magnetosphere

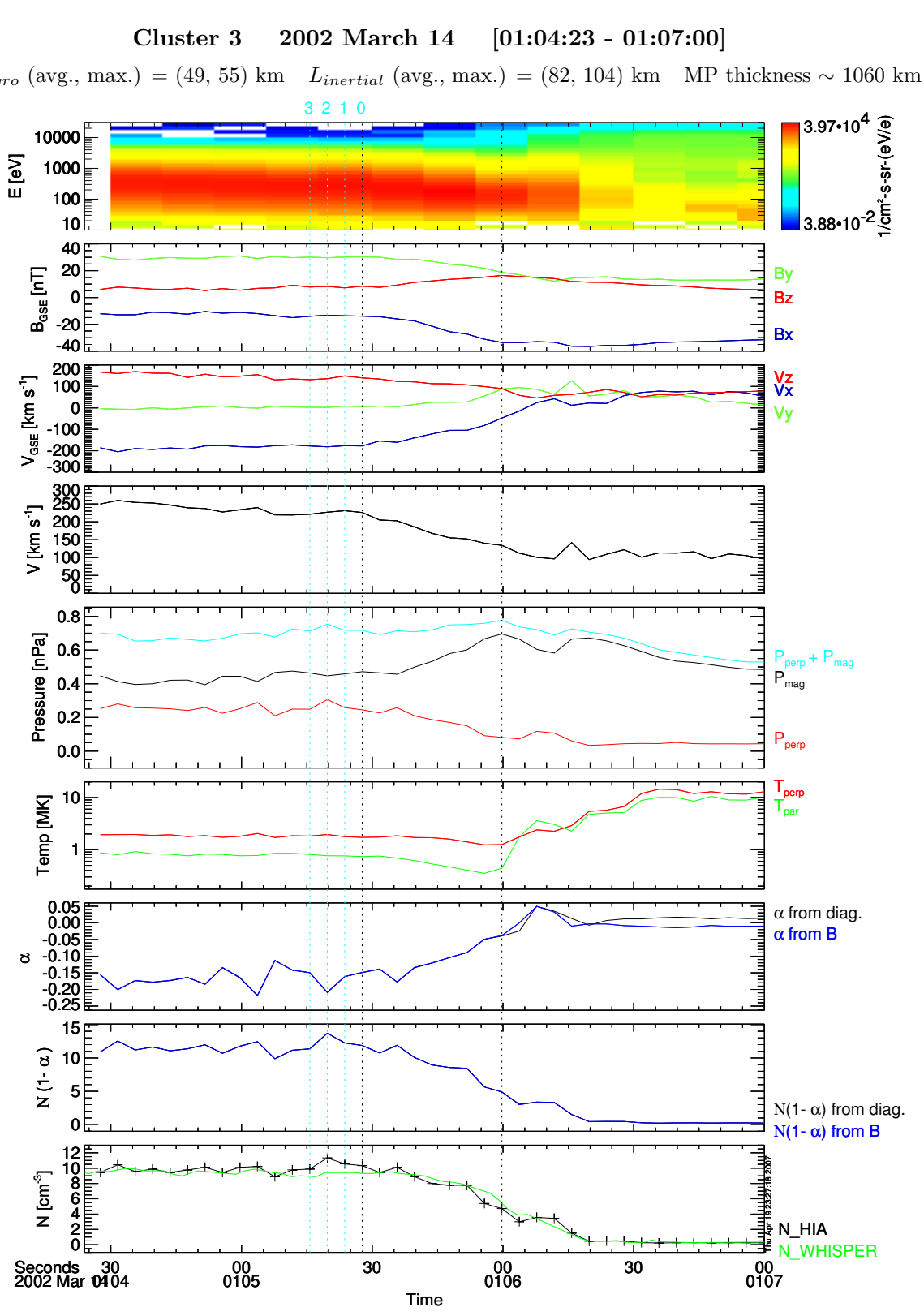

Figure 5.7: Plasma (ions) and magnetic field parameters for the inbout transition from 14 March 2002 as measured by Cluster 3 satellite. In the text, a detailed description of the displayed physical quantities is given. The black vertical dashed lines indicate the interval of analysis, whereas the blue vertical dashed lines designate points in the magnetosheath taken as reference in the Walén test.

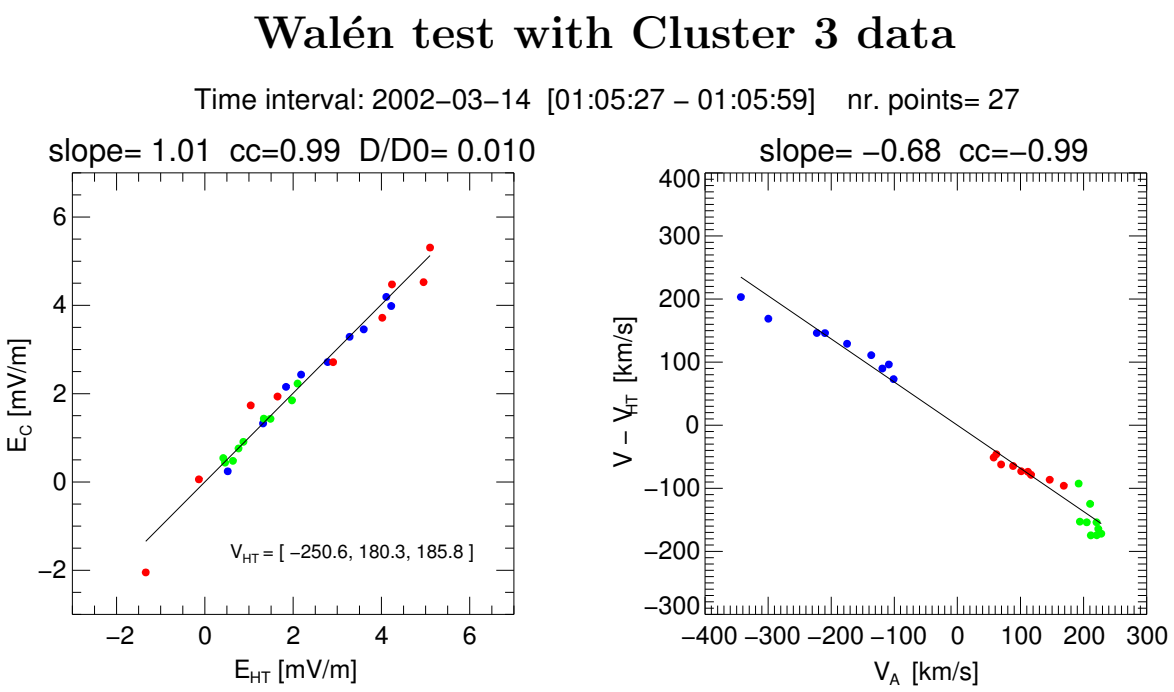

Figure 5.8: *Left-hand side:* The result from deHoffmann-Teller analysis is shown. The plot presents the fit between the electric field $\vec{E}_c = -\vec{v} \times \vec{B}$ (on ordinate) and the convection electric field $\vec{E}_{HT} = -\vec{V}_{HT} \times \vec{B}$ associated with a time-stationary structure moving with the determined HT velocity (on abscissa). The GSE components of HT velocity are indicated. *Right-hand side:* The Walén test result, obtained when the relation $\rho(1-\alpha) = const.$ is not incorporated in the tangential stress balance equation. The fit between the Alfvén velocity components (on abscissa) and the plasma velocity components in the HT frame (on ordinate) is shown. In both pictures different components are indicated by different colours.

level (see Figure 5.3 and the accompanying comments) we have a consistent picture for the sequence of phenomena. A few minutes before Cluster detects the event, the IMF B_z turned from stable, slightly negative values to stable positive ones (i.e. pointing northward). That triggered the reconnection onset at high magnetic latitudes (above the northen cusp) leading to the RD formation at the MP.

The non-constancy of $\rho(1-\alpha)$ in experimental data.
From the second-last panel of Figure 5.7 we notice that $N(1-\alpha)$, which is proportional to $\rho(1-\alpha)$, if we neglect the electron contributions, is not constant across the discontinuity. The evolution of this quantity mimics the evolution of the number density N, depicted in the last panel, as if the $(1-\alpha)$ term plays no important role.

When selecting the event from 14 March 2002 we had in mind to present a case for which the conditions are as close as possible to the requirements of the RD theory. The following list summarize the experimental facts presented so far:

- when investigating the MP orientation by two independent methods (MVAB and timing analysis) we arrived at the conclusion of a planar discontinuity
- the MP thickness was computed to be around 1060 km, much greater than the proton gyro radius (average and maximum values are 49 and 55 km, respectively, for this event) and the proton inertial length (with the average and maximum values of 82 and, respectively,

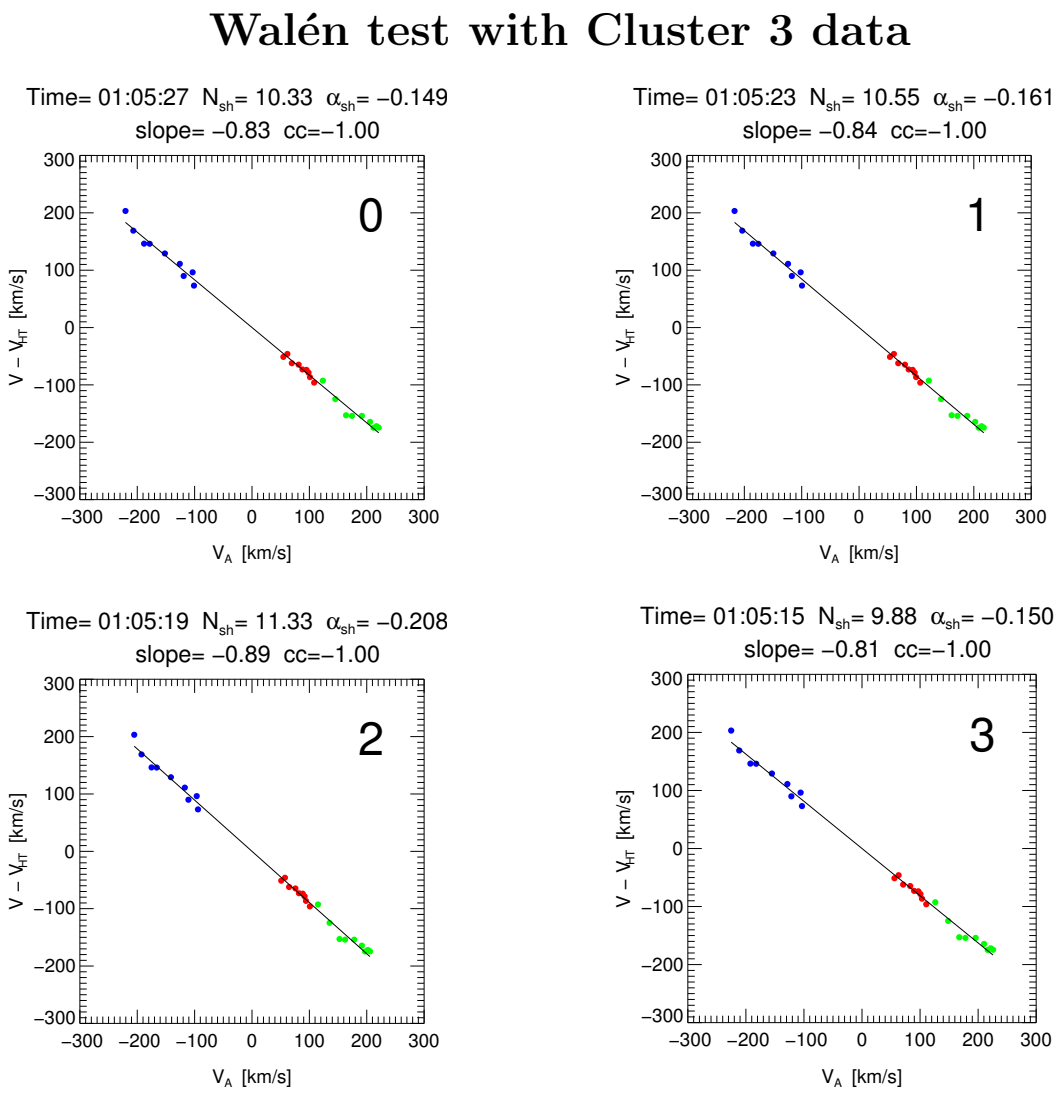

Figure 5.9: The Walén test results, obtained when the relation $\rho(1-\alpha) = const.$ is incorporated in the tangential stress balance equation. The considered time interval and satellite are the same as in Figure 5.8 and different reference points in the magnetosheath were used, indicated by the blue vertical dashed lines, labelled 0, 1, 2, and 3 in Figure 5.7. Note that the first such reference point (corresponding to the result presented in the upper right panel) is the starting point of the analyzed interval.

104 km). Therefore the MHD treatment is well justified.

- there is evidence in support of a stationary discontinuity. The clear and smooth transition in the magnetic field seen by all satellites and also the conservation of total pressure (i.e. plasma pressure perpendicular to $\vec{B}$ and magnetic pressure; see the fifth panel in Figure 5.7 and (5.14)) across the MP are evidences in this direction.
- according to the discussion at the end of Section 5.3, the presence of minor ion species for this event is faint and does not influence significantly way the various conservation laws deduced for a RD
- the deHoffmann-Teller and Walén tests were successful, indicating the presence of a RD

Yet, despite the above experimental facts, the quantity $\rho(1-\alpha)$ is not constant as expected

according to the theory for a RD. Notice that we computed the plasma pressure anisotropy in two ways (and obtained practically the same result) and that the ion density as determined with HIA was cross-checked with the electron density provided by the WHISPER instrument.

The experimental finding that $\rho(1-\alpha) \neq const$ is not unique for the transition in question: in general, the observations at the MP show that $p_{\parallel} < p_{\perp}$ in the magnetosheath, like in Figure 5.7. This means that $\alpha \equiv (p_{\parallel} - p_{\perp})\mu_0/B^2 < 0$ resulting in $(1-\alpha) > 1$. From the observations we know that $N_{Msheath}/N_{Msphere} > 1$; if we take a rather small value for this ratio, like 3, one would need values for $\alpha < -2$ in the boundary layer in order to save the relation. The realization of this last condition is very improbable in that region, where sometimes we have $p_{\parallel} > p_{\perp}$ (and therefore $\alpha > 0$ (see for example the superposed epoch analysis and the individual events presented in the studies of *Bauer* [1997] and in *Phan and Paschmann* [1996], dedicated to the low-latitude dayside magnetopause and boundary layer).

An even more puzzling aspect is that we obtain better results for the Walén test when the relation $\rho(1-\alpha) = const$ is incorporated in the tangential stress balance equation (see discussion from Section 5.2 and Figure 5.1, the bottom panel). In Figure 5.9 we showed four results of the test (labelled '0', '1', '2' and '3') performed on the same time-interval as for Figure 5.8 in the variant that uses the running α, with the magnetosheath reference points indicated in Figure 5.7 by the cyan dotted vertical lines. Note that in the first plot (upper left panel, labelled '0'), where the reference point is actually the first data point of the analyzed interval, we used exactly the same information as in Figure 5.8 but organized differently, by incorporating the relation $\rho(1-\alpha) = const$. The Walén slope improves from -0.68 to -0.83. and the correlation coefficient becomes 1.0. The best result is obtained when using the reference point labelled '2' in Figure 5.7, when the slope becomes -0.89.

This type of behaviour is not specific to the event presented: in general by using the running α in the Walén test we obtain values of the slope closer to ± 1, even when the presence of minor ions is negligible. As discussed in Section 5.2, this way of performing the tangential stress balance test was introduced by *Paschmann et al.* [1986], as a way to take into account the contributions from minor ion species when the plasma instrument is unable to discriminate between different type of ions (see also *Phan et al.* [2004]).

The contribution of the current density in the Walén relation.
In case when no minor species are present or when their overall contribution in the equations describing the conservation of various quantities across the discontinuity is so small that it could be ignored, a better approximation for the Walén relation could be obtained. The idea is to use indirectly, via the experimentally determined current density, the Walén relation based on electron moments, a form of the test that is thought to be obeyed with a higher degree than the classical form, based on ions.

In *Scudder et al.* [1999], the authors used the approximation

$$\vec{E}(z) = -\vec{V}_e(z) \times \vec{B}(z) \tag{5.16}$$

for the electric field all the way through the current carring layer of an RD, arriving at the following formula for the jump condition in the proton velocity:

$$\left[\vec{V}_p(z)\right] = \pm \kappa_e \left[\frac{\vec{B}(z)}{\rho(z)}\right] + \left[\frac{\nabla \times \vec{B}(z)}{\mu_0 e N(z)}\right] \tag{5.17}$$

(formula 43b from the cited paper).

The quantities appearing in these formulas are the electric field vector $\vec{E}$, electron fluid velocity $\vec{V}_e$, magnetic field vector $\vec{B}$, proton fluid velocity $\vec{V}_p$, a constant of proportionality κ_e, the density N and the mass density ρ of the uni-fluid. We indicated by z dependence, the quantities variation along the normal direction and by [ ] the differences between the values at any two points of measurement. The constant of proportionality κ_e for an electron - proton plasma takes the well known form appearing in the standard Walén relation

$$\kappa_e = \sqrt{\frac{\rho}{\mu_0}}\sqrt{1-\frac{\mu_0(p_{\parallel}-p_{\perp})}{B^2}} = \sqrt{\frac{\rho}{\mu_0}(1-\alpha)} \tag{5.18}$$

where $p_{\parallel}$ and $p_{\perp}$ and α are uni-fluid quantities. Note that (5.16) offers a better approximation for the electric field than the ideal MHD approximation $\vec{E} = -\vec{V}\times\vec{B}$, because of the known fact that the electrons are following closer the magnetic field lines than the ions do.

By introducing in (5.17) the expression for κ_e, we arrive at

$$\left[\vec{V}_p(z)\right] = \left[\sqrt{\frac{1-\alpha(z)}{\mu_0\rho(z)}}\vec{B}(z)\right] + \left[\frac{\nabla\times\vec{B}(z)}{\mu_0 eN(z)}\right] \tag{5.19}$$

We will work with this formula, considering (like throughout this thesis) that the uni-fluid quantity α appearing in (5.19) could be approximated by using the proton parallel and perpendicular pressures (see discussion in Section 5.2) One notices that the term on LHS and the second (or correction) term from RHS could be coupled to give the electron velocity $\vec{V}_e$ in case of a proton - electron plasma

$$\vec{V}_e = \vec{V}_p - \vec{J}/eN \tag{5.20}$$

The correction term $\vec{J}/eN$ was roughly evaluated in other papers either by using the total magnetic field variation across the MP and the MP thickness (see for example *Paschmann et al.* [2005a]) or by using an approximate value for the magnitude of $\nabla\times\vec{B}$ (*Phan et al.* [2004]). The authors arrived at the conclusion that the differences between ion and electron velocities are small in the analyzed events (below 10%) and therefore unimportant. For our event, the small inter-spacecraft separation (roughly 100 km) compared with the MP thickness and the clean transitions seen by all satellites makes it possible to use the full three-dimensional current density vector to asses the correction implied by this term in the Walén results.

In figures Figure 5.10 and Figure 5.11 we showed the results of applying (5.19) to Cluster 1 and Cluster 3 data, the only two satellites for which the HIA data are available. Starting from top to bottom we have:

- the first three panels contained the same quantities as in Figure 5.8, namely the HIA differential energy flux time-spectrogram, magnetic field components in GSE and plasma bulk velocity components in GSE (coloured lines)
- with crosses, we overplotted on the third panel the GSE components of $\vec{V}_p - \vec{J}/eN$
- the two panels at the bottom contain the GSE components of the current density $\vec{J}$, calculated from the curlometer technique, and the ions number density N. In obtaining $\vec{J}$ we used the same magnetic data as in the timing analysis (i.e. 0.8 second time-resolution) and we averaged the result by using a boxcar of 4 seconds width, imposing the same time tags as for the HIA on-board moments of the satellite in question.

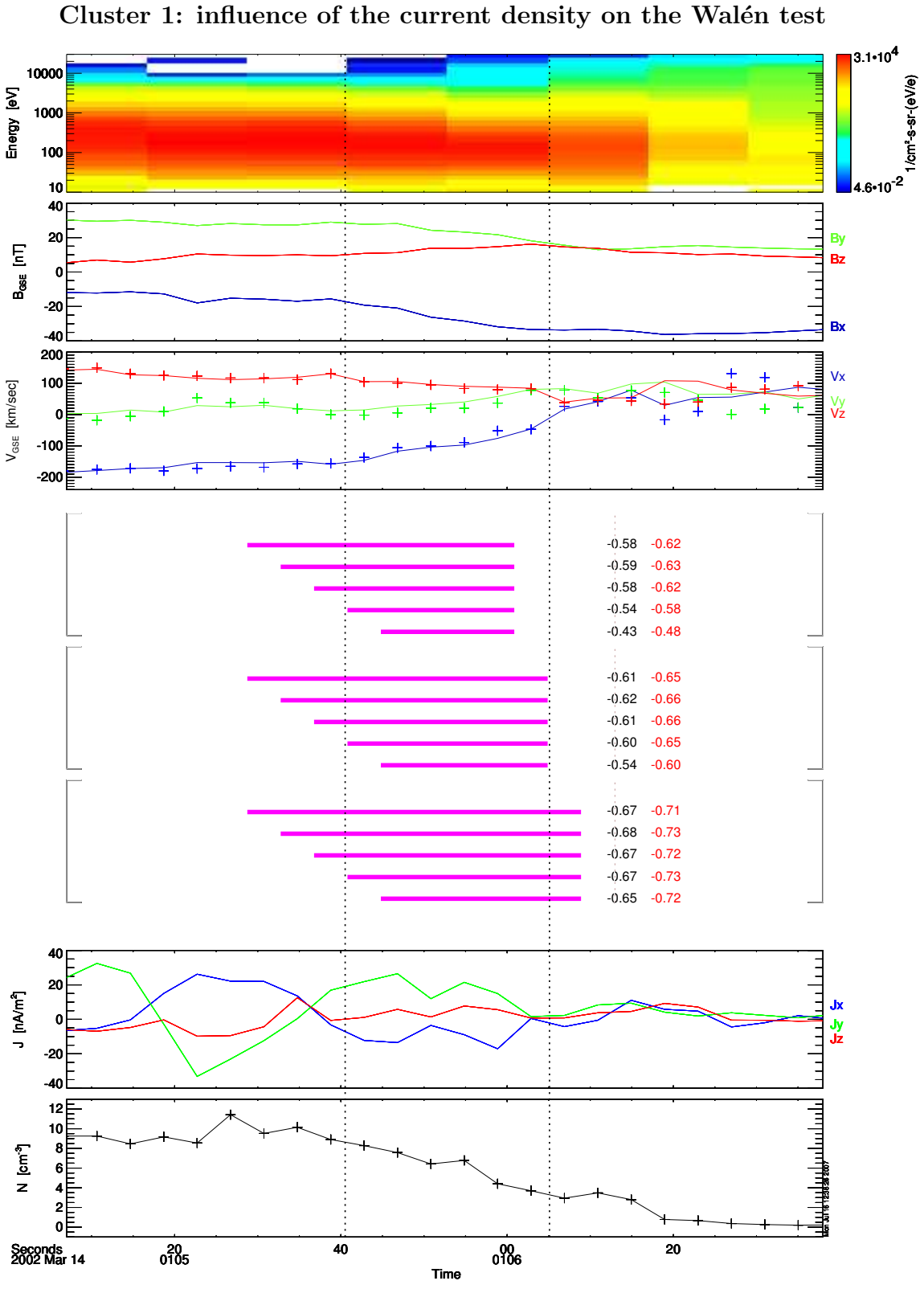

Figure 5.10: Results of the Walén test when the current density term is taken into account. Data from Cluster 1 are shown. The format of this figure, as well as the physical parameters displayed are described in the text.

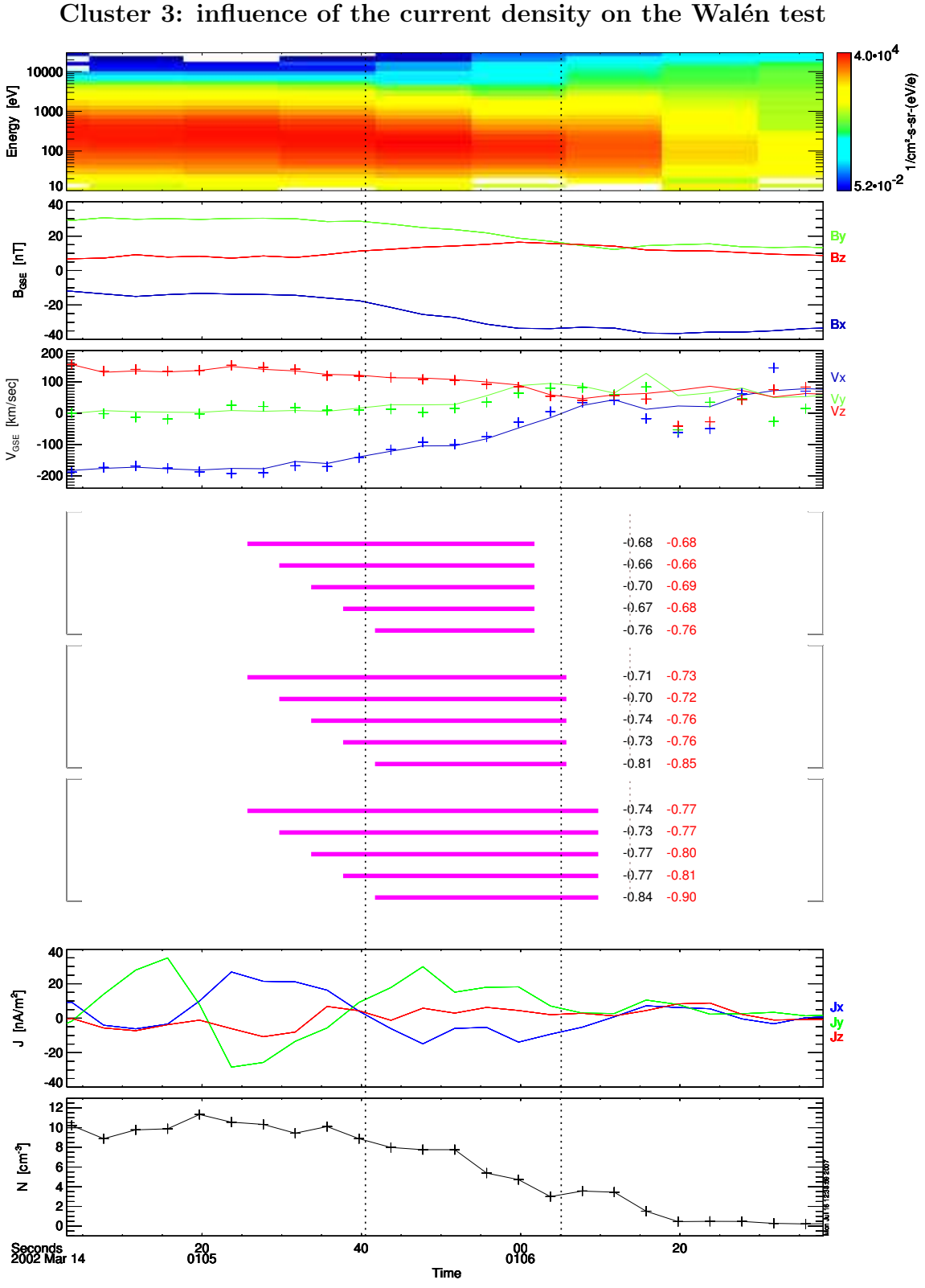

Figure 5.11: Results of the Walén test when the current density term is taken into account. Data from Cluster 3 are shown. The format of this figure, as well as the physical parameters displayed are described in the text.

The vertical dotted lines designate the time interval when all four satellites are located within the MP interior (as discussed for Figure 5.4) and therefore, strictly speaking, one should consider as valid only values for $\vec{J}$ from this time span. Between the two groups of panels we present the results of the Walén test, (in terms of the regression line slope) when the current density term was neglected (black numbers) and when this correction was applied (red numbers). In order to show that the effect is not caused by some local fluctuation in the measurements, different intervals were used in the analysis, indicated with magenta horizontal segments. For example in case of Cluster 1, the first interval extends over 8 points of measurements, starting roughly at 01:05:29 and ending roughly at 01:06:01. For this interval the Walén test improves from -0.58 to -0.62. In total, in these two figures a total of 60 Walén test are shown (30 for each satellite, corresponding to 15 data intervals, with and without incorporating the $\vec{J}/eN$ quantity).

It is clear from Figure 5.10 and Figure 5.11 that the corrected form of the Walén test brings better values in term of the regression line slope practically in all cases, although this effect is small. If we consider the intervals just contained within the vertical dotted lines (where the correction term is reliable determined) we obtained an improvement from -0.60 to -0.65 ($\sim 8\%$) for Cluster 1 and from -0.81 to -0.85 ($\sim 5\%$) for Cluster 3. The fact that the amelioration is relatively small and that we have still obtained results far from the ideal situation of ± 1, differentiate us from the work of *Scudder et al.* [1999], were the authors made a comparison by performing the Walén test using electrons ('cleaned' from the photoelectric effect) and ions on the same MP transitions.

When plotting Figure 5.10 and Figure 5.11, and in all the Walén tests presented there which include the correction term, we took into account that the current density, computed with the curlometer technique (see the Footnote 3 on page 87), is associated with the barycentre of the spacecraft configuration. This aspect brings practically no changes in the conclusions presented on this topic but nevertheless we implemented the needed changes for the sake of consistency. Therefore, because Cluster 1 - the last satellite entering the MP - is roughly 46 km behind the barycentre in the MP normal direction and considering a velocity for this structure of approximately 39 km/sec (as resulted from the timing analysis) we arrive at the conclusion that a delay of 1.17 seconds should be introduced in the current density time evolution. A similar argument can be applied for Cluster 3, where an opposite compensation of 1.35 seconds was used.

5.5 Overview on the 26 January 2001 event

The next issue to be discussed in this chapter will be illustrated with data from 26 January 2001, when the Cluster spacecraft recorded multiple MP transitions in the high-latitude northern hemisphere, around 15:00 magnetic local time. This event has been studied in *Phan et al.* [2004], where the authors presented evidence in favour of a continuous reconnection process, active over a period of more than 2 hours. During this time interval, an average of 10 complete MP crossings per satellite were detected, for each of them the Walén relation being satisfied with remarkable accuracy.

From our point of view, the particular feature of interest characterizing these transitions is the occurrence of O^+ ions in relative high abundance. We will investigate, from an experimental perspective, whether the presence of this minor species has a noticeable effect in the outcome of the tangential stress balance test. In following this, we will focus our attention on two particular transitions, identifiable on Cluster 3 data at around 10:43:30 and around 11:03:00.

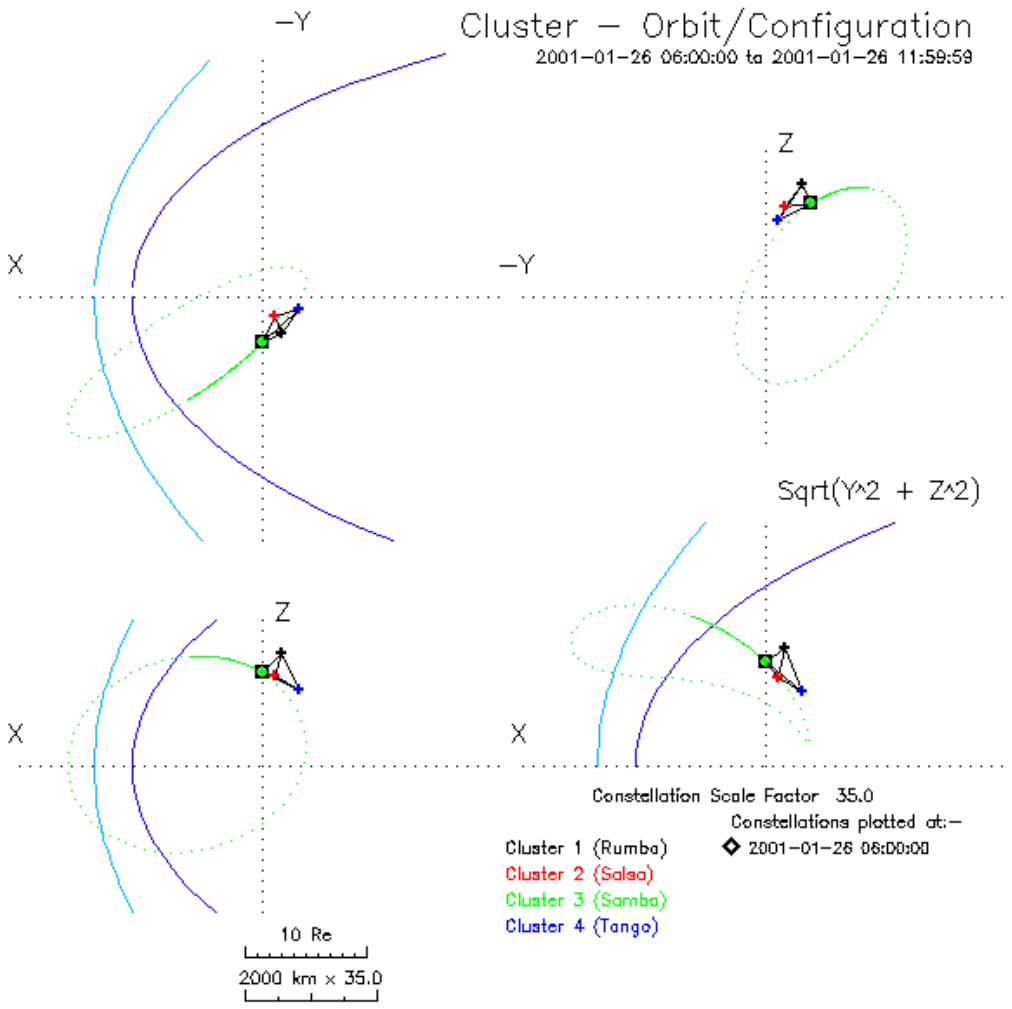

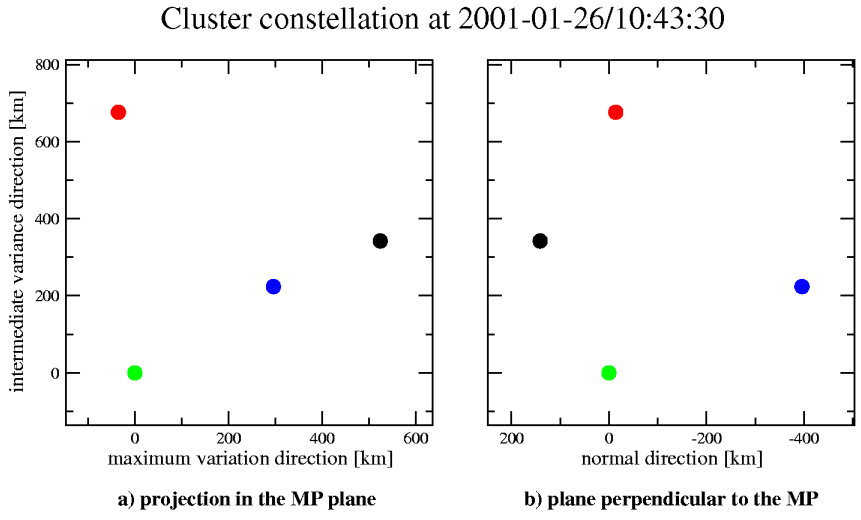

Figure 5.12: *Upper part:* Cluster orbit projections on the planes of the GSE coordinate system for the time of event. The distance between the satellites was increased by a factor of 35. *Lower part:* Projection of Cluster configuration at the time of transition on the MP plane and on a plane containing the MP normal. See text for a detailed explanation.

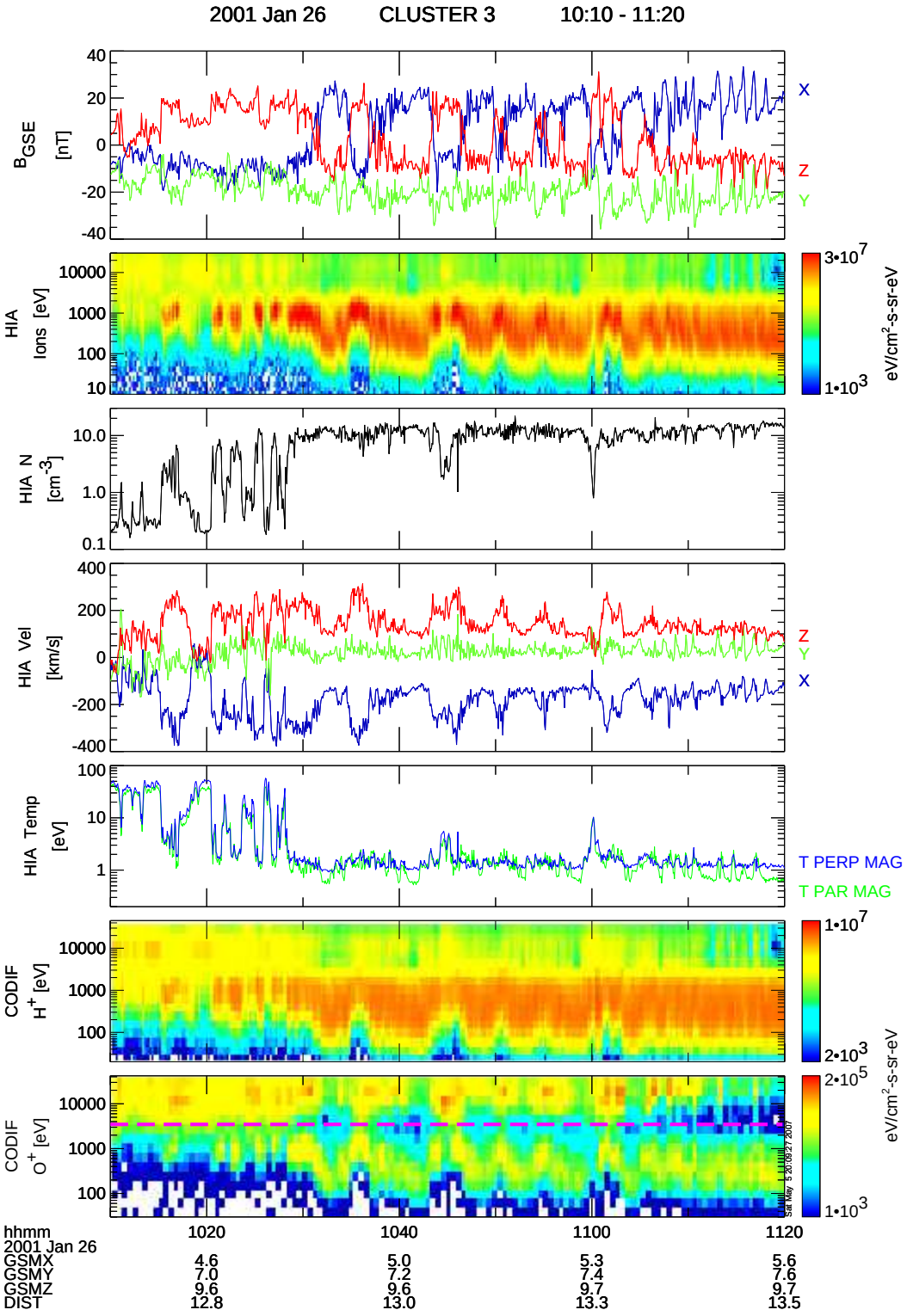

Figure 5.13: Magnetic field and ions measurements for the event taking place on 26 January, 2001. From top to bottom we show magnetic field GSE components, HIA differential energy flux time-spectrogram, plasma density, GSE components of plasma bulk velocity, parallel and perpendicular temperatures and CODIF differential energy flux time-spectrograms for protons and Oxygen ions. In the last panel we indicated by an horizontal dashed line the energy level above which we expect 'real' Oxygen events (not produced by the spillover effect).

General conditions.
In Figure 5.12 the Cluster satellites orbit and configuration at the time of the event are shown. The transition occurs around [5.0, 7.2, 9.6] R_E in the GSM coordinate system. In the upper part of the figure, showing the orbit (taken from Cluster Science Data System home page), a model MP and bow-shock were drawn and the distance between the satellites was scaled by a factor of 35. The four spacecraft are in a tetrahedral configuration, the separation distance being around 650 km.

On the bottom part of that figure two plane projections of the Cluster configuration at the time of the traversal are shown, both of them with Cluster 3 at the origin of the coordinate system. In the plot showing the projection on the MP plane - the plane perpendicular to the direction resulted by averaging the individual normals obtained from constrained MVAB method - the $\vec{x}$ axis corresponds to the direction along which the magnetic field exhibits the maximum variance whereas the $\vec{y}$ axis indicates the magnetic intermediate - variance direction. The adjacent projection has the average MVAB normal direction as $\vec{x}$ axis and the same $\vec{y}$ axis. The picture indicates an inbound transition (consistent with the plasma data presented in Figure 5.17), with the satellites' crossings sequence being Cluster 4, Cluster 3, Cluster 2 and Cluster 1.

Figure 5.13 presents various physical quantities characterizing the conditions in the plasma for the multi-crossing event of 26 January 2001. The displayed measurements were taken by the Cluster 3 satellite. From top to bottom we have:

- magnetic field components in the GSE from Cluster FGM experiment
- HIA differential energy flux spectrogram for the whole sensor energy range
- plasma density, measured and computed on-board by HIA sensor of the CIS experiment.
- plasma velocity components in the GSE calculated on-board from HIA measurements
- plasma temperatures perpendicular (blue) and parallel (green) to the magnetic field computed on-board by HIA
- CODIF protons differential energy flux spectrogram
- CODIF Oxygen differential energy flux spectrogram. In computing the 3D (i.e. based on the velocity distribution function send by the CODIF instrument to the ground) plasma moments for this ion species later on in this chapter, only the 5 upper-most energy channels (roughly above 3.5 keV, indicated by the magenta horizontal line) will be considered. Below this threshold, the events counted as Oxygen particles by the instrument are actually a manifestation of the spillover effect, i.e. produced by protons. See also the discussions related to Figure 5.14 and Figure 5.15.

The favourable circumstances of the 26 January 2001 event.
In case of 26 January 2001 event there are several favourable circumstances for fulfilling the intention declared at the beginning of this section, namely to establish (from an experimental point of view) whether a minor species contributes in a sizable manner to the outcome of the Walén test.

Firstly, such an effect could be investigated with Cluster more easily when the minor species in questions is O^+, and not He^{2+} or He^+, because the CODIF instrument separates this ions better from the protons in the time-of-flight section. This fact and taking into account that the O^+ energy range and the energy range of magnetosheath protons are roughly separated (as is seen from Figure 5.13 and Figure 5.15), makes a relative accurate estimation on the O^+

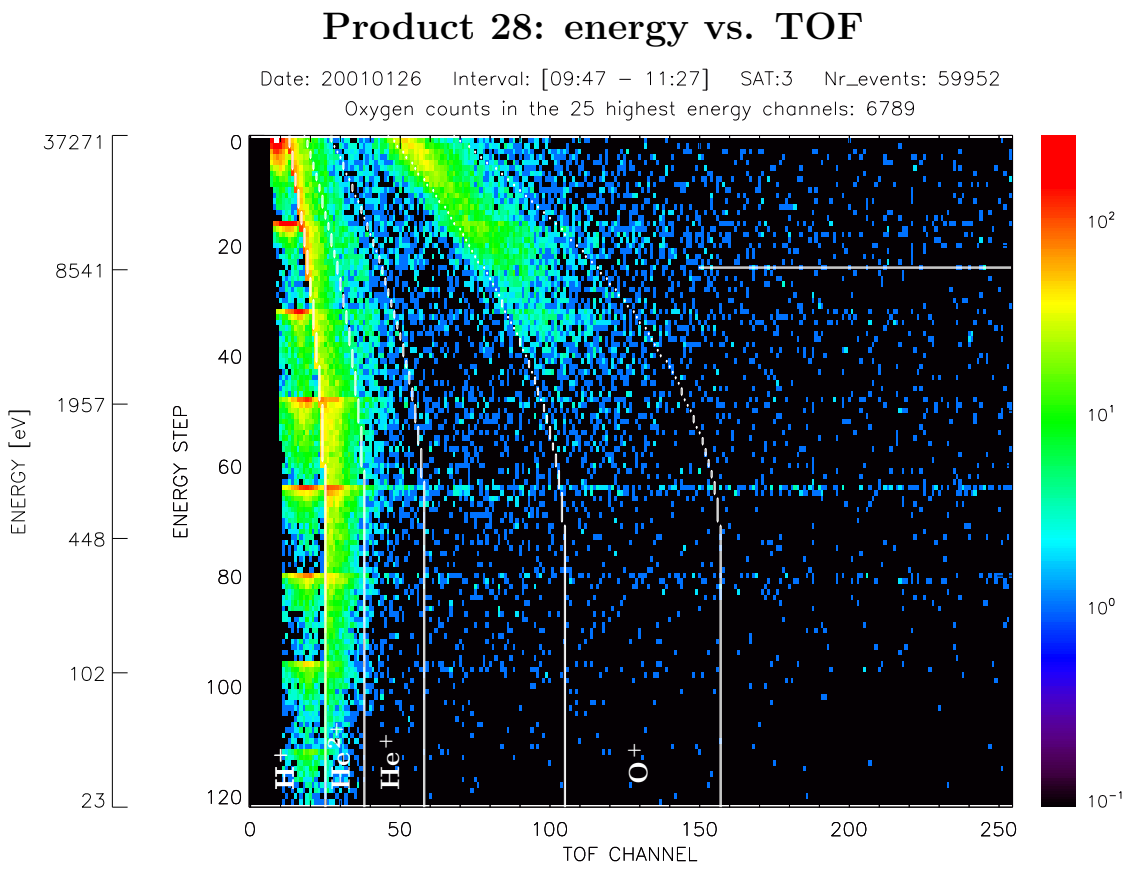

Figure 5.14: The distribution of events registered by the product P28 according to the TOF channel (on abscissa) and energy channel (on ordinate). As in Figure 5.5, the events collected during 100 minutes which include the analyzed transition are shown. In both figures we take care that the satellite spent approximately the same amount of time inside and outside the magnetosphere, so that a direct visual comparison is meaningfull.

moments possible. In addition, the Oxygen ions are 4 times heavier that the He^{2+} or He^{+} meaning that, in case of the same abundance, their contribution to the uni-fluid (i.e. COM) moments will be higher. It is therefore advisable to look for a case with high presence of Oxygen ions.

Figure 5.14 is similar to Figure 5.5, but refers to the event taking place on 26 January 2001. It refers to the Product 28 data measured by the same satellite (Cluster 3) and the length of the time interval is again 100 minutes. During this period, which includes our transitions, the satellite spends about the same amount of time inside and outside the magnetosphere. Therefore, because the conditions corresponding to the plots were similar, one can compare directly the number of O^{+} counts in the highest 25 elementary energy channels (approximately between 8.5 keV and 40 keV; above the horizontal white line indicated in the plot) that roughly contains this population in both events. We obtain that for the event analyzed in this section the number of O^{+} ions is approximately 4.5 times higher. Note that, very probable, above the CODIF energy range there is still a significant fraction from this ion species.

Another favourable circumstance is that, for the analyzed event, the CODIF instrument on Cluster 4 satellite happened to be in the low-sensitivity mode and as a consequence the detector was not saturated by the high proton fluxes in the magnetosheath. We will illustrate this aspect with the help of Figure 5.15, where a comparison between the Cluster 3 (first

3 panels) and Cluster 4 (the remaining panels) plasma data is shown for the time interval $[10:40,\ 10:48]$. From top to bottom we have:

- the distribution of the number of raw counts as a function of energy (on abscissa) and time (on ordinate) detected by CODIF on Cluster 3. The colour scale goes up to the maximum number of counts registered in one sample.
- the next panel presents a comparison between the plasma density computed on-board by the HIA instrument (green trace) and the plasma density computed from the CODIF measurements (ground computed density is shown in blue whereas the on-board density is shown in red).
- the same type of comparison, corresponding to the plasma velocity, is presented in the third panel. In order to avoid figure overloading, only the GSE x velocity component is shown.
- the distribution of the number of raw counts as a function of energy and time detected by CODIF on Cluster 4. Like in the first panel, the colour scale goes up to the maximum number of counts registered in one sample, which is about 4 times lower than in case of Cluster 3. In both these panels, an horizontal dashed line, situated just above the magnetosheath proton energy, indicates the lowest energy level used in the next section for computing the Oxygen 3D plasma moments.
- the next four panels show a comparison between the CODIF ground computed (in blue) and on-board computed (in green) plasma moments in terms of density, GSE x velocity component, parallel and perpendicular temperatures. Note that for Cluster 4 there are no HIA measurements available.

Two main conclusions can be obtained from Figure 5.15. On one hand, the plasma moments provided by the CODIF instrument being in the high sensitivity mode, are heavily affected by the saturation process. Due to the faster electronics, the HIA instrument has no such problems and therefore its measurements are reliable. Looking for example at the density panel, there is roughly a factor of 2.5 between the CODIF ground computed density and HIA on-board computed density in the magnetosheath. Also, between the ground and on-board computed CODIF densities there is roughly another factor of 3 missing.

On the other hand, in case of the Cluster 4 satellite when CODIF happens to be in the low sensitivity mode, there is a very good agreement between the on-board and ground based moments. This is remarkable considering that the on-board moments are computed based on a higher time, energy and angular resolution (4 seconds, 128 energy channels and (8 x 32) angular bins instead of 12 seconds, 16 energy channels and 88 angular bins for the ground computed moments). We can also notice that the plasma densities provided by CODIF on Cluster 4 and by HIA on Cluster 3 (and Cluster 1, not shown) are similar both in terms of variations and in terms of absolute values.

Based on these observation, we conclude that for this event the CODIF detector provides reliable plasma measurements in case of Cluster 4 and therefore we will make use of them in the next section.

Inferring the magnetopause thickness.
An important aspect to be investigated in the analysis refers to how the MP thickness compares with the kinetic parameters of ion gyro radius and ion inertial length. This comparison tells us how good the simple MHD treatment of plasma as a fluid is in our particular case.

Because of the relatively perturbed character of the magnetic traces for this event, we were

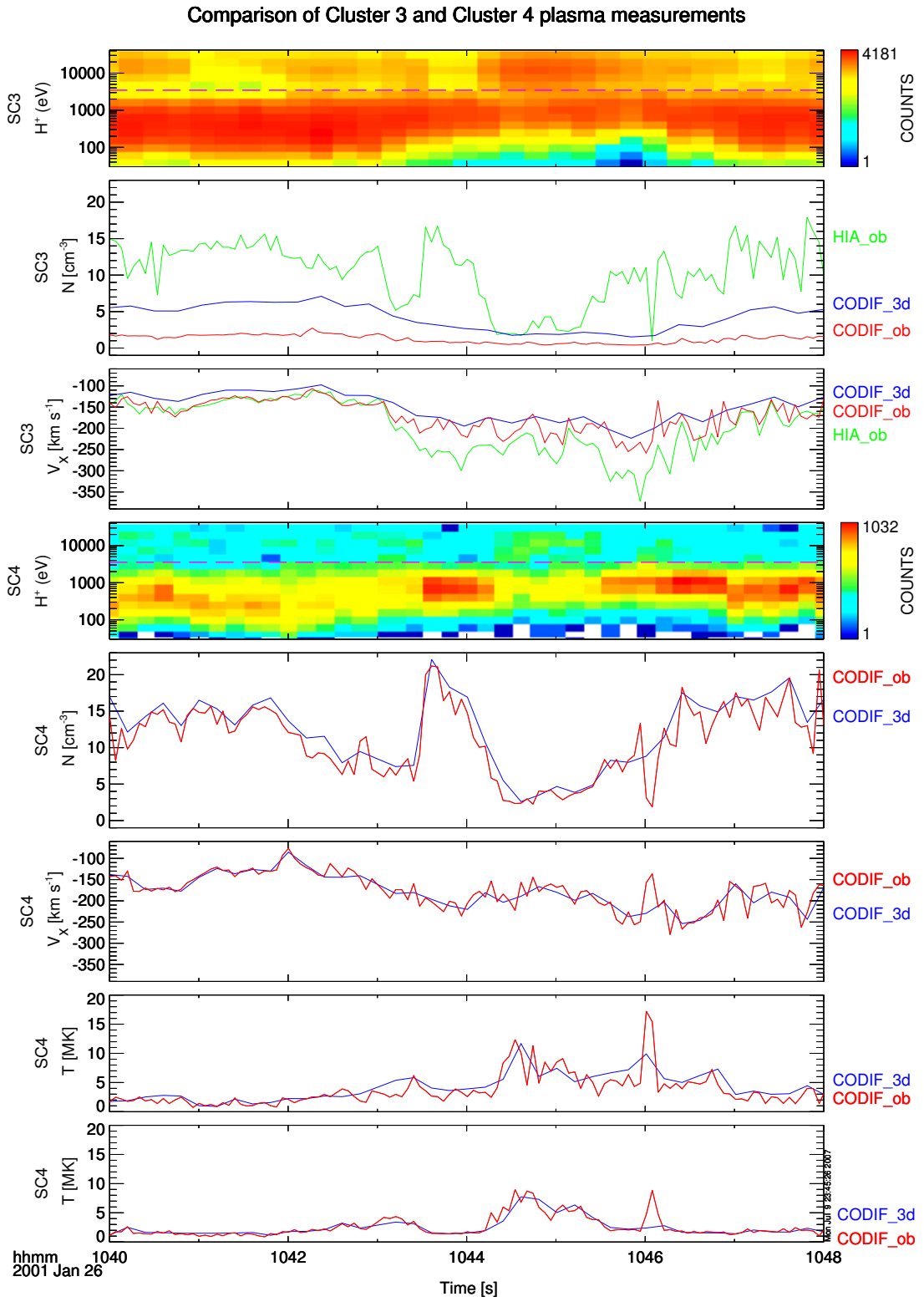

Figure 5.15: Comparison between CODIF measurements on Cluster 3 (first 3 panels) and Cluster 4 (the following five panels) for the 26 January 2001 event. A detailed description of each panel is presented in the text. For Cluster 3 we compare ground (in blue) and on-board (in red) computed CODIF proton number density and velocity GSE x component with similar quantities from HIA (in green). For Cluster 4 we compare ground (in blue) and on-board (in red) CODIF proton number density, velocity GSE x component, parallel and perpendicular temperatures.

reluctant in pursuing a timing analysis. However, as will be shown below, the MP normal direction and normal velocity can be estimated in a convincing way by the use of single spacecraft techniques. We have done this for the transition taking place at 10:43:30 and then, taking into account that a relatively clear identification of the magnetosheath and magnetospheric magnetic levels is possible for that crossing, the crossing duration was computed leading thus to an estimation for the MP thickness. In the remaining of this section we will deal with this transition only.

In Table 5.2 we present the results obtained when various techniques for determining the MP orientation and normal velocity were applied. More precisely, we used the constrained (to $\langle B_n \rangle = 0$) MVAB method (upper part in the table), the constrained (to $\langle B_n \rangle = 0$) MFR technique (in the middle) and deHoffmann-Teller analysis (at the bottom). In the first two columns in that table, the satellites and the intervals of analysis are indicated. The right most

Table 5.2: Results from the constrained MVAB of the magnetic field (upper part, all satellites), constrained MFR and HT analysis (middle and lower part, Cluster 1 and Cluster 3 satellites only). In the text, a description of the table format is given.

Satelite	Interval	constrained (to $\langle B_n \rangle = 0$) nested MVAB				
		$\lambda\ [nT]^2$	n_x	n_y	n_z	
		0.0	0.1322	−0.9476	0.2907	
Cluster1	10:42:52.0 - 10:44:26.5	**44.69**	**0.4755**	**0.3181**	**0.8200**	
		244.68	−0.8694	0.0299	0.4926	
		0.0	0.1179	−0.9457	0.3027	
Cluster2	10:42:50.0 - 10:44:23.0	**44.15**	**0.4717**	**0.3218**	**0.8207**	
		246.29	−0.8735	0.0460	0.4840	
		0.0	0.1545	−0.9445	0.2899	
Cluster3	10:42:47.5 - 10:44:23.0	**40.62**	**0.4804**	**0.3283**	**0.8132**	
		237.84	−0.8632	0.0136	0.5044	
		0.0	0.1096	−0.9417	0.3182	
Cluster4	10:42:35.0 - 10:44:29.5	**27.02**	**0.4851**	**0.3301**	**0.8097**	
		124.88	−0.8675	0.0657	0.4930	
		constrained (to $\langle B_n \rangle = 0$) MFR				
		$\lambda\ [mV/m]^2$	n_x	n_y	n_z	$V_n\ [km/s]$
		0.0	0.0465	−0.9375	0.3449	
Cluster1	10:43:01.0 - 10:44:29.0	**5.40**	**0.4756**	**0.3244**	**0.8177**	50.1
		8.92	−0.8784	0.1260	0.4610	
		0.0	−0.0907	0.9395	−0.3304	
Cluster3	10:42:58.0 - 10:44:22.0	**5.23**	**0.4950**	**0.3304**	**0.8036**	55.6
		9.33	0.8641	−0.0907	−0.4950	
		deHoffmann - Teller analysis				
		slope	*cc*	V_x	V_y	V_z	$V_n\ [km/s]$
Cluster1	10:43:01.0 - 10:44:29.0	1.004	0.985	-246.1	115.5	165.0	55.0
Cluster3	10:42:58.0 - 10:44:22.0	1.005	0.977	-247.1	113.6	168.0	55.2

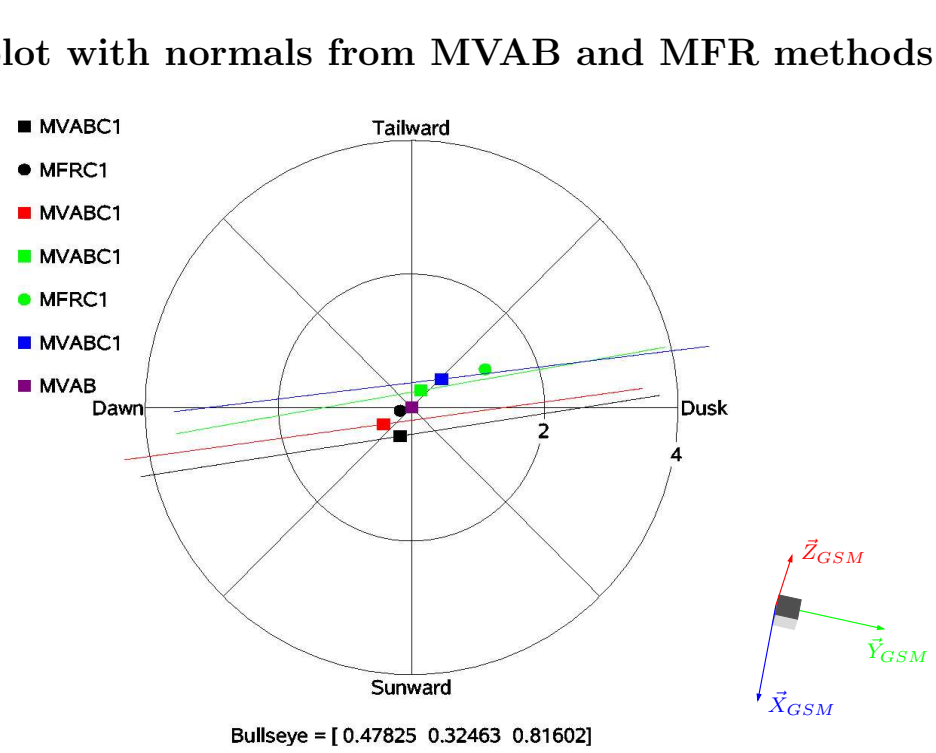

Figure 5.16: Polar plot with the normals obtained from the constrained MVA of the magnetic field (the symbols MVABC1) and by using the constrained MFR technique (the symbols MFRC1; only Cluster 1 and Cluster 3 normals, where HIA measurements are available, are shown). The reference direction in the polar plot is the average orientation of the MVABC1 normals; for these normals also the orientation uncertainties of statistical origin are indicated by the coloured segments. In the lower right corner the orientation of GSM unit vectors in the MP reference frame is shown.

columns contain information specific to each technique as follows: for the MVA method the magnetic variances along the $\langle B \rangle$, minimum and maximum magnetic variance direction (λ column) together with the GSE components of these directions are shown. With bold faces we indicated the predicted MP normals. For MFR technique the first four columns are similar to the ones from the MVA case but we have in addition a column with the values of the inferred MP normal velocity. The columns presenting the results from HT analysis contain the slope and the correlation coefficient of the fit between the electric field $\vec{E}_c = -\vec{v} \times \vec{B}$ and the convection electric field $\vec{E}_{HT} = -\vec{V}_{HT} \times \vec{B}$, the three components of V_{HT} velocity in GSE and the component of this velocity along the MVA normal.

In interpreting the outcome, we show in Figure 5.16 a polar plot with the normals orientation. The reference direction in this plot (magenta square, symbol MVAB) is the average of individual MVAB normals (coloured squares, symbols MVABC1; the accompanying line segments correspond to the orientation uncertainties due to the statistical errors). Note that all normals, including those provided by the constrained MFR method (coloured circles, symbol MFR, shown without the related error segments) have a very similar orientation, their direction being contained within an angular cone of approximately 1° half-width.

The following remarks have to be made

- the constrained MVAB method was applied on 5 nested intervals, for all 4 satellites, the average individual MP normal directions appearing in the table with bold faces. The ratio $\lambda_{max}/\lambda_{int}$ at each spacecraft level is in the range $4.7 \div 5.9$, which is not a satisfactory

result. Nevertheless, taking into account that for all satellites the normal predictions are very close, we concluded that the constrained MVAB technique provides a reliable result for this transition.

- the results from unconstrained MVAB method had to be discarded because the predicted MP normals imply unreasonably high values for the normal magnetic field component (around 23 nT for each satellite).
- the constrained MFR method was applied on Cluster 1 and Cluster 3 data (the only satellites with an operational HIA sensor) making use of the MHD approximation $\vec{E} = -\vec{V} \times \vec{B}$. As in the previous technique, the MP normals are not well identified by the individual satellites ($\lambda_{max}/\lambda_{int} \approx 1.7$) but, nevertheless, the predicted directions are very close to the MVAB normals. Another fact that adds confidence to the results are the very similar values for normal MP velocities obtained by this method and by deHoffmann-Teller analysis (last column in the table).
- The deHoffmann-Teller analysis was also applied on Cluster 1 and Cluster 3 data, using the same time intervals as in the MFR method. A good HT reference frame was obtained in each case (the slope and the correlation coefficient close to unity). The values for the MP normal velocity were determined by projecting the HT velocity on the individual MVAB normals.

Taking the above arguments into account one can say that, although the individual application of the above methods provides results with considerably uncertainties, the consistency of these results lends credence on their validity. Because for the analyzed transition relatively good magnetic levels for the magnetosphere and magnetosheath could be identified, the MP crossing duration could be estimated to be around 29.8 seconds. This results in a MP thickness of roughly 1600 km, much greater than the proton gyro radius (average and maximum values are 50 and, respectively, 59 km for this transition) and the proton inertial length (with the average and maximum values of 85 and, respectively, 105 km). Therefore the use of MHD approximation on treating the protons is well justified.

5.6 Oxygen influence on the Walén test

In this section we will compare the results obtained from the Walén analysis when the presence of the Oxygen ions is neglected (i.e. the standard mode to perform the analysis) with the results obtained when the contribution of this minor species is taken into account. More precisely, for the latter case we will compute in the first instance the centre-of-mass (COM) or uni-fluid ion moments (i.e. density, velocity, parallel and perpendicular temperatures) and apply the Walén test by using these quantities.

Depending on the available plasma detectors on each satellite and on the quality of their measurements, we will use in our study:

- CODIF proton and Oxygen data, in case of Cluster 4. Specifically, we will use the on-board computed moments because they are based on measurements acquired with a higher time, energy and directional resolution (as described in Section 2.2). The on-board processed density, velocity vector, and pressure tensor for each species of interest (i.e. H^+, He^{2+}, He^+ and O^+) are computed for 3 adjacent energy intervals and send continuously to the ground. The highest such energy interval corresponds exactly to the energy interval we used in the preceding section for calculating the 3D (ground based) O^+ moments, i.e. the 5 uppermost energy channels of the distribution function received

at ground. The lower limit of the energy range is indicated by the horizontal dashed lines in Figure 5.15, situated at around 3.5 keV, which is just above the upper limit of the magnetosheath proton population In order to avoid the false counts in the O^+ channels produced by the spillover effect, we will use O^+ on-board moments (and, for comparison, the ground moments as well) corresponding to this upper energy range of the detector[4].

- data from the HIA instrument, where all incident ions are considered protons, and CODIF O^+ data in case of Cluster 1 and Cluster 3. We will use HIA on-board moments, and not the moments computed on ground, because they are based on measurements taken with higher time, energy and angular bin resolution. As for the O^+ information, we will use the ground computed moments, based on CODIF measurements corresponding to the 5 uppermost energy channels (indicated by the horizontal dashed lines in Figure 5.15). In doing that we avoid the spillover effect produced by the magnetosheath protons in the lower energy channels. Moreover, even for the selected energy range we implemented a routine for correcting the spillover effect, using the available documentation about the instrument ground calibration (*Kistler* [2000]). However, we did not find a satisfactory solution to the problem of detector saturation and therefore the measurements we used are still influenced by this effect. Because for the time of the MP crossings investigated by us, the ground based O^+ moments have 32 seconds time resolution, we interpolated them to the time tags of the HIA measurements.

The details about how to combine proton and O^+ moments (Cluster 4), or HIA and O^+ moments (Cluster 1 and 3), in order to obtain the corresponding uni-fluid quantities are described in detail in Appendix H.

Among the multiple MP crossings seen by each satellite during the 26 January 2001 event we selected two transitions, already mentioned at the beginning of the preceding section, having in mind the following aspects:

- a significant change in the O^+ density shown by the plasma detector, from the relatively higher values in the magnetosphere to the lower levels in the magnetosheath.
- the results of the standard Walén test are relatively stable with respect of the analysis interval.

The magnetopause transition around 10:43:30

Figure 5.17 provides a comprehensive picture of the evolution of some important physical quantities for this MP crossing. All data refer to Cluster 4 and therefore the plasma measurements were taken by the CODIF detector. The different panels present:

- the proton differential energy flux spectrogram for the whole energy range of the sensor. As one can see, in this case we have an in-bound transition from the magnetosheath plasma regime to the magnetopause boundary layer region.
- the GSE components of the magnetic field vector. The MP characteristic signature, namely the change in the magnetic field orientation, is clearly seen by the evolution of the x and z components in the interval indicated with vertical dashed lines.
- the GSE components of the proton velocity in blue, green and red (for the x, y and z components respectively). Superposed, we plotted with magenta the corresponding GSE velocity components of the uni-fluid.

[4]We are grateful to Alain Barthe from Centre d'Etude Spatiale des Rayonnements, Toulouse, for providing us the on-board computed plasma density, velocity vector and pressure tensor for protons (corresponding to the entire detector energy range) and O^+ (corresponding to the highest energy range).

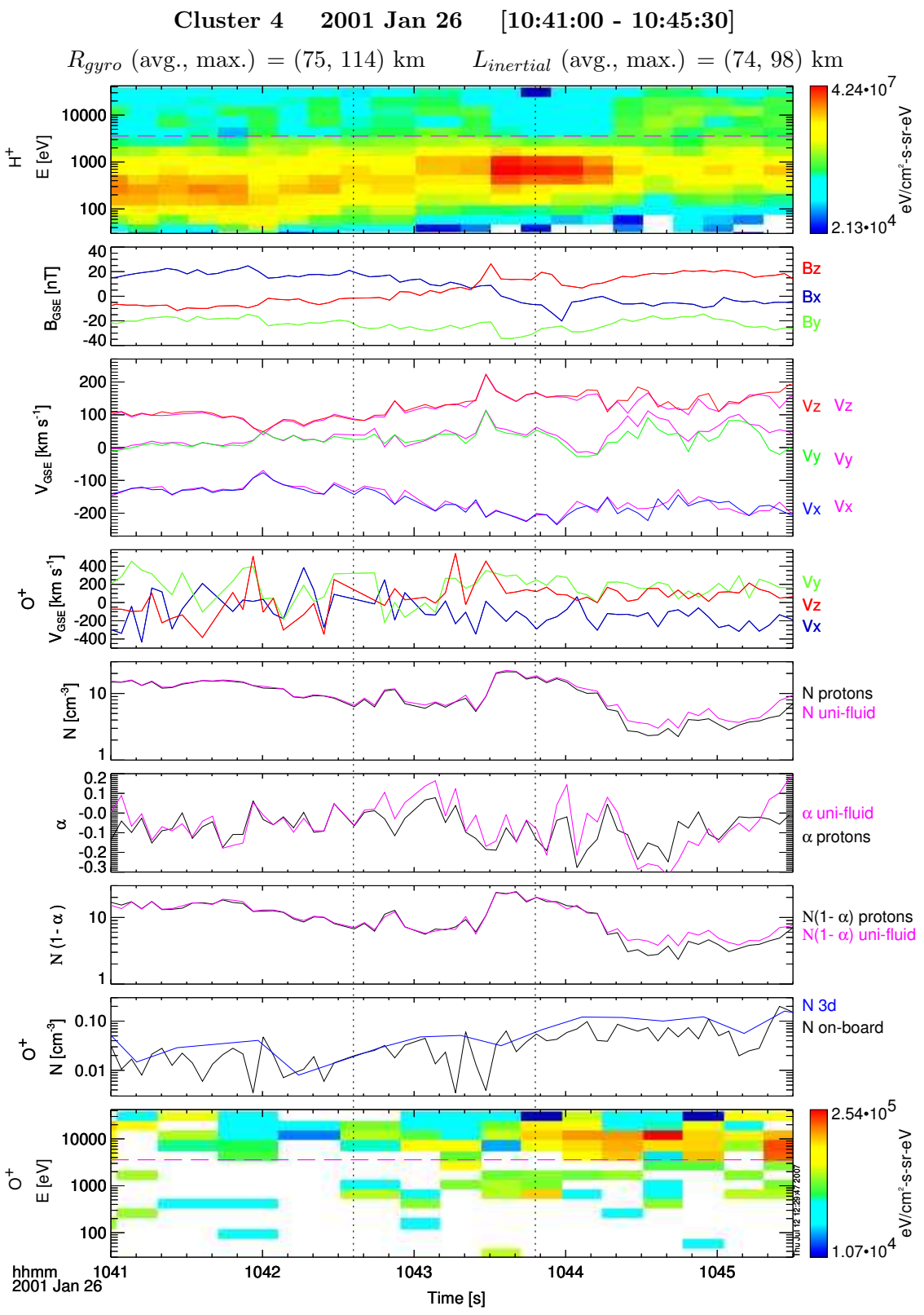

Figure 5.17: FGM and CODIF (proton and Oxygen) measurements as recorded by Cluster 4, corresponding to the first MP crossing analyzed in this section. See the text for a detailed description of all panels. The computed uni-fluid parameters (velocity, density and plasma pressure anisotropy factor) are shown in magenta in the third, fifth and eighth panel respectively.

- the GSE components of the O^+ velocity.
- the number density N for protons (in black) and the for the uni-fluid (in magenta)
- the plasma pressure anisotropy factor α (defined in Section 5.1) for protons (in black) and for the uni-fluid (in magenta). We computed these quantities using the magnetic field orientation for calculating the parallel and perpendicular temperatures, to avoid uncertainties due to the method usually used, i.e. diagonalization of the pressure tensor.
- the evolution of the $N(1-\alpha)$ quantity based on protons (in black) and uni-fluid (in magenta) quantities.
- the O^+ number density calculated on-board (in black) and at ground (in blue) for the higher part of the detector energy range (in accordance with the explanations given at the beginning of this section). The ground computed number density is shown here only to indicate the good agreement between the two ways of obtaining the O^+ moments.
- the O^+ differential energy flux spectrogram for the whole energy range of the sensor. The upper part of the spectra, above the dashed horizontal line, indicates the energy range used in the O^+ moment calculations.

By looking at the fourth and eighth panels from Figure 5.17, we observe that indeed the O^+ number density experiences a significant change across the MP, from around 0.01 particles/cm^3 in the magnetosheath (around 10:42:20) to roughly 0.08 in the magnetosphere (around 10:44:30) whereas the proton number density drops from around 10 particles/cm^3 in the magnetosheath to below 3 at the magnetospheric side of the boundary layer. We also notice that the uni-fluid density and velocity do not differ much from the proton moments in the MP interior. In that region the difference is in the range of a few percent but, as expected, it becomes significant inside the magnetosphere. The biggest change inside the MP is observed in the plasma pressure anisotropy factor.

In table Table 5.3 we present the results of the Walén test for different intervals of analysis. All the intervals have as start time the values in the leftmost column and as stop time the values listed across the top. The black numbers denote the Walén slope in the standard test, whereas the red, cyan and magenta numbers are the Walén slopes obtained when the Oxygen contribution is taken into account. The red numbers were obtained when the 'raw' O^+ on-board moments, i.e. the 4 seconds density, velocity and pressure tensor, were combined with the proton moments. Then, to suppress the role of fluctuations in the measurements, we decided to average the O^+ moments. We used a 'boxcar-smoothing' procedure, with a boxcar width extended over 3 adjacent data points and keeping the original time resolution (4 seconds). The Walén slopes obtained in this case are indicated in Table 5.3 with the small cyan numbers. For comparison, we performed exactly the same calculations by using the 3D, ground computed O^+ moments, corresponding to the highest energy range of the detector (as explained above). The results of this analysis are indicated with the small magenta numbers.

The deHoffmann-Teller correlation coefficient was higher or equal to 0.95 for all the tests. The number of points participating in the analysis for each of the 20 intervals we considered is indicated by the blue numbers. The improvement in the Walén slope is clearly visible when O^+ contribution is taken into account and will be discussed later in this section.

The largest interval appearing in this table is shown in Figure 5.17 by the vertical dashed lines. Also, the proton gyro radius and inertial length for that interval are indicated at the top of the plot. In Figure 5.18 we present the Walén test results corresponding to one of the intervals we examined, when the one-fluid quantities (based on protons and 'raw' O^+ moments) were used in the analysis.

The same transition was investigated by using the Cluster 3 data, with the main difference being that we combined HIA measurements with CODIF O^+ measurements. Therefore in Figure 5.19, which is similar to Figure 5.17, instead of CODIF protons moments we plotted HIA moments. Also, in Table 5.4, similar to Table 5.3, we showed for different intervals the Walén test results based on HIA data (black numbers) and the results obtained when the O^+ information (ground computed moments) was taken into account. Again, the largest interval from that table is indicated in Figure 5.19 with the vertical dashed lines.

By inspecting the numbers appearing in Table 5.4, one sees that the O^+ correction brings practically no improvement, in the sense that the Walén slope does not approach unity. We have arrived at the same conclusion when we used Cluster 1 data in the analysis (not shown). At the end of this section we will give a few reasons that, in our opinion, could explain this outcome.

The magnetopause transition around 11:03:00

A study was carried-out in exactly the same manner for the second MP transition from 26 January 2001 that passed the selection criteria described above. Figure 5.20, containing data acquired by Cluster 4, is similar to Figure 5.17. It describes an out-bound crossing as we can see for example from the decrease in the average protons differential energy flux (first spectrogram, panel 1) and from the drop in the O^+ number density (panel 7). The accompanying Table

Table 5.3: Results from the Walén test using Cluster 4 data corresponding to the first MP transition analyzed in this section. All intervals with start times as listed in the leftmost column and stop times as shown across the top were considered. For each interval we show with black numbers the Walén slope obtained in the standard test (i.e. without taking into account the O^+ influence). The red, cyan and magenta numbers correspond to the Walén slopes obtained when the correction was implemented using the 'raw' on-board moments, averaged on-board moments and 3D ground based moments for the O^+, respectively. In blue we indicated the number of points taking part in each test.

start \ stop	10:43:32		10:43:36		10:43:40		10:43:44		10:43:48	
10:42:36	0.660 0.737 0.748 0.743	14pt	0.602 0.679 0.681 0.696	15pt	0.563 0.633 0.634 0.661	16pt	0.551 0.617 0.618 0.651	17pt	0.517 0.586 0.581 0.618	18pt
10:42:40	0.685 0.769 0.775 0.770	13pt	0.620 0.703 0.700 0.716	14pt	0.576 0.652 0.648 0.677	15pt	0.562 0.633 0.630 0.665	16pt	0.525 0.598 0.589 0.628	17pt
10:42:44	0.646 0.737 0.733 0.733	12pt	0.581 0.670 0.657 0.680	13pt	0.540 0.619 0.608 0.642	14pt	0.528 0.602 0.592 0.633	15pt	0.491 0.567 0.551 0.595	16pt
10:42:48	0.626 0.717 0.695 0.708	11pt	0.557 0.644 0.615 0.650	12pt	0.514 0.592 0.566 0.612	13pt	0.504 0.576 0.552 0.604	14pt	0.465 0.540 0.510 0.565	15pt

5.5 compares, for different intervals of analysis, the Walén test results obtained when the O^+ influence was neglected in the study (black numbers) and when their contribution was considered. The red numbers were obtained by using the 'raw' O^+ on-board moments whereas the cyan numbers correspond to the results obtained when the smoothing procedure was applied to the O^+ moments in the first place. Because the transition is relatively short and only two data points from the 3D ground based moments fall within the interval of analysis, we shall not provide a comparison with the results based on this data.

For this transition we will present no results from the investigations carried-out with data acquired by Cluster 1 and Cluster 3 satellites. The outcome we obtained in these cases was not different from the one shown from the previous transition, namely that practically no change in the Walén test results occurred when the O^+ correction was implemented.

Interpretation of the results

As we can see from Table 5.3 and Table 5.5, based on data acquired by Cluster 4 during the two MP transitions, considering the O^+ contribution results in significant corrections for all intervals. Indeed, a comparison between the black and the red numbers indicates that the Walén slope increases. In case of the first crossing, the improvements range somewhere between 12 - 15 %. For the second transition the improvement was between also 12 - 15 %, however, with one interval showing an increase in the Walén slope of 22.5 %.

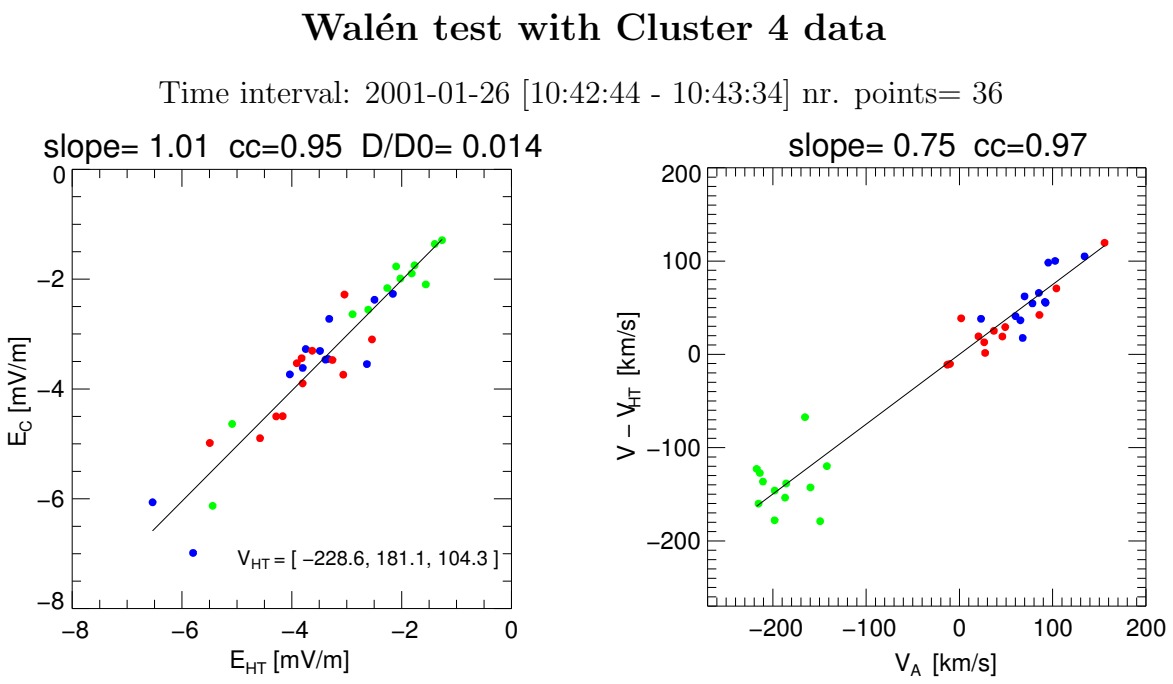

Figure 5.18: Walén analysis using uni-fluid quantities for one of the intervals appearing in Table 5.3. *Left side:* The result from deHoffmann-Teller analysis is shown. The plot presents the fit between the electric field $\vec{E}_c = -\vec{v} \times \vec{B}$ (on ordinate) and the convection electric field $\vec{E}_{HT} = -\vec{V}_{HT} \times \vec{B}$ associated with a time-stationary structure moving with the determined HT velocity (on abscissa). The GSE components of HT velocity are indicated. *Right side:* The fit between the Alfvén velocity components (on abscissa) and the plasma velocity components in the deHoffmann -Teller frame (on ordinate) is shown. In both pictures different components are indicated by different colours.

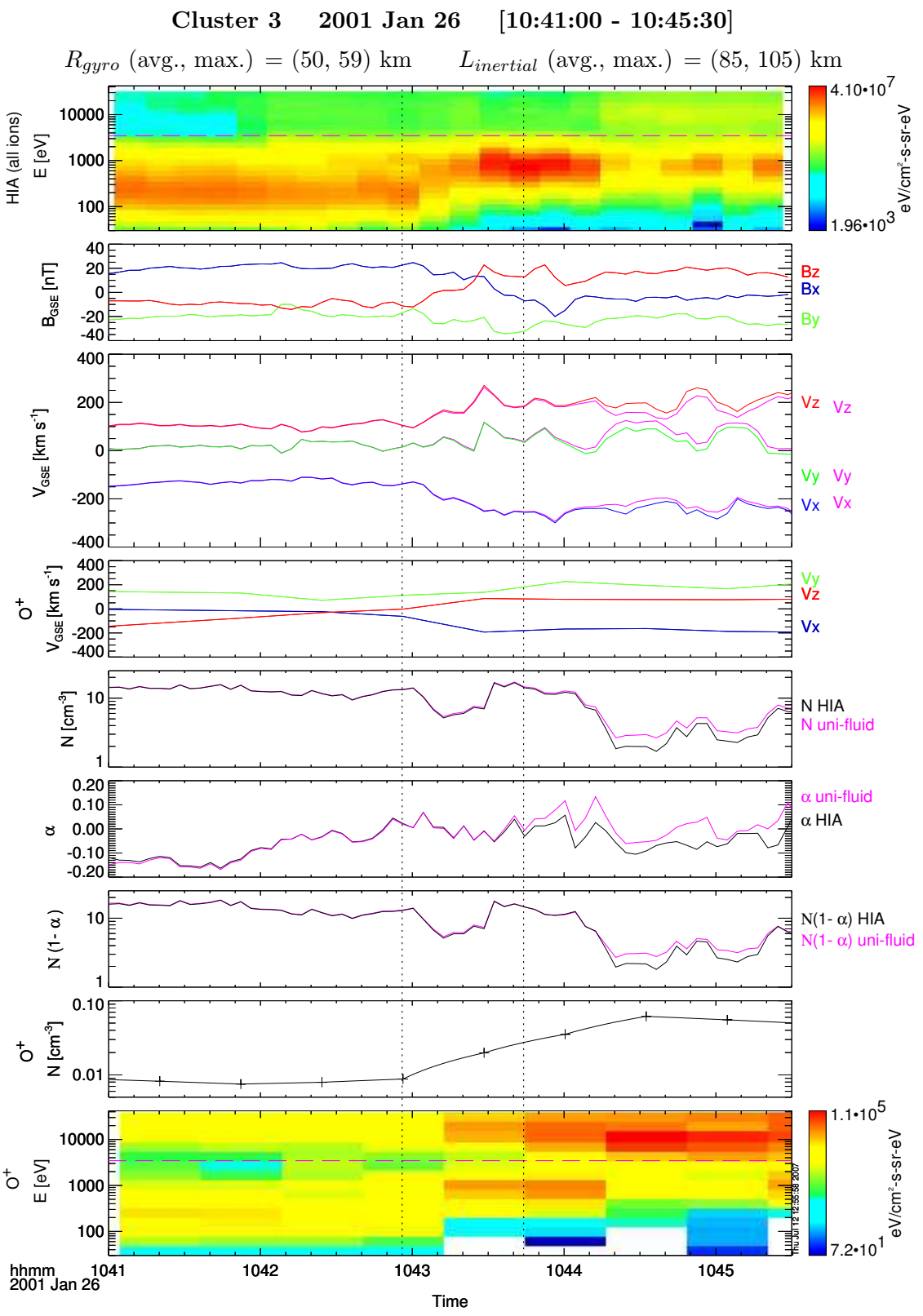

Figure 5.19: FGM, HIA and CODIF Oxygen measurements recorded by Cluster 3, corresponding to the first MP crossing analyzed in this section. See the text for a detailed description of all panels appearing in the figure. The computed uni-fluid parameters (velocity, density and plasma pressure anisotropy factor) are shown in magenta in the third, fifth and eighth panel respectively.

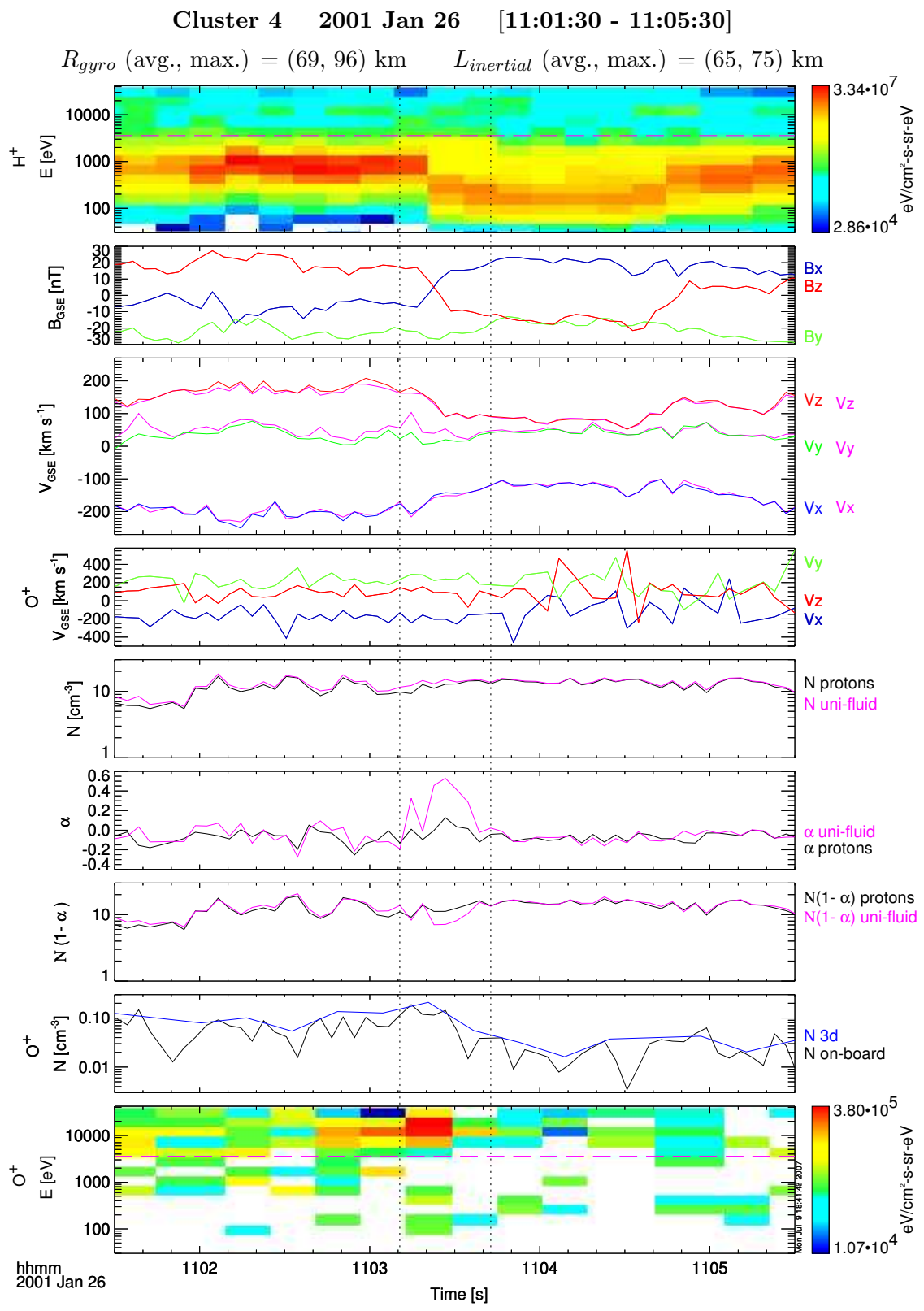

Figure 5.20: FGM and CODIF (proton and Oxygen) measurements as recorded by Cluster 4, corresponding to the second MP crossing analyzed. See the text for a detailed description of all panels appearing in the figure. The computed uni-fluid parameters (velocity, density and plasma pressure anisotropy factor) are shown in magenta in the third, fifth and eighth panel respectively.

Table 5.4: Results from the Walén test using Cluster 3 data corresponding to the first MP transition. All intervals with start times as listed in the leftmost column and stop times as shown across the top were considered. For each interval we show with black numbers the Walén slope obtained in the standard test (i.e. without taking into account the O^+ influence) and with red numbers the same parameter after the O^+ correction was implemented. In blue we indicated the number of points taking part in each test.

start \ stop	10:43:28	10:43:32	10:43:36	10:43:40	10:43:44
10:42:56	0.665 9pt 0.646	0.633 10pt 0.624	0.592 11pt 0.586	0.551 12pt 0.547	0.514 13pt 0.512
10:43:00	0.665 8pt 0.649	0.625 9pt 0.617	0.581 10pt 0.577	0.539 11pt 0.537	0.500 12pt 0.500
10:43:04	0.742 7pt 0.728	0.663 8pt 0.660	0.601 9pt 0.602	0.549 10pt 0.552	0.501 11pt 0.504
10:43:08	0.827 6pt 0.817	0.697 7pt 0.699	0.616 8pt 0.621	0.555 9pt 0.561	0.497 10pt 0.503
10:43:12	0.816 5pt 0.807	0.656 6pt 0.660	0.578 7pt 0.583	0.520 8pt 0.527	0.463 9pt 0.470

Table 5.5: Results from the Walén test using Cluster 4 data corresponding to the second MP transition. All intervals with start times as listed in the leftmost columns and stop times as shown across the top were considered. For each interval we show with black numbers the Walén slope obtained in the standard test (i.e. without taking into account the O^+ influence). The red and cyan numbers correspond to the Walén slopes obtained when the O^+ correction was implemented using the 'raw' on-board moments and averaged on-board moments for the O^+, respectively. In blue we indicated the number of points taking part in each test.

start \ stop	11:03:26	11:03:30	11:03:34	11:03:38	11:03:42
11:03:10	0.527 0.594 5pt 0.552	0.448 0.479 6pt 0.474	0.450 0.488 7pt 0.479	0.441 0.475 8pt 0.468	0.442 0.475 9pt 0.464
11:03:14	0.605 0.741 4pt 0.655	0.501 0.578 5pt 0.544	0.499 0.578 6pt 0.543	0.484 0.554 7pt 0.523	0.481 0.544 8pt 0.511

Because the effect of considering Oxygen ions in the analysis is systematic and because the improvement is relatively big, we do not think that the changes are produced by some fluctuations or error measurements. In fact, practically similar conclusions are obtained when the results based on the smoothed O^+ data (cyan numbers), or when the 3D ground computed O^+ moments are considered (for the second transition, the smoothing procedure had a bigger effect, probably because the duration of this crossing is shorter). In case of the first transition, the Walén slopes increase even when only the O^+ density and velocity information is used, without correcting the plasma pressure anisotropy factor by the minor ion contribution (not shown). As described in the text, we took all the precautions in the study, like using the

best available data, computing the parallel and perpendicular temperatures using the actual magnetic field orientation and choosing intervals of analysis in accordance with the general requirements for experimentally identification of a RD.

Nevertheles, the values of the Walén slope remained significantly below unity, indicated that maybe other causes are responsible for the deviation from the ideal RD model. In this connection one should mention that one such possible cause would be the fact that the O^+ gyro radius was only approximately 3 times smaller than the MP thickness, defined as the interval where 76% of the total magnetic rotation occurred. Therefore, some finite Larmor radius effects are expected to be present in these cases.

In *Puhl-Quinn and Scudder* [2000] a comprehensive study is performed about the influence of minor ions on the Walén test. Using as minor ions He^{2+}, the authors simulated an ideal RD for various parameters characterizing the constituents of the ion mixture like ratio of the number density and relative velocity along the magnetic field. Then, considering that most of the existing plasma detectors - like HIA - do not discriminate between different species (therefore assuming that all ions are protons) they studied how such a miss-assignment is reflected in the result of the Walén test. The conclusion of the study was that, at least in typical plasma regime usually encountered at the MP, the presence of the minor ions could not account entirely for the lower values (i.e. subunitary) of the experimentally determined Walén slope.

As discussed in Section 5.1, the jump conditions for a rotational discontinuity require that the quantity $\rho(1-\alpha)$ (ρ being the plasma density and α the plasma pressure anisotropy factor) should be constant across the transition but the experimental evidence does not support this (see the event discussed in Section 5.4). From Figure 5.17 one can clearly see that by considering the O^+ influence the situation did not improve. Again, the evolution in plasma density dictates the trend in $\rho(1-\alpha)$, as if α plays no significant role. Note also that we did not use this relation when applying the Walén tests.

When performing the study by using data from Cluster 1 or Cluster 3, the results from Table 5.4 show that practically no change in the values of the Walén slope was achieved. Below we present a few reasons that in our opinion could explain this outcome:

- the CODIF sensors on both Cluster 1 and Cluster 3 were saturated, as shown in Section 5.5 (see the discussions related to Figure 5.15). This means that not all O^+ particles were detected, leading to an underestimation of the correction terms for the quantities entering the Walén relation.
- usually when one combines measurements from different instruments (HIA and CODIF in our case), uncertainties appear due to the intercalibration aspect.
- the 32 seconds time resolution of the O^+ distribution function, available from CODIF for this transition and used for moment computation at ground, is too low when compared with the length of the analyzed intervals.

5.7 Observations about the Oxygen at the magnetopause

In addition to the effect of influencing the result of the Walén test discussed in Section 5.6, there are other noteworthy aspects about the observed O^+ near the MP that we will discuss in the present section, based upon Cluster 4 measurements on 26 January 2001.

Looking at the second and fourth panels of Figure 5.17, one can notice a certain correlation between the change in magnetic field direction and in the direction of the O^+ bulk velocity at the MP. This synchronous rotation of the two vectors is similar with what we expect to

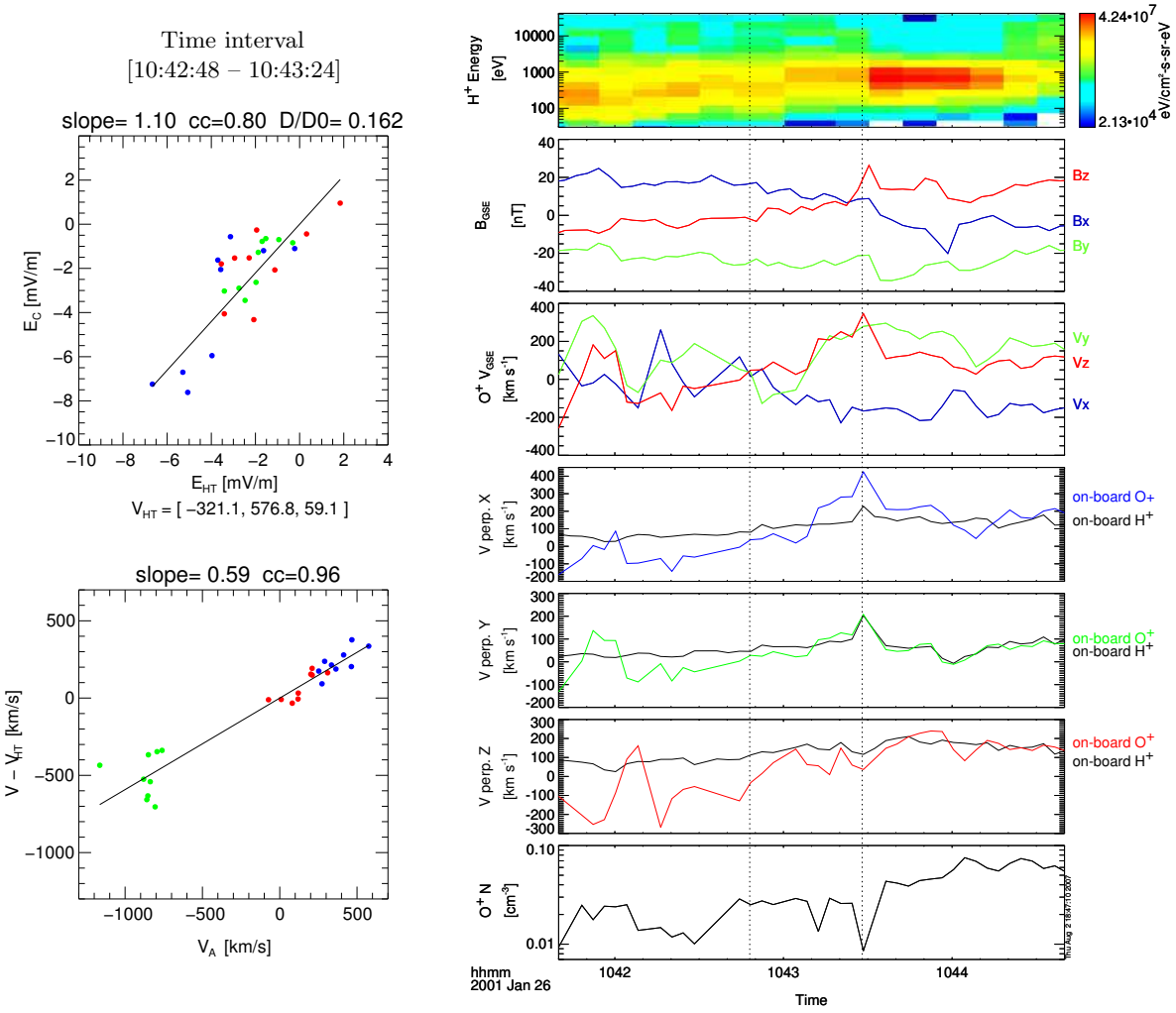

Figure 5.21: *Right part:* The first three panels, from top to bottom we present the proton differential energy flux, magnetic field, O^+ velocity in GSE. The next three panels present the x, y and z GSE components of the O^+ (in colour) and protons (in black) velocities perpendicular to the magnetic field. The bottom panel shows the O^+ number density. *Left part:* The deHoffmann-Teller and Walén plots are presented for the time interval [10:42:48 - 10:43:24]. The format in the same as in Figure 5.8.

happen for a RD between the plasma COM velocity and the magnetic field. Therefore we decided to investigate whether also the O^+ component obeys individually a kind of Walén relation. We recall here that no such relation is prescribed in the general theory of the RD, where all concepts (deHoffmann-Teller frame, Alfvén velocity etc.) and quantities refer to the uni-fluid (see Section 5.1).

In the right part of Figures 5.21 and 5.22 we present the evolution of some physical parameters referring to the two MP transitions studied in the preceding section. From top to bottom, we have:

- the proton differential energy flux spectrogram.
- the GSE components of the magnetic field vector.

- the GSE components of the O^+ velocity. Throughtout this section we will use only the averaged on-board O^+ moments, obtained according to the procedure we already described in Section 5.6.
- in the next three panels we show the GSE components (x, y and z in blue, green and red traces, respectively) of the O^+ velocity perpendicular to the magnetic field, i.e. the components of the vector $\vec{V}_{perp}^{ox} = \vec{V}_{ox} \times \vec{b}$, where $\vec{V}_{ox}$ designates the O^+ velocity vector and $\vec{b}$ a unit vector oriented along the magnetic field. Superposed, with black traces in each panel, we show the GSE components of the proton velocity perpendicular to the magnetic field, i.e. the components of the vector $\vec{V}_{perp}^{pr} = \vec{V}_{pr} \times \vec{b}$, where $\vec{V}_{pr}$ designates the proton velocity vector.
- the last panel presents the O^+ number density.

For an ideal RD, the velocity of all plasma constituents (protons, electrons and minor ion species) perpendicular to the magnetic field should be the same in the asymptotic adjacent regions, because all the particles are experiencing the same electric drift, with velocity $(\vec{E} \times \vec{B})/B^2$. By inspecting the panels 4, 5 and 6 from Figures 5.21 and 5.22, comparing the GSE components of protons and O^+ perpendicular velocities, we can see that this requirement is approximately fulfilled in the magnetosphere region (to the right in Figure 5.21 and to the felt in Figure 5.22) but not so much in the magnetosheath. A possible explanation for the relatively large differences observed in the latter region could be ascribed to the low O^+ concentration, below the CODIF reliability threshold.

In the MP region itself (identified as the region of magnetic field rotation), one notices also relatively large differences between the O^+ and proton perpendicular velocities, the disagreement between the two having a bipolar aspect. This is better seen in the fourth panels, where the blue traces indicate higher values for the x GSE component of O^+ perpendicular velocity on the magnetospheric side and lower values on the magnetosheath side. The explanation for this behaviour deserves further investigation; possibly the finite gyro radius aspect for the O^+ component plays a role.

Table 5.6: Results from the Walén and HT analyses using O^+ Cluster 4 data corresponding to the first MP transition. All intervals with start times as listed in the leftmost columns and stop times as shown across the top were considered. For each interval we show with black numbers the Walén slope and correlation coefficient (black numbers), the deHoffmann-Teller slope and correlation coefficient (red numbers) and the deHoffmann-Teller GSE velocity components (in blue). The largest interval appearing in this table is indicated in the right part of Figure 5.21 by the vertical dashed lines.

start \ stop	10:43:20	10:43:24	10:43:28	quantity
10:42:48	0.61 0.96	0.59 0.96	0.50 0.92	Walén (slope, cc)
	1.13 0.76	1.10 0.80	1.05 0.90	HofTel (slope, cc)
	[-330.9, 583.9, 56.4]	[-321.1, 576.8, 59.1]	[-316.0, 573.8, 59.7]	$\vec{V}_{HT}$ in GSE
10:42:52	0.82 0.97	0.73 0.97	0.53 0.92	Walén (slope, cc)
	1.11 0.75	1.09 0.79	1.05 0.90	HofTel (slope, cc)
	[-405.5, 770.8, 22.9]	[-368.6, 702.6, 32.6]	[-328.9, 615.1, 45.9]	$\vec{V}_{HT}$ in GSE
10:42:56	1.08 0.98	0.82 0.98	0.50 0.93	Walén (slope, cc)
	1.10 0.75	1.09 0.78	1.05 0.89	HofTel (slope, cc)
	[-508.9, 1054.4, -27.9]	[-409.0, 826.2, 7.6]	[-329.4, 630.0, 43.1]	$\vec{V}_{HT}$ in GSE

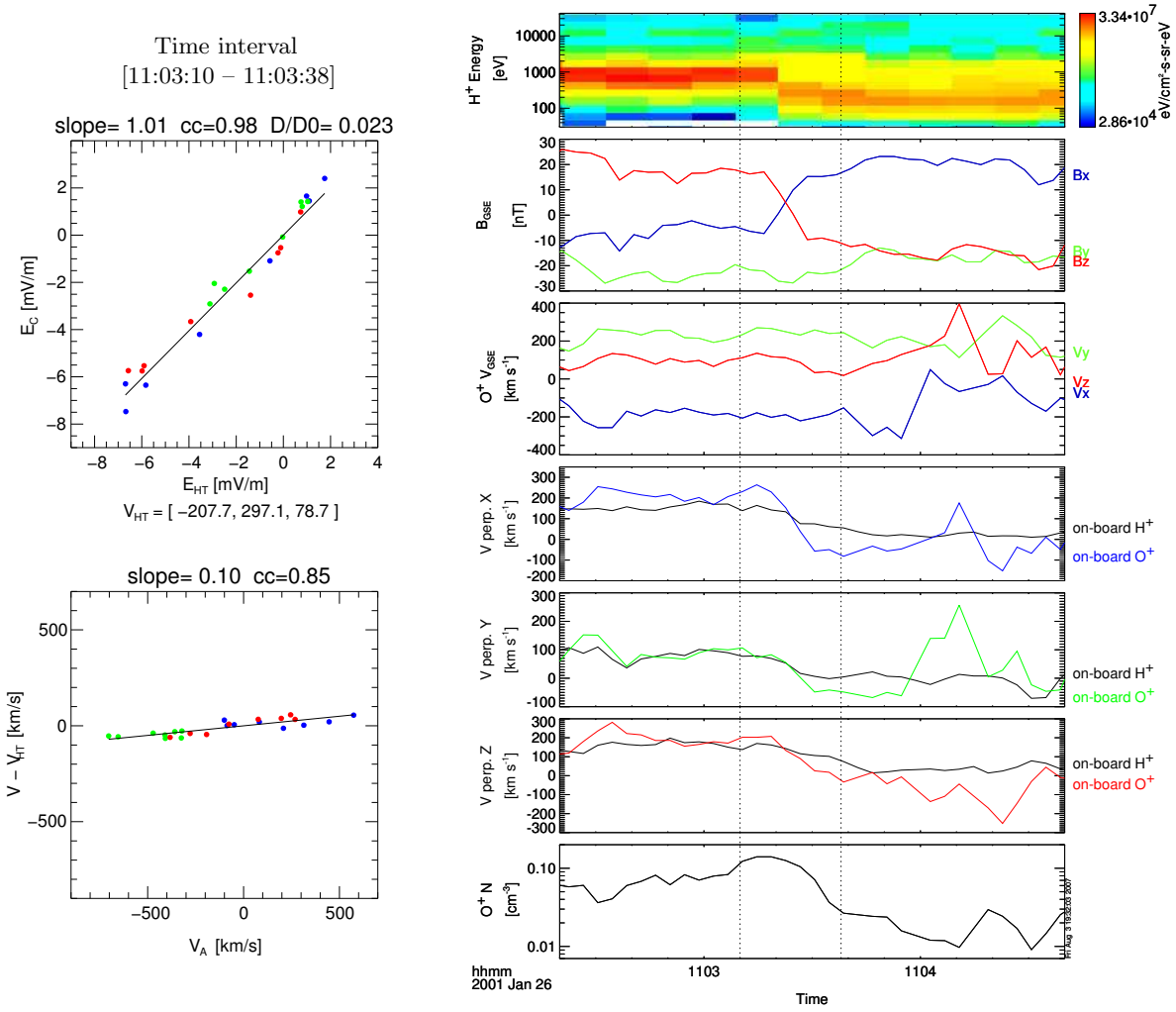

Figure 5.22: *Right part:* The first three panels, from top to bottom we present the proton differential energy flux, magnetic field, O^+ velocity in GSE. The next three panels present the x, y and z GSE components of the O^+ (in colour) and protons (in black) velocities perpendicular to the magnetic field. The bottom panel shows the O^+ number density. *Left part:* The deHoffmann-Teller and Walén plots are presented for the time interval [11:03:10 - 11:03:38]. The format in the same as in Figure 5.8.

In Table 5.6 we present the results of the Walén and deHoffmann-Teller analyses performed with the O^+ moments, using intervals belonging to the first MP transition. All the intervals having start times listed in the leftmost column and stop times as shown across the top line were considered. In each case we show the Walén slope and correlation coefficient (black numbers), the deHoffmann-Teller slope and correlation coefficient (red numbers) and the deHoffmann-Teller GSE velocity components (in blue). The largest interval appearing in this table is indicated in the right part of Figure 5.21 by the vertical dashed lines.

In the left part of the same figure we plotted the results of the Walén and deHoffmann-Teller analysis corresponding to the [10:42:48 - 10:43:24] time period (we used the same format as in Figure 5.8). In what follows we will analyse only this interval but the same type of behaviour was observed for other intervals belonging to this transition.

As the upper left plot from Figure 5.21 shows, the identification of the HT frame was not as good, with a correlation coefficient of only 0.8 and the slope of 1.10. The large value of the D/D_0 parameter, indicates that a significant part of the electric field in the GSE frame was not transformed away when going to the HT frame. Nevertheless, as the lower left plot shows, the Walén analysis based on O^+ indicate a clear correlation between the velocity in HT frame and the Alfvén velocity (the correlation coefficient was 0.96 and the Walén slope was 0.59). The data points corresponding to different components are distributed more ore less along the regression line, showing a fairly convincing large excursion along that line.

We performed a similar study by imposing from exterior a deHoffmann - Teller transformation with the velocity found in the uni-fluid analysis. For example, for the same interval we found in the previous section a HT velocity of [-189.4, 97.2, 111.6] km/s in GSE. In this reference frame the whole aspect of the Walén and HT plots change, showing no characteristics which we usually attributed to a RD (e.g the HT correlation coefficient was 0.3 and the Walén slope 0.08, with many points situated far from the regression line).

Figure 5.22, referring to the second transition, shows a different situation. From the right-hand panel we see that at the MP there is no correlation between the change in magnetic field direction and the O^+ velocity vector. For all of the intervals belonging to this transition, the Walén analysis based on O^+ indicates a small slope, typically ~ 0.1 or below. But, on the other hand, in the deHoffmann-Teller analysis a good transformation was found for all analyzed intervals. As an example, we present in the left part of the figure the Walén and HT plots corresponding to the [11:03:10 - 11:03:38] time period (indicated with the vertical dashed lines on right-hand panel). One can see that the obtained correlation coefficient and the slope of the regression line (0.98 and 1.01, respectively) are close to the ideal values of 1.

We have so far no explanation for the facts presented in this section. As said earlier, in the general theory of the RD the concepts of Alfvén velocity and of deHoffmann-Teller frame refer to the centre-of-mass quantities and there are no specific requirements in this sense for the individual fluid components. Why and under which conditions minor ions show this behaviour needs further investigation.

CHAPTER 6

Conclusions

In this chapter we shall summarise the conclusions at which we arrived in this thesis. Details about the arguments supporting these conclusions were given in the thesis, at the locations where each particular aspect was discussed.

A new technique for determining the crossing parameters of a non-planar MP
Almost all methods used in inferring the macroscopic characteristics of the magnetopause assume a planar geometry for this boundary and consider that all physical quantities vary only along the normal direction. In the first part of this thesis we developed a new technique, designed to deal with the more realistic situation when the MP behaves like a 2-D, non-planar discontinuity, and we applied this new technique on one test case.

A non-planarity may occur at the MP due to the presence of a local bulge or indentation, or when a large amplitude wave is travelling along that surface. We recognize a 2-D, non-planar MP in Cluster data when the single-spacecraft techniques provide different orientations for the MP normal at each satellite but all these normals are roughly contained in the same plane. The analysis of a MP crossing by Cluster on 24 June 2003 indicates this type of behaviour. Between the individual normals provided by the (constrained to $\langle B_n \rangle = 0$) MVAB technique, the difference in orientation is about 13° while all these normals lie within 0.7° from a plane situated in between (i.e from what we called the *plane of the normals* in Section 3.4). A similar conclusion was obtained based on the results provided by the (constrained to $\langle B_n \rangle = 0$) MFR technique (see Subsection 4.3.2): although the electric field data have a lesser quality for the analysed event, the individual MFR normals lie within 5° from the plane of the normals. These results, together with the fact that the existing planar timing techniques provided a MP normal well apart from the individual normals, allowed us to conclude that the planar assumption is not valid and that actually the MP behaves like a 2-D, non-planar discontinuity in the analysed case.

As a consequence, we proposed a 2-D, non-planar model for the MP that assumes either a parabolic or a cylindrical shape for this layer. The 2-D assumption means that the layer does not change its shape perpendicular to the plane of the normals (i.e. along what we called the invariant direction). We also assumed a constant thickness for the MP. How valid this latter

assumption is depends on the particular case under investigation: nevertheless it has some justification because, contrary to the MP velocity and orientation, the MP thickness is not expected to vary under pressure imbalance. In the proposed model the MP is allowed to move in the plane of the normals either along one direction or along two mutually perpendicular directions. Along the third direction, perpendicular to the plane of the normals, any motion has no physical significance because it introduces no changes. In this way one can describe two features of the non-planar MP: its 'normal' (i.e radial) motion caused by any pressure imbalance across the discontinuity, and, by allowing for a second degree of freedom, the large-scale waves travelling along that surface.

In the first approach, we proposed a procedure for determining the MP crossing parameters that relies only on the timing information, i.e. on the times when each of the four Cluster satellites detects the MP leading and trailing edges. A system of eight equations was established, allowing us to obtain the parameters of the model. These are: the direction of the MP movement (an angle in the plane of the normals), the MP radius of curvature (in the cylindrical case) or the parabolic coefficient (in the parabolic case), the magnetopause thickness, the initial position of the MP (two coordinates in the plane of the normals) and three coefficients that describe the MP velocity-time dependence, which is assumed to be polynomial.

In the second approach, we improved the method by incorporating in the algorithm the requirement of minimum normal magnetic field variance. The reason why this improvement was possible is because in our 2-D model for the MP the direction of the MP movement is fully prescribed by an angle in the plane of the normals. Therefore, we can impose from the very beginning different values for this quantity in the range $[-\pi, \pi]$, and solve the system of eight equations under this condition. For each angle (i.e for each direction of the MP movement), we obtain one solution and we can compute the magnetic variance along the normal of this surface for each satellite. Finally we select that direction of the MP movement for which the *global* normal magnetic field variance is minimum (see Section B.5).

The solution obtained in that way has two advantages: on the one hand, it combines in a self-consistent way the timing information with the requirement of minimum normal magnetic variance. On the other hand, in the improved version of the method, we can use four (instead of three) coefficients to characterize the MP velocity time-dependence, resulting in a better description of the MP motion. This is possible because the direction of MP movement is now determined from an additional condition, and not from the system of equations.

When applying to our test case the different implementations of the new method (parabolic or cylindrical geometry, one or two degrees of freedom, plain timing-analysis or the optimized, timing-MVAB analysis) we obtained eight distinct solutions. In the parabolic case the solutions were obtained algebraically, whereas in the cylindrical model we solved the system of timing conditions by using numerical algorithms.

Two of the solutions, namely Prbl_2deg_TA and Cyl_1deg_TA (see the nomenclature introduced in Section 4.2), have to be abandoned because, although mathematically correct, they do not offer a satisfactory description of the MP crossing parameters for the analysed event. The remaining six solutions were consistent and stable (see Appendix D). Based on the values obtained for the MP velocity, thickness and radius of curvature, these solutions were classified in three groups. For the solutions belonging to the first such group (i.e. for Prbl_2deg_OpTA, Cyl_2deg_TA and Cyl_2deg_OpTA_solA) we obtained the lowest values for the global normal magnetic variance but we also need to limit their range of validity in order to avoid an artificial return in the MP of the first pairs of satellites. The second group, consisting of solutions Prbl_1deg_OpTA and Cyl_1deg_OpTA imply a unidirectional displacement of the MP (one degree of freedom). The remaining solution, i.e. Cyl_2deg_OpTA_solB implies a back and forth

tangential MP movement whereas the movement along the 'normal' (i.e radial) direction is with constant velocity.

We have compared the results obtained in the various implementations of the method designed for a 2-D, non-planar MP, with the results provided by the planar, single-spacecraft methods of MVAB, MFR and deHoffmann-Teller. In Appendix E we compared the global magnetic field variance along the instantaneous (geometrical) normals provided by the 2-D method (more precisely by the mixed timing-MVAB implementations) with the similar quantity based on the normals obtained from the planar MVAB technique. In the former case, depending on the particular implementation, the value of the global normal magnetic field variance was lower or approximately the same as in the planar case, when only data from the central intervals $[\, T_{ci} - \tau_i,\ T_{ci} + \tau_i \,]$ were considered in the analysis. The global normal magnetic field variance based on the result provided by the planar nested MVAB technique (i.e., according to the standard way of obtaining MP normals in the planar assumption) is systematically higher than in the case of the 2-D solutions. Considering these facts we concluded that the 2-D method performs 'better' than the planar method from MVAB point of view.

We arrived at similar conclusions (see Section 4.4) when we compared the Faraday residue computed based on the instantaneous MP velocities and normal directions obtained with the 2-D method, with the same quantity computed from the parameters provided by planar MFR technique. As for the comparison with the result provided by the deHoffmann-Teller analysis, despite a good identification of a HT frame for each satellite transition, this technique gives in case of Cluster 4 and Cluster 3 negative values for the MP velocity along the normals obtained in the planar, nested MVAB analysis. This result is inconsistent with the inbound crossing event we are analysing.

There is another strong argument in favour of 2-D method: in the single-spacecraft techniques, the estimated individual normal directions and velocities are, per definition, decoupled from each other. This is because we are using the measurements recorded by each satellite separately. In the 2-D method however, we are looking for a global solution. The data from all four spacecraft are simultaneously participating in the analysis and the MP normal directions and velocities at each satellite are linked all the time through the geometry and through the motion we determine in the analysis. This provides a more realistic solution for the MP orientation and motion.

Turning to the physics underlying the observed behaviour of the magnetopause, we have provided strong evidence that the 2-D MP feature, inferred from the Cluster measurements for the crossing on 24 June 2003, was produced by the Kelvin - Helmholtz mechanism (producing 'wind over water' type waves). It was shown that the flow shear across the MP was relatively large (more that 350 km/sec) and roughly contained in the plane of the normals. The method developed in the thesis provides a new powerful tool to study the characteristic of such surface waves, i.e. their wavelength and frequency. For example, by considering the parabolic model and allowing for two degrees of freedom in the magnetopause movement, we obtained a wavelength of ~ 8 Earth radii and a period of $\sim 10-11$ minutes in the analyzed case. The tangential velocity, oriented perpendicular to the invariant direction was ~ 80 km/sec. (see Section 4.4).

Observation of magnetic reconnection at the magnetopause

In the second part of this thesis we studied the so called Walén test, which has been developed in the past to identify whether or not the MP behaves like a rotational discontinuity (RD) for one particular transition. The MP becomes an RD if the phenomenon called magnetic reconnection

is acting at the MP. The Walén relation combines in one single expression the conservation of the normal mass flux, of the tangential electric field and of the tangential momentum across the discontinuity. According to this relation, the plasma velocity in a particular frame of reference (the so-called deHoffmann-Teller frame, the existence of which has to be first established) should be equal to the local Alfvén velocity.

The Walén test has proven very successful in deciding whether a discontinuity has rotational character or not, but a long standing issue remains, namely that in experimental data the factor of proportionality between the plasma velocity and the Alfvén velocity is usually less than the ideal value of one. Typical values obtained are around 0.6 to 0.8. This discrepancy might have an explanation in the fact that, when we performed the Walén test we are usually relying on some simplifying assumptions.

The main assumptions are the following:

- the MP is a planar, time-stationary discontinuity.
- the plasma can be treated as a fluid, for which $\vec{E} + \vec{v} \times \vec{B} = 0$
- when performing the Walén test, instead of using the plasma centre of mass (COM) moments as is required by the theory, we may use the proton moments (i.e. the proton density, velocity and temperatures).

When we perform the Walén test in this way we actually neglect two aspects. Firstly, we neglect the role of electrons in the analysis; their contribution brings corrections to the $\vec{E} + \vec{v} \times \vec{B} = 0$ relation, mainly through the effect of electric currents that flow perpendicular to the magnetic field (i.e. through the $\vec{J} \times \vec{B}$ term appearing in the generalized Ohm's law (5.15) from Section 5.2). Secondly, we consider that all the ions are protons. In the MP environment this is usually justified, because the relative abundance of protons is close to 100 %. Nevertheless, sometimes minor ion species like He^+, He^{2+} or O^+ may be present that could significantly change the values of plasma moments.

In the thesis we studied the effects described in the last paragraph by carefully analysing two MP events by Cluster. In these two events we provided evidence that the other simplifying assumptions are well justified (i.e. that the MP behaved like a planar, time-stationary rotational discontinuity, and that the magnetohydrodynamic treatment was justified because the MP thickness was found to be much greater than the ion gyro-radius and ion inertial length).

It is known that obtaining reliable electron moments in the space plasma environment is a difficult task. The electron measurements are heavily affected by the presence of photoelectrons, produced by the solar radiation incident on the spacecraft surface. Also, the electron bulk velocity is small (compared to their thermal velocity) and consequently much affected by the error in the measurements. Therefore in the first event, we estimate the electron quantities in an indirect way. Having established that no ions other than protons were involved in this case, it follows from the charge neutrality condition that the electron density should equal the (measured) ion density. Knowing the density, and having determined the electric current density (from applying Ampère's law to the magnetic field measurements at the four Cluster satellites), one can determine the difference between electron and ion bulk velocities. Since the ion velocity is measured, the electron velocity then follows. This allowed us to assess the contributions from electrons in the Walén test, concluding that it is of second order. Indeed, the improvement in the Walén factor of proportionality was around 8%, from 0.60 to 0.65 in case of Cluster 1 and around 5%, from 0.81 to 0.85 in case of Cluster 3.

For the second event, the large content of O^+, originating at the ionosphere, and the appropriate instrument mode allowed us to study the influence of minor ions on the Walén relation. The detected relative abundance of O^+ ions was around 1% in number density;

considering that these ions are 16 times heavier than the protons, we may expect a significant effect on the COM moments.

We investigated two magnetopause transitions belonging to the second reconnection event. In both cases, by using the corrected moments - and not simply the proton moments as in the standard procedure - in the Walén test, we found an improvement in the outcome. The factor of proportionality increased by between 12 - 15 %, with one interval showing an increase of even 22.5 %, to 0.74, and thus becoming closer to one. We may conclude that, in general, the influence of minor ions is small, but in case of rare events, like the one investigated in the thesis having a large O^+ presence, their influence could be an important factor in establishing whether one discontinuity is rotational or not.

Importantly, the two simplifying assumptions studied in the thesis cannot fully explain the sub-unitary constant of proportionality between the plasma flow velocity and the local Alfvén velocity, although they offer partial answers in the right direction. Other aspects should be considered and this is a still open question in the problem of identifying a rotational discontinuity at the MP.

In the thesis another important open issue related as well to the identification of a RD was investigated. For such a discontinuity, besides the Walén relation, we have the relation $\rho(1-\alpha) = const$, i.e. a balance between changes in the plasma mass density and in the pressure anisotropy factor, being based on the same conservation laws. The reconnection event from 14 March 2002 is almost ideally suited to experimentally check this relation. However, despite the strong evidence that the magnetopause behaves like a thick, planar and stationary discontinuity for that transition, the quantity $\rho(1-\alpha)$ proved to be not constant across the discontinuity. In fact, we provided arguments that this experimental invalidation seems not to be a peculiarity of the transition in question, but a more general result; as discussed in Section 5.4, the way the quantities α and ρ vary at the MP makes the realisation of $\rho(1-\alpha) = const$ improbable. An even more baffling aspect is the following: when we use a variant of the Walén relation that incorporates the $\rho(1-\alpha) = const$ relation (therefore assuming its validity), we typically obtain better results in the test. In our particular case the factor of proportionality in the Walén test has improved by around 23 %, to 0.84.

In case of the second reconnection event, the large content of O^+ particles allowed us to make another interesting observation. A correlation between the change in magnetic field direction and in the direction of the O^+ bulk velocity at the magnetopause was noticed, similar with what we expect to happen for a RD between the plasma velocity and the magnetic field. When performing a Walén test by using only O^+ quantities, the data clearly indicate a correlation between the O^+ velocity in the (O^+ based) HT frame and the (O^+ based) Alfvén velocity, although the identification of the HT frame was not as good. No such relation is prescribed in the general theory of the rotational discontinuity, where all concepts (deHoffmann-Teller frame, Alfvén velocity etc.) and quantities refer to the COM fluid.

Thus the experimental findings on magnetic reconnection reported in this thesis appear to require a re-evaluation of the underlying theoretical description.

Appendices

APPENDIX A

Minimum variance analysis

The first technique to address the problem of MP orientation (applicable also to any other plasma discontinuity), and to establish in this way whether the data recorded during the crossing of this boundary implies a non-zero normal magnetic component or not, was the minimum variance analysis of the magnetic field (MVAB), proposed by *Sonnerup and Cahill* [1967]. In this appendix we will present the MVAB technique following the description given in the review article from *Sonnerup and Scheible* [1998].

The method is based on the absence of magnetic poles law, $\nabla \vec{B} = 0$, using measurements acquired by a single spacecraft not only on the two sides of the discontinuity but also within it. A planar geometry is assumed, as well as that all physical quantities vary only along the normal direction. In these conditions we have

$$\nabla \vec{B} = \partial B_z / \partial z = 0$$

in a (x, y, z) Cartesian reference frame with the $\vec{z}$ axis oriented along the discontinuity normal. Therefore, B_z is independent of z. Also, the z component of the Faraday's law gives

$$\frac{\partial E_x}{\partial y} - \frac{\partial E_y}{\partial x} = -\partial B_z / \partial t = 0$$

meaning that, with the assumptions we made, the spacecraft will see all the time a constant component along the normal direction. Consequently, given the measurements recorded during a discontinuity traversal, the MVAB algorithm searches for the direction of minimum magnetic variance and associates it with the normal direction.

Lets consider a set of experimental data, consisting of magnetic field data $\vec{B}^{(k)}$ corresponding to K points of measurements $k = 1, 2 \ldots K$. The direction of the unit vector $\vec{n}$, designating the MP normal, is determined by minimizing the quantity

$$\sigma^2 = \frac{1}{K} \sum_{k=1}^{K} \left| \left(\vec{B}^{(k)} - \langle \vec{B} \rangle \right) \cdot \vec{n} \right|^2 \tag{A.1}$$

performed with the condition that $|\vec{n}|^2 = n_x^2 + n_y^2 + n_z^2 = 1$. In (A.1) by $\langle \cdots \rangle$ we indicate the average of a given quantity over the set of K points of measurements, i.e.

$$\langle \vec{B} \rangle = \frac{1}{K} \sum_{k=1}^{K} \vec{B}^{(k)}$$

Therefore σ, called magnetic variance, is a measure of the magnetic field fluctuation from its mean value $\langle \vec{B} \rangle$.

In *Sonnerup and Scheible* [1998] a solution of this problem was obtained by using the Lagrange multiplier method. If we define the magnetic variance matrix M^B, having the elements given by

$$M_{ij}^B = \langle B_i B_j \rangle - \langle B_i \rangle \langle B_j \rangle$$

the problem reduces to finding the eigenvectors and eigenvalues for this matrix. The eigenvector corresponding to the smallest eigenvalue is then associated with the discontinuity normal direction while the other two eigenvectors, corresponding to the maximum and intermediate eigenvalues, respectively, are tangent to the discontinuity.

Sometimes we know from other consideration that the MP behaves like a tangential discontinuity, i.e. that $\langle \vec{B} \rangle \cdot \vec{n} = 0$. This additional constraint on the orientation of $\vec{n}$ can be easily implemented if we replace the matrix M^B by the matrix product PM^BP, where P represents the so-called projection matrix, having the elements given by

$$P_{ij} = \delta_{ij} - m_i m_j$$

with $\vec{m} = \langle \vec{B} \rangle / \left| \langle \vec{B} \rangle \right|$ (see for example *Sonnerup et al.* [2006]). This way of performing the analysis is know as the *constrained MVAB technique*.

In fact, on many occasions the result provided by the constrained MVAB technique is closer to the correct normal direction than the result provided by the standard, unconstrained technique. One such example is given in *Sonnerup et al.* [2006] and we also discuss other three examples in this thesis (see the Sections 3.4, 5.3 and 5.5). The last two cases show that sometimes the above conclusion is valid even when the magnetopause behaves as a rotational discontinuity, i.e. when $\langle \vec{B} \rangle \cdot \vec{n} \neq 0$. The reason is that the standard technique is more prone to errors due to the small-scale magnetic field fluctuations, which are frequently present and have an undesired influence on the magnetic variance computation. The constraint $\langle B_n \rangle = 0$ limits in some sense these errors. In general it is advisable to perform both types of analysis and to compare their results before deciding which are more reliable.

An important issue of the MVAB technique refers to the reliability of the determined normal direction. Mathematically, this can be judged by comparing the three eigenvalues of the magnetic variance matrix M^B. If $\lambda_1 \geq \lambda_2 \geq \lambda_3$ designate the eigenvalues corresponding to the maximum, intermediate and minimum magnetic variance, respectively, a rule of thumb requires a value for the ratio $\lambda_2/\lambda_3 \gtrsim 10$ in order to have a reliable normal from the unconstrained MVAB method. In case of the constained MVAB, where $\lambda_3 = 0$, a similar rule requires a ratio $\lambda_1/\lambda_2 \gtrsim 15$.

In various polar plots we are using in the thesis for showing the normals provided by the MVAB technique (see for example Figure 3.7), we indicate by an error ellipsis the uncertainty in the orientation. The error ellipsis transforms into an error bar when the normal is computed with the constrained variant of the method. The only uncertainties taken into account here are of statistical nature. This type of uncertainties were computed in *Sonnerup and Scheible*

[1998] by assuming that the magnetic measurements are affected by a stationary, isotropic and spatially uncorrelated noise component. Other causes like non-stationarity or deviations from the planar assumption were not considered.

A partial check on the time-stationarity can be performed by doing the so called *nested MVAB analysis*, i.e using as time-intervals for MVAB a set of nested intervals centered near the middle of the discontinuity and observing the stability of the corresponding normals. Such an analysis is presented in Section 3.4. Throughout the thesis, in order to minimize the dependence of the result from the interval of analysis, we determine the MP normal by performing a nested MVAB analysis and then averaging the direction of the normals obtained for each nested interval.

There are different ways to perform the averaging operation. In the simplest way, applied throughout the present thesis, we take the vectorial sum of the normals. Another possible way is to perform a variance analysis on the resulted normals and select the direction corresponding to the minimum variance.

APPENDIX B

Timing methods

In a timing analysis, the times when the four Cluster satellites encounter the magnetopause (MP), together with the information about the spacecraft relative positions at these instants is used. It is the purpose of this Appendix to review the existing planar timing analysis techniques and to introduce a new one, conceived to be used when the MP behaves locally as a 2-D, non-planar discontinuity.

We will assume throughtout this Appendix that the timing information was extracted from data, e.g by the use of the procedure described in Chapter 3. In addition, in case of the 2-D MP, we will consider that the invariant direction, i.e. the direction perpendicular to the plane that contains the MP normals, was determined (see the procedure from Section 3.4).

Data preparation and notations

In all the algorithms to be presented in the next sections the satellites are first ordered by their central crossing times. Therefore hereafter by satellite 1 we understand the first spacecraft that crosses the MP centre, by satellite 2 the second one and so on. We choose as origin of time the moment when the MP leading edge encounters the satellite 1 and as origin of the space the satellite 1 position.

The satellites positions are regarded as fixed points in space, an assumption well-justified considering their small orbital velocity relative to the typical MP velocity. For example in the case analyzed in Chapters 3 and 4, the satellite orbital velocity along the MP normal at the time of the event is around 0.11 km/s, to be compared with an average MP normal velocity of 50 km/s.

The following notations are made (see Figures B.1, B.2 and B.3):

- ▷ $\mathbf{T_{ci}}$ is the central crossing moment corresponding to satellite i, $i = 1, ...4$
- ▷ $\mathbf{t_i}$ are defined by the relations $t_i = T_{ci} - T_{c1}$. Evidently, $t_1 = 0$
- ▷ $\tau_\mathbf{i}$ is the half-time crossing duration corresponding to satellite i.
- ▷ $\mathbf{M_{i1}} = T_{ci} - \tau_i$ and $\mathbf{M_{i2}} = T_{ci} + \tau_i$, $i = 1, ...4$ are the moments when the leading, respectively the trailing MP edge is at the satellite i position.

- ▷ $\overrightarrow{\mathbf{R_i}}$ designates the position vector of satellite i relative to the origin (i.e. relative to the position of the first satellite). Evidently, $\vec{R}_1 = 0$
- ▷ $\overrightarrow{\mathbf{l}}$ is the unit vector along the 2-D, non-planar MP invariant direction.
- ▷ $\overrightarrow{\mathbf{m}}$ is the unit vector along the $\vec{R}_2 \times \vec{l}$ direction. We could have chosen equally well $\vec{R}_3$ or $\vec{R}_4$ instead of $\vec{R}_2$; this is only for establishing a reference direction in the plane perpendicular to $\vec{l}$ (i.e. in the plane of the normals).
- ▷ $\overrightarrow{\mathbf{s}}$ is the unit vector defined by $\vec{s} = \vec{m} \times \vec{l}$.
- ▷ $\mathbf{E_i}, \mathbf{F_i}$ are the first and, respectively, the second component of $\vec{R}_i$ in the reference frame defined by the $(\vec{s}, \vec{m}, \vec{l})$ unit vectors. The third components of $\vec{R}_i$ are of no interest for us, being along the invariant direction.
- ▷ $\overrightarrow{\mathbf{x}}$ and $\overrightarrow{\mathbf{y}}$ represent two orthogonal axes in the plane perpendicular to $\vec{l}$. Their orientation is specified by the angle β (see below). All the necessary conditions used for inferring the motion and orientation of the 2-D MP will be put in this reference frame. It has the $\vec{y}$ axis oriented along the direction of primary MP movement (see next paragraph) and $\vec{x}$ is defined by the relation $\vec{x} \times \vec{y} = \vec{l}$.

  As will be seen, the method developed in this appendix assumes either one or two degrees of freedom for the MP displacements in the plane normal to $\vec{l}$. The displacement along $\vec{l}$ are of no interest for us. In the former case, by *primary* direction we mean hereafter the only possible direction of MP displacement. In the latter case, when the MP has a compound movement, along two mutually perpendicular directions, by *primary* direction we designate the direction along which a polynomial description for the velocity is proposed (therefore allowing for an acceleration or even higher terms in the velocity change). Along the other direction, called hereafter the *secondary* direction, we assume the MP is moving with a constant velocity in the positive or negative sense.
- ▷ $\mathbf{X_i}, \mathbf{Y_i}$ are the x and, respectively, y components of $\vec{R}_i$ in the $(\vec{x}, \vec{y}, \vec{l})$ reference frame.
- ▷ β is the angle between $\vec{m}$ and $\vec{y}$, positive in the sense from $\vec{s}$ to $\vec{m}$. In case of plain timing analysis, β is an unknown to be found by solving a system of equations; in the combined analysis it is a parameter set from outside.
- ▷ $\overrightarrow{\mathbf{n_P}}$ is a unit vector introduced only for a simpler characterization of 2-D MP orientation. It lies along the principal direction $\vec{y}$, pointing towards the exterior of the parabola or cylinder. As will be seen in Section B.2, for the parabolic model $\overrightarrow{n_P}$ lies also along the parabola axis. Note that $\overrightarrow{n_P}$ could be parallel or anti-parallel to $\vec{y}$. In Figure B.2 we chose to represent the case when $\vec{n}_P$ and $\vec{y}$ are anti-parallel but what situation occurs in one particular event depends on the timing information and on the spacecraft position and will result directly from the algorithm.

  This vector quantity is usefull when we have to decide wheather the local 2-D feature under investigation is a bump or an indentation on the MP surface. For that purpose we have to decide wheather $\overrightarrow{n_P}$ points towards the MP exterior (i.e outwards from the magnetosphere) or in the opposite direction. Actually, in our test case we will not compute or represent this vector; we used instead a positive or negative value for the local radius of curvature to indicate this aspect (see Section B.4).
- ▷ $\mathbf{A_0}, \mathbf{A_1} \ldots \mathbf{A_N}$ are the polynomial coefficients that describe the MP primary velocity (i.e. along our $\vec{y}$ direction) $U(t) = A_0 + A_1 t + \ldots + A_N t^N$. Here N varies from case to case, depending on the number of degrees of freedom we allowed for the MP movement and

on whether we are performing a plain or combined timing analysis.

- ▷ $\mathbf{D_{i1}} = A_0 M_{i1} + A_1 M_{i1}^2/2 + \ldots + A_N M_{i1}^{N+1}/(N+1)$ and $\mathbf{D_{i2}} = A_0 M_{i2} + A_1 M_{i2}^2/2 + \ldots + A_N M_{i2}^{N+1}/(N+1)$, $i = 1, ...4$ are the instantaneous MP displacements, from the origin along $\vec{y}$ direction, at times when its leading, respectively trailing edge encounters the satellite i position.
- ▷ **v** is the speed along $\vec{x}$ direction, when we allowed a second degree of freedom for the MP layer.
- ▷ **d** is the magnetopause half-thickness
- ▷ **w** and **C** designate the initial position of the 2-D magnetopause. More precisely, in case of the parabolic layer they refer to the leading edge peak's location at the initial moment (w is the x coordinate and C is the y coordinate; see Figure B.2). In case of the cylindrical layer they designate the coordinates of the centre of curvature at the initial moment (see Figure B.3)
- ▷ **a**, appearing in the parabolic model, describes the parabola shape. For example, at the initial moment the parabola has the equation: $y(x) = C + a(x-w)^2$
- ▷ **R** designates the radius of the inner circle in the cylindrical layer model (see Figure B.3).

B.1 Timing analysis in the planar model

In this section we will present the timing analysis techniques based on the planar model for the MP. More specific, we will discuss the method which assumes a constant velocity for the MP during the whole time-interval needed for the transition of the four satellites (constant velocity approach or CVA technique) and the one which assumes a constant thickness for the MP during the same interval (constant thickness approach or CTA technique). They are discussed in detail in *Haaland et al.* [2004b] (called the *CTA paper* in Section 3.1), where CTA was actually introduced and applied on a MP traversal. We will also propose a variant of the CTA, implying a small change in the way the timing information is used in this technique.

Constant velocity approach

Assuming that the MP central surface is a plane, we have the problem of determining the normal and the velocity along that normal, assumed constant, of a moving plane that intersects the satellites positions at times T_{ci}. Therefore in this case the unknowns are the velocity, expressed as $U(t) = A_0$, and the normal unit vector $\vec{n}$.

The conditions are:

$$\begin{aligned} \vec{R}_2 \cdot \vec{n} &= A_0(T_{c2} - T_{c1}) = A_0 t_2 \\ \vec{R}_3 \cdot \vec{n} &= A_0(T_{c3} - T_{c1}) = A_0 t_3 \\ \vec{R}_4 \cdot \vec{n} &= A_0(T_{c4} - T_{c1}) = A_0 t_4 \end{aligned} \tag{B.1}$$

These three equations can readily be solved to find the three components of the vector $\vec{P} = \vec{n}/A_0$. Then the values for the MP velocity and orientation are given by

$$\begin{aligned} A_0 &= 1/|\vec{P}| \\ \vec{n} &= A_0 \vec{P} \end{aligned} \tag{B.2}$$

The thickness of the magnetopause at each satellite is given by

$$2d_i = 2\tau_i A_0 \tag{B.3}$$

Constant thickness approach

The assumption is now that the MP layer is a slab of plasma with constant thickness $2d$. The velocity dependence is expressed as

$$U(t) = A_0 + A_1 t + A_2 t^2 + A_3 t^3 \tag{B.4}$$

The unknowns are A_i (for $i = 0...3$), the half-thickness d and the unit vector $\vec{n}$.

First we will show how the technique was introduced in the *CTA paper*. Basically the velocity dependence (B.4) is found out by imposing two conditions: a) that the MP centre meets the satellites positions at central times T_{ci} and b) that the integral of the velocity over the time-intervals $[T_{ci} - \tau_i, T_{ci} + \tau_i]$ is the same. The value of this integral is then associated with the MP thickness.

Explicitly, by integrating the expression (B.4) for the crossing duration at each satellite and setting it equal to $2d$ we obtain the following:

$$\begin{aligned} 2d &= \int_{T_{ci}-\tau_i}^{T_{ci}+\tau_i} U(t)dt = A_0 t + A_1 t^2/2 + A_2 t^3/3 + A_3 t^4/4 \Big|_{T_{ci}-\tau_i}^{T_{ci}+\tau_i} \\ &= 2\tau_i \left[A_0 + A_1 T_{ci} + A_2 \left(T_{ci}^2 + \frac{\tau_i^2}{3} \right) + A_3 \Big(T_{ci}^3 + T_{ci}\tau_i^2 \Big) \right], \quad i = 1...4 \end{aligned} \tag{B.5}$$

We can immediately solve the above system of equations for the quantities A_i/d. We now set the conditions that the MP centre travels the right distances in the normal directions to meet the satellites positions:

$$\vec{R}_i \cdot \vec{n} = \int_{T_{c1}}^{T_{ci}} U(t)dt, \quad i = 2...4$$

Dividing these equations by d and putting $\vec{P} = \vec{n}/d$ we obtain the following equations:

$$\vec{R}_i \cdot \vec{P} = \frac{A_0(T_{ci} - T_{c1})}{d} + \frac{A_1(T_{ci}^2 - T_{c1}^2)}{2d} + \frac{A_2(T_{ci}^3 - T_{c1}^3)}{3d} + \frac{A_3(T_{ci}^4 - T_{c1}^4)}{4d} \tag{B.6}$$

for $i = 2...4$. In the RHS of the above equations there are only known quantities and solving for vector $\vec{P}$ we can express the solutions for the half-thickness and for the normal vector as:

$$\begin{aligned} d &= 1/|\vec{P}| \\ \vec{n} &= d\,\vec{P} \end{aligned} \tag{B.7}$$

At this point we make the following observations: in *CTA paper* the quantities T_{ci} and τ_i are obtained by fitting the magnetic field time-series corresponding to the MP crossings with a hyperbolic tangent function. Then T_{ci} represents the time when the MP centre is at the position of satellite i and $2\tau_i$ represents the time-interval, centred on T_{ci}, during which the `tanh` function varies by a fraction of $\texttt{tanh}(1) \approx 0.76$ of its total variation (i.e. of the difference between the `tanh` asymptotic levels). According to the line of reasoning presented for determining the velocity evolution (point *b* in the second paragraph of this subsection) the moments $T_{ci} - \tau_i$ and $T_{ci} + \tau_i$ are not exactly the times when the leading and, respectively, the trailing MP margins encounter the position of satellite i. Indeed, the velocity is presumably variable during the crossing interval and therefore the MP centre could travel, for example, more than d during the first part $[T_{ci}-\tau_i, T_{ci}]$ and less than d during the second part $[T_{ci}, T_{ci}+\tau_i]$.

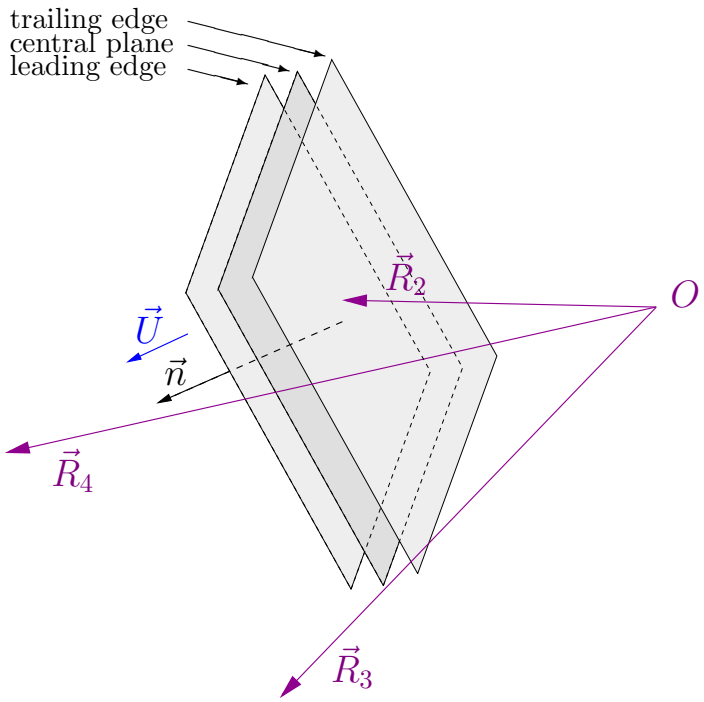

Figure B.1: A sketch of a planar magnetopause moving past the Cluster satellites location. The first spacecraft detecting the MP is located at O, whereas the other three satellites have the relative positions indicated by $\vec{R}_2$, $\vec{R}_3$ and $\vec{R}_4$. The central plane, together with the leading and trailing MP edges are shown. The velocity $\vec{U}$ is oriented along the normal $\vec{n}$ in this model, being a constant vector in the CVA approach. In the standard implementation of CTA, the distance along $\vec{n}$ travelled by the central plane during each crossing duration is constant, whereas in our variant of CTA the distance between the MP edges is constant.

In analysing the MP transition from Chapters 3 and 4 we employed, apart from the standard CTA, a slightly different approach that considers the MP as a planar structure of constant thickness whose *edges* encounters the satellites positions at the times $T_{ci} - \tau_i$ and $T_{ci} + \tau_i$ (therefore not using conditions implying the MP centre). This line of reasoning is consistent with the procedure that will be followed in the 2-D method.

The conditions that MP edges meet the satellites position at the proper moments are:

$$\vec{R}_i \cdot \vec{n} = \int_{M_{11}}^{M_{i1}} U(t)dt, \quad i = 2...4 \qquad \text{for the leading edge} \tag{B.8}$$

$$\vec{R}_i \cdot \vec{n} + 2d = \int_{M_{11}}^{M_{i2}} U(t)dt, \quad i = 1...4 \qquad \text{for the trailing edge}$$

with $U(t)$ described by (B.4).

After a division with d we obtain a linear system of 7 equations and 7 unknowns, namely $\mathbf{n_1/d}$, $\mathbf{n_2/d}$, $\mathbf{n_3/d}$, $\mathbf{A_0/d}$, $\mathbf{A_1/d}$, $\mathbf{A_2/d}$, $\mathbf{A_3/d}$. Using the relation $n_1^2 + n_2^2 + n_3^2 = 1$ we can readily obtain d and afterwards all other quantities.

Another observation is that, in principle, we are not bound to use a symmetric function (like the hyperbolic tangent) for fitting the magnetic profiles. Strictly speaking this fitting function should be chosen consistently with the variation of the MP normal velocity and with the MP structure. Using a symmetric function we actually make the approximation that the net effect of the MP movement and MP structure is a symmetric magnetic trace recorded by

the spacecraft. Nevertheless, in our test case we use the (symmetric) *tanh* function, judging that the quality of the fit is very good for this particular event.

B.2 The parabolic layer model

The model to be introduced in this section assumes that the MP behaves locally as a parabolic layer of constant thickness, whose primary movement is perpendicular to the invariant direction $\vec{l}$ and along the (common) axes of the parabolas making the MP leading and trailing edges.

In Figure B.2 we showed the MP cross-section perpendicular to $\vec{l}$ (pointing into the paper) at different successive times when its edges encounter the satelites positions (located at origin and at $\vec{R}_2$, $\vec{R}_3$ and $\vec{R}_4$). The primary movement direction is along $\vec{y}$, which is also an axis of symmetry for the layer. By *constant thickness* we mean that the distance along $\vec{y}$ between the leading and trailing edges is the same throughtout the layer. The vector $\vec{n}_p$ in this picture, lying along $\vec{y}$ and pointing to the exterior of the parabola, is introduced for a simpler characterization of the MP orientation. In Figure B.2 we chose to represent the situation when $\vec{n}_p$ is anti-parallel to $\vec{y}$ and when also a tangential velocity is present (along the secondary direction $\vec{x}$). Wheather $\vec{n}_p$ and $\vec{y}$ are parallel or anti-parallel in one particular case depends on the actual timing information and on the spacraft configuration and results directly from the algorithms to be described.

In each implementation of the parabolic model we will give an analytical solution of the timing analysis problem.

B.2.1 Plain timing analysis

The unknown quantities in this model are (see Figure B.2): the orientation of the primary direction $\vec{y}$ in the plane perpendicular to $\vec{l}$ (i.e. the angle β made by $\vec{y}$ with the reference direction $\vec{m} = \vec{R}_2 \times \vec{l}$ in that plane, positive in the sense of $\vec{l}$), the scale of the parabola (given by the quadratic factor a), the initial position of the MP leading edge peak (given by the coordinates w and C in the plane perpendicular to $\vec{l}$), the half-thickness d of the layer, and the parameters that describe the movement (A_0, A_1 for the primary motion and v for the velocity along the secondary direction). It will be made clear in Subsection B.2.2 that we need a MP having two degrees of freedom in this implementation of the parabolic model.

In order to determine the unknowns we impose the conditions that the margins of the parabolic layer meet the satellites positions at the proper times (four conditions for encountering the leading MP edge at $M_{i1} = T_{ci} - \tau_i$ and four conditions for encountering the trailing MP edge at $M_{i2} = T_{ci} + \tau_i$). For satellite 1, situated at the origin of the reference system having the axes along $\vec{x}$ and $\vec{y}$, the encounter with the MP leading edge gives:

$$\begin{aligned} &\text{time}: \quad M_{11} = 0 \\ &\qquad C + a(-w)^2 = 0 \end{aligned} \tag{B.9}$$

and the encounter with the trailing edge:

$$\begin{aligned} &\text{time}: \quad M_{12} = 2\tau_1 \\ &\qquad C - 2d + a(-w - vM_{12})^2 + A_0 M_{12} + A_1 \frac{M_{12}^2}{2} = 0 \end{aligned} \tag{B.10}$$

In case of the second satellite and in the same reference frame, we have the following expressions

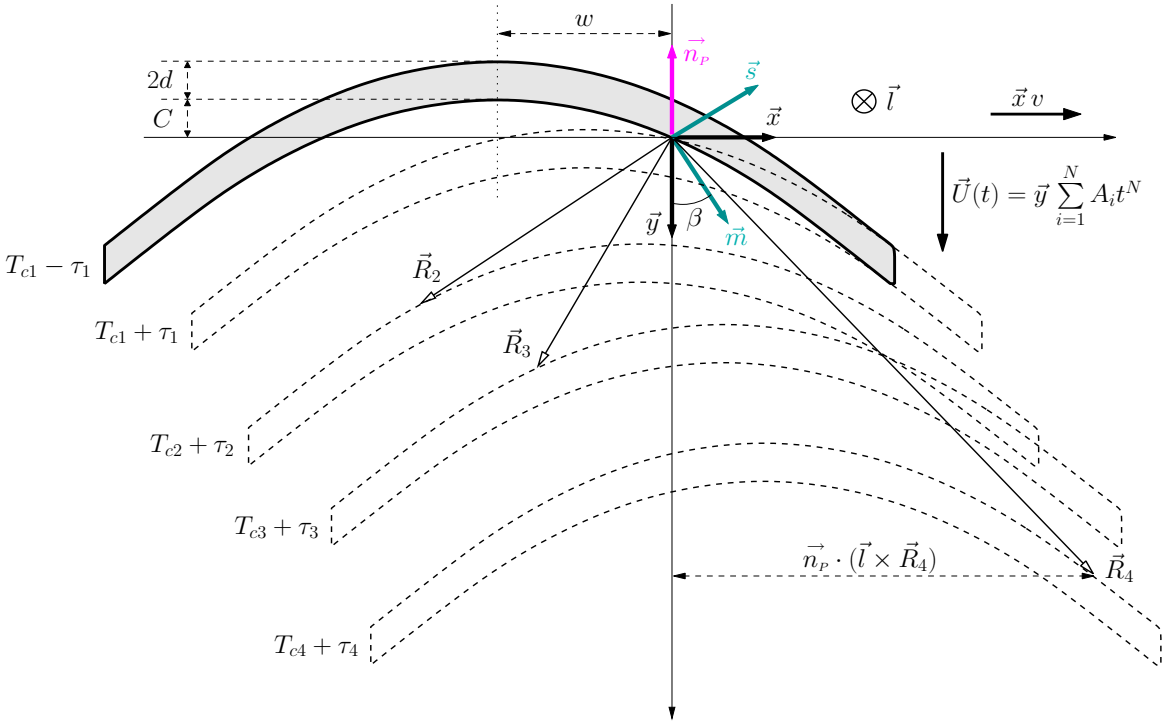

Figure B.2: Magnetopause cross-sections in the plane normal to the invariant direction at successive times when the discontinuity is modeled as a parabolic layer of constant thickness. $\vec{y}$ designates the primary direction, along which the MP velocity is described by a polynomial time dependence. Also, the layer has a constant thickness along $\vec{y}$. The secondary movement, allowed in one variant of this model, takes place along $\vec{x}$. We depict here the situation when $\vec{n_P}$ (the unit vector along $\vec{y}$ pointing towards exterior) is anti-parallel to $\vec{y}$. The Cluster satellites are located at $\vec{R}_i,\ i = 1...4$ with $\vec{R}_1 \equiv 0$. At the initial time $T_{c1} - \tau_1$, the MP leading edge encounters the first satellite, situated at origin: in the other four configurations shown, the MP trailing edges is detected by satellites 1 to 4 at $T_{ci} + \tau_i,\ i = 1...4$. The initial coordinates (w, C) of the leading edge apex as well as the MP thickness $2d$ are indicated. Other quantities appearing in this figure are introduced in the text.

for the x and y coordinates:

x : $\vec{x} \cdot \vec{R}_2 = (\vec{y} \times \vec{l}) \cdot \vec{R}_2 = \vec{y} \cdot (\vec{l} \times \vec{R}_2)$

y : $\vec{y} \cdot \vec{R}_2$

These quantities, being invariants, can be evaluated in the $(\vec{s}, \vec{m}, \vec{l})$ frame (see the definition of this system at the beginning of this appendix). In the latter frame the components of the unit vector $\vec{y}$ are $(-\sin\beta, \cos\beta, 0)$ and therefore we have:

x : $E_2 \cos\beta + F_2 \sin\beta$

y : $-E_2 \sin\beta + F_2 \cos\beta$

The condition of the MP leading edge encounter by satellite 2 is:

time : $M_{21} = t_2 + \tau_1 - \tau_2$

$$C + a(E_2 \cos\beta + F_2 \sin\beta - w - vM_{21})^2 + A_0 M_{21} + A_1 \frac{M_{21}^2}{2} = -E_2 \sin\beta + F_2 \cos\beta \tag{B.11}$$

and the similar relation for the MP trailing edge encounter:

$$\text{time}: \quad M_{22} = t_2 + \tau_1 + \tau_2$$

$$C - 2d + a(E_2\cos\beta + F_2\sin\beta - w - vM_{22})^2 + A_0 M_{22} + A_1\frac{M_{22}^2}{2} = -E_2\sin\beta + F_2\cos\beta \tag{B.12}$$

We write directly the conditions corresponding to satellites 3 and 4:

$$C + a(E_3\cos\beta + F_3\sin\beta - w - vM_{31})^2 + A_0 M_{31} + A_1\frac{M_{31}^2}{2} = -E_3\sin\beta + F_3\cos\beta$$

$$C - 2d + a(E_3\cos\beta + F_3\sin\beta - w - vM_{32})^2 + A_0 M_{32} + A_1\frac{M_{32}^2}{2} = -E_3\sin\beta + F_3\cos\beta$$

$$C + a(E_4\cos\beta + F_4\sin\beta - w - vM_{41})^2 + A_0 M_{41} + A_1\frac{M_{41}^2}{2} = -E_4\sin\beta + F_4\cos\beta$$

$$C - 2d + a(E_4\cos\beta + F_4\sin\beta - w - vM_{42})^2 + A_0 M_{42} + A_1\frac{M_{42}^2}{2} = -E_4\sin\beta + F_4\cos\beta$$

By subtracting (B.9) from (B.10) and making use of the definitions for the quantities M_{11} and M_{12} we obtain:

$$-d + 2avw\tau_1 + 2av^2\tau_1^2 + A_0\tau_1 + A_1\tau_1^2 = 0$$

Similarly, taking the difference (B.12) – (B.11) we obtain:

$$-d + 2avw\tau_2 - 2av\tau_2[E_2\cos\beta + F_2\sin\beta] + 2av^2\tau_2(t_2+\tau_1) + A_0\tau_2 + A_1\tau_2(t_2+\tau_1) = 0$$

Eliminating $2avw$ from the last two equations we arrive at the following:

$$-d\left(1 - \frac{\tau_2}{\tau_1}\right) + A_1 t_2\tau_2 + 2av^2 t_2\tau_2 - 2av\tau_2[E_2\cos\beta + F_2\sin\beta] = 0$$

Dividing this by d and using also the conditions corresponding to satellites 3 and 4 we obtain the following system of linear equations in the unknowns $(\mathbf{av/d})\,\mathbf{cos}\beta$, $(\mathbf{av/d})\,\mathbf{sin}\beta$ and $(\mathbf{2av^2 + A_1})/\mathbf{d}$:

$$\begin{aligned}
2E_2\tau_2\frac{\mathbf{av}}{\mathbf{d}}\,\mathbf{cos}\beta + 2F_2\tau_2\frac{\mathbf{av}}{\mathbf{d}}\,\mathbf{sin}\beta - t_2\tau_2\frac{\mathbf{2av^2 + A_1}}{\mathbf{d}} &= \frac{\tau_2}{\tau_1} - 1\\
2E_3\tau_3\frac{\mathbf{av}}{\mathbf{d}}\,\mathbf{cos}\beta + 2F_3\tau_3\frac{\mathbf{av}}{\mathbf{d}}\,\mathbf{sin}\beta - t_3\tau_3\frac{\mathbf{2av^2 + A_1}}{\mathbf{d}} &= \frac{\tau_3}{\tau_1} - 1\\
2E_4\tau_4\frac{\mathbf{av}}{\mathbf{d}}\,\mathbf{cos}\beta + 2F_4\tau_4\frac{\mathbf{av}}{\mathbf{d}}\,\mathbf{sin}\beta - t_4\tau_4\frac{\mathbf{2av^2 + A_1}}{\mathbf{d}} &= \frac{\tau_4}{\tau_1} - 1
\end{aligned} \tag{B.13}$$

By solving this we find a solution, say

$$r_1 = \frac{av}{d}\cos\beta \tag{B.14a}$$

$$r_2 = \frac{av}{d}\sin\beta \tag{B.14b}$$

$$r_3 = \frac{2av^2 + A_1}{d} \tag{B.14c}$$

From (B.14a) and (B.14b) one can immediately obtain the value of β angle:

$$\beta = \arctan\left(\frac{r_2}{r_1}\right) + k\pi, \quad k = 0, 1$$

We have two potential solutions because the possible values for β are in the range $[0, 2\pi]$. It will be clear later that the condition $d > 0$ selects only one solution.

We will designate the quantity $\mathbf{av/d}$ as r

$$\frac{av}{d} = r = \pm\sqrt{r_1^2 + r_2^2} \tag{B.15}$$

Now, expanding (B.10) and using (B.9) and (B.14c) we arrive at the relation

$$\frac{2awv}{d} + \frac{A_0}{d} = \frac{1 - r_3\tau_1^2}{\tau_1} \tag{B.16}$$

When we divide equation (B.12) by d, expand its first quadratic term and use the relation (B.9) we obtain

$$\begin{aligned} &-2 + \frac{a}{d}[E_2\cos\beta + F_2\sin\beta]^2 + \left(\frac{av^2}{d} + \frac{A_1}{2d}\right)M_{22}^2 + \left(\frac{2avw}{d} + \frac{A_0}{d}\right)M_{22} \\ &\quad - \frac{2aw}{d}[E_2\cos\beta + F_2\sin\beta] - 2\frac{av}{d}M_{22}[E_2\cos\beta + F_2\sin\beta] = -\frac{1}{d}[E_2\sin\beta - F_2\cos\beta] \end{aligned}$$

Taking into account the definition of r_3 and r (see (B.14c) and (B.15)) we can arrange the previous equation like

$$\begin{aligned} &\frac{a}{d}[E_2\cos\beta + F_2\sin\beta]^2 + \left(\frac{2avw}{d} + \frac{A_0}{d}\right)M_{22} - \frac{2aw}{d}[E_2\cos\beta + F_2\sin\beta] \\ &\qquad + \frac{1}{d}[E_2\sin\beta - F_2\cos\beta] = 2rM_{22}[E_2\cos\beta + F_2\sin\beta] + 2 - \frac{r_3}{2}M_{22}^2 \end{aligned}$$

By using (B.16) and considering the similar equations for satellites 3 and 4 we arrive at the following system of linear equations in the unknowns $\mathbf{a/d}$, $\mathbf{aw/d}$ and $\mathbf{1/d}$

$$\begin{aligned} &[E_2\cos\beta + F_2\sin\beta]^2\frac{\mathbf{a}}{\mathbf{d}} - 2[E_2\cos\beta + F_2\sin\beta]\frac{\mathbf{aw}}{\mathbf{d}} + [E_2\sin\beta - F_2\cos\beta]\frac{\mathbf{1}}{\mathbf{d}} = \\ &\qquad \left\{2r[E_2\cos\beta + F_2\sin\beta] - \frac{r_3}{2}M_{22} - \frac{1 - r_3\tau_1^2}{\tau_1}\right\}M_{22} + 2 \\ &[E_3\cos\beta + F_3\sin\beta]^2\frac{\mathbf{a}}{\mathbf{d}} - 2[E_3\cos\beta + F_3\sin\beta]\frac{\mathbf{aw}}{\mathbf{d}} + [E_3\sin\beta - F_3\cos\beta]\frac{\mathbf{1}}{\mathbf{d}} = \\ &\qquad \left\{2r[E_3\cos\beta + F_3\sin\beta] - \frac{r_3}{2}M_{32} - \frac{1 - r_3\tau_1^2}{\tau_1}\right\}M_{32} + 2 \\ &[E_4\cos\beta + F_4\sin\beta]^2\frac{\mathbf{a}}{\mathbf{d}} - 2[E_4\cos\beta + F_4\sin\beta]\frac{\mathbf{aw}}{\mathbf{d}} + [E_4\sin\beta - F_4\cos\beta]\frac{\mathbf{1}}{\mathbf{d}} = \\ &\qquad \left\{2r[E_4\cos\beta + F_4\sin\beta] - \frac{r_3}{2}M_{42} - \frac{1 - r_3\tau_1^2}{\tau_1}\right\}M_{42} + 2 \end{aligned} \tag{B.17}$$

If we make the transformation $\beta \longmapsto \beta + \pi$ in the above system, the RHS will not change because we could write, for example, $r[E_2 \cos\beta + F_2 \sin\beta]$ as $r_1 E_2 + r_2 F_2$ and the values r_1, r_2, r_3 are fixed, being a solution of (B.13). On the other hand the coefficients on the LHS will change to

$$\begin{aligned}
[E_2 \cos\beta + F_2 \sin\beta]^2 &\longmapsto [E_2 \cos\beta + F_2 \sin\beta]^2 \\
[E_2 \cos\beta + F_2 \sin\beta] &\longmapsto -[E_2 \cos\beta + F_2 \sin\beta] \\
[E_2 \sin\beta - F_2 \cos\beta] &\longmapsto -[E_2 \sin\beta - F_2 \cos\beta]
\end{aligned}$$

Let $\left(a_0/d_0,\, a_0 w_0/d_0,\, 1/d_0\right)$ be the solution obtained for the value $\beta_0 = \arctan\left(r_2/r_1\right)$ and $\left(a_1/d_1,\, a_1 w_1/d_1,\, 1/d_1\right)$ be the solution obtained for the value $\beta_1 = \arctan\left(r_2/r_1\right) + \pi$. From the above observation it means that $\left(a_0/d_0,\, -a_0 w_0/d_0,\, -1/d_0\right)$ is a solution for the value β_1. In addition, this is the only solution because (B.17) is a system of linear equations. This demonstrates that by requesting $d > 0$ we actually validate only one value for β.

If p_1, p_2 and p_3 is the solution of system (B.17) we can finally write down the expressions for all our unknowns:

$$\begin{aligned}
\beta &= \arctan(r_2/r_1) + k\pi, \quad k = 0, 1 \quad \text{so that } d > 0 \\
a &= p_1/p_3 \\
d &= 1/p_3 \\
w &= p_2/p_1 \\
C &= -p_2^2/(p_1 p_3) \\
v &= r/p_1 \\
A0 &= \frac{1}{p_3}\left(\frac{1 - r_3\tau_1^2}{\tau_1} - \frac{2 r p_2}{p_1}\right) \\
A1 &= \frac{r_3}{p_3} - \frac{2r^2}{p_1 p_3}
\end{aligned}$$

B.2.2 Combined analysis

In the combined analysis algorithm, the angle β is an input parameter and therefore we have at our disposal one more place for an additional unknown to describe the MP movement. We can chose to increase by one or by two the degree of polynomial describing the velocity in the primary motion, not allowing anymore for a tangential velocity in the latter case. Note that now the quantities X_i and Y_i (the components of $\vec{R}_i$ in the plane perpendicular to the invariant direction $\vec{l}$) are known.

Case 1: allowing only an unidirectional movement for the MP. In this case the unknowns are $C, d, a, w, A_0, A_1, A_2$ and A_3 (see the definitions at the beginning of this appendix). The conditions corresponding to the first and second satellite are:

$$C + aw^2 = 0 \tag{B.18}$$

$$C - 2d + aw^2 + A_0 M_{12} + A_1 \frac{M_{12}^2}{2} + A_2 \frac{M_{12}^3}{3} + A_3 \frac{M_{12}^3}{4} = 0 \tag{B.19}$$

$$C + a(X_2 - w)^2 + A_0 M_{21} + A_1 \frac{M_{21}^2}{2} + A_2 \frac{M_{21}^3}{3} + A_3 \frac{M_{21}^3}{4} = Y_2 \tag{B.20}$$

$$C - 2d + a(X_2 - w)^2 + A_0 M_{22} + A_1 \frac{M_{22}^2}{2} + A_2 \frac{M_{22}^3}{3} + A_3 \frac{M_{22}^3}{4} = Y_2 \tag{B.21}$$

We can readily find out the polynomial coefficients $A_0, \dots A_3$ by taking the differences (B.19) - (B.18), (B.21) - (B.20) and the corresponding ones for the third and fourth satellites. We obtain in this way the distances the MP is travelling during the crossing period of each satellite. Because the MP moves parallel to its axis of symmetry, the differences are all equal with $2d$. We arrive at the following system of linear equations in the unknowns $\mathbf{A_0/d}$, $\mathbf{A_1/d}$, $\mathbf{A_2/d}$ and $\mathbf{A_3/d}$

This is exactly the distance MP travels during the crossing period of each satellite and because now it moves parallel to its axis the differences are all equal with $2d$. We arrive at the following system of linear equations in the unknowns $\mathbf{A_0/d}$, $\mathbf{A_1/d}$, $\mathbf{A_2/d}$ and $\mathbf{A_3/d}$

$$\begin{aligned}
(M_{12}-M_{11})\,\frac{\mathbf{A_0}}{\mathbf{d}}+\frac{M_{12}^2-M_{11}^2}{2}\,\frac{\mathbf{A_1}}{\mathbf{d}}+\frac{M_{12}^3-M_{11}^3}{3}\,\frac{\mathbf{A_2}}{\mathbf{d}}+\frac{M_{12}^4-M_{11}^4}{4}\,\frac{\mathbf{A_3}}{\mathbf{d}}&=2\\
(M_{22}-M_{21})\,\frac{\mathbf{A_0}}{\mathbf{d}}+\frac{M_{22}^2-M_{21}^2}{2}\,\frac{\mathbf{A_1}}{\mathbf{d}}+\frac{M_{22}^3-M_{21}^3}{3}\,\frac{\mathbf{A_2}}{\mathbf{d}}+\frac{M_{22}^4-M_{21}^4}{4}\,\frac{\mathbf{A_3}}{\mathbf{d}}&=2\\
(M_{32}-M_{31})\,\frac{\mathbf{A_0}}{\mathbf{d}}+\frac{M_{32}^2-M_{31}^2}{2}\,\frac{\mathbf{A_1}}{\mathbf{d}}+\frac{M_{32}^3-M_{31}^3}{3}\,\frac{\mathbf{A_2}}{\mathbf{d}}+\frac{M_{32}^4-M_{31}^4}{4}\,\frac{\mathbf{A_3}}{\mathbf{d}}&=2\\
(M_{42}-M_{41})\,\frac{\mathbf{A_0}}{\mathbf{d}}+\frac{M_{42}^2-M_{41}^2}{2}\,\frac{\mathbf{A_1}}{\mathbf{d}}+\frac{M_{42}^3-M_{41}^3}{3}\,\frac{\mathbf{A_2}}{\mathbf{d}}+\frac{M_{42}^4-M_{41}^4}{4}\,\frac{\mathbf{A_3}}{\mathbf{d}}&=2
\end{aligned} \tag{B.22}$$

with the solution say (q_0, q_1, q_2, q_3). We define the following sums:

$$\begin{aligned}
S_2&=\frac{1}{d}\left(A_0M_{21}+A_1\frac{M_{21}^2}{2}+A_2\frac{M_{21}^3}{3}+A_3\frac{M_{21}^4}{4}\right)=\frac{D_{21}}{d}\\
S_3&=\frac{1}{d}\left(A_0M_{31}+A_1\frac{M_{31}^2}{2}+A_2\frac{M_{31}^3}{3}+A_3\frac{M_{31}^4}{4}\right)=\frac{D_{31}}{d}\\
S_4&=\frac{1}{d}\left(A_0M_{31}+A_1\frac{M_{31}^2}{2}+A_2\frac{M_{31}^3}{3}+A_3\frac{M_{31}^4}{4}\right)=\frac{D_{41}}{d}
\end{aligned}$$

The conditions that the leading MP edge encounters the satellites positions at the proper times are:

$$C+aw^2=0 \tag{B.23}$$
$$C+a(X_2-w)^2+dS_2=Y_2 \tag{B.24}$$
$$\begin{aligned}
C+a(X_3-w)^2+dS_3&=Y_3\\
C+a(X_4-w)^2+dS_4&=Y_4
\end{aligned}$$

By subtracting (B.23) from the other ones we arrive at the following linear system in the unknowns $\mathbf{a}$, $\mathbf{aw}$ and $\mathbf{d}$

$$\begin{aligned}
X_2^2\mathbf{a}-2X_2\mathbf{aw}+S_2\mathbf{d}&=Y_2\\
X_3^2\mathbf{a}-2X_3\mathbf{aw}+S_3\mathbf{d}&=Y_3\\
X_4^2\mathbf{a}-2X_4\mathbf{aw}+S_4\mathbf{d}&=Y_4
\end{aligned}$$

If the solution for the above system of equations is (r_1, r_2, r_3) then the expressions for the

initial unknowns are:

$$\begin{aligned} a &= r_1 \\ d &= r_3 \\ w &= r_2/r_1 \\ C &= -r_2^2/r_1 \\ A_0 &= r_3 q_0 \\ A_1 &= r_3 q_1 \\ A_2 &= r_3 q_2 \\ A_3 &= r_3 q_3 \end{aligned} \tag{B.25}$$

For each direction (each angle β that determines the values of X_i and Y_i) we have one solution and, as will be presented in Section B.4, we can then readily compute a set of quantities that characterize the MP orientation and motion, like the instantaneous normal and normal velocity at each satellite position. The algorithm developed in this implementation changes β in steps, finds the solution (B.25) and computes the above mentioned set of quantities. Finally, that angle β is selected for which the corresponding solution better agrees with a specified criterion (like for example the minimization of the normal magnetic variance in a global sense; this procedure will be presented in Section B.5).

We make here an observation about the plain timing approach in the parabolic case (see previous section). There we were forced to introduced a tangential displacement for the MP because if the movement takes place along the parabola axis only (i.e. only along the primary direction) then the conditions that the satellites encounter the MP edges gives immediately a system of equations like (B.22). In that case we would need four coefficients A_i for a general solution and this is too much: the MP initial position (w and C), geometry (a, d) and the direction of its motion in the plane perpendicular to $\vec{l}$ (angle β) require five quantities and there are only eight conditions in total. We will see in the next section that for a cylindrical MP we do not have this restriction. Indeed, there the MP layer has a constant thickness along the radial direction and not along the $\vec{y}$.

Case 2: allowing two degrees of freedom for the MP movement. In this case we have the unknowns corresponding to the initial position (C and w), the ones specifying the geometry (a and d), the coefficients describing the velocity along the primary direction (A_0, A_1 and A_2), and the velocity along the secondary direction (v). The conditions for the first and second satellites to encounter the MP leading and trailing edge at the proper times are:

$$C + aw^2 = 0 \tag{B.26}$$

$$C - 2d + a(w + vM_{12})^2 + A_0 M_{12} + A_1 \frac{M_{12}^2}{2} + A_2 \frac{M_{12}^3}{3} = 0 \tag{B.27}$$

and respectively

$$C + a(X_2 - w - vM_{21})^2 + A_0 M_{21} + A_1 \frac{M_{21}^2}{2} + A_2 \frac{M_{21}^3}{3} = Y_2 \tag{B.28}$$

$$C - 2d + a(X_2 - w - vM_{22})^2 + A_0 M_{22} + A_1 \frac{M_{22}^2}{2} + A_2 \frac{M_{22}^3}{3} = Y_2 \tag{B.29}$$

As in the previous situation, X_i and Y_i are known quantities because the angle β is an input parameter of the algorithm. We will make the difference between (B.28) and (B.26) and

rearrange the terms just to show how the linear system of equation that we have to solve in this case is obtained.

$$a(X_2 - vM_{21})(X_2 - 2w - vM_{21}) + A_0M_{21} + A_1\frac{M_{21}^2}{2} + A_2\frac{M_{21}^3}{3} = Y_2 \qquad \Rightarrow$$
$$aX_2^2 - 2aX_2(w + vM_{21}) + avM_{21}(2w + vM_{21}) + A_0M_{21} + A_1\frac{M_{21}^2}{2} + A_2\frac{M_{21}^3}{3} = Y_2 \qquad \Rightarrow$$
$$aX_2^2 - 2X_2aw - 2X_2avM_{21} + (A_0 + 2vwa)M_{21} + \left(\frac{A_1}{2} + av^2\right)M_{21}^2 + \frac{A_2}{3}M_{21}^3 = Y_2$$

Subtracting (B.26) from all the other conditions of MP edge encounters we arrive at the following linear system in the unknowns $\mathbf{d}$, $\mathbf{a}$, $\mathbf{aw}$, $\mathbf{av}$, $\mathbf{A_0 + 2vwa}$, $(\mathbf{A_1/2 + av_2})$ and $\mathbf{A_2}$

$$-2\mathbf{d} + M_{12}(\mathbf{A_0} + \mathbf{2vwa}) + M_{12}^2\left(\frac{\mathbf{A_1}}{\mathbf{2}} + \mathbf{av_2}\right) + \frac{M_{12}^3}{3}\mathbf{A_2} = 0$$
$$X_2^2\mathbf{a} - 2X_2\mathbf{aw} - 2X_2M_{21}\mathbf{av} + M_{21}(\mathbf{A_0} + \mathbf{2vwa}) + M_{21}^2\left(\frac{\mathbf{A_1}}{\mathbf{2}} + \mathbf{av^2}\right) + \frac{M_{21}^3}{3}\mathbf{A_2} = Y_2$$
$$-2\mathbf{d} + X_2^2\mathbf{a} - 2X_2\mathbf{aw} - 2X_2M_{22}\mathbf{av} + M_{22}(\mathbf{A_0} + \mathbf{2vwa}) + M_{22}^2\left(\frac{\mathbf{A_1}}{\mathbf{2}} + \mathbf{av^2}\right) + \frac{M_{22}^3}{3}\mathbf{A_2} = Y_2$$
$$X_3^2\mathbf{a} - 2X_3\mathbf{aw} - 2X_3M_{31}\mathbf{av} + M_{31}(\mathbf{A_0} + \mathbf{2vwa}) + M_{31}^2\left(\frac{\mathbf{A_1}}{\mathbf{2}} + \mathbf{av^2}\right) + \frac{M_{31}^3}{3}\mathbf{A_2} = Y_3$$
$$-2\mathbf{d} + X_3^2\mathbf{a} - 2X_3\mathbf{aw} - 2X_3M_{32}\mathbf{av} + M_{32}(\mathbf{A_0} + \mathbf{2vwa}) + M_{32}^2\left(\frac{\mathbf{A_1}}{\mathbf{2}} + \mathbf{av^2}\right) + \frac{M_{32}^3}{3}\mathbf{A_2} = Y_3$$
$$X_4^2\mathbf{a} - 2X_4\mathbf{aw} - 2X_4M_{41}\mathbf{av} + M_{41}(\mathbf{A_0} + \mathbf{2vwa}) + M_{41}^2\left(\frac{\mathbf{A_1}}{\mathbf{2}} + \mathbf{av^2}\right) + \frac{M_{41}^3}{3}\mathbf{A_2} = Y_4$$
$$-2\mathbf{d} + X_4^2\mathbf{a} - 2X_4\mathbf{aw} - 2X_4M_{42}\mathbf{av} + M_{42}(\mathbf{A_0} + \mathbf{2vwa}) + M_{42}^2\left(\frac{\mathbf{A_1}}{\mathbf{2}} + \mathbf{av^2}\right) + \frac{M_{42}^3}{3}\mathbf{A_2} = Y_4$$

If $(r_1, r_2, \ldots r_7)$ is the solution of the above system of equations then we can express the unknowns as:

$$\begin{aligned} a &= r_2 \\ d &= r_1 \\ w &= r_3/r_2 \\ C &= -r_3^2/r_2 \\ v &= r_4/r_2 \\ A_0 &= r_5 - 2r_4r_3/r_2 \\ A_1 &= 2\left(r_6 - r_4^2/r_2\right) \\ A_2 &= r_7 \end{aligned} \tag{B.30}$$

Like in the previous case, we have a solution for each β and the algorithm selects that one which better agrees with some optimization criterion (see Section B.5).

B.3 The cylindrical layer model

In this section we modeled the MP locally as a cylindrical layer, oriented along the invariant direction $\vec{l}$. The structure is allowed to move in the plane perpendicular to $\vec{l}$ either along

one (i.e. primary) direction or along two perpendicular directions. In the latter case, for the adjacent movement, called secondary, we assumed a constant velocity.

Figure B.3 is the analog of Figure B.2 for the cylindrical, or constant curvature layer. Now w and C designate the coordinates of the centre of curvature at the initial moment. The other variables with geometrical meaning are R and d - the radius of the inner circle and the MP half-thickness. The angle β designates the direction of primary movement, which in this model is radial.

In the plain timing analysis where the MP is locally modeled as a cylindrical layer we can allow for a second degree of freedom (a constant velocity along the secondary direction) or we can cast all the remaining three unknowns to describe the primary motion only. This is because now, unlike in the parabolic case, the MP has a constant thickness along the actual geometrical normal in each point of its surface and not along the direction of primary movement. Therefore we do not have constrains leading to a system of equations like (B.22), that forces a description with four polynomial coefficients for the primary movement.

In this model we were not able to solve analytically the system of eight conditions, describing the encounter of the MP leading and trailing edges with the spacecraft positions, and therefore we resort to methods for finding a numerical solution. As such algorithms work more efficient when the number of equations are small, in all the following sub-cases we transform the system of conditions, expressing some of the unknowns as a function of the others. More specific, we arrived at a set of equations in β, A_i and v - in cases when we allowed for a movement along the secondary direction. The reason for keeping these variables is that we also have to provide an initial guess for the solution and these quantities seemed for us more suitable in this respect. For example the angle β has a limited range of variation (i.e. from $-\pi$ to π) and we could search for the solutions in a loop that varies the initial point for β in this range with a step of a few degrees. Also for the MP velocity we have a better presumption than, say for the initial position of the cylinder axis.

In this model it is very difficult to asses the number of solutions with physical significance in the general case. Therefore when the search for a numerical solution is performed, one has to start from initial points sufficiently close to each other and covering a sufficiently broad range of values. What 'sufficient' means depends on the actual information about timing and position, and one gets a feeling about that by looking how far an initial point can be that still leads to a valid solution.

B.3.1 Plain timing analysis

Case 1: allowing only an unidirectional MP movement. In this case we have a movement only along the primary direction and the system of eight conditions, describing the encounter of the MP leading and trailing edges with the spacecraft positions are:

$$w^2 + C^2 = (R + 2d)^2 \tag{B.31}$$
$$w^2 + (C + D_{12})^2 = R^2 \tag{B.32}$$

$$(X_2 - w)^2 + (Y_2 - C - D_{21})^2 = (R + 2d)^2 \tag{B.33}$$
$$(X_2 - w)^2 + (Y_2 - C - D_{22})^2 = R^2 \tag{B.34}$$

$$(X_3 - w)^2 + (Y_3 - C - D_{31})^2 = (R + 2d)^2 \tag{B.35}$$
$$(X_3 - w)^2 + (Y_3 - C - D_{32})^2 = R^2 \tag{B.36}$$

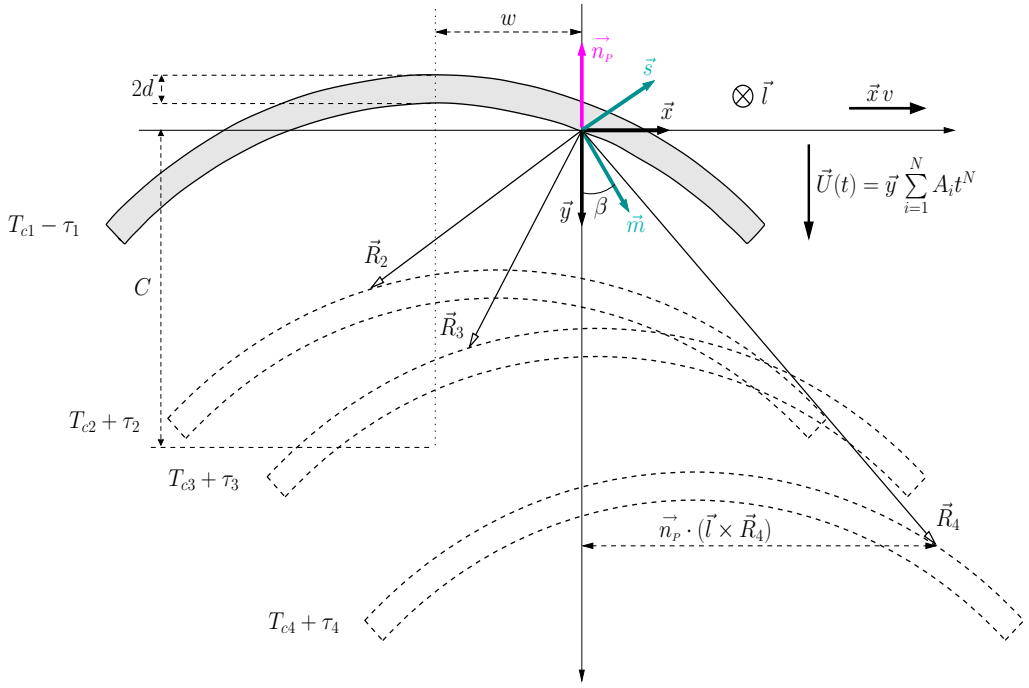

Figure B.3: Magnetopause cross-sections in the plane normal to the invariant direction at successive times when the discontinuity is modeled as a cylindrical layer of constant thickness. $\vec{y}$ designates the primary direction. The secondary movement, allowed in one variant of this model, takes place along $\vec{x}$. We depict here the situation when $\vec{n_P}$ (the unit vector in the primary direction of movement, pointing towards exterior) is anti-parallel to $\vec{y}$. The Cluster satellites are located at $\vec{R}_i,\ i=1...4$ with $\vec{R}_1\equiv 0$. At the initial time $T_{c1}-\tau_1$, the MP leading edge encounters the first satellite, situated at origin: in the other three configurations shown, the MP trailing edges is detected by satellites 2, 3 and 4 at $T_{ci}+\tau_i,\ i=2,3,4$. The coordinates (w,C) of the centre of curvature at the initial moment as well as the MP thickness $2d$ are indicated. Other quantities appearing in this figure are introduced in the text.

$$(X_4-w)^2+(Y_4-C-D_{41})^2=(R+2d)^2 \tag{B.37}$$
$$(X_4-w)^2+(Y_4-C-D_{42})^2=R^2 \tag{B.38}$$

with

$$D_{ij}=A_0M_{ij}+A_1M_{ij}^2/2+A_2M_{ij}^3/3 \tag{B.39}$$

and the unknown β entering in the expressions for X_i and Y_i. In the above equations we assumed that the satellites and the cylinder axis are initially on opposite sides of the MP (i.e. the first encounter is with the surface having the greater radius of curvature). As will be clear in the following, this presumption does not affect our algorithm but in its very last stage because we first find all the other unknowns, apart from R and d, in a way independent of this. At the end, the algorithm tests both possibilities (satellites and the axis position at initial moment on the same side or on opposite sides of the MP) rejecting the one which implies a negative value for d.

In order to find the reduced system of equations, containing only the unknowns A_0, A_1, v and β, for which we search for a numerical solution we will proceed in the following way: we take the differences (B.33) - (B.31), (B.35) - (B.31), (B.37) - (B.31). All these conditions refer

to the encounter of MP leading edge with the spacecraft positions. We also take the differences (B.34) - (B.32), (B.36) - (B.32) and (B.38) - (B.32), implying the conditions that describe the encounter of MP trailing edge with the spacecraft positions. Note that these differences are independent of the initial presumption we mention in the above paragraph. The variables R and d are eliminated and we obtain the following equations:

$$G_2^2 - 2wX_2 - 2CY_2 - 2Y_2D_{21} + D_{21}^2 + 2CD_{21} = 0 \tag{B.40}$$

$$G_2^2 - 2wX_2 - 2CY_2 - 2Y_2D_{22} + D_{22}^2 - D_{12}^2 + 2C(D_{22} - D_{12}) = 0 \tag{B.41}$$

$$G_3^2 - 2wX_3 - 2CY_3 - 2Y_3D_{31} + D_{31}^2 + 2CD_{31} = 0 \tag{B.42}$$

$$G_3^2 - 2wX_3 - 2CY_3 - 2Y_3D_{32} + D_{32}^2 - D_{12}^2 + 2C(D_{32} - D_{12}) = 0 \tag{B.43}$$

$$G_4^2 - 2wX_4 - 2CY_4 - 2Y_4D_{41} + D_{41}^2 + 2CD_{41} = 0 \tag{B.44}$$

$$G_4^2 - 2wX_4 - 2CY_4 - 2Y_4D_{42} + D_{42}^2 - D_{12}^2 + 2C(D_{42} - D_{12}) = 0 \tag{B.45}$$

where we used the notations $G_i^2 = X_i^2 + Y_i^2$

Making now the differences (B.41) - (B.40), (B.43) - (B.42) and (B.45) - (B.44) we obtain three equations without w. Also, we eliminate the unknown w between (B.42) and (B.40) and between (B.44) and (B.40). This is what we obtain:

$$2C(D_{22} - D_{21} - D_{12}) - 2Y_2(D_{22} - D_{21}) + D_{22}^2 - D_{21}^2 - D_{12}^2 = 0 \tag{B.46}$$

$$2C(D_{32} - D_{31} - D_{12}) - 2Y_3(D_{32} - D_{31}) + D_{32}^2 - D_{31}^2 - D_{12}^2 = 0 \tag{B.47}$$

$$2C(D_{42} - D_{41} - D_{12}) - 2Y_4(D_{42} - D_{41}) + D_{42}^2 - D_{41}^2 - D_{12}^2 = 0 \tag{B.48}$$

$$X_2(G_3^2 - 2Y_3D_{31} + D_{31}^2) - X_3(G_2^2 - 2Y_2D_{21} + D_{21}^2) + 2C(Y_2X_3 - Y_3X_2 + X_2D_{31} - X_3D_{21}) = 0 \tag{B.49}$$

$$X_2(G_4^2 - 2Y_4D_{41} + D_{41}^2) - X_4(G_2^2 - 2Y_2D_{21} + D_{21}^2) + 2C(Y_2X_4 - Y_4X_2 + X_2D_{41} - X_4D_{21}) = 0 \tag{B.50}$$

Solving (B.46) for C we have:

$$C = \frac{2Y_2(D_{22} - D_{21}) - (D_{22}^2 - D_{21}^2 - D_{12}^2)}{2(D_{22} - D_{21} - D_{12})} \tag{B.51}$$

The algorithm used in this case relies on equations (B.47) - (B.50) with the above expression (B.51) for C.

After the substitution we obtain:

$$[2Y_2(D_{22}-D_{21})-(D_{22}^2-D_{21}^2-D_{12}^2)](D_{32}-D_{31}-D_{12})$$
$$-[2Y_3(D_{32}-D_{31})-(D_{32}^2-D_{31}^2-D_{12}^2)](D_{22}-D_{21}-D_{12})=0$$

$$[2Y_2(D_{22}-D_{21})-(D_{22}^2-D_{21}^2-D_{12}^2)](D_{42}-D_{41}-D_{12})$$
$$-[2Y_4(D_{42}-D_{41})-(D_{42}^2-D_{41}^2-D_{12}^2)](D_{22}-D_{21}-D_{12})=0$$

$$X_2(G_3^2-2Y_3D_{31}+D_{31}^2)-X_3(G_2^2-2Y_2D_{21}+D_{21}^2) \tag{B.52}$$
$$+\frac{2Y_2(D_{22}-D_{21})-(D_{22}^2-D_{21}^2-D_{12}^2)}{D_{22}-D_{21}-D_{12}}(Y_2X_3-Y_3X_2+X_2D_{31}-X_3D_{21})=0$$

$$X_2(G_4^2-2Y_4D_{41}+D_{41}^2)-X_4(G_2^2-2Y_2D_{21}+D_{21}^2)$$
$$+\frac{2Y_2(D_{22}-D_{21})-(D_{22}^2-D_{21}^2-D_{12}^2)}{D_{22}-D_{21}-D_{12}}(Y_2X_4-Y_4X_2+X_2D_{41}-X_4D_{21})=0$$

In the above equations only the unknowns A_0, A_1, A_2 (through D_{ij}) and β (through X_i and Y_i appear. After solving (B.52) numerically we have for C the relation (B.51). In order to determine w one can use relation (B.40) for example. R and d are obtained from (B.31) and (B.32) and if the value for d is negative we have to use the equations

$$w^2+C^2=R^2$$
$$w^2+(C+D_{12})^2=(R+2d)^2$$

instead.

Case 2: allowing two degrees of freedom for the MP movement. In this case there is a compound movement of the MP: a primary movement, described by two polynomial coefficients A_0 and A_1 and a displacement with a constant velocity v along the secondary direction. The reduced system of equations, for which we search a numerical solution, will contain only these variables and the variable β.

The equations are:

$$w^2+C^2=(R+2d)^2 \tag{B.53}$$
$$(w+vM_{12})^2+(C+D_{12})^2=R^2 \tag{B.54}$$

for the first satellite and

$$(X_2-w-vM_{21})^2+(Y_2-C-D_{21})^2=(R+2d)^2 \tag{B.55}$$
$$(X_2-w-vM_{22})^2+(Y_2-C-D_{22})^2=R^2 \tag{B.56}$$

for the second one. Here the variables A_0, A_1 are hidden in the expressions $D_{ij}=A_0M_{ij}+A_1M_{ij}^2/2$ and β is entering in the expressions for X_i and Y_i. We start following the same procedure as in **case 1** by taking the differences (B.55) - (B.53) (which are the condition for the MP leading edge encounter), open the quadratic terms and rearrange the terms:

$$G_2^2-2w(X_2-vM_{21})+v^2M_{21}^2-2X_2vM_{21}-2C(Y_2-D_{21})+D_{21}^2-2Y_2D_{21}=0 \tag{B.57}$$

Similar equations are obtained when instead of satellite 2 we use the corresponding conditions pertaining to satellites 3 and 4

$$G_3^2 - 2w(X_3 - vM_{31}) + v^2M_{31}^2 - 2X_3vM_{31} - 2C(Y_3 - D_{31}) + D_{31}^2 - 2Y_3D_{31} = 0 \tag{B.58}$$

$$G_4^2 - 2w(X_4 - vM_{41}) + v^2M_{41}^2 - 2X_4vM_{41} - 2C(Y_4 - D_{41}) + D_{41}^2 - 2Y_4D_{41} = 0 \tag{B.59}$$

In the above expressions we used again the notations $G_i^2 = X_i^2 + Y_i^2$. We do the same thing with the conditions referring to MP trailing edge encounter, taking the difference (B.56) - (B.54), and rearranging terms

$$\begin{aligned} G_2^2 - 2w[X_2 - v(M_{22} - M_{12})] - 2X_2vM_{22} + v^2(M_{22}^2 - M_{12}^2) \\ - 2Y_2D_{22} - 2C[Y_2 - (D_{22} - D_{12})] + D_{22}^2 - D_{12}^2 = 0 \end{aligned} \tag{B.60}$$

The similar equations, obtained when conditions corresponding to satellites 3 and 4 are used instead of satellite 2, provide

$$\begin{aligned} G_3^2 - 2w[X_3 - v(M_{32} - M_{12})] - 2X_3vM_{32} + v^2(M_{32}^2 - M_{12}^2) \\ - 2Y_3D_{32} - 2C[Y_3 - (D_{32} - D_{12})] + D_{32}^2 - D_{12}^2 = 0 \end{aligned} \tag{B.61}$$

$$\begin{aligned} G_4^2 - 2w[X_4 - v(M_{42} - M_{12})] - 2X_4vM_{42} + v^2(M_{42}^2 - M_{12}^2) \\ + 2Y_4D_{42} - 2C[Y_4 - (D_{42} - D_{12})] + D_{42}^2 - D_{12}^2 = 0 \end{aligned} \tag{B.62}$$

If we put $v = 0$ in equations (B.57) - (B.62) we recover, as expected, the similar equations from the previous case. Because in this case there is a more complicate dependence for w and C as a function of β, A_0, A_1 and v, it is very difficult to write down the reduced system of equations in a form like (B.52). Therefore here we only deduce the expressions for w and C, and indicate the remaining unused equations where these variable should be substituted. We find it more convenient to proceed in a way slightly different from the previous case: we eliminate C from (B.57) and (B.58) and express the variable w as function of the remaining unknowns. Then we eliminate w from (B.60) and (B.61) in order to obtain C as a function of the same remaining unknowns. We write down directly the expressions we obtain:

$$\begin{aligned} C = \Big\{ & G_3^2[X_2 - v(M_{22} - M_{12})] - G_2^2[X_3 - v(M_{32} - M_{12})] \\ & + 2[Y_2D_{22} + X_2vM_{22}][X_3 - v(M_{32} - M_{12})] - 2[Y_3D_{32} + X_3vM_{32}][X_2 - v(M_{22} - M_{12})] \\ & + v^2(M_{32}^2 - M_{12}^2)[X_2 - v(M_{22} - M_{12})] - v^2(M_{22}^2 - M_{12}^2)[X_3 - v(M_{32} - M_{12})] \\ & + (D_{32}^2 - D_{12}^2)[X_2 - v(M_{22} - M_{12})] - (D_{22}^2 - D_{12}^2)[X_3 - v(M_{32} - M_{12})] \Big\} \\ & \Big\{ 2[Y_3 - (D_{32} - D_{12})][X_2 - v(M_{22} - M_{12})] - 2[Y_2 - (D_{22} - D_{12})][X_3 - v(M_{32} - M_{12})] \Big\}^{-1} \end{aligned} \tag{B.63}$$

$$w = \Big\{ G_3^2(Y_2 - D_{21}) - G_2^2(Y_3 - D_{31}) + vM_{31}(vM_{31} - 2X_3)(Y_2 - D_{21}) \tag{B.64}$$
$$- vM_{21}(vM_{21} - 2X_2)(Y_3 - D_{31}) + D_{31}(D_{31} - 2Y_3)(Y_2 - D_{21})$$
$$- D_{21}(D_{21} - 2Y_2)(Y_3 - D_{31}) \Big\}$$
$$\Big\{ 2(X_3 - vM_{31})(Y_2 - D_{21}) - 2(X_2 - vM_{21})(Y_3 - D_{31}) \Big\}^{-1}$$

The equations used for finding a numerical solution are (B.58), (B.59), (B.61) and (B.62) where the unknowns C and w are replaced by the expressions (B.63) and (B.64), respectively. At the end we find the values for R and d in the same way as in the previous case.

Observation: If we put $v = 0$ in the expression (B.63) we obtain a different form for this variables than (B.51) from case 1 and this is because here we took a slightly different path. The two forms are equivalent and produce the same results.

B.3.2 Combined analysis

By transforming the β angle from an unknown to an input parameter, we can better characterize the MP movement increasing the degree of polynomial describing the primary velocity. Actually, in this combined-analysis we are using the same system of equations as in the plain timing analysis.

Case 1: allowing only an unidirectional MP movement. The equations (B.31) - (B.38) are still valid, as well as the reduced system of equations (B.52). The only differences consist in the fact that now X_I and Y_i are known quantities and that in this case

$$D_{ij} = A_0 M_{ij} + A_1 M_{ij}^2/2 + A_2 M_{ij}^3/3 + A_3 M_{ij}^4/4$$

The algorithm looking for a numerical solution will search after solutions for A_0, A_1, A_2 and A_3

Case 2: allowing two degrees of freedom for the MP movement. The same (initial and reduced) system of equations hold as in the corresponding plain timing analysis but now

$$D_{ij} = A_0 M_{ij} + A_1 M_{ij}^2/2 + A_2 M_{ij}^3/3$$

The algorithm search after a solution for A_0, A_1, A_2 and v.

In the combined analysis, we change, in steps, the value of the input parameter β and select that value for which the corresponding solution better agrees with some optimization criterion (procedure to be discussed in Section B.5).

B.4 Geometrical and dynamical parameters of the solutions

In this sections we will deduce expressions for various average quantities characterizing the MP movement and orientation for a satellite traversal. During such a time interval the MP velocity and orientation are in general not constant; also, in the parabolic layer case, the actual thickness (i.e. along the local normal) varies. The expressions derived here are used in all the

implementations of combined analysis as well as when we compare the results provided by the timing method applied to a 2-D, non-planar MP with the results obtained from the single-spacecraft, planar, techniques (like MVA on magnetic field, Minimum Faraday Residue and deHoffmann-Teller analysis; see Section 4.3).

B.4.1 Parabolic layer case

In the parabolic case, for computing the thickness, orientation and normal velocity at one satellite position we refer to Figure B.4 where two successive infinitesimally-close MP configurations are shown. The displacement of the boundary layer over the satellite position, located at $P(x_i, y_i)$ and considered as a fix point in space, results in a transition in the sense of the (geometrical) exterior normal.

We can imagine that at any moment of observation t the point P will be found also on a moving parabola, described in the xOy reference frame by the equation:

$$y(x, l, t) = C - l + \sum_{k=0}^{N} \frac{A_k t^{k+1}}{k+1} + a(x - w - vt)^2 \tag{B.65}$$

Here $(w, C-l)$ represents the peak's initial coordinate (i.e. at $t = 0$) of that particular parabola. The parameter l is equal to 0 when our point is located on the MP leading edge and to $2d$ when it is situated on the MP trailing edge. In what follows, by instantaneous normal direction we will understand the direction perpendicular to the curve (B.65), at the point where the satellite is located.

The instantaneous tangent has the direction

$$\vec{t} = (\cos\theta, \quad \sin\theta) \qquad \text{with} \qquad \tan\theta = \left(\frac{\partial y}{\partial x}\right)_{x_i,\, t} = 2a(x_i - w - vt) \tag{B.66}$$

therefore

$$\vec{t} = \left(\frac{1}{\sqrt{4a^2(x_i - w - vt)^2 + 1}}, \quad \frac{2a(x_i - w - vt)}{\sqrt{4a^2(x_i - w - vt)^2 + 1}}\right) \tag{B.67}$$

and the exterior normal is

$$\vec{n}_{ext} = \sigma_a(\sin\theta, -\cos\theta) = \sigma_a\left(\frac{2a(x_i - w - vt)}{\sqrt{4a^2(x_i - w - vt)^2 + 1}}, \; -\frac{1}{\sqrt{4a^2(x_i - w - vt)^2 + 1}}\right) \tag{B.68}$$

where σ_a designates the sign of a. Here the term 'exterior' was used by referring to the MP geometry only, which means that this normal can point either towards the interior or exterior of the magnetosphere.

Each point of the MP, considered as a rigid structure, has a compound movement along the primary and secondary directions with the corresponding velocities. Therefore the instantaneous velocity vector is

$$\vec{v}_{inst} = \left(v, \quad \sum_{k=0}^{N} A_k t^k\right) \tag{B.69}$$

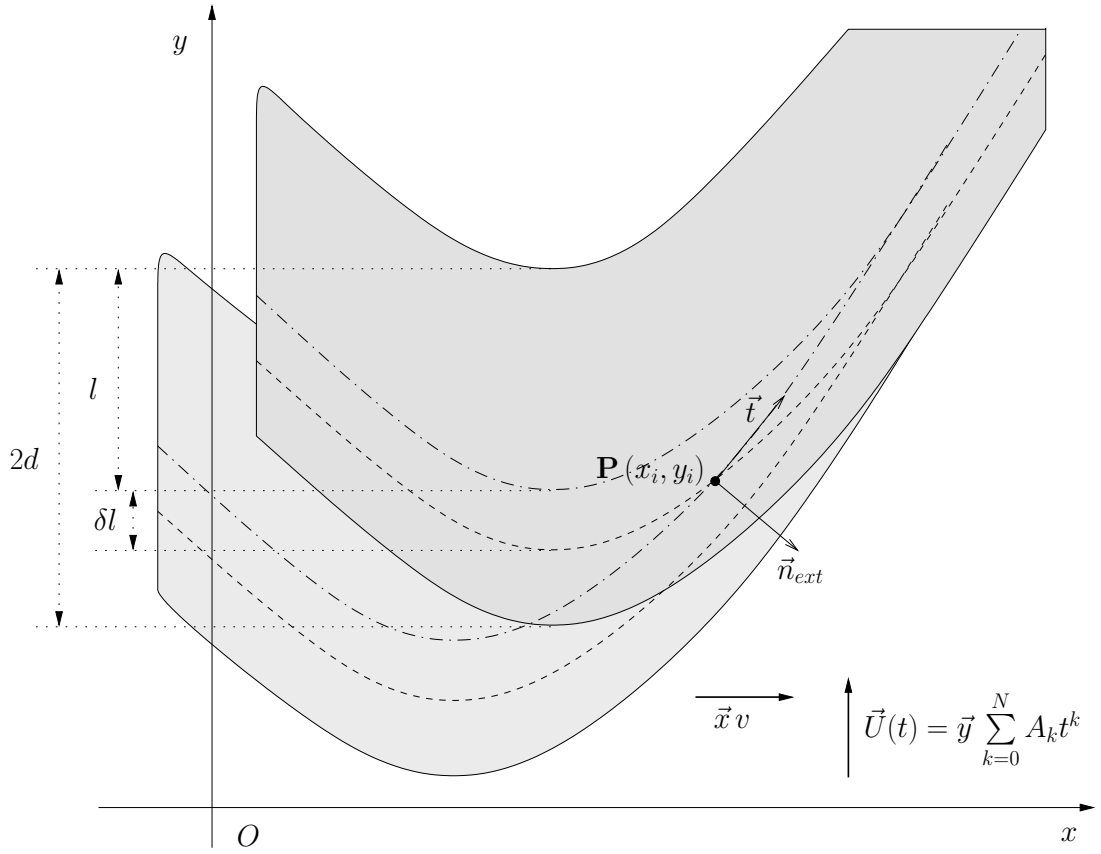

Figure B.4: Magnetopause cross-sections in the plane normal to the invariant direction at successive, infinitesimally-close times. $\vec{y}$ designates the primary direction, along which the MP velocity is described by the polynomial. In case when we allow a second degree of freedom, the MP is moving with constant velocity along $\vec{x}$ as well. The position of the satellite is indicated by P, together with the orientation of the instantaneous exterior normal $\vec{n}_{ext}$ and tangent $\vec{t}$. Other quantities appearing in this figure are introduced in the text.

In order to find the normal velocity at moment t we have to project this vector along the normal (B.68) (shown as $\vec{n}_{ext}$ in Figure B.4).

$$v_{i,\,norm} = \sigma_a \frac{2a(x_i - w - vt)}{\sqrt{4a^2(x_i - w - vt)^2 + 1}}\, v \;-\; \sigma_a \frac{1}{\sqrt{4a^2(x_i - w - vt)^2 + 1}} \sum_{k=0}^{N} A_k t^k \tag{B.70}$$

Considering now that we have four satellites, the average normal velocity $\mathcal{V}_{i,n}$ and the associated distance $\mathcal{T}_i$ corresponding to satellite $i,\ i = 1...4$ are computed from

$$\mathcal{T}_i \;=\; (M_{i,2} - M_{i,1})\mathcal{V}_{i,n} = 2\tau_i \mathcal{V}_{i,n} = \int_{M_{i,1}}^{M_{i,2}} \vec{v}_{inst} \cdot \vec{n}_{ext}\, \delta t$$

$$= \sigma_a\, v \int_{M_{i,1}}^{M_{i,2}} \frac{2a(x_i - w - vt)}{\sqrt{4a^2(x_i - w - vt)^2 + 1}}\, \delta t \;- \sigma_a \int_{M_{i,1}}^{M_{i,2}} \frac{\sum_{k=0}^{N} A_k t^k}{\sqrt{4a^2(x_i - w - vt)^2 + 1}}\, \delta t \tag{B.71}$$

If we adopt the opposite perspective, i.e that the MP is a fixed structure and the satellite is moving relative to it, than the quantity $\mathcal{T}_i$ represents the distance, along the instantaneous

normal, covered by the spacecraft. The sign of this quantity allows us to establish on which side of the discontinuity the centre of curvature is situated: when $\mathcal{T}_i > 0$ the satellite is moving towards the interior with respect to the MP. From now on, we will understand by magnetopause thickness, as seen by the satellite i during its transition, the quantity

$$T_i = |\mathcal{T}_i| \tag{B.72}$$

In order to solve the integrals (B.71) we make the substitution $u = 2a(x_i - w - vt)$ and put $L_{i,1} = 2a(x_i - w - vM_{i,1})$ and $L_{i,2} = 2a(x_i - w - vM_{i,2})$. The different expressions for (B.71), corresponding to all the variants in the parabolic layer model are the following.

Plain time analysis $(N = 1, v \neq 0)$:

$$\begin{aligned}\mathcal{T}_i &= 2\tau_i \mathcal{V}_{i,n} = \sigma_a \frac{1}{2av}\left(A_0 + A_1\frac{x_i - w}{v}\right)\ln\left(u + \sqrt{u^2+1}\right)\Big|_{L_{i,1}}^{L_{i,2}} \\ &\quad - \sigma_a\left(\frac{1}{2a} + \frac{A_1}{4a^2v^2}\right)\sqrt{u^2+1}\Big|_{L_{i,1}}^{L_{i,2}}\end{aligned} \tag{B.73}$$

Combined analysis, unidirectional movement $(N = 3, v = 0)$

$$\mathcal{T}_i = 2\tau_i \mathcal{V}_{i,n} = -\sigma_a \frac{1}{\sqrt{4a^2(x_i - w)^2 + 1}} \sum_{k=0}^{3} \frac{A_k t^{k+1}}{k+1}\Big|_{M_{i,1}}^{M_{i,2}} \tag{B.74}$$

Combined analysis, bidirectional movement $(N = 2, v \neq 0)$

$$\begin{aligned}\mathcal{T}_i &= 2\tau_i \mathcal{V}_{i,n} = \sigma_a \frac{1}{2av}\left(A_0 + A_1\frac{x_i - w}{v} + A_2\left(\frac{x_i - w}{v}\right)^2 - \frac{A_2}{8a^2v^2}\right)\ln\left(u + \sqrt{u^2+1}\right)\Big|_{L_{i,1}}^{L_{i,2}} \\ &\quad - \sigma_a\left(\frac{1}{2a} + \frac{A_1}{4a^2v^2} + \frac{x_i - w}{2a^2v^3}A_2\right)\sqrt{u^2+1}\Big|_{L_{i,1}}^{L_{i,2}} + \sigma_a \frac{A_2}{16a^3v^3}\, u\sqrt{u^2+1}\Big|_{L_{i,1}}^{L_{i,2}}\end{aligned} \tag{B.75}$$

For the case of a parabolic layer, it is worth knowing what is the MP thickness variation during one satellite transition. More precisely, for each satellite we compute the quantity:

$$\delta T_i = \left|\frac{D_{i,\,in} - D_{i,\,out}}{T_i}\right| \tag{B.76}$$

$D_{i,\,in}$ refers to the moment when the satellite i encounters the MP leading edge. It is the distance between the MP margins from the satellite position and along the leading edge normal at that instance of time. Similarly, $D_{i,\,out}$ refers to the moment when the satellite i encounters the MP trailing edge. It is the distance between the MP margins from the satellite position and along the trailing edge normal at that instance of time.

After a straightforward calculation we arrive at the following expressions:

$$D_{i,\,in} = \left| \frac{L_{i,1} + 1/L_{i,1} \pm \sqrt{(L_{i,1} + 1/L_{i,1})^2 + 8ad}}{2a} \right| \sqrt{1 + 1/L_{i,1}^2} \tag{B.77}$$

$$D_{i,\,out} = \left| \frac{L_{i,2} + 1/L_{i,2} \pm \sqrt{(L_{i,2} + 1/L_{i,2})^2 - 8ad}}{2a} \right| \sqrt{1 + 1/L_{i,2}^2} \tag{B.78}$$

where in the above formulas the $-$ or $+$ sign are selected so that the corresponding quantities take the smaller values.

Another important quantity that characterize one satellite traversal is the average orientation of the (exterior) normal $\mathcal{N}_{i,ext}$. This is obtained by integrating the components of (B.68) over the crossing time-interval

$$\mathcal{N}_{i,ext} \;=\; \sigma_a \frac{1}{2\tau_i} \left(\int_{M_{i,1}}^{M_{i,2}} \frac{2a(x_i - w - vt)}{\sqrt{4a^2(x_i - w - vt)^2 + 1}}\,\delta t \;,\quad -\int_{M_{i,1}}^{M_{i,2}} \frac{1}{\sqrt{4a^2(x_i - w - vt)^2 + 1}}\,\delta t \right)$$

When $v = 0$ the normal has a constant orientation given by (B.68): in all the other subcases corresponding to the parabolic model the average normal is

$$\mathcal{N}_{i,ext} \;=\; \sigma_a \frac{1}{4av\tau_i} \left(-\sqrt{u^2+1}\,,\quad \ln\left(u + \sqrt{u^2+1}\right) \right) \Bigg|_{L_{i,1}}^{L_{i,2}} \tag{B.79}$$

The instantaneous radius of curvature of the MP could be computed using the formula

$$R_{i,inst} = \frac{\left(1 + \dfrac{dy}{dx}\right)^{3/2}}{\dfrac{d^2y}{dx^2}} \tag{B.80}$$

where the function y is given by (B.65). This leads us to the following result for the average MP curvature corresponding to the transition made by satellite i

$$R_{i,inst} = \frac{1}{4a\tau_i} \int_{M_{i,1}}^{M_{i,2}} \left(1 + 4a^2(x - w - vt)^2\right)^{3/2} \delta t \tag{B.81}$$

which after the integration gives

$$R_{i,ave} = -\frac{1}{64a^2v\tau_i} \left(u(2u^2+5)\sqrt{u^2+1} + 3\ln\left(u + \sqrt{u^2+1}\right) \right) \Bigg|_{L_{i,1}}^{L_{i,2}} \tag{B.82}$$

We judge whether a transition is inbound or outbound according to the satellite relative movement along the normal. The sense of this normal is considered positive from the magnetosphere towards the magnetosheath and therefore when the satellite is moving towards the magnetosphere it has a negative velocity. Equivalently, the MP relative velocity to be indicated

by $V_{i,ave}$, will be positive in this case. In the tables presenting the various crossing parameters corresponding to the test case (next chapter) we will show this velocity. Of course,

$$V_{i,ave} = \pm \mathcal{V}_{i,n} \tag{B.83}$$

depending whether the two normals (the one provided by the geometry and the one established from physical considerations) are parallel or anti-parallel. We also make the following definition: if the direction provided by the geometry and the one established from physical considerations coincide, we will chose a positive sign for the radius of curvature (this corresponds to a bump in the MP). In the opposite situation we will put minus sign in front of that quantity (this corresponds to an indentation in the MP).

B.4.2 Cylindrical layer case

Because in this situation the MP thickness is fixed by the model to $2d$, the average MP velocity for the transition of satellite i is simply

$$V_{i,ave} = \pm \frac{d}{\tau_i} \tag{B.84}$$

depending on whether we have an inbound or outbond transition. The instantaneous exterior normal (in the geometrical sense) is along the vector joining the centre of the cylinder and the point of observation

$$\vec{n}_{i,ext} = \frac{1}{\sqrt{(x-w-vt)^2 + \left(y - C - \sum\limits_{k=0}^{N} \frac{A_k t^{k+1}}{k+1}\right)^2}} \left(x - w - vt, \quad y - C - \sum_{k=0}^{N} \frac{A_k t^{k+1}}{k+1}\right)$$

For finding the angle between the average normal and the $\vec{x}$ axis we then numerically compute the integral

$$\phi_i = \frac{1}{2\tau i} \int\limits_{M_{i,1}}^{M_{i,2}} \arctan \left(\frac{y - C - \sum\limits_{k=0}^{N} \frac{A_k t^{k+1}}{k+1}}{x - w - vt} \right) \delta t \tag{B.85}$$

and used the relation

$$\mathcal{N}_{i,ext} = (\cos \phi_i, \ \sin \phi_i)$$

We will characterize the MP curvature by the geometrical mean of the inner and outer radius, that is $\sqrt{(R(R+2d))}$, affected by the sign + or − according to the convention presented in the previous case.

We computed in this section quantities with a direct physical significance that locally describe the MP, as resulted from solutions obtained in various implementations of the new 2-D timing technique. By 'locally' we mean in the vicinity of the Cluster constellation and around the time of the event. The parameters A_i and v characterize more globally the solutions but have no physical sense in general. We could not say, for example, that the MP moves with the initial velocity A_0 and acceleration A_1; only when the principal direction is close to the local normal this assertion becomes justified.

B.5 Combining MVAB with the timing analysis

We recall that in this technique we first impose the direction of the primary MP movement (i.e. the angle β in the plane perpendicular to the invariant direction) and than seek for the solution that satisfies the timing conditions. After such a solution has been found, than, with the help of formulas presented in Section B.4, we are in the position to compute the variance along the instantaneous normal or tangential direction for any quantities during the crossing time.

If a quantity obeys some conservation law at the MP then its variance will have a minimum across the discontinuity. Indeed, we know that, for example, in case of the magnetic field and for a planar geometry, the variance of this vector should be minimum along the MP normal (see Appendix A). This relies on the relation $\nabla \cdot \vec{B} = 0$, expressing the absence of magnetic poles, from which one obtains immediately that $\vec{B}_n$ is constant. For a 2-D MP the same condition should hold provided that the MP local radius of curvature is much bigger than its thickness. To see this we consider a cylindrical geometry and consider that all quantities depends only on the radial distance, when the expression of the divergence equation takes the form

$$\nabla \cdot \vec{B} = \frac{B_n}{r} + \frac{\partial B_n}{\partial r} = 0$$

resulting in the relation $rB_n = const.$. If the MP has a thickness of $2d$ and the local radius of curvature is R then the relative variation of the magnetic radial component during the crossing is

$$\frac{B_{n,R+2d} - B_{n,R}}{B_{n,R}} = -\frac{2d}{R} \ll 1 \tag{B.86}$$

Therefore, the variance along the radial direction (i.e. along $\vec{n}$) should be minimum. This implies that, in case of a 2-D combined analysis, it is well justified to select an optimum orientation for the primary direction (an optimum β) so that for the corresponding solution the global magnetic variance is minimum. By global we mean a weighted sum of the individual variances

$$\sigma_i^2 = \frac{1}{M_i} \sum_{m=1}^{M_i} \left| \left(\vec{B}_i^{(m)} - \langle \vec{B} \rangle_i \right) \cdot \vec{n}_{GEO,i}^{(m)} \right|^2 \qquad i = 1...4 \tag{B.87}$$

computed from the measurements $\vec{B}_i^{(m)}$, $m = 1...M_i$ taken by each of the four Cluster satellites. Here $n_{GEO,i}^{(m)}$ designates the 2-D, instantaneous geometrical normal, corresponding to satellite i. The super-script m indicates that these normals are changing in time and therefore, in the above formulas, the orientation of the normals at the time when the $B^{(m)}$ measurement is taken will be considered.

To be more specific about the way we implemented this criterion in the combined-analysis algorithms we say that:

- for each satellite, the time interval used for computing the variance is $\Delta_i = [T_{ci} - \tau_i, T_{ci} + \tau_i]$, i.e. the interval corresponding to the timing conditions. Strictly speaking, the solutions refer to these periods only and extrapolating them to longer intervals, although possible, should be made with care (see the discusions in Section 4.3)
- the weighting factors w_i we used for computing the global variance are inverse proportional to the sums of eigenvalues (the trace of the magnetic variance matrix) obtained

when a constrained MVA analysis on the magnetic field is performed for the intervals Δ_i. Here by constrained we mean in the plane perpendicular to the invariant direction $\vec{l}$.

$$w_i = \mathbf{Tr}_{c,i}^{-1}(\lambda) \Big/ \sum_{k=1}^{k=4} \mathbf{Tr}_{c,k}^{-1}(\lambda) \tag{B.88}$$

where $\mathbf{Tr}_{c,i}$ is the trace from the constrained MVA corresponding to satellite i.

As it was pointed out by *Sonnerup et al.* [2006], this is not the only way to chose the weighting factors w_i. The underlying argument we followed when addopting it was that the magnetic field measured by one satellite could be more 'agitated' (by whatever natural reason). In this case its contribution to the global variance should be diminished. Because the instantaneous normals are all contained in one plane we used the eigenvalues provided by MVA constrained in that plane too.

A similar procedure of combining the timing analysis could be imagined for any other quantity which obeys a conservation law at the MP traversal (like, for example, the magnetic flux, at the base of Minimum Faraday Residue technique). We can even combine different type of quantities and use them simultaneously by summing their variance (with some proper weighting factors) following the same procedure developed by *Sonnerup et al.* [2006] in case of the planar assumption.

Note that in the technique presented in this appendix, the algorithm finds self-consistently (i.e. in the same time) the parameters describing the MP orientation, curvature, thickness and motion. That aspect differentiates this work from that of *Mottez and Chanteur* [1994] and *Dunlop and Woodward* [1998, 1999], devoted also to characterize the curvature of a discontinuity and its motion when four points of measurements are available.

In these papers, the authors first apply the planar MVAB technique for each satellite and associate the result with the MP normal corresponding to the central crossing times at the satellite positions. Afterwards, the curvature and motion of the central MP surface is obtained by imposing a system of timing conditions. Proceeding in this way, the authors assume that the influence of the discontinuity motion and curvature on the result of the MVAB planar technique is of the second order. *Dunlop and Woodward* [1998, 1999] used simulated data to show how the determination of the normal, using the planar MVAB method, is influenced, in case of a curved boundary, by various effects like data interval length and spacecraft trajectory. If one wants to limit these effects, the analyzed discontinuity should be characterized by a large radius of curvature (relative to the thickness) and to use for MVAB only points from a thin interval around its centre (see also the discussions from Section 4.5).

In the method we developed, the possibility of self-consistently determine the MP crossing parameters is a consequence of the constant thickness assumption, adopted from the beginning in our models.

APPENDIX C

Tables and figures with the solutions found for the non-planar magnetopause

In this appendix we present the solutions obtained in various implementations of the 2-D, non-planar method. For each solution, a table containing values of several characteristic parameters (to be explained below), and an associated figure are provided.

Tables description

Parameters of the solution section presents the values of the unknowns that appear in the system of timing conditions. These are:

- the polynomial coefficients $A_0, A_1, ...$ describing the velocity along the primary direction and the velocity V along the secondary direction in cases when we allowed for two degrees of freedom for the MP movement.
- the parabolic coefficient a, or, in the case of the cylindrical model, the inner radius R. These quantities indicate the scale of the MP's 2-D feature.
- the initial coordinates of the MP leading edge peak in the parabolic model, or of the centre of curvature in the cylindrical model. C is along the primary direction (along $\vec{y}$ axis in Figures A to H) and w is along the other (i.e. $\vec{x}$) axis.
- the (constant) separation distance between the inner and outer MP edges in the parabolic model. According to the proposed model, this distance is along the primary direction (and not along the local MP normal). For the cylindrical model, the similar quantity represents the MP thickness and appears further down in the table.
- the angle between the principal direction and $\langle\vec{n}\rangle_{MVAB}$, representing the average of MVAB normals obtained in the nested analysis (and shown in Table 3.1). Both these directions are contained in the plane perpendicular to the invariant direction $\vec{l}$, with $\langle\vec{n}\rangle_{MVAB}$ being the reference direction in the Figures 3.7, 4.1 and 4.4. The angle is positive when the rotation from $\langle\vec{n}\rangle_{MVAB}$ to $\vec{y}$ is in the sense of $\vec{l}$.

Transition parameters section presents the individual and global values of normal velocity, thickness and radius of curvature. These quantities were computed using the formulas from Section B.4. For the parabolic model we show also how the thickness - defined as the distance

along the normal between the inner and outer edges - varies during transition (see equation (B.76)). In the cylindrical model, the geometrical mean of the inner and outer radius is shown. For the global quantities we computed the arithmetical mean (normal velocity and thickness) or the geometrical mean (radius of curvature) of the corresponding individual ones. Note that, according to the convention adopted in Section B.4, a negative radius of curvature means an indentation in the MP and a positive value means a bulge on this boundary.

Comparison with planar normals section presents:

- for each satellite, the angle between the average geometrical normal $\vec{n}_{GEO}^{\,ave}$ and the projection of the normal obtained from nested MVAB analysis on the plane perpendicular to the invariant direction $\vec{l}$. The quantities are positive when the rotation from $\vec{n}_{MVAB,}$ projection to $\vec{n}_{GEO}^{\,ave}$ is associated with the orientation for $\vec{l}$.
- for each satellite, the angle between the average geometrical normal $\vec{n}_{GEO}^{\,ave}$ and the constrained (i.e. perpendicular to $\vec{l}$) planar normal $\vec{n}_{MVAB,\,\perp\vec{l}}^{\,central}$ obtained when the constrained MVAB is applied on the central points of the transition.
- the variation in the orientation of the instantaneous geometrical normals during the crossing. Positive values correspond to a positive rotation from the leading edge normal to the trailing edge normal.

In calculating the global values (which in this case are simple arithmetical means) we used the absolute values of the individual quantities. For the global value of $\sphericalangle\left(\vec{n}_{GEO}^{\,ave},\ \vec{n}_{MVAB,\,\perp\vec{l}}^{\,central}\right)$ we showed in blue the result obtained when only Cluster 4, 3 and 1 were considered. All angles are expressed in degrees.

In **MVAB results** section all the quantities refer to the central crossing intervals (i.e. the intervals used in the timing equations) with the exception of the last line, containing the results from the nested MVAB analysis, where the procedure described in Section 3.4 applies. **2D** indicates that the corresponding parameters were computed by using only quantities contained in the plane perpendicular to $\vec{l}$, whereas **3D** parameters were computed without this restriction. The different lines refer to:

- the weighting factors used in computing the global values (i.e. in computing the average values over all four spacecraft). They are described by the equation (B.88).
- the magnetic field variance and the average normal magnetic field obtained when the instantaneous, geometrical normal is used.
- the magnetic field variance and the average normal magnetic field resulting when the planar MVAB technique is applied to the central crossing intervals. These quantities were obtained under the constraint that the normals are perpendicular to $\vec{l}$.
- the magnetic field variance along a constructed 3D normal, having the projection perpendicular to $\vec{l}$ given by the instantaneous geometrical normal $\vec{n}_{GEO}^{\,ave}$. The component along $\vec{l}$ is equal to the component of the corresponding nested MVAB normal along the same direction.
- the magnetic field variance from the nested MVAB analysis (also shown in the second column of Table 3.1).

We indicated in blue the global values obtained when only the results from Cluster 4, 3 and 1 are considered.

In **MFR results** section all the Faraday residues refer to the points from the central crossing intervals. $\vec{n}_{MFR}$ and $\vec{v}_{MFR}$ designate the normal vectors and normal velocities obtained in the planar MFR analysis (values appearing also in Table 4.1). Note that these quantities were

obtained from the constrained (to $B_n = 0$) MFR analysis applied to the intervals shown in Figure 4.4. **2D** and **3D** have the same meaning as in the **MVAB results** section. The different lines refer to:

- the weighting factors used in computing the global values. They are described by the equation (4.4).
- Faraday residues (FR) obtained when the instantaneous normal velocity and normal direction provided by the 2-D method are used.
- Faraday residues computed by using the projection on the plane perpendicular to $\vec{l}$ of $\vec{n}_{MFR}$ and $\vec{v}_{MFR}$.
- Faraday residues computed by using a 3D normal and an associated velocity along it. These 3D quantities are constructed from the instantaneous normal and velocity provided by the 2-D solution by adding to them a component along $\vec{l}$ so that the resulting vectors have the same inclination with respect to $\vec{l}$ as the corresponding $\vec{n}_{MFR}$.
- Faraday residues on the central intervals computed by using $\vec{n}_{MFR}$ and $\vec{v}_{MFR}$.

We indicated in red the global values obtained when only the results from the trailing pair of satellites (i.e. from Cluster 3 and Cluster 1) are considered.
DeHoffmann–Teller results section presents:

- the projection of $\vec{V}_{HT}$ along the average geometrical normal, computed for the time interval of the HT analysis (i.e. the time interval appearing in the second column of Table 4.1). Because these intervals are nearly identical to the central crossing intervals, the above mentioned normals are practically identical to $\vec{n}_{GEO}^{ave}$.
- the projection of $\vec{V}_{HT}$ along the normals provided by the nested MVAB analysis.

Figures description

The Figures A to H present the solutions for the 2-D, non-planar MP found in various implementations of the new method. Primary movement takes place along $\vec{y}$ while the so-called secondary direction is oriented along $\vec{x}$. Therefore the drawings are MP cuts made with a plane perpendicular to the invariant direction $\vec{l}$ (which points into the page). The satellite positions are indicated by the dots coloured according to the mission convention (Cluster 1 - black, Cluster 2 - red, Cluster 3 - green and Cluster 4 - blue).

Each of the four panels is associated with one satellite and shows the MP configuration at two moments: when the satellite in question enters the layer (light gray) and when it leaves the layer (darker gray). The MP geometrical normals at these two moments and at the satellite position are shown, together with the individual normal obtained from the planar, nested MVAB technique (actually the projection of this on the plane perpendicular to the invariant direction).

In the third panel, besides $\vec{y}$ and $\vec{x}$ unit vectors, the average of the planar, nested MVAB normals as well as a 'global' normal, obtained as the vectorial mean of the individual average geometrical normals $\vec{n}_{GEO}^{ave}$ are shown with $\langle\vec{n}\rangle_{MVAB}$ and $\langle\vec{n}\rangle_{ext}$ symbols, respectively. In the fourth panel, the orientation of the $\vec{X}_{GSM}$, $\vec{Y}_{GSM}$ and $\vec{Z}_{GSM}$ unit vectors are indicated.

In Figure G, presenting the Cyl_2deg_OpTA_solA solution, we showed in each panel with orange arrows the $\vec{n}_{MVAB,\perp\vec{l}}^{central}$ normals, obtained from the constrained (i.e. perpendicular to $\vec{l}$) planar MVAB normals corresponding to the central intervals.

Table A: Parabolic MP with 2 degrees of freedom
Parameters from the plain timing analysis

			Average/global quantity	Satellite Cluster 2	Cluster 4	Cluster 3	Cluster 1
Parameters of the solution							
velocity coefficients	A_0	$[km/s]$	-6226.6				
	A_1	$[km/s^2]$	-598.6				
	V	$[km/s]$	-2556.2				
parabolic coefficient	a	$[km^{-1}]$	$4.58 \cdot 10^{-5}$				
peak initial coord.	w	$[km]$	-28093.8				
	C	$[km]$	-36144.3				
inter-margins distance	$2d$	$[km]$	4509.4				
$\sphericalangle$ (primary dir., $\langle\vec{n}\rangle_{MVAB}$)		$[deg]$	-88.8				
Transition parameters							
normal velocity		$[km/s]$	50.58	86.79	75.73	20.86	18.96
thickness		$[km]$	704.5	1118.4	975.8	371.8	352.1
thickness variation		$[\%]$	62	71	72	34	34
radius of curvature		$[R_E]$	-784.7	-143.1	-214.6	-3240.6	-3810.3
Comparison with planar normals							
$\sphericalangle\ (\vec{n}_{GEO}^{\,ave}\,,\ \vec{n}_{MVAB,\perp\vec{l}}^{\,nested})$		$[deg]$	10.51	-19.60	-17.11	2.13	3.19
$\sphericalangle\ (\vec{n}_{GEO}^{\,ave}\,,\ \vec{n}_{MVAB,\perp\vec{l}}^{\,central})$		$[deg]$	18.92 15.76	-28.41	-16.09	14.83	16.35
$\Delta\vec{n}_{GEO}$		$[deg]$	5.95	11.10	9.52	1.64	1.53
MVAB results		$[nT]^2$ or $[nT]$					
	weighting factors			0.223	0.285	0.215	0.276
2D	variance using $\vec{n}_{GEO}$		7.505 5.811	13.409	4.168	6.276	7.146
	$\langle B_n\rangle$ using $\vec{n}_{GEO}$			-2.85	-3.54	0.41	0.51
	variance using $\vec{n}_{MVAB,\perp\vec{l}}^{\,central}$		2.724 2.697	2.820	1.163	2.794	4.206
	$\langle B_n\rangle$ using $\vec{n}_{MVAB,\perp\vec{l}}^{\,central}$			1.44	-1.75	-1.35	-1.58
3D	variance using $\vec{n}_{GEO,\,3D}$		7.461 5.929	12.797	4.458	6.436	7.054
	variance from nested MVAB		3.587 3.448	4.088	4.639	2.580	2.894
MFR results		$[mV/m]^2$					
	weighting factors			0.289	0.362	0.176	0.173
2D	FR using $\vec{n}_{GEO}$ and $\vec{v}_{GEO}$		2.077 3.737	1.752	0.736	2.677	4.818
	FR using $\vec{n}_{MFR,\,2D}$ and $\vec{v}_{MFR,\,2D}$		2.724 2.920	0.559	4.267	2.415	3.434
3D	FR using $\vec{n}_{GEO,\,3D}$ and $\vec{v}_{GEO,\,3D}$		2.144 3.802	1.871	0.763	2.799	4.824
	FR using $\vec{n}_{MFR}$ and $\vec{v}_{MFR}$		2.649 2.847	0.464	4.206	2.282	3.422
deHoffmann–Teller results		$[km/s]$					
	V_{HT} along $\vec{n}_{GEO}^{\,ave}$		25.09	72.95	23.45	-21.54	25.52
	V_{HT} along $\vec{n}_{MVAB}^{\,nested}$		22.25	86.64	-5.78	-14.44	22.56

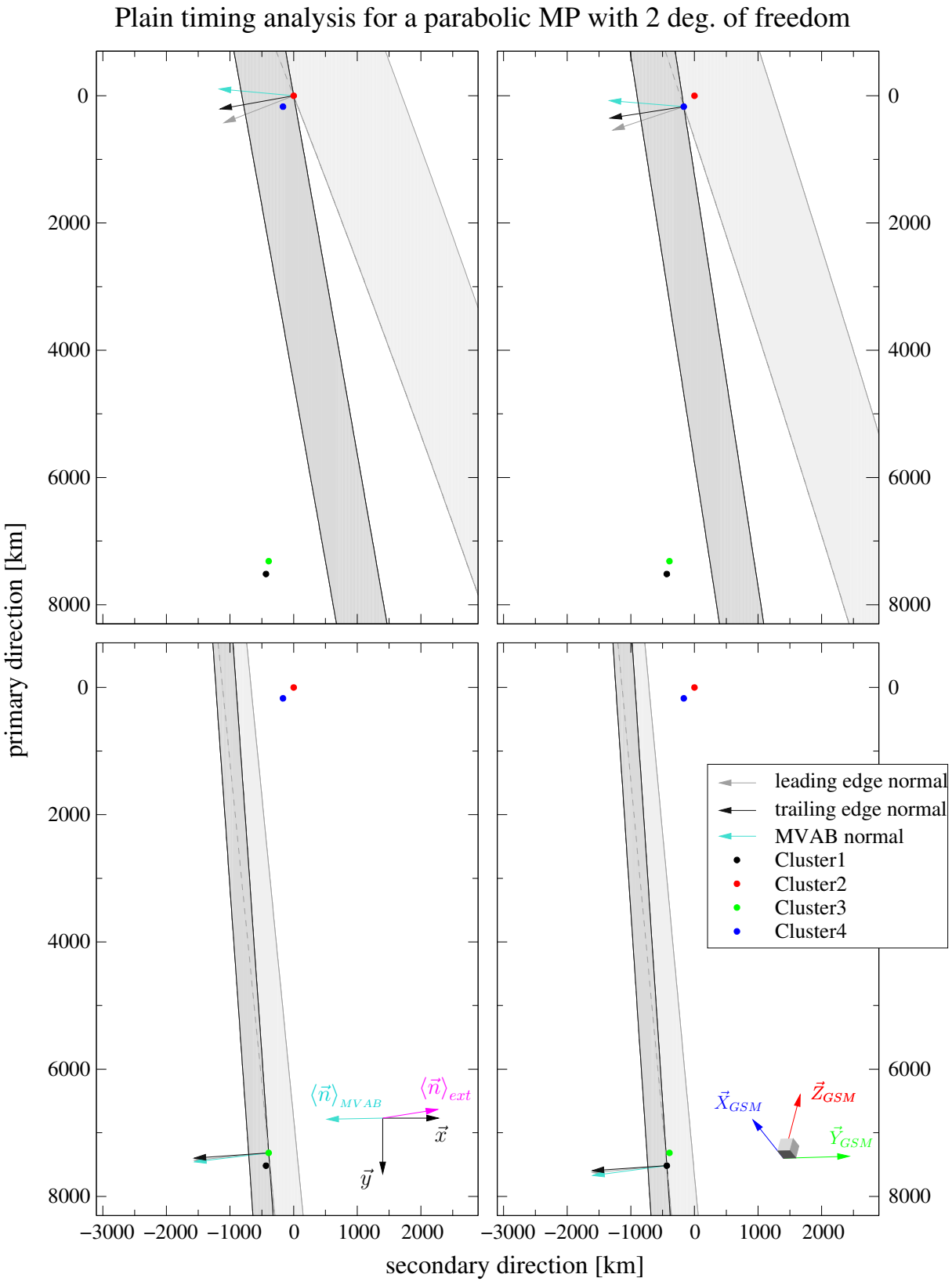

Figure A: For details see the explanations at page 165

Table B: Parabolic MP with 1 degree of freedom
Parameters from combined timing - magnetic variance analysis

			Average/global quantity	Satellite			
				Cluster 2	Cluster 4	Cluster 3	Cluster 1
Parameters of the solution							
velocity coefficients	A_0	$[km/s]$	89.60				
	A_1	$[km/s^2]$	-5.374				
	A_2	$[km/s^3]$	0.1925				
	A_3	$[km/s^4]$	$2.10 \cdot 10^{-3}$				
parabolic coefficient	a	$[km^{-1}]$	$-2.96 \cdot 10^{-5}$				
peak initial coord.	w	$[km]$	2109.2				
	C	$[km]$	131.5				
inter-margins distance	$2d$	$[km]$	831.4				
$\sphericalangle$ (primary dir., $\langle\vec{n}\rangle_{MVAB}$)		$[deg]$	-3.9				
Transition parameters							
normal velocity		$[km/s]$	52.04	64.02	56.84	44.63	42.68
thickness		$[km]$	809.8	825.0	825.9	795.4	792.8
thickness variation		$[\%]$	0.2	0.1	0.1	0.4	0.4
radius of curvature		$[R_E]$	2.87	2.72	2.71	3.03	3.06
Comparison with planar normals							
$\sphericalangle\ (\vec{n}^{\,ave}_{GEO}\,,\ \vec{n}^{\,nested}_{MVAB,\perp\vec{l}})$		$[deg]$	9.08	-3.20	-3.10	-15.12	-14.92
$\sphericalangle\ (\vec{n}^{\,ave}_{GEO}\,,\ \vec{n}^{\,central}_{MVAB,\perp\vec{l}})$		$[deg]$	4.57 2.09	-12.01	-2.08	-2.42	-1.76
$\Delta\vec{n}_{GEO}$		$[deg]$	0.0	0.0	0.0	0.0	0.0
MVAB results		$[nT]^2$ or $[nT]$					
	weighting factors			0.223	0.285	0.215	0.276
2D	variance using $\vec{n}_{GEO}$		3.276 2.758	5.085	1.219	2.891	4.243
	$\langle B_n\rangle$ using $\vec{n}_{GEO}$			-0.53	-2.03	-1.63	-1.79
	variance using $\vec{n}^{\,central}_{MVAB,\perp\vec{l}}$		2.724 2.697	2.820	1.163	2.794	4.206
	$\langle B_n\rangle$ using $\vec{n}^{\,central}_{MVAB,\perp\vec{l}}$			1.44	-1.75	-1.35	-1.58
3D	variance using $\vec{n}_{GEO,\,3D}$		3.235 2.798	4.761	1.238	2.625	4.543
	variance from nested MVAB		3.587 3.448	4.088	4.639	2.580	2.894
MFR results		$[mV/m]^2$					
	weighting factors			0.289	0.362	0.176	0.173
2D	FR using $\vec{n}_{GEO}$ and $\vec{v}_{GEO}$		1.706 2.672	1.419	1.004	1.982	3.374
	FR using $\vec{n}_{MFR,\,2D}$ and $\vec{v}_{MFR,\,2D}$		2.724 2.920	0.559	4.267	2.415	3.434
3D	FR using $\vec{n}_{GEO,\,3D}$ and $\vec{v}_{GEO,\,3D}$		1.763 2.781	1.473	1.014	2.182	3.391
	FR using $\vec{n}_{MFR}$ and $\vec{v}_{MFR}$		2.649 2.847	0.464	4.206	2.282	3.422
deHoffmann–Teller results		$[km/s]$					
	V_{HT} along $\vec{n}^{\,ave}_{GEO}$		32.61	83.47	1.75	17.96	27.24
	V_{HT} along $\vec{n}^{\,nested}_{MVAB}$		22.25	86.64	-5.78	-14.44	22.56

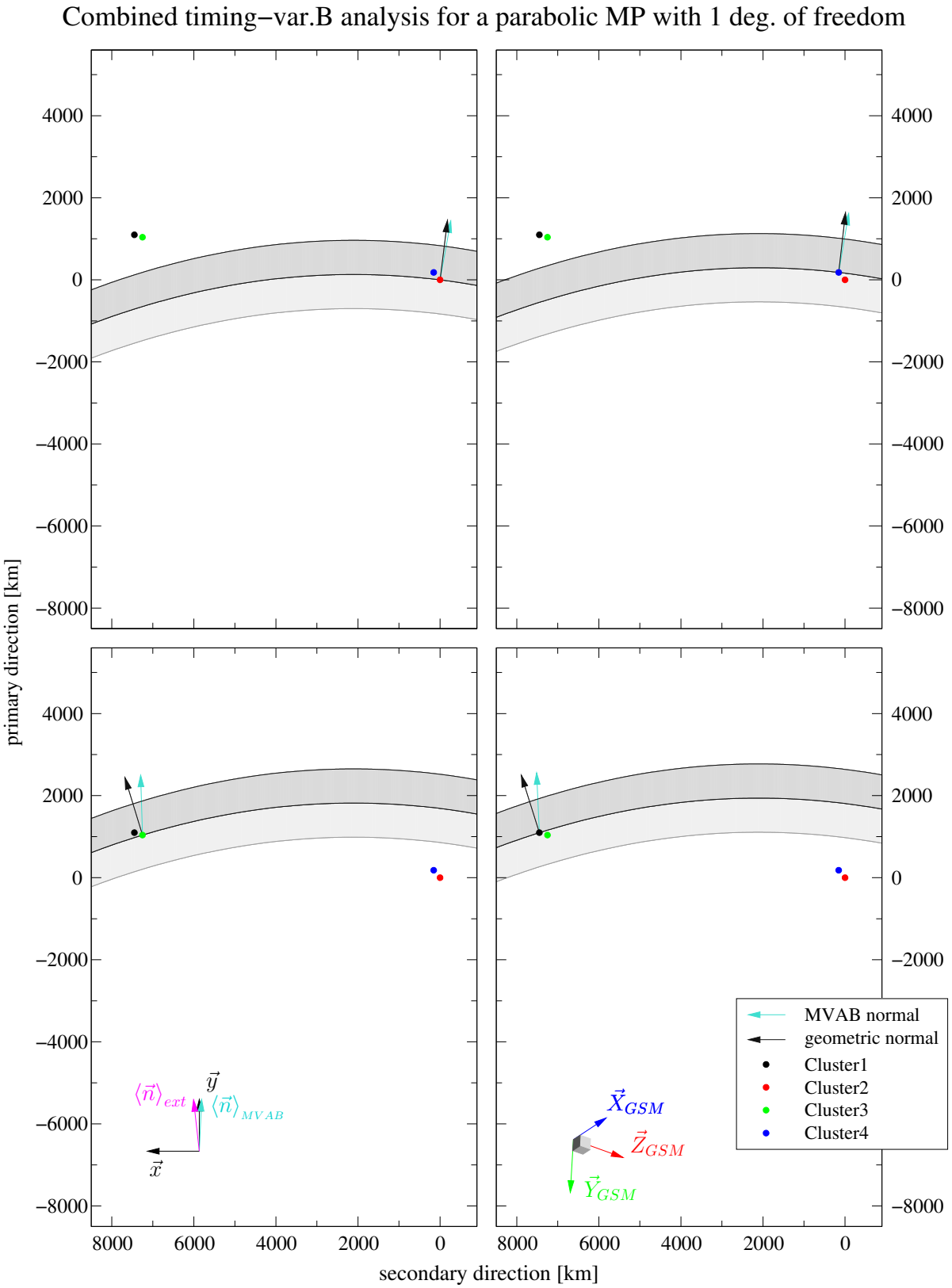

Figure B: For details see the explanations at page 165

Table C: Parabolic MP with 2 degrees of freedom
Parameters from combined timing - magnetic variance analysis

			Average/global	Satellite			
			quantity	Cluster 2	Cluster 4	Cluster 3	Cluster 1
Parameters of the solution							
velocity coefficients	A_0	$[km/s]$	70.92				
	A_1	$[km/s^2]$	-3.26				
	A_2	$[km/s^3]$	$3.10 \cdot 10^{-2}$				
	V	$[km/s]$	77.88				
parabolic coefficient	a	$[km^{-1}]$	$-6.25 \cdot 10^{-5}$				
peak initial coord.	w	$[km]$	-2058.6				
	C	$[km]$	265.0				
inter-margins distance	$2d$	$[km]$	860.8				
$\sphericalangle$ (primary dir., $\langle\vec{n}\rangle_{MVAB}$)		$[deg]$	16.8				
Transition parameters							
normal velocity		$[km/s]$	49.74	65.44	58.00	38.51	37.00
thickness		$[km]$	764.9	843.3	842.8	686.2	687.3
thickness variation		$[\%]$	4	2	2	6	6
radius of curvature		$[R_E]$	1.81	1.33	1.33	2.46	2.45
Comparison with planar normals							
$\sphericalangle\ (\vec{n}_{GEO}^{\,ave}\,,\ \vec{n}_{MVAB,\perp\vec{l}}^{\,nested})$		$[deg]$	7.09	-0.61	0.05	-14.32	-13.39
$\sphericalangle\ (\vec{n}_{GEO}^{\,ave}\,,\ \vec{n}_{MVAB,\perp\vec{l}}^{\,central})$		$[deg]$	3.09 0.97	-9.42	1.07	-1.62	-0.23
$\Delta\vec{n}_{GEO}$		$[deg]$	6.94	6.92	7.80	6.37	6.66
MVAB results		$[nT]^2$ or $[nT]$					
	weighting factors			0.223	0.285	0.215	0.276
2D	variance using $\vec{n}_{GEO}$		2.764 2.518	3.624	1.446	2.579	3.577
	$\langle B_n\rangle$ using $\vec{n}_{GEO}$			0.11	-1.37	-1.37	-1.43
	variance using $\vec{n}_{MVAB,\perp\vec{l}}^{\,central}$		2.724 2.697	2.820	1.163	2.794	4.206
	$\langle B_n\rangle$ using $\vec{n}_{MVAB,\perp\vec{l}}^{\,central}$			1.44	-1.75	-1.35	-1.58
3D	variance using $\vec{n}_{GEO,3D}$		2.701 2.501	3.402	1.344	2.367	3.800
	variance from nested MVAB		3.587 3.448	4.088	4.639	2.580	2.894
MFR results		$[mV/m]^2$					
	weighting factors			0.289	0.362	0.176	0.173
2D	FR using $\vec{n}_{GEO}$ and $\vec{v}_{GEO}$		1.762 2.751	1.246	1.219	2.033	3.483
	FR using $\vec{n}_{MFR,2D}$ and $\vec{v}_{MFR,2D}$		2.724 2.920	0.559	4.267	2.415	3.434
3D	FR using $\vec{n}_{GEO,3D}$ and $\vec{v}_{GEO,3D}$		1.812 2.851	1.297	1.222	2.215	3.498
	FR using $\vec{n}_{MFR}$ and $\vec{v}_{MFR}$		2.649 2.847	0.464	4.206	2.282	3.422
deHoffmann–Teller results		$[km/s]$					
	V_{HT} along $\vec{n}_{GEO}^{\,ave}$		31.47	84.53	-2.70	16.85	27.19
	V_{HT} along $\vec{n}_{MVAB}^{\,nested}$		22.25	86.64	-5.78	-14.44	22.56

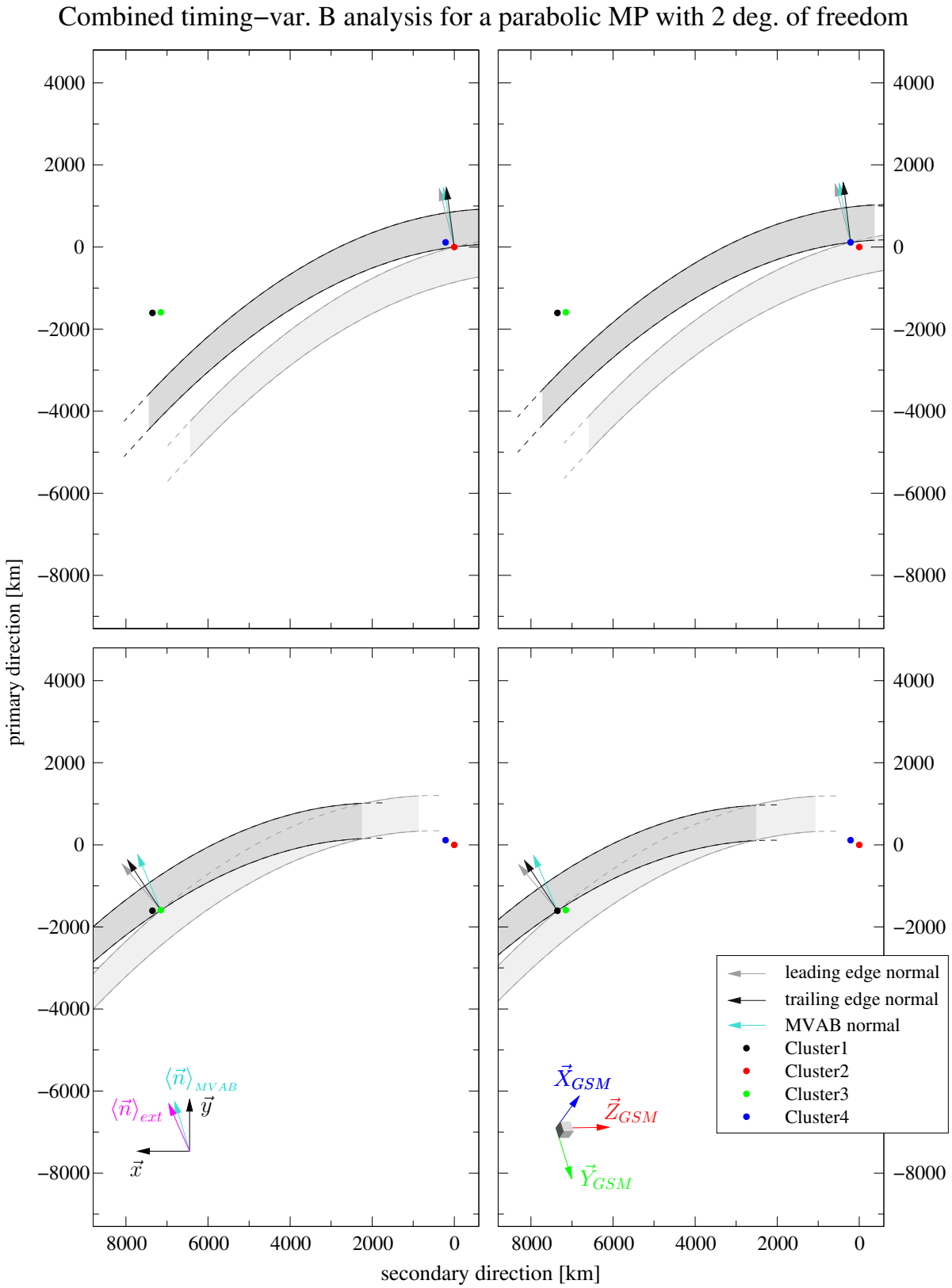

Figure C: For details see the explanations at page 165

Table D: Cylindrical MP with 1 degree of freedom
Parameters from the plain timing analysis

			Average/global	Satellite			
			quantity	Cluster 2	Cluster 4	Cluster 3	Cluster 1
Parameters of the solution							
velocity coefficients	A_0	$[km/s]$	-161.58				
	A_1	$[km/s^2]$	8.397				
	A_2	$[km/s^3]$	-0.2505				
inner radius	R	$[km]$	30277.3				
centre initial coord.	w	$[km]$	25624.6				
	C	$[km]$	17691.1				
$\sphericalangle$ (primary dir., $\langle\vec{n}\rangle_{MVAB}$)		$[deg]$	-122.9				
Transition parameters							
normal velocity		$[km/s]$	55.19	66.82	59.26	48.32	46.35
thickness		$[km]$	861.1	861.1	861.1	861.1	861.1
radius of curvature		$[R_E]$	4.82	4.82	4.82	4.82	4.82
Comparison with planar normals							
$\sphericalangle\ (\vec{n}_{GEO}^{\,ave}\,,\ \vec{n}_{MVAB,\,\perp\vec{l}}^{\,nested})$		$[deg]$	10.96	-5.96	-6.14	-15.38	-16.36
$\sphericalangle\ (\vec{n}_{GEO}^{\,ave}\,,\ \vec{n}_{MVAB,\,\perp\vec{l}}^{\,central})$		$[deg]$	6.44 3.67	-14.77	-5.12	-2.68	-3.20
$\Delta\vec{n}_{GEO}$		$[deg]$	5.73	-2.44	-2.51	-8.12	-9.86
MVAB results		$[nT]^2$ or $[nT]$					
	weighting factors			0.223	0.285	0.215	0.276
2D	variance using $\vec{n}_{GEO}$		4.191 3.527	6.507	1.530	3.451	5.647
	$\langle B_n\rangle$ using $\vec{n}_{GEO}$			-1.07	-2.51	-1.85	-2.20
	variance using $\vec{n}_{MVAB,\,\perp\vec{l}}^{\,central}$		2.724 2.697	2.820	1.163	2.794	4.206
	$\langle B_n\rangle$ using $\vec{n}_{MVAB,\,\perp\vec{l}}^{\,central}$			1.44	-1.75	-1.35	-1.58
3D	variance using $\vec{n}_{GEO,\,3D}$		4.172 3.618	6.108	1.632	3.131	6.048
	variance from nested MVAB		3.587 3.448	4.088	4.639	2.580	2.894
MFR results		$[mV/m]^2$					
	weighting factors			0.289	0.362	0.176	0.173
2D	FR using $\vec{n}_{GEO}$ and $\vec{v}_{GEO}$		1.687 2.617	1.545	0.903	1.945	3.303
	FR using $\vec{n}_{MFR,\,2D}$ and $\vec{v}_{MFR,\,2D}$		2.724 2.920	0.559	4.267	2.415	3.434
3D	FR using $\vec{n}_{GEO,\,3D}$ and $\vec{v}_{GEO,\,3D}$		1.746 2.726	1.602	0.917	2.142	3.321
	FR using $\vec{n}_{MFR}$ and $\vec{v}_{MFR}$		2.649 2.847	0.464	4.206	2.282	3.422
deHoffmann–Teller results		$[km/s]$					
	V_{HT} along $\vec{n}_{GEO}^{\,ave}$		33.34	82.16	6.14	17.79	27.27
	V_{HT} along $\vec{n}_{MVAB}^{\,nested}$		22.25	86.64	-5.78	-14.44	22.56

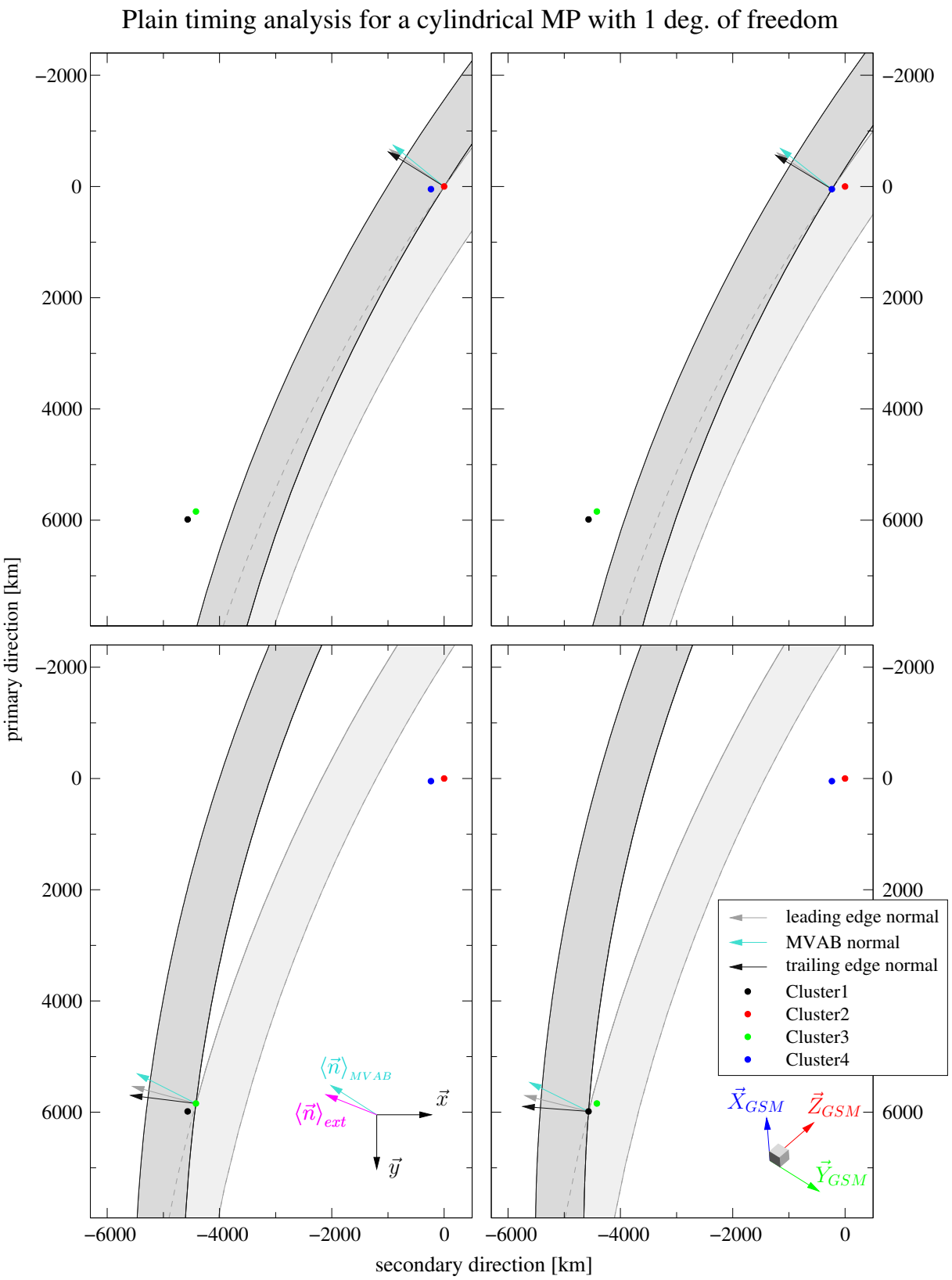

Figure D: For details see the explanations at page 165

Table E: Cylindrical MP with 2 degrees of freedom
Parameters from the plain timing analysis

			Average/global	Satellite			
			quantity	Cluster 2	Cluster 4	Cluster 3	Cluster 1
Parameters of the solution							
velocity coefficients	A_0	$[km/s]$	−87.47				
	A_1	$[km/s^2]$	4.961				
	V	$[km/s]$	−36.65				
inner radius	R	$[km]$	11418.5				
centre initial coord.	w	$[km]$	10801.9				
	C	$[km]$	5581.7				
◁ (primary dir., $\langle\vec{n}\rangle_{MVAB}$)		$[deg]$	−105.3				
Transition parameters							
normal velocity		$[km/s]$	47.45	57.45	50.95	41.54	39.85
thickness		$[km]$	740.3	740.3	740.3	740.3	740.3
radius of curvature		$[R_E]$	1.85	1.85	1.85	1.85	1.85
Comparison with planar normals							
◁ $\left(\vec{n}_{GEO}^{\,ave}\,,\ \vec{n}_{MVAB,\,\perp\vec{l}}^{\,nested}\right)$		$[deg]$	7.88	4.35	3.68	−12.63	−10.87
◁ $\left(\vec{n}_{GEO}^{\,ave}\,,\ \vec{n}_{MVAB,\,\perp\vec{l}}^{\,central}\right)$		$[deg]$	2.88 2.35	−4.46	4.70	0.07	2.29
$\Delta\vec{n}_{GEO}$		$[deg]$	6.40	−2.10	−1.58	10.05	11.87
MVAB results		$[nT]^2$ or $[nT]$					
	weighting factors			0.223	0.285	0.215	0.276
2D	variance using $\vec{n}_{GEO}$		2.497 2.261	3.321	1.395	2.282	3.138
	$\langle B_n\rangle$ using $\vec{n}_{GEO}$			0.64	−1.17	−1.09	−1.00
	variance using $\vec{n}_{MVAB,\,\perp\vec{l}}^{\,central}$		2.724 2.697	2.820	1.163	2.794	4.206
	$\langle B_n\rangle$ using $\vec{n}_{MVAB,\,\perp\vec{l}}^{\,central}$			1.44	−1.75	−1.35	−1.58
3D	variance using $\vec{n}_{GEO,\,3D}$		2.427 2.219	3.154	1.268	2.139	3.263
	variance from nested MVAB		3.587 3.448	4.088	4.639	2.580	2.894
MFR results		$[mV/m]^2$					
	weighting factors			0.289	0.362	0.176	0.173
2D	FR using $\vec{n}_{GEO}$ and $\vec{v}_{GEO}$		1.783 2.867	1.188	1.214	2.135	3.613
	FR using $\vec{n}_{MFR,\,2D}$ and $\vec{v}_{MFR,\,2D}$		2.724 2.920	0.559	4.267	2.415	3.434
3D	FR using $\vec{n}_{GEO,\,3D}$ and $\vec{v}_{GEO,\,3D}$		1.822 2.958	1.215	1.212	2.303	3.626
	FR using $\vec{n}_{MFR}$ and $\vec{v}_{MFR}$		2.649 2.847	0.464	4.206	2.282	3.422
deHoffmann–Teller results		$[km/s]$					
	V_{HT} along $\vec{n}_{GEO}^{\,ave}$		29.42	86.06	−8.61	13.18	27.06
	V_{HT} along $\vec{n}_{MVAB}^{\,nested}$		22.25	86.64	−5.78	−14.44	22.56

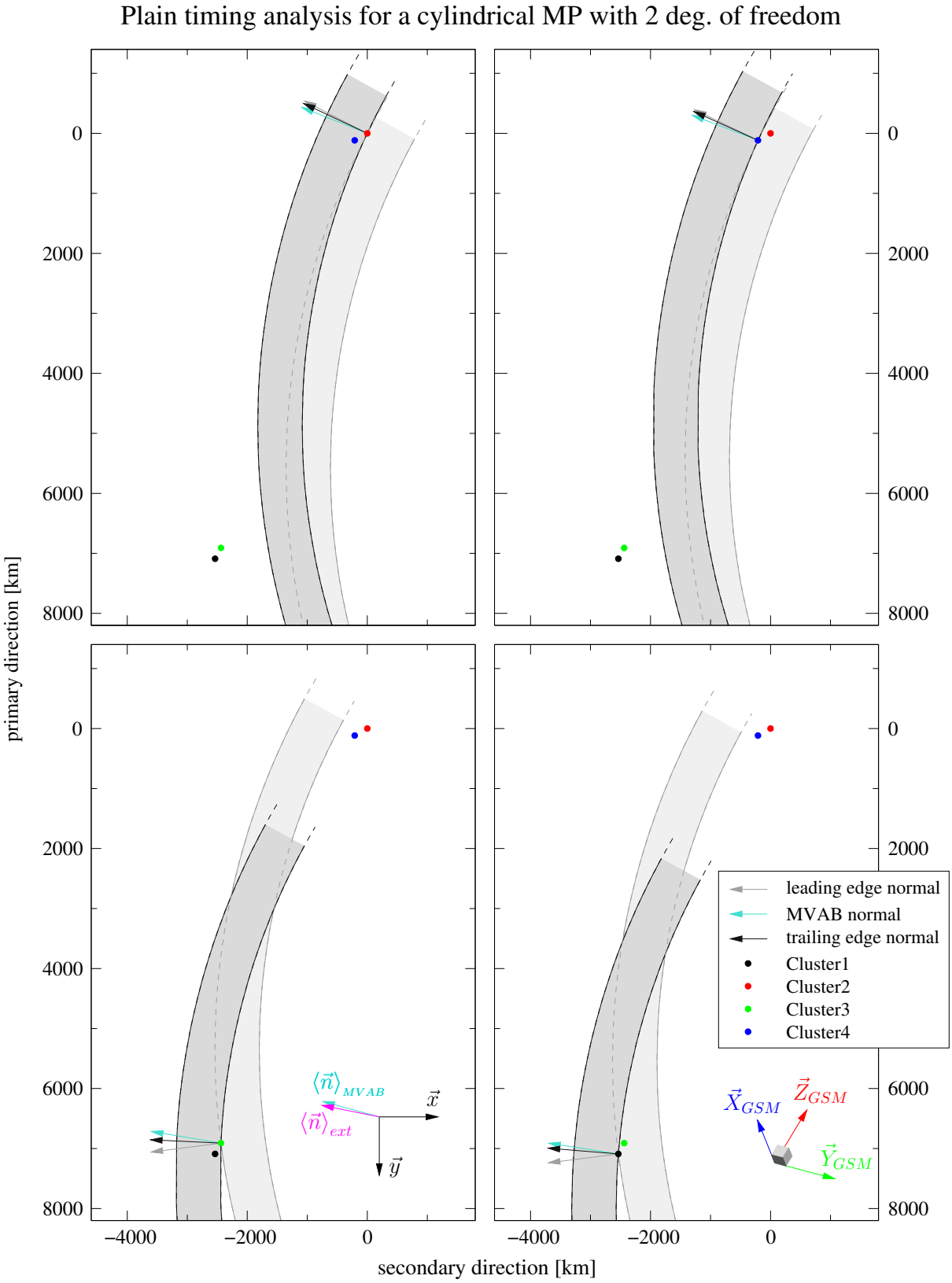

Figure E: For details see the explanations at page 165

Table F: Cylindrical MP with 1 degree of freedom
Parameters from combined timing - magnetic variance analysis

			Average/global	Satellite			
			quantity	Cluster 2	Cluster 4	Cluster 3	Cluster 1
Parameters of the solution							
velocity coefficients	A_0	$[km/s]$	116.01				
	A_1	$[km/s^2]$	-6.430				
	A_2	$[km/s^3]$	0.201				
	A_3	$[km/s^4]$	$2.05 \cdot 10^{-3}$				
inner radius	R	$[km]$	12904.9				
centre initial coord.	w	$[km]$	8708.4				
	C	$[km]$	-10613.9				
$\sphericalangle$ (primary dir., $\langle\vec{n}\rangle_{MVAB}$)		$[deg]$	-37.1				
Transition parameters							
normal velocity		$[km/s]$	52.84	63.97	56.73	46.26	44.38
thickness		$[km]$	824.4	824.4	824.4	824.4	824.4
radius of curvature		$[R_E]$	2.09	2.09	2.09	2.09	2.09
Comparison with planar normals							
$\sphericalangle\ (\vec{n}_{GEO}^{\,ave}\,,\ \vec{n}_{MVAB,\perp\vec{l}}^{\,nested})$		$[deg]$	9.75	-2.42	-1.97	-17.43	-17.19
$\sphericalangle\ (\vec{n}_{GEO}^{\,ave}\,,\ \vec{n}_{MVAB,\perp\vec{l}}^{\,central})$		$[deg]$	5.24 3.24	-11.23	-0.95	-4.73	-4.03
$\Delta\vec{n}_{GEO}$		$[deg]$	1.96	3.07	3.05	0.88	0.84
MVAB results		$[nT]^2$ or $[nT]$					
	weighting factors			0.223	0.285	0.215	0.276
2D	variance using $\vec{n}_{GEO}$		3.220 2.852	4.503	1.225	3.132	4.315
	$\langle B_n\rangle$ using $\vec{n}_{GEO}$			-0.31	-1.79	-1.87	-2.05
	variance using $\vec{n}_{MVAB,\perp\vec{l}}^{\,central}$		2.724 2.697	2.820	1.163	2.794	4.206
	$\langle B_n\rangle$ using $\vec{n}_{MVAB,\perp\vec{l}}^{\,central}$			1.44	-1.75	-1.35	-1.58
3D	variance using $\vec{n}_{GEO,\,3D}$		3.175 2.877	4.214	1.200	2.816	4.656
	variance from nested MVAB		3.587 3.448	4.088	4.639	2.580	2.894
MFR results		$[mV/m]^2$					
	weighting factors			0.289	0.362	0.176	0.173
2D	FR using $\vec{n}_{GEO}$ and $\vec{v}_{GEO}$		1.684 2.581	1.366	1.073	1.951	3.224
	FR using $\vec{n}_{MFR,\,2D}$ and $\vec{v}_{MFR,\,2D}$		2.724 2.920	0.559	4.267	2.415	3.434
3D	FR using $\vec{n}_{GEO,\,3D}$ and $\vec{v}_{GEO,\,3D}$		1.736 2.687	1.411	1.078	2.143	3.241
	FR using $\vec{n}_{MFR}$ and $\vec{v}_{MFR}$		2.649 2.847	0.464	4.206	2.282	3.422
deHoffmann–Teller results		$[km/s]$					
	V_{HT} along $\vec{n}_{GEO}^{\,ave}$		33.67	83.81	0.27	23.33	27.27
	V_{HT} along $\vec{n}_{MVAB}^{\,nested}$		22.25	86.64	-5.78	-14.44	22.56

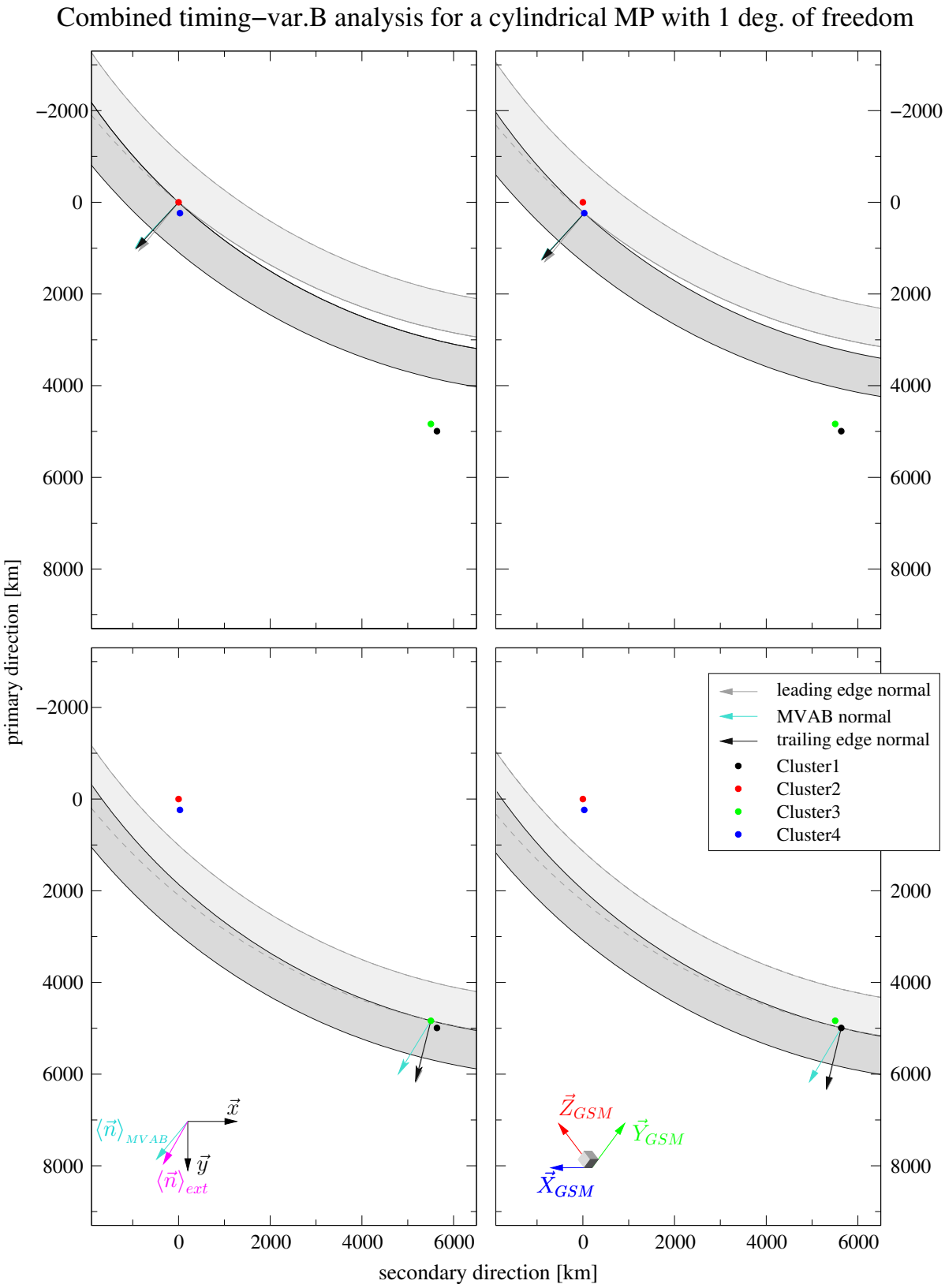

Figure F: For details see the explanations at page 165

Table G: Cylindrical MP with 2 degrees of freedom
Parameters from combined timing - magnetic variance analysis. Solution A

			Average/global	Satellite			
			quantity	Cluster 2	Cluster 4	Cluster 3	Cluster 1
Parameters of the solution							
velocity coefficients	A_0	$[km/s]$	-87.68				
	A_1	$[km/s^2]$	4.961				
	A_2	$[km/s^3]$	$2.56 \cdot 10^{-4}$				
	V	$[km/s]$	-36.59				
inner radius	R	$[km]$	11431.8				
centre initial coord.	w	$[km]$	10817.9				
	C	$[km]$	5579.7				
$\sphericalangle$ (primary dir., $\langle\vec{n}\rangle_{MVAB}$)		$[deg]$	-105.2				
Transition parameters							
normal velocity		$[km/s]$	47.45	57.44	50.94	41.54	39.85
thickness		$[km]$	740.3	740.3	740.3	740.3	740.3
radius of curvature		$[R_E]$	1.85	1.85	1.85	1.85	1.85
Comparison with planar normals							
$\sphericalangle$ $(\vec{n}_{GEO}^{\,ave}, \vec{n}_{MVAB,\perp\vec{l}}^{\,nested})$		$[deg]$	7.87	4.35	3.68	-12.61	-10.85
$\sphericalangle$ $(\vec{n}_{GEO}^{\,ave}, \vec{n}_{MVAB,\perp\vec{l}}^{\,central})$		$[deg]$	2.89 2.36	-4.46	4.69	0.09	2.31
$\Delta\vec{n}_{GEO}$		$[deg]$	6.41	-2.11	-1.60	10.06	11.88
MVAB results		$[nT]^2$ or $[nT]$					
	weighting factors			0.223	0.285	0.215	0.276
2D	variance using $\vec{n}_{GEO}$		2.497 2.260	3.323	1.394	2.281	3.138
	$\langle B_n\rangle$ using $\vec{n}_{GEO}$			0.63	-1.17	-1.09	-0.99
	variance using $\vec{n}_{MVAB,\perp\vec{l}}^{\,central}$		2.724 2.697	2.820	1.163	2.794	4.206
	$\langle B_n\rangle$ using $\vec{n}_{MVAB,\perp\vec{l}}^{\,central}$			1.44	-1.75	-1.35	-1.58
3D	variance using $\vec{n}_{GEO,3D}$		2.427 2.218	3.155	1.267	2.138	3.263
	variance from nested MVAB		3.587 3.448	4.088	4.639	2.580	2.894
MFR results		$[mV/m]^2$					
	weighting factors			0.289	0.362	0.176	0.173
2D	FR using $\vec{n}_{GEO}$ and $\vec{v}_{GEO}$		1.784 2.868	1.189	1.214	2.136	3.614
	FR using $\vec{n}_{MFR,2D}$ and $\vec{v}_{MFR,2D}$		2.724 2.920	0.559	4.267	2.415	3.434
3D	FR using $\vec{n}_{GEO,3D}$ and $\vec{v}_{GEO,3D}$		1.823 2.959	1.215	1.212	2.303	3.628
	FR using $\vec{n}_{MFR}$ and $\vec{v}_{MFR}$		2.649 2.847	0.464	4.206	2.282	3.422
deHoffmann–Teller results		$[km/s]$					
	V_{HT} along $\vec{n}_{GEO}^{\,ave}$		29.41	86.06	-8.61	13.14	27.06
	V_{HT} along $\vec{n}_{MVAB}^{\,nested}$		22.25	86.64	-5.78	-14.44	22.56

Combined timing – var. B analysis for a cylindrical MP with 2 deg. of freedom. Solution A

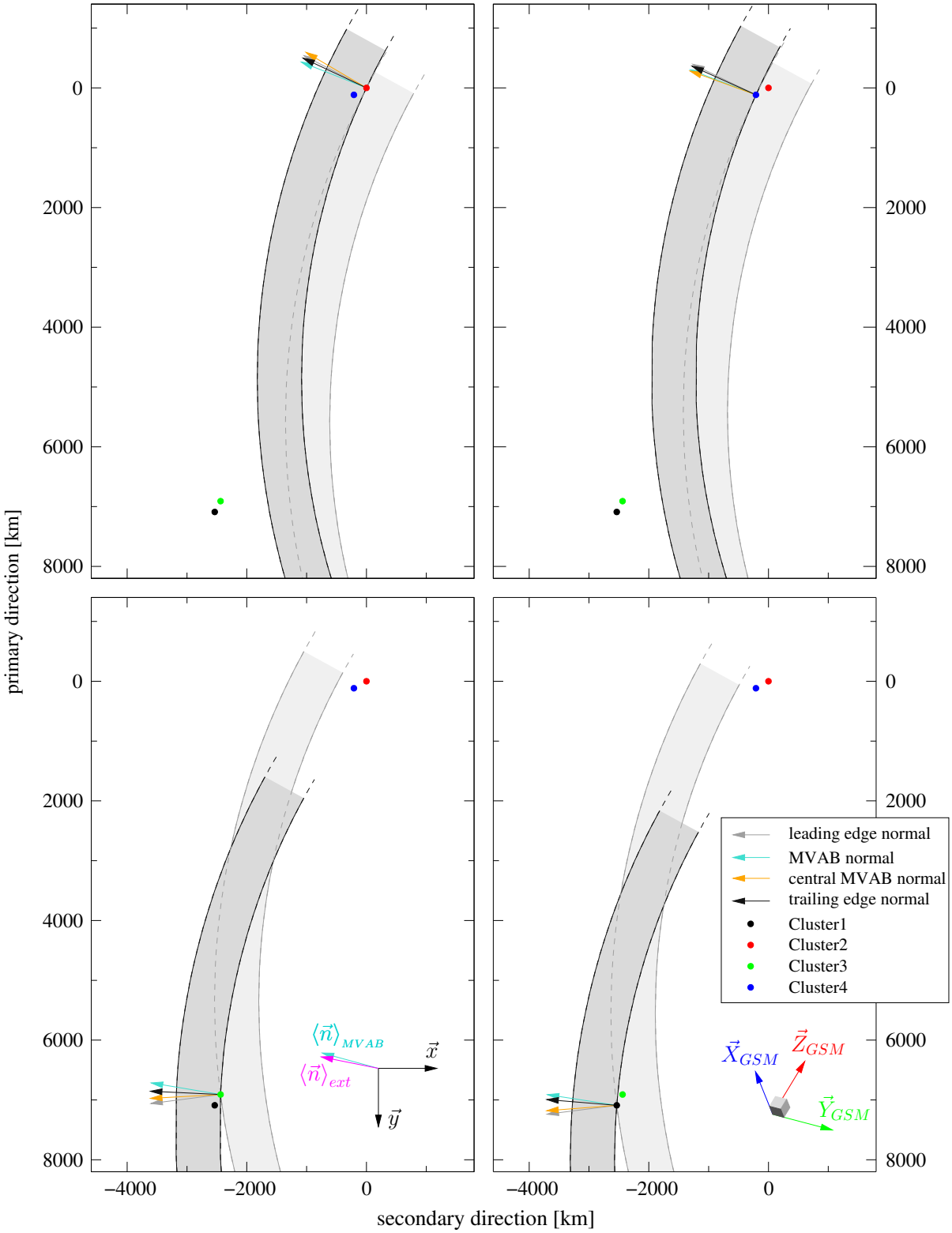

Figure G: For details see the explanations at page 165

Table H: Cylindrical MP with 2 degrees of freedom
Parameters from combined timing - magnetic variance analysis. Solution B

			Average/global	Satellite			
			quantity	Cluster 2	Cluster 4	Cluster 3	Cluster 1
Parameters of the solution							
velocity coefficients	A_0	$[km/s]$	-156.35				
	A_1	$[km/s^2]$	10.62				
	A_2	$[km/s^3]$	-0.149				
	V	$[km/s]$	-37.45				
inner radius	R	$[km]$	14857.5				
centre initial coord.	w	$[km]$	15055.8				
	C	$[km]$	4132.3				
$\sphericalangle$ (primary dir., $\langle\vec{n}\rangle_{MVAB}$)		$[deg]$	-95.0				
Transition parameters							
normal velocity		$[km/s]$	48.40	58.60	51.97	42.37	40.65
thickness		$[km]$	755.1	755.1	755.1	755.1	755.1
radius of curvature		$[R_E]$	2.39	2.39	2.39	2.39	2.39
Comparison with planar normals							
$\sphericalangle\left(\vec{n}_{GEO}^{\,ave}, \vec{n}_{MVAB,\perp\vec{l}}^{\,nested}\right)$		$[deg]$	7.80	1.53	0.72	-14.62	-14.35
$\sphericalangle\left(\vec{n}_{GEO}^{\,ave}, \vec{n}_{MVAB,\perp\vec{l}}^{\,central}\right)$		$[deg]$	3.03 1.62	-7.28	1.74	-1.92	-1.19
$\Delta\vec{n}_{GEO}$		$[deg]$	2.22	-4.12	-3.53	0.85	0.40
MVAB results		$[nT]^2$ or $[nT]$					
	weighting factors			0.223	0.285	0.215	0.276
2D	variance using $\vec{n}_{GEO}$		3.014 2.712	4.066	1.132	2.851	4.236
	$\langle B_n\rangle$ using $\vec{n}_{GEO}$			0.10	-1.63	-1.54	-1.70
	variance using $\vec{n}_{MVAB,\perp\vec{l}}^{\,central}$		2.724 2.697	2.820	1.163	2.794	4.206
	$\langle B_n\rangle$ using $\vec{n}_{MVAB,\perp\vec{l}}^{\,central}$			1.44	-1.75	-1.35	-1.58
3D	variance using $\vec{n}_{GEO,3D}$		2.971 2.728	3.824	1.084	2.600	4.524
	variance from nested MVAB		3.587 3.448	4.088	4.639	2.580	2.894
MFR results		$[mV/m]^2$					
	weighting factors			0.289	0.362	0.176	0.173
2D	FR using $\vec{n}_{GEO}$ and $\vec{v}_{GEO}$		1.714 2.708	1.311	1.079	2.014	3.414
	FR using $\vec{n}_{MFR,2D}$ and $\vec{v}_{MFR,2D}$		2.724 2.920	0.559	4.267	2.415	3.434
3D	FR using $\vec{n}_{GEO,3D}$ and $\vec{v}_{GEO,3D}$		1.759 2.806	1.343	1.082	2.194	3.430
	FR using $\vec{n}_{MFR}$ and $\vec{v}_{MFR}$		2.649 2.847	0.464	4.206	2.282	3.422
deHoffmann–Teller results		$[km/s]$					
	V_{HT} along $\vec{n}_{GEO}^{\,ave}$		31.27	85.26	-4.36	16.95	27.23
	V_{HT} along $\vec{n}_{MVAB}^{\,nested}$		22.25	86.64	-5.78	-14.44	22.56

Combined timing – var.B analysis for a cylindrical MP with 2 deg. of freedom. Solution B

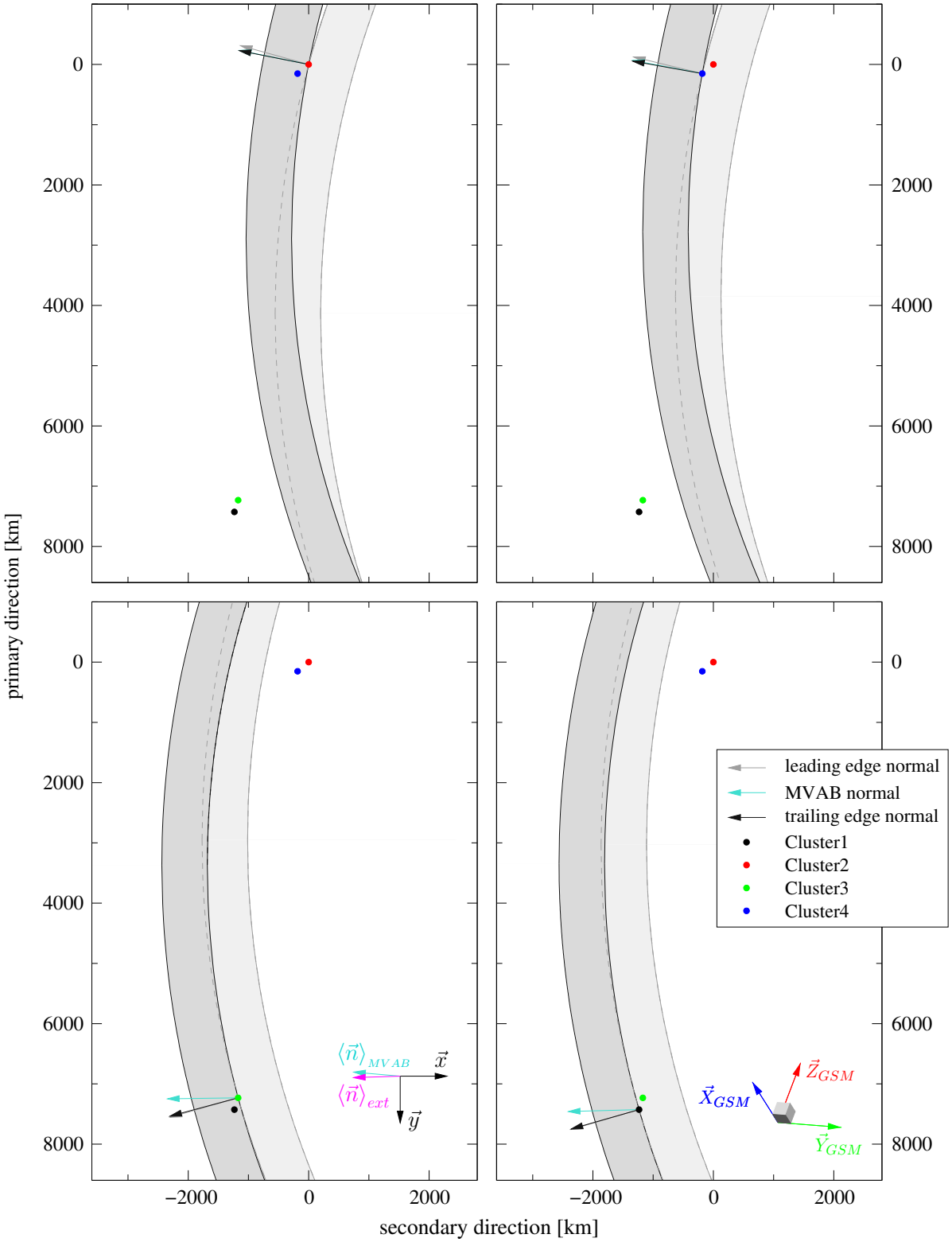

Figure H: For details see the explanations at page 165

APPENDIX D

Stability of the solutions found for the non-planar magnetopause

In order to illustrate how the results that describe the MP configuration and movement depend on the magnetic levels used to set the timing conditions, we select the same solution discussed in Subsection 4.3.1, namely Cyl_2deg_OpTA_solA obtained from the combined timing-MVAB technique. We choose to discuss this case because it implies one of the highest dynamical behavior for the MP. As one can see from Table G in Appendix C, it implies a small radius of curvature, high variations in the instantaneous normal velocity (see in this respect also Figure 4.5) and relative high variations in the orientation of the instantaneous geometrical normal (the parameter $\Delta\vec{n}_{GEO}$ appearing in Tables A to H from Appendix C). Therefore one can presume that the characteristics of this solution depend more on the timing information than in other cases. Besides, due to the fact that this solution is very close to the one from the plain timing analysis (i.e. from the solution Cyl_2deg_TA), the investigation will also indicate how stable the latter technique is.

We change the magnetic levels used to extract the timing information in the following way: in the original implementation the values $B_m \pm (1/2)\,\texttt{tanh(1)}\,\Delta B$ were employed (see equations (3.3) and (3.4)), meaning a symmetric (with respect to the mean value B_m) magnetic variation of $\texttt{tanh(1)} \approx 76.2\,\%$ of the total magnetic jump ΔB (i.e. the jump between the asymptotic levels). We test the stability of the results by using other three, symmetric to B_m, intervals implying magnetic variations equal to $\texttt{tanh(1.1)} \approx 80.0\,\%$, $\texttt{tanh(1.2)} \approx 83.4\,\%$ and $\texttt{tanh(1.3)} \approx 86.2\,\%$ of ΔB. That corresponds to an increase in the crossing times by 10%, 20 % and 30 % respectively. The results from the new solutions are presented in Table D.1, Table D.2 and Table D.3 respectively. In these tables we also compare the geometrical and dynamical parameters corresponding to the $76.2\,\% \cdot \Delta B$ magnetic extension band with the same parametes from the original solution. In other words we kept the definition for the MP extension and present how its thickness, normal velocity, radius of curvature etc. changes when the time-interval used in the conditions of satellites encounter by the MP edges changes.

To understand the quantities appearing in Tables D.1, D.2 and D.3 we refer to the explanations at the beginning of Appendix C, where a description of the Tables A to H, presenting the various 2-D MP solutions, is provided. In this stability study no results from MFR analysis are shown. The changes in the MP geometrical and dynamical parameters due to the different implementation of the timing conditions could be seen under the '`76 % interval`'

Table D.1: Stability of the solution when the interval used in the timing conditions increases by 10 %. Parameters from combined timing - magnetic variance analysis for a cylindrical MP with 2 degrees of freedom, solution A

			Average/global quantity	Satellite			
				Cluster 2	Cluster 4	Cluster 3	Cluster 1
Parameters of the solution							
velocity coefficients	A_0	$[km/s]$	-99.92				
	A_1	$[km/s^2]$	5.274				
	A_2	$[km/s^3]$	$8.98 \cdot 10^{-4}$				
	V	$[km/s]$	-36.26				
inner radius	R	$[km]$	11851.5				
centre initial coord.	w	$[km]$	11404.0				
	C	$[km]$	5561.8				
$\sphericalangle$ (principal dir., $\langle\vec{n}\rangle_{MVAB}$)		$[deg]$	-104.2				
			-105.2				
Transition parameters							
normal velocity		$[km/s]$	48.74	59.01	52.33	42.67	40.94
thickness		$[km]$	836.5	836.5	836.5	836.5	836.5
radius of curvature		$[R_E]$	1.92	1.92	1.92	1.92	1.92
			1.85	1.85	1.85	1.85	1.85
76 % interval							
normal velocity		$[km/s]$	48.97	58.94	52.27	43.15	41.53
			47.45	57.44	50.94	41.54	39.85
thickness		$[km]$	764.8	759.6	759.5	768.9	771.4
			740.3	740.3	740.3	740.3	740.3
Comparison with planar normals							
$\sphericalangle\left(\vec{n}_{GEO}^{\,ave}, \vec{n}_{MVAB,\perp\vec{l}}^{\,nested}\right)$		$[deg]$	7.39	3.72	3.02	-12.31	-10.51
$\Delta\vec{n}_{GEO}$		$[deg]$	7.30	-2.76	-2.21	11.09	13.15
76 % interval							
$\sphericalangle\left(\vec{n}_{GEO}^{\,ave}, \vec{n}_{MVAB,\perp\vec{l}}^{\,nested}\right)$		$[deg]$	7.41	3.69	2.98	-12.39	-10.60
			7.87	4.35	3.68	-12.61	-10.85
$\Delta\vec{n}_{GEO}$		$[deg]$	6.64	-2.52	-2.02	10.07	11.94
			6.41	-2.11	-1.60	10.06	11.88
MVAB results		$[nT]^2$					
	weighting factors			0.225	0.283	0.222	0.270
2D	variance using $\vec{n}_{GEO}$		2.424	3.610	1.221	2.194	2.888
	$\langle B_n\rangle$ using $\vec{n}_{GEO}$			0.37	-1.28	-1.05	-0.95
	variance using $\vec{n}_{MVAB,\perp\vec{l}}^{\,central}$		2.750	3.158	1.115	2.785	4.098
	$\langle B_n\rangle$ using $\vec{n}_{MVAB,\perp\vec{l}}^{\,central}$			1.03	-1.64	-1.26	-1.42
3D	variance using $\vec{n}_{GEO,\,3D}$		2.359	3.445	1.123	2.037	3.015
	variance from nested MVAB		3.587	4.088	4.639	2.580	2.894

Table D.2: Stability of the solution when the interval used in the timing conditions increases by 20 %. Parameters from combined timing - magnetic variance analysis for a cylindrical MP with 2 degrees of freedom, solution A

			Average/global	Satellite			
			quantity	Cluster 2	Cluster 4	Cluster 3	Cluster 1
Parameters of the solution							
velocity coefficients	A_0	$[km/s]$	-111.35				
	A_1	$[km/s^2]$	5.679				
	A_2	$[km/s^3]$	$-2.40 \cdot 10^{-3}$				
	V	$[km/s]$	-36.84				
inner radius	R	$[km]$	12177.4				
centre initial coord.	w	$[km]$	11874.3				
	C	$[km]$	5573.1				
$\sphericalangle$ (principal dir., $\langle\vec{n}\rangle_{MVAB}$)		$[deg]$	-103.7				
			-105.2				
Transition parameters							
normal velocity		$[km/s]$	50.19	60.76	53.89	43.94	42.15
thickness		$[km]$	939.6	939.6	939.6	939.6	939.6
radius of curvature		$[R_E]$	1.98	1.98	1.98	1.98	1.98
			1.85	1.85	1.85	1.85	1.85
76 % interval							
normal velocity		$[km/s]$	50.67	60.59	53.72	44.95	43.41
			47.45	57.44	50.94	41.54	39.85
thickness		$[km]$	792.2	780.8	780.6	801.0	806.3
			740.3	740.3	740.3	740.3	740.3
Comparison with planar normals							
$\sphericalangle\left(\vec{n}_{GEO}^{\,ave}, \vec{n}_{MVAB,\perp\vec{l}}^{\,nested}\right)$		$[deg]$	6.97	3.00	2.30	-12.20	-10.38
$\Delta\vec{n}_{GEO}$		$[deg]$	8.08	-3.32	-2.71	12.03	14.25
76 % interval							
$\sphericalangle\left(\vec{n}_{GEO}^{\,ave}, \vec{n}_{MVAB,\perp\vec{l}}^{\,nested}\right)$		$[deg]$	7.02	2.94	2.21	-12.37	-10.57
			7.87	4.35	3.68	-12.61	-10.85
$\Delta\vec{n}_{GEO}$		$[deg]$	6.73	-2.78	-2.28	10.00	11.86
			6.41	-2.11	-1.60	10.06	11.88
MVAB results		$[nT]^2$					
weighting factors				0.221	0.299	0.223	0.258
2D variance using $\vec{n}_{GEO}$			2.378	3.899	1.137	2.230	2.641
2D $\langle B_n\rangle$ using $\vec{n}_{GEO}$				0.00	-1.40	-1.05	-0.95
2D variance using $\vec{n}_{MVAB,\perp\vec{l}}^{\,central}$			2.764	3.536	1.132	2.915	3.862
2D $\langle B_n\rangle$ using $\vec{n}_{MVAB,\perp\vec{l}}^{\,central}$				0.43	-1.57	-1.17	-1.38
3D variance using $\vec{n}_{GEO,3D}$			2.321	3.750	1.095	2.037	2.762
3D variance from nested MVAB			3.587	4.088	4.639	2.580	2.894

Table D.3: Stability of the solution when the interval used in the timing conditions increases by 30 %. Parameters from combined timing - magnetic variance analysis for a cylindrical MP with 2 degrees of freedom, solution A

			Average/global	Satellite			
			quantity	Cluster 2	Cluster 4	Cluster 3	Cluster 1
Parameters of the solution							
velocity coefficients	A_0	$[km/s]$	-120.35				
	A_1	$[km/s^2]$	6.133				
	A_2	$[km/s^3]$	$9.55 \cdot 10^{-3}$				
	V	$[km/s]$	-38.26				
inner radius	R	$[km]$	12267.9				
centre initial coord.	w	$[km]$	12080.4				
	C	$[km]$	5601.8				
$\sphericalangle$ (principal dir., $\langle\vec{n}\rangle_{MVAB}$)		$[deg]$	-103.8				
			-105.2				
Transition parameters							
normal velocity		$[km/s]$	51.68	62.57	55.49	45.24	43.41
thickness		$[km]$	1048.2	1048.2	1048.2	1048.2	1048.2
radius of curvature		$[R_E]$	2.01	2.01	2.01	2.01	2.01
			1.85	1.85	1.85	1.85	1.85
76 % interval							
normal velocity		$[km/s]$	52.37	62.24	55.17	46.78	45.29
			47.45	57.44	50.94	41.54	39.85
thickness		$[km]$	819.7	802.1	801.7	833.7	841.3
			740.3	740.3	740.3	740.3	740.3
Comparison with planar normals							
$\sphericalangle\left(\vec{n}_{GEO}^{\,ave}, \vec{n}_{MVAB,\perp\vec{l}}^{\,nested}\right)$		$[deg]$	6.73	2.35	1.66	-12.37	-10.54
$\Delta\vec{n}_{GEO}$		$[deg]$	8.73	-3.70	-3.00	12.93	15.27
76 % interval							
$\sphericalangle\left(\vec{n}_{GEO}^{\,ave}, \vec{n}_{MVAB,\perp\vec{l}}^{\,nested}\right)$		$[deg]$	6.80	2.24	1.52	-12.62	-10.82
			7.87	4.35	3.68	-12.61	-10.85
$\Delta\vec{n}_{GEO}$		$[deg]$	6.71	-2.87	-2.33	9.93	11.73
			6.41	-2.11	-1.60	10.06	11.88
MVAB results		$[nT]^2$					
	weighting factors			0.226	0.305	0.217	0.251
2D	variance using $\vec{n}_{GEO}$		2.394	4.020	1.110	2.408	2.479
	$\langle B_n\rangle$ using $\vec{n}_{GEO}$			-0.22	-1.48	-1.06	-0.97
	variance using $\vec{n}_{MVAB,\perp\vec{l}}^{\,central}$		2.777	3.634	1.141	3.079	3.731
	$\langle B_n\rangle$ using $\vec{n}_{MVAB,\perp\vec{l}}^{\,central}$			0.22	-1.43	-1.04	-1.35
3D	variance using $\vec{n}_{GEO,\,3D}$		2.343	3.860	1.130	2.161	2.607
	variance from nested MVAB		3.587	4.088	4.639	2.580	2.894

sections. The values corresponding to the original implementation of the timing conditions ($\texttt{tanh}(1) \approx 76.2\,\%$ of the total magnetic jump ΔB) appear in green and they are taken from Table G in Appendix C.

As far as the geometrical parameters are concerned we notice that the solution is very stable: the orientation of the principal direction changed only within 1.5 degrees. Also, the values for the angles $\sphericalangle\,(\vec{n}_{GEO}^{\,ave}, \vec{n}_{MVAB})$ (between the average geometrical normal and the normal from the planar nested MVAB) and $\Delta\vec{n}_{GEO}$ (indicating the variation of the geometrical normal during one transition) are very similar, both for the individual transitions and in the global sense.

The dynamical parameters have a somewhat larger variation, with the average normal velocity varying by $\approx 3.2\,\%$, $\approx 6.8\,\%$ and $\approx 10.3\,\%$ when the timing information was set at $\texttt{tanh}(1.1)$, $\texttt{tanh}(1.3)$ and $\texttt{tanh}(1.3)$ ΔB magnetic extension, respectively. In the latter case, for individual satellites the variation could rise by as much as $\approx 13.7\,\%$. A similar behavior is noticed for the corresponding thicknesses. We believe that this has to do with the relative large variation in the normal velocity at each spacecraft (see in Figure 4.5, the evolution of the blue line), when perhaps the use of a symmetrical profile to fit the magnetic traces and extract the timing information is not so appropriate. Indeed, we carry-out a similar investigation for a solution implying less variation in the normal velocity namely the solution Cyl_2deg_OpTA_solB. In Figure 4.5 the latter solution appears in yellow trace. In this case, the stability analysis indicates that the relative variations in the average normal velocity are only $\approx 1.0\,\%$, $\approx 2.2\,\%$ and $\approx 3.6\,\%$, respectively.

APPENDIX E

Magnetic variance in the planar and 2-D, non-planar methods

In order to compare the results obtained from the planar MVAB technique with the results from the non-planar method we will concentrate on one particular solution of the 2-D problem, namely solution Cyl_2deg_OpTA_solA. Later, we will present a similar analysis corresponding to the other solutions obtained in the combined timing-MVAB analysis.

As mentioned in Subsection 4.3.1, such a comparison involves the problem of different data sets used by each method: the planar MVAB requires intervals large enough to encompass the whole magnetic field rotation, whereas in our 2-D method we use only the central intervals, between $B_m + (1/2)\,\texttt{tanh}(-1)\,\Delta\texttt{B}$ and $B_m + (1/2)\,\texttt{tanh}(1)\,\Delta\texttt{B}$, according to the system of conditions describing the satellites encounter with the MP edges. In this respect, compare, for example, in the upper part of Figure 3.10, the intervals between the vertical grey stripes (marking the extent of the eleven nested intervals used in the planar nested MVAB technique) with the interval between the magenta vertical dashed lines (used for imposing the timing conditions).

In consequence, for the task of this section, different intervals of comparison will be used. Namely, we will use intervals of increased width, centred on the central crossing times T_{ci}, and we will show how the normal magnetic variance and normal magnetic component $\langle B_n \rangle$ implied by the chosen 2-D solutions, compare with the similar quantities obtained from the single-spacecraft, planar MVAB technique. More precisely, for the time-intervals mentioned above, we computed the global and the individual (i.e. referring to each satellite) quantities of normal magnetic filed variance and $\langle B_n \rangle$ using the following normals:

- the instantaneous, geometrical normals implied by the 2-D, non-planar MP. Clearly, the direction of these normals is changing in time, according to the MP movement prescribed by the solution we analyse. For simplicity, in this section we will refer to them as the *instantaneous 2-D* normals.
- the normals compiled in Table 3.1, i.e. provided by the (constrained to $\langle B_n \rangle = 0$) planar MVAB on the eleven nested intervals, and used in Section 3.4 for inferring the invariant direction $\vec{l}$. To be more precise, we used their projection on the plane perpendicular to $\vec{l}$ but this is a minor detail in the following discussion. Indeed, because the nested individual normals already lie very close to that plane, taking the projections results in

only minor differences in the computed values. The directions of these normals are fixed in space; for simplicity, in this section we will refer to them as the *fixed, planar MVAB* normals.

- the normals obtained when, for each satellite and for the time-interval in question, a constrained planar MVAB is performed. By 'constrained' we mean here perpendicular to the invariant direction $\vec{l}$. As a consequence, in this case the directions of the normals are changing with the interval of analysis according to the planar MVAB theory. In this section we will refer to these normals as *planar, interval-specific MVAB* normals.

The results of the comparison are illustrated in Figure E.1. On the left column we show how the normal magnetic field variance and average normal magnetic component $\langle B_n \rangle$ changes with the width of the interval of analysis, when the planar or the 2-D assumptions were adopted. Panels 1 to 4 in that column refer to Cluster 2, Cluster 4, Cluster 3 and Cluster 1 respectively (the order corresponds to the sequence of MP encounter). As mentioned, all the results were computed by using symmetrically centred intervals, i.e. for satellite i the intervals are centred at Tc_i. In each panel, on the abscissa, the half-width of the interval of analysis appears, in seconds from τ_i, and therefore the origin of this axis corresponds to the central intervals $[Tc_i - \tau_i,\, Tc_i + \tau_i]$ used in the timing conditions. The range of the $\vec{x}$ axis starts with an interval of $\tau_i - 2$ seconds half-width and stops at the half-width of the largest possible central interval that is still included in the largest interval from the planar nested analysis. In each panel, the vertical dashed lines (in grey) are drawn at multiples of τ_i. In panel 5 the weighted sums of the individual normal magnetic field variances are shown (i.e. the so called 'global' variances). For computing the global values we used the weighting factors provided by (B.88), defined in Section B.5.

Two sets of planar results are presented: in cyan the normal magnetic field variance (continuous lines) and $\langle B_n \rangle$ quantity (dashed lines) were computed using the *fixed, planar MVAB* normals. For that purpose, the following formulas for the magnetic field variance and for $\langle B_n \rangle$ were used:

$$\sigma_i^2 = \frac{1}{M_i} \sum_{m=1}^{M_i} \left| \left(\vec{B}_i^{(m)} - \langle \vec{B} \rangle_i \right) \cdot \vec{n}_{MVAB,i}^{\,nested} \right|^2$$

$$\langle B_n \rangle_i = \frac{1}{M_i} \sum_{m=1}^{M_i} \vec{B}_i^{(m)} \cdot \vec{n}_{MVAB,i}^{\,nested} \qquad\qquad i = 1...4$$

Here by i we indicated a specific satellite and M_i represents the total number of points contained in the data interval for which we compute the above quantities. $\vec{n}_{MVAB,i}^{\,nested}$ designates the *fixed planar MVAB* normals.

The second set of planar results is shown in orange; with this colour we present the evolution of the normal magnetic field variance (continuous lines) and of the average normal magnetic component $\langle B_n \rangle$ (dashed lines) obtained with the *planar, interval - dependant MVAB* normals (i.e. by applying the standard MVAB technique, imposing the constaint that $\vec{n} \cdot \vec{l} = 0$, on each of the central intervals used for comparison).

For each satellite, the normal magnetic field variance and $\langle B_n \rangle$ along the *2-D, instantaneous*, geometrical normals are shown in the corresponding panels using the mission colour code (i.e. red for Cluster 2, blue for Cluster 4, green for Cluster 3 and black for Cluster 1). More precisely, the above mentioned quantities were computed based on the Cyl_2deg_OpTA_solA solution by extending its validity on each of the central intervals used for comparison. Therefore the formula (B.87) from Section B.5 was applied on smaller and larger central intervals, having

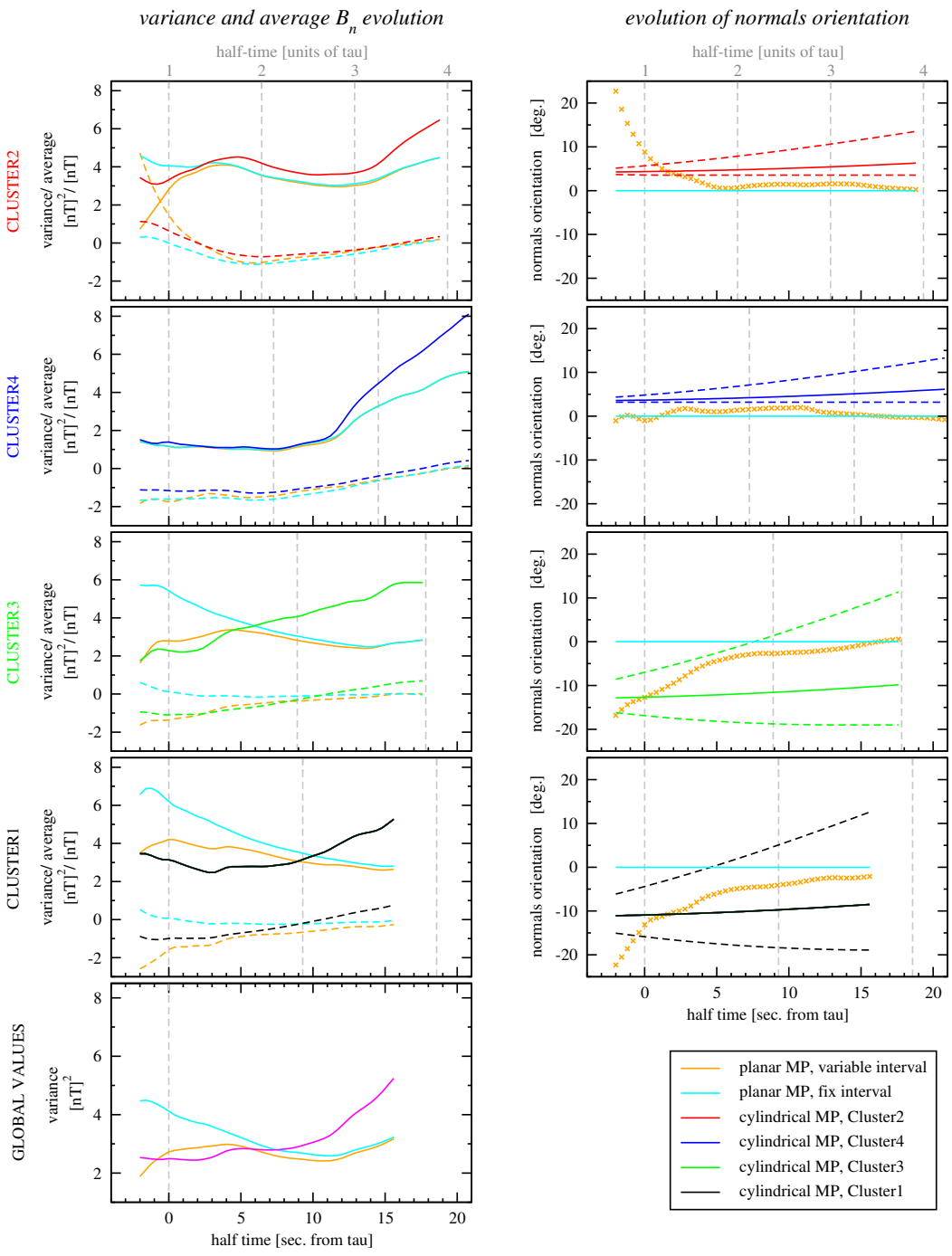

Figure E.1: *Left column:* Magnetic variance (continuous lines) and average quantity $\langle B_n \rangle$ (dashed lines) computed for different central intervals, with the half-width appearing on the abscissa, in case when the normals are provided by the nested, planar MVAB (cyan), by the running, planar MVAB (orange) and by the 2-D cylindrical model for the MP presented at pages 178 and 179 (colour coded according to the mission convention). *Right column:* The change in normals orientation as a function of interval half-width for the above mentioned cases. See text for more explanations.

the half-width appearing on the abscissa):

$$\sigma_i^2 = \frac{1}{M_i}\sum_{m=1}^{M_i}\left|\left(\vec{B}_i^{(m)} - \langle\vec{B}\rangle_i\right)\cdot\vec{n}_{GEO,i}^{(m)}\right|^2$$

$$\langle B_n\rangle_i = \frac{1}{M_i}\sum_{m=1}^{M_i}\vec{B}_i^{(m)}\cdot\vec{n}_{GEO,i}^{(m)} \qquad i = 1...4$$

Here $n_{GEO,i}^{(m)}$ designates the *2-D, instantaneous* normals. The super-script m indicates that the direction of these normals is changing in time. Therefore in the above formulas, for the satellite i the orientation of the normal at the moment when the $B_i^{(m)}$ measurement was taken is considered.

The four panels on the right column present the change in the orientation of the corresponding normals as a function of interval half-width. In each panel we have the *fixed, planar MVAB* normals in cyan, the *planar, interval-specific MVAB* normals in orange, and the *2-D, instantaneous* normals shown in the mission colour code. For that purpose we took for each satellite a reference direction in the plane perpendicular to the invariant direction $\vec{l}$, specifically the direction along the *fixed, planar MVAB* normal. In consequence, in each panel, the cyan continuous trace lies along the $\vec{x}$ axis. Along the $\vec{y}$ axis we represent the angles (in degrees) relative to the reference direction we have chosen. The orientation of *planar, interval-specific MVAB* normals is shown with orange crosses (by using crosses, instead of continuous lines, one can see also the actual extent of each interval of analysis). As for the *2-D, instantaneous* normals, in each panel we plotted three lines. The continuous line shows the evolution of the average geometric normal, as computed for the satellite in question and for the corresponding interval of analysis (see the formula (B.85) from Section B.4). In the same time the range of angular variation for the *2-D instantaneous* normals are indicated with the two dashed lines. It means that, during each particular interval of analysis the *2-D, instantaneous* normals will move between the dashed lines, having an average orientation indicated by the continuous line.

By looking at each of the right panels, as a first observation one notices that the magnetic field variance curve based on the *planar, interval-specific MVAB* normal (orange continuous lines), always lies below the magnetic field variance along the *fixed, planar MVAB* normal (cyan continuous lines), as it should be the case because the former is the minimum value possible for each interval. At the same time, we expect to have close results from the two sets of planar MVAB normals as the interval increases. Therefore it is no surprise that all the orange and cyan curves (referring to the magnetic field variances, to the average magnetic components or to the orientation of the normals indicated in the panels from the right column) meet at the end of the plotted range. In addition the orange and cyan dashed lines, designating the $\langle B_n\rangle$ quantities computed from the two sets of planar MVAB normals, are approaching zero for larger intervals, because we used a constrained (to $\langle B_n\rangle = 0$) MVAB in our nested analysis.

Analysing the right column, we notice, for Cluster 2 and Cluster 1, big variations in the orientation of the *planar, interval-specific MVAB* normals as the width of the analysis interval decreases. This evolution could be ascribed to the MP rotation or/and to the local, internal (temporal or structural) irregularities of this discontinuity. It is difficult to separate these two factors but we think that in these cases the local effects dominate for intervals of half-width below or around τ_2 and τ_1, respectively. Indeed, as one can see at the beginning of the corresponding traces, the *planar, interval-specific MVAB* normals change their orientation by more than 2 degrees from one interval of analysis to the other, i.e. when two magnetic field measurements, 0.4 seconds apart are successively included in the analysis (one at the right

and one at the left of the central time). Considering the general smoothness of the magnetic traces for this event, it is difficult to imagine a MP movement causing such a rapid change in orientation. Also, the corresponding $\langle B_n \rangle$ values (orange dashed lines in the panel on the left column) are relatively big in that region. Therefore, most probably, these are the manifestation of the 'non-ideal' features of the 2-D MP, meaning by this expression that the local, internal irregularities (magnetic islands, noise etc.) are playing an important role.

The effects we discussed in the above paragraph can be neglected in case of Cluster 1 for intervals of analysis having the half-width equal or bigger than τ_1, but in case of Cluster 2 (the top panels on both columns) the effects are still important for an interval of half-width τ_2. As a result, we conclude that the planar MVAB result on $[T_{c2} - \tau_2, T_{c2} + \tau_2]$ interval is spoiled by the local fluctuations or by the internal structure. This is the reason why, in tables A to H from Appendix C, presenting the parameters of each 2-D, non-planar solution, we used for comparison with the planar results both the global magnetic field variance based on data from all four satellites (black numbers in the MVAB section of these tables) and the same quantity based only on data from Cluster 1, Cluster 3 and Cluster 4 (the blue numbers).

The behaviour of the results obtained for Cluster 2 would suggest a slightly larger definition of the magnetic levels used to extract the timing information but, as we showed in Appendix D devoted to investigate the stability of the 2-D solutions, the predicted MP shape, orientation and motion is practically not affected by this aspect.

In the section entitled **Comparison with the planar normals** of Tables A to H from Appendix C, we made a comparison, for each satellite, between the orientation of the average geometrical normal and the orientation of the planar normal obtained in the MVAB nested analysis (what we called in this section *fixed, planar MVAB* normal). By looking at these values and at the accompanying figures, one would be inclined to say that all 2-D, non-planar solutions imply, in case of Cluster 3 and Cluster 1, a systematic difference between the two normals. Actually, the last two panels on the right column in Figure E.1 make clear that the difference in orientation is due to the different time-intervals on which the two normals are based. In fact, in case of Cluster 3 and Cluster 1 for the intervals having the half-width of τ_3, respectively τ_1, the planar MVAB analysis provides normals very close to the average geometrical normals. Moreover, for all the central intervals with the half-width greater than τ_3, respectively τ_1, the *planar, interval-specific MVAB* normals lie in the range of angular variation for the *2-D, instantaneous* normals (i.e. lie between the dashed, colour coded lines). This is exactly the result that we expect when the planar MVAB technique is applied on a ideal 2-D discontinuity (see *Dunlop and Woodward* [1998]). The result is remarkable, particularly if we take into account the fact that the analyzed 2-D solution is practically the same as obtained from the plain timing analysis (solution Cyl_2deg_TA, from 174 and 175).

From the panels on the left column we see that the average normal magnetic components computed with the *2-D, instantaneous* normals are not zero. While in general it could happen that the timing conditions introduce an undesired and non-realistic offset in the values of these quantities, this is not the situation for the particular solution we discuss. Indeed, for all satellites the corresponding curves are closer to the $\vec{x}$ axis than the $\langle B_n \rangle$ curves computed with the *planar, interval-specific* normals, for most of the intervals with a half-width smaller than $2\tau_i$.

It is important to notice that the existence of non-zero values for $\langle B_n \rangle$ does not necessarily imply an inconsistency with the results of the planar nested analysis or with the outcome from the Walén analysis. In the nested analysis, in order to obtain reliable normals, we imposed $B_n = 0$ *on average* for the eleven nested intervals but this does not mean $\langle B_n \rangle = 0$ for smaller intervals. This aspect can be observed in the evolution of the cyan dashed lines (see for example

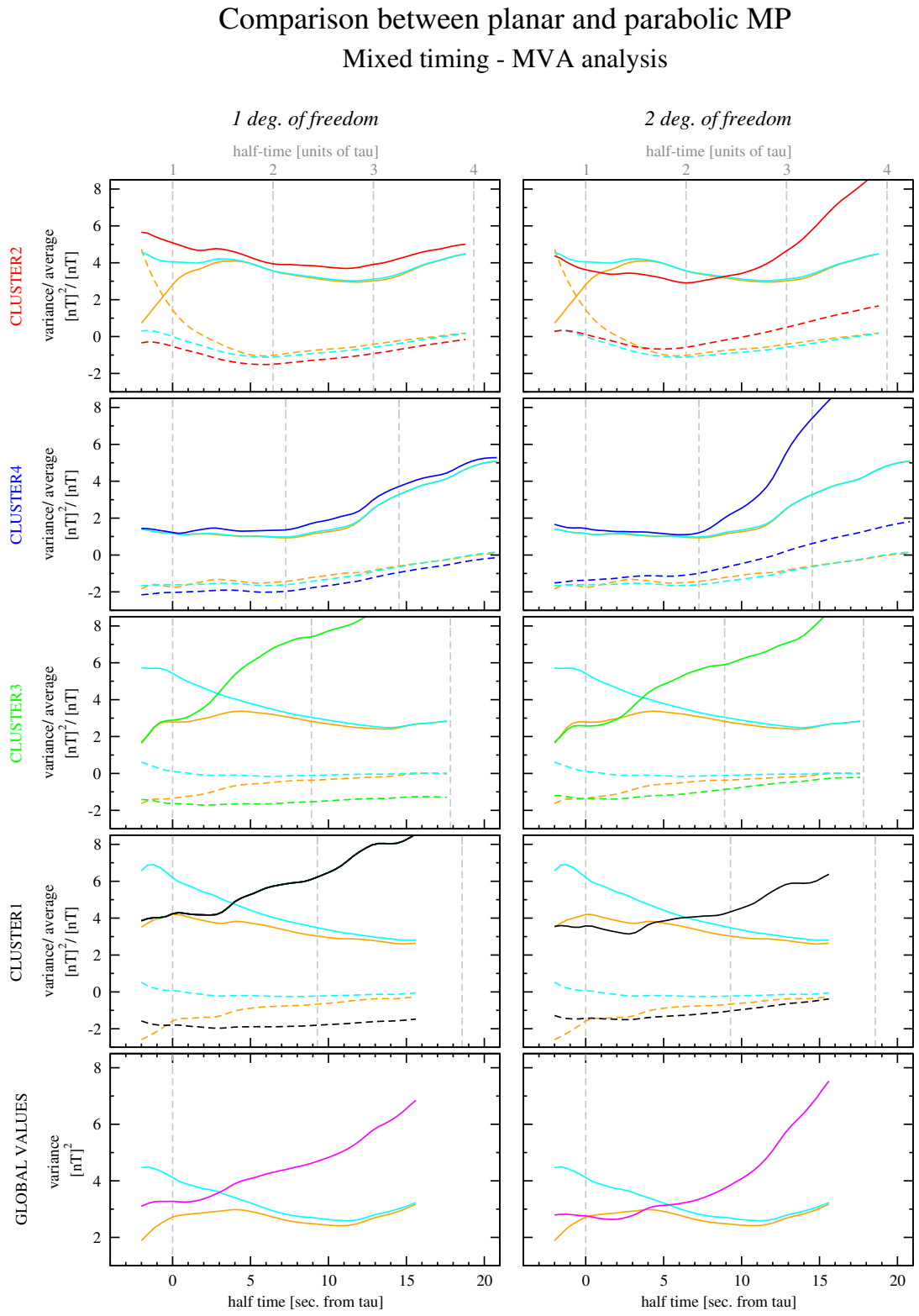

Figure E.2: The same descriptions as for the left column of Figure E.1 applies here, the only differences being that now the comparison is made with the solution provided by the mixed timing – MVAB analysis for a parabolic MP having 1 degree of freedom (left column) or 2 degrees of freedom (right column).

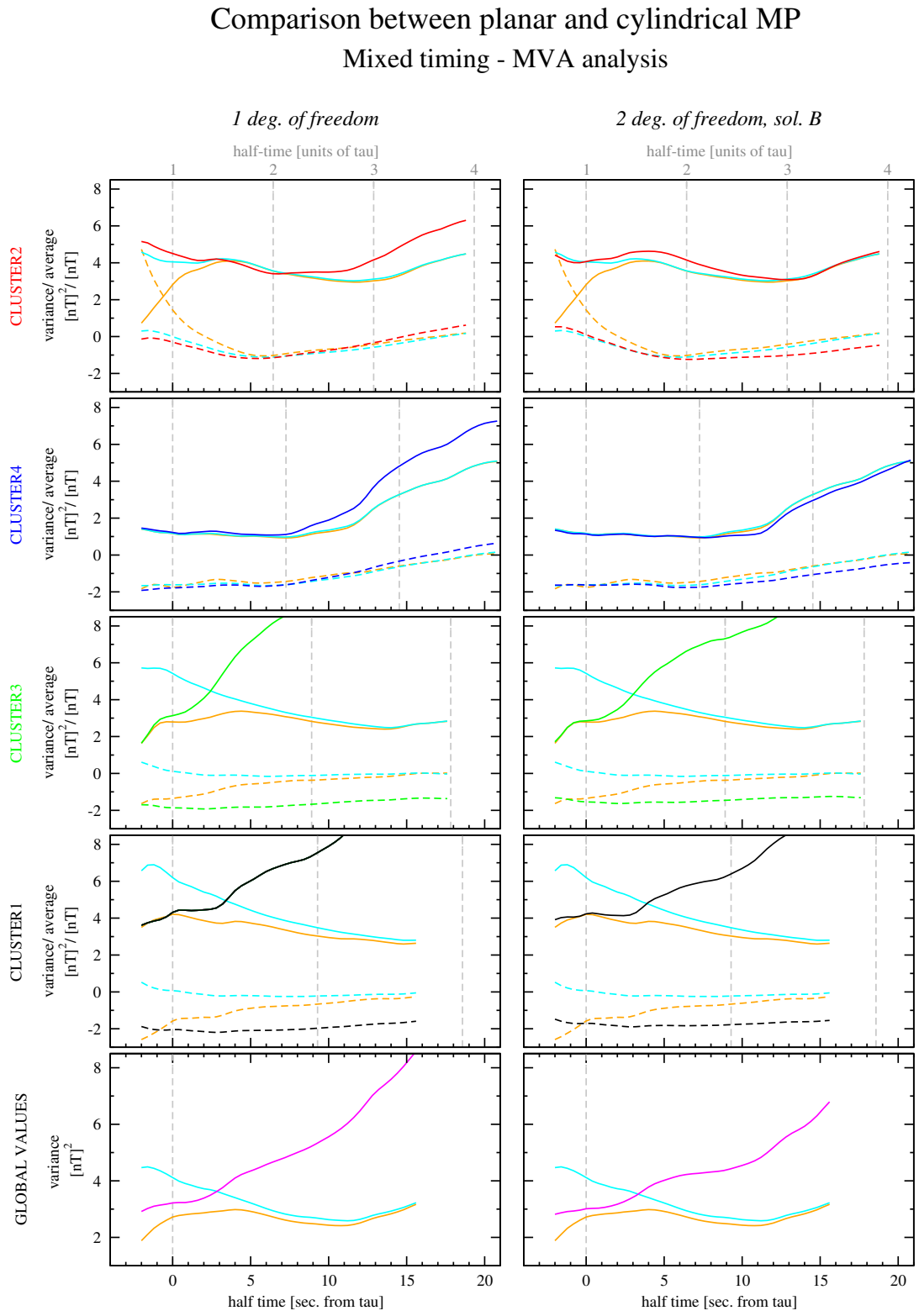

Figure E.3: The same descriptions as for the left column of Figure E.1 applies here, the only differences being that now the comparison is made with the solution provided by the mixed timing – MVAB analysis for a cylindrical MP having 1 degree of freedom (left column) or 2 degrees of freedom, solution B (right column).

the panels on the left column of Figure E.1 referring to Cluster 2 and Cluster 4). As for the Walén tests (see Section 3.3), they were performed by using magnetic data averaged over 4 seconds (the time resolution of the plasma sensor) and assuming a planar MP.

The curves in the bottom left panel (presenting the global normal magnetic field variances) show that even for central intervals having the half-width as large as $\approx \tau_i + 5$ seconds, the *2-D, instantaneous* normals imply a smaller global magnetic variance (magenta line) than the *planar, interval-specific* normals (orange line), which are the 'best' normals obtained in the planar assumption (i.e. implying the minimum magnetic variance). In fact, a similar statement can be made at the individual level in case of Cluster 3 and Cluster 1, while in case of Cluster 4 the two curves are very close to each other. The situation is reversed on Cluster 2 (allthough the curves are still very close) but, as we already mentioned, in this case the local irregularities play an important role. Considering the above arguments, one can definitely endorse the assertion that, for the above mentioned intervals, the 2-D solution performs better than the planar solution from MVAB point of view.

Nevertheless, in judging one particular solution relying on the 2-D, non-planar assumption it is not necessary to adopt such a strict criterion (namely that the curve representing the global magnetic variance based on the *2-D, instantaneous* normals to be situated below the similar curve based on the *planar, interval-specific MVAB* normals). The individual *planar, interval-specific MVAB* normals are independent from one another and, so to speak, free to change their direction from one interval to the other, according to the measurements acquired by each satellite. On the other hand the instantaneous normals for a 2-D solution are linked at each moment by the geometry proposed for the MP (parabolic or cylindrical) and evolve in time according to the global MP dynamics. Therefore, it is reasonable to think that in case of the 2-D problem, values for the global normal variances greater than (but close to) the global variances based on *planar, interval-specific MVAB* normals, might still define a solution that performs better, from the MVAB perspective, than the one obtained in the planar assumption.

With respect to the interval of validity for a particular 2-D, non-planar solution, the left panels in Figure E.1 allows us to set an upper - limit. We notice that starting with a certain width of the interval of analysis, in each panel, the individual and global normal magnetic variances begin to rise monotonically; from that point on the solution should be abandoned.

In Figure E.2 and Figure E.3 we have plotted the curves corresponding to the normal magnetic variances and to the $\langle B_n \rangle$ quantities (in the same format as in the left column of Figure E.1) for the remaining 2-D, non-planar solutions obtained in the combined timing-MVAB analysis. Using the same line of reasoning it is possible to carry-out a similar comparison between these solutions and the results obtained in the planar MVAB technique.

APPENDIX F

The deHoffmann-Teller analysis

In this appendix we briefly present the non-iterative, matrix based technique of finding the deHoffmann - Teller (HT) frame, developed by *Sonnerup et al.* [1987] and reviewed in *Khrabrov and Sonnerup* [1998]. In their original work, devoted to the analysis of jump conditions across MHD shock waves, *deHoffmann and Teller* [1950] introduced a particular reference frame in which the plasma flow on either side of the shock becomes aligned with the magnetic field. In other words, the convection electric field vanishes in these regions.

As we discussed in Section 5.2, in the context of performing the Walén analysis at the MP, of interest is the search for a HT frame by using not only measurements taken in the adjacent asymptotic regimes but also measurements inside the boundary. If the identification of such a reference frame is successful, it means that we can interpret the time variations registered during the MP transition as being produced by a time-stationary structure, without an intrinsic electric field, moving over the spacecraft.

Giving a set of experimental data, consisting of electric field $\vec{E}^{(m)}$ and magnetic field $\vec{B}^{(m)}$ corresponding to M points of measurements $m = 1, 2 \ldots M$, (or, equivalently when the MHD approximation $\vec{E} = -\vec{V} \times \vec{B}$ is valid, consisting of plasma bulk velocities $\vec{V}^{(m)}$ and magnetic field $\vec{B}^{(m)}$) the problem of identifying a HT reference frame is equivalent to finding a velocity vector $\vec{V}_{HT}$ so that the quantity

$$D(\vec{V}) = \frac{1}{M}\sum_{m=1}^{M}\left|\vec{E}^{(m)} + \vec{V}\times\vec{B}^{(m)}\right|^2 = \frac{1}{M}\sum_{m=1}^{M}\left|\left(\vec{V}^{(m)} - \vec{V}\right)\times\vec{B}^{(m)}\right|^2$$

become as small as possible. The solution to this problem is obtained from the condition $\nabla_{\vec{V}} D = 0$ and is given by the following linear system for $\vec{V}_{HT}$:

$$\mathrm{K}_0\vec{V}_{HT} = \left\langle \mathrm{K}^{(m)}\vec{V}^{(m)}\right\rangle \tag{F.1}$$

In the above expression, each $\mathrm{K}^{(m)}$ is a 3 X 3 matrix, with the elements $\mu\nu$ defined by

$$\mathrm{K}^{(m)}_{\mu\nu} = {B^{(m)}}^2\left(\delta_{\mu\nu} - \frac{B^{(m)}_\mu B^{(m)}_\nu}{{B^{(m)}}^2}\right)$$

where $\delta_{\mu\nu}$ is the Kronecker symbol. In (F.1) the $\langle \ldots \rangle$ denotes the averaging operation over the M points of measurements and $\mathrm{K}_0 \equiv \left\langle \mathrm{K}^{(m)} \right\rangle$. If K_0 is not a singular matrix, then the solution for (F.1) is

$$\vec{V}_{HT} = \mathrm{K}_0^{-1} \left\langle \mathrm{K}^{(m)} \vec{V}^{(m)} \right\rangle$$

To judge the quality of the HT frame determination, the electric field in the starting reference frame $\vec{E}^{(m)} = -\vec{V}^{(m)} \times \vec{B}^{(m)}$ is plotted against the electric field in the HT frame $\vec{E}^{(m)}_{HT} = -\vec{V}_{HT} \times \vec{B}^{(m)}$ component by component (see for example the left-hand side of Figure 5.8). Ideally, in this type of plot the slope of the regression line would be 1 and the correlation coefficient c between the two fields would also be 1.

Another way to measure the quality of the HT frame is by computing $D(\vec{V}_{HT})/D(\vec{V})$, i.e. the ratio between the average (magnitude square of) electric field in HT frame and the same quantity in the starting reference frame. The two quantities c and $D(\vec{V}_{HT})/D(\vec{V})$ are related by the formula

$$c^2 + \frac{D(\vec{V}_{HT})}{D(\vec{V})} = 1$$

Khrabrov and Sonnerup [1998] have shown that, even for three points of measurements, the situation of finding one reference frame in which the convection electric field vanishes, is very unlikely to be satisfied by chance. In our thesis, when investigating the rotational vs. tangential character of the MP we used as threshold for a good HT identification a correlation coefficient $c \gtrsim 0.95$.

APPENDIX G

The Minimum Faraday Residue technique

The Minimum Faraday Residue (MFR) is a single-spacecraft technique, relying on a planar, 1-D assumption for the MP (or any other discontinuity). The method was introduced by *Terasawa et al.* [1996] and *Kawano and Higuchi* [1996] and is based on the magnetic flux conservation law. In this appendix, we will closely follow the presentation of the technique from *Khrabrov and Sonnerup* [1998], where an analytical solution, based on an eigenvector/eigenvalue determination problem was given.

The MFR technique provides both the orientation of the discontinuity (i.e. the unit vector $\vec{n}$ normal to the surface) and its velocity u_n, assumed constant, along this normal. In the above mentioned assumptions all variables recorded by the satellite depend only on the variable $\xi = \vec{r} \cdot \vec{n} - u_n t$, and the Faraday's law

$$\frac{\partial \vec{B}}{\partial t} = - \nabla \times \vec{E}$$

becomes

$$u_n \frac{d\vec{B}}{d\xi} = \vec{n} \times \frac{d\vec{E}}{d\xi}$$

This equation can be integrated to give

$$u_n \vec{B} = \vec{n} \times \vec{E} + \vec{C}$$

Lets consider a set of experimental data, consisting of electric field $\vec{E}^{(k)}$ and magnetic field $\vec{B}^{(k)}$ corresponding to K points of measurements $k = 1, 2 \ldots K$, (or, equivalently when the MHD approximation $\vec{E} = - \vec{V} \times \vec{B}$ is valid, consisting of plasma bulk velocities $\vec{V}^{(k)}$ and magnetic field $\vec{B}^{(k)}$). The problem to be solved consists in finding those values for the parameters $\vec{C}$, u_n and $\vec{n}$ that minimize the quantity

$$I_F(\vec{C}, u_n, \vec{n}) = \frac{1}{K} \sum_{k=1}^{K} \left| u_n \vec{B}^{(k)} - \vec{n} \times \vec{E}^{(k)} - \vec{C} \right|^2 \tag{G.1}$$

called the *Faraday residue*. The last parameter, $\vec{n}$, is subject to the constraint that $|\vec{n}|^2 = 1$.

The first parameter is obtained from the condition $\nabla_{\vec{C}} I_F = 0$ and brings the solution

$$\vec{C} = \left\langle u_n \vec{B} - \vec{n} \times \vec{E} \right\rangle \tag{G.2}$$

where here and in what follows, by $\langle \cdots \rangle$ we indicate the average of a given quantity over the set of K points of measurements, i.e. $(\sum_{k=1}^{K} \cdots)/K$. When the value (G.2) for $\vec{C}$ is substituted in (G.1), the result we obtain can be expressed in the following way

$$I_F(u_n, \vec{n}) = \left\langle |\delta \vec{E}_{\perp}{}'|^2 \right\rangle + u_n^2 \left\langle (\vec{n} \cdot \delta \vec{B})^2 \right\rangle \tag{G.3}$$

Here and below, the symbol δ denotes the fluctuation of a given quantity from its mean value, i.e. $\delta \vec{B}^{(k)} = \vec{B}^{(k)} - \langle \vec{B} \rangle$. The quantity $\vec{E}\,' = \vec{E} + u_n \vec{n} \times \vec{B}$ represents the electric field as measured in the reference frame moving with the discontinuity, i.e. at velocity $u_n \vec{n}$. The subscript $\perp$ indicate the tangential (i.e. to the discontinuity) component of a vector. From (G.3) we see that in the MFR method the parameters u_n and $\vec{n}$ are found by minimizing the variance of the tangent electric field, in the reference frame of the discontinuity, plus u_n^2 times the variance of the normal magnetic component $B_n = \vec{n} \cdot \vec{B}$. This interpretation of the Faraday residue was used in Subsection 4.3.2 when we discussed how sensitive the planar MFR technique is, when applied to a 2-D, non-planar structure.

The analysis go further by minimizing the expression of I_F from (G.3) with respect to u_n and $\vec{n}$. All the details of the calculation are presented in the paper from *Khrabrov and Sonnerup* [1998]; here we only repeat from that paper the practical steps to be followed in order to obtain the parameters that provide the orientation and the boundary normal velocity.

1. The average values of the electric $\left\langle \vec{E} \right\rangle$ and magnetic $\left\langle \vec{B} \right\rangle$ fields are computed
2. The electric field variance matrix M^E is constructed

   $$M_{ij}^E = \left\langle \big(E_i - \langle E_i \rangle\big)\big(E_j - \langle E_j \rangle\big) \right\rangle$$

3. The electric and magnetic variances are formed

   $$\left\langle \left|\delta \vec{B}\right|^2 \right\rangle = \left\langle \left|\vec{B} - \langle \vec{B} \rangle\right|^2 \right\rangle \qquad \left\langle \left|\delta \vec{E}\right|^2 \right\rangle = \left\langle \left|\vec{E} - \langle \vec{E} \rangle\right|^2 \right\rangle$$

4. The Poynting vector, associated with the electromagnetic disturbance from the mean field is calculated

   $$\vec{P} = \left\langle \delta \vec{E} \times \delta \vec{B} \right\rangle$$

5. The following matrix is formed:

   $$Q_{ij} = \left\langle \left|\delta \vec{E}\right|^2 \right\rangle \delta_{ij} - M_{ij}^E - \frac{P_i P_j}{\left\langle \left|\delta \vec{B}\right|^2 \right\rangle}$$

   with δ_{ij} designating the Kronecker symbol
6. The direction of $\vec{n}$ is given by the eigenvector (say, $\vec{x}_3$) corresponding to the smallest eigenvalue of Q.

7. The normal velocity is given by

$$u_n = \frac{\vec{P} \cdot \vec{x}_3}{\left\langle \left| \delta \vec{B} \right|^2 \right\rangle}$$

Like in case of the constrained MVAB technique (see Appendix A), sometimes it is desirable to determine the normal vector $\vec{n}$ with the additional constraint that its direction is perpendicular to a known unit vector $\vec{m}$. Such a condition can be easily implemented if on step 5 we replace the matrix Q by the matrix product PQP, where P represents the so-called projection matrix, having the elements given by

$$P_{ij} = \delta_{ij} - m_i m_j$$

(see for example *Sonnerup et al.* [2006]).

APPENDIX H

Computing the ion single - fluid moments

The present appendix presents the procedure we followed in order to obtain the centre of mass (COM) moments for the ion fluid, in case when a minor ion species is present. Two situations are analyzed: first, when only CODIF measurements corresponding to the protons and the secondary component are employed and second, when HIA measurements together with CODIF data referring to the minor ion species are used. In treating the above mentioned topic we rely on the work of *Paschmann et al.* [1986], their Appendix 2, where the scaffold of the subsequent argumentation is presented.

Below we assume that the ion population consists of two species, protons (having the mass m_p) and another singly charged ions (with the mass m_i). The parameters characterizing each component are the number density N_p, respectively N_i, bulk velocity $\vec{V_p}$ and $\vec{V_i}$ and total pressure tensors (the sum of the thermal and dynamical parts) $\mathcal{P}_p$ and $\mathcal{P}_i$. The ions single - fluid quantities are:

- number density

$$N = N_p + N_i \tag{H.1}$$

- mass density

$$\rho = \rho_p + \rho_i \tag{H.2}$$

- bulk velocity

$$\vec{V} = \frac{m_p N_p \vec{V_p} + m_i N_i \vec{V_i}}{m_p N_p + m_i N_i} \tag{H.3}$$

- total pressure tensor or momentum flux density tensor

$$\mathcal{P} = \mathcal{P}_p + \mathcal{P}_i \tag{H.4}$$

leading to the following expression for the components of the thermal pressure tensor

$$P^{xy} = \mathcal{P}_p^{xy} + \mathcal{P}_i^{xy} - \rho V^x V^y \tag{H.5}$$

Using CODIF protons and minor species moments
In this case we have access to the following experimentally determined quantities: N_p, $\vec{V}_p$, $\mathcal{P}_p$ (protons) and N_i, $\vec{V}_i$, $\mathcal{P}_i$ (ions). Consequently, we apply directly the equations (H.1) - (H.5).

One should say that, although this way of computing the ion single - fluid moments is more straightforward, in the MP context we often encounter the situation when the CODIF sensor is saturated (see the discussions in Section 2.2). Therefore, in those cases we expect HIA to provide more reliable plasma moments and the results from the next paragraph apply.

Using HIA moments and CODIF moments corresponding to the minor specie
Consider an energy/charge sensor that cannot discriminate between species, when a particle of type i having the velocity (magnitude) V_i enters its entrance aperture. Then, to its velocity the value $\sqrt{m_i/m_p}\,V_i$ is wrongly assigned because the event is attributed to a proton.

In case of a Top Hat analyser (*Carlson et al.* [1982]), like HIA, the various plasma moments are obtained by the on-board software by proper summations over the elements of the count rates matrix, recorded during one spin or multiples of spin periods. For example the number density will be proportional to the sum

$$N \;\sim\; \sum_l \frac{1}{V(E_l)} \sum_m \sum_n C(E_l,\phi_m,\theta_n) = \sqrt{m} \sum_l \frac{1}{\sqrt{E_l}} \sum_m \sum_n C(E_l,\phi_m,\theta_n) \tag{H.6}$$

(see *Fazakerley et al.* [1998] and *Paschmann et al.* [1998] for the derivation of this and next similar expressions). In this formula $C(E_l,\phi_m,\theta_n)$ designates an element of the count rates matrix corresponding to the measurement made by the detector along the direction in space identified by the angles ϕ_m and θ_n, in the energy channel E_l. We indicated by m the mass of the particles being detected and with V the magnitude of their velocity; the constant of proportionality involves only the detector geometry factor and constants for the volume integration.

When the sensor samples a mixture of protons and particles of type i, the registered count rates will be the sum of the individual count rates

$$C(E_l,\phi_m,\theta_n) = C_p(E_l,\phi_m,\theta_n) + C_i(E_l,\phi_m,\theta_n)$$

and the number density reported by the detector will be

$$N' \;\sim\; \sqrt{m_p} \sum_l \frac{1}{\sqrt{E_l}} \sum_m \sum_n \left[C_p(E_l,\phi_m,\theta_n) + C_i(E_l,\phi_m,\theta_n)\right] \tag{H.7}$$

because all events are considered as being produced by the protons. (H.7) can be written as

$$N' \;\sim\; \left(\sqrt{m_p} \sum_l \frac{1}{\sqrt{E_l}} \sum_m \sum_n C_p(E_l,\phi_m,\theta_n)\right) + \frac{1}{\gamma}\left(\sqrt{m_i} \sum_l \frac{1}{\sqrt{E_l}} \sum_m \sum_n C_i(E_l,\phi_m,\theta_n)\right)$$

with $\gamma = \sqrt{m_i/m_p}$. In the above expression, the terms in parenthesis are proportional (with the same factor as in (H.6)) to the real N_p and N_i, i. e. the protons and particles i number densities detected if the instrument could have correctly identified each specie. Therefore we arrived at the formula

$$N' = N_p + \frac{1}{\gamma} N_i \tag{H.8}$$

and the ion mass density estimate by HIA will be

$$\rho^{'} = m_p N^{'} = \rho_p + \frac{1}{\gamma^3}\rho_i \tag{H.9}$$

In determining the ions bulk velocity from the measurements of a Top Hat analyser, one first computes the number flux density vector $N\vec{V}$ and then divides the result by N given by (H.6). The formula that gives the x component of the number flux density vector is based on

$$NV_x \sim \sum_l \sum_m \cos\phi_m \sum_n \cos\theta_n C(E_l, \phi_m, \theta_n) \tag{H.10}$$

the expressions for the other two components having the same structure. Considering again the situation when the instrument is sampling an ion mixture, we arrive at the conclusion that this quantity will be correctly computed, even if the detector is not able to differentiate between species, the reason for that being the independence of (H.10) from the particles mass. However, the computed bulk velocity will be wrong, namely

$$\vec{V}^{'} = \frac{N_p\vec{V}_p + N_i\vec{V}_i}{N^{'}} \tag{H.11}$$

which is different from (H.3).

The momentum flux density tensor, i. e. the quantity defined as

$$\mathcal{P} = \int f(\vec{v})\,\vec{v}\,\vec{v}\,d^3v$$

with $f(\vec{v})$ being the velocity distribution function, is computed for an HIA type instrument by the use of the formula

$$\begin{aligned}\mathcal{P}^{\,xy} &\sim m\sum_l V(E_l)\sum_m \cos^2\phi_m \sum_n \cos^2\theta_n C(E_l, \phi_m, \theta_n) \\ &\sim \sqrt{m}\sum_l \sqrt{E_l}\sum_m \cos^2\phi_m \sum_n \cos^2\theta_n C(E_l, \phi_m, \theta_n)\end{aligned} \tag{H.12}$$

and the analogous ones, with the same structure, for the other components. Expression (H.12) is similar to (H.6) as far as the mass dependence is concerned and by applying the same arguments we arrive at the following relation for the components of the HIA estimated momentum flux density tensor, when the instruments measures a mixture of ions

$$\mathcal{P}^{'\,xy} = \mathcal{P}_p^{\,xy} + \frac{1}{\gamma}\,\mathcal{P}_i^{\,xy} \tag{H.13}$$

with the accompanying relation for the estimated components of the thermal pressure tensor

$$P^{'\,xy} = \mathcal{P}_p^{\,xy} + \frac{1}{\gamma}\,\mathcal{P}_i^{\,xy} - m_p N^{'}\vec{V}^{'x}V^{'y} \tag{H.14}$$

In case when the HIA (contaminated) moments together with the CODIF moments corresponding to the minor specie i are available, we have access to the following parameters, which are sent to the ground by the CIS/Cluster instrument: $N^{'}$, $\vec{V}^{'}$, $\mathcal{P}^{'}$ (HIA) and N_i, $\vec{V}_i$,

$\mathcal{P}_i$ (CODIF). In order to apply the formulas (H.1) - (H.5), that supply the needed ion single-fluid moments, we express the proton moments as a function of the experimentally determined quantities. The equations are:

$$\begin{aligned} N_p &= N^{'} - \frac{1}{\gamma} N_i \\ \rho_p &= m_p \left(N^{'} - \frac{1}{\gamma} N_i \right) \\ \vec{V_p} &= \frac{N^{'} \vec{V}^{'} - N_i \vec{V_i}}{N_p} \\ \mathcal{P}_p{}^{xy} &= \mathcal{P}^{'\,xy} - \frac{1}{\gamma} \mathcal{P}_i{}^{xy} \\ P_p{}^{xy} &= \mathcal{P}_p{}^{xy} - \rho_p V_p^x V_p^y \end{aligned} \tag{H.15}$$

Bibliography

Alfvén, H., and C. G. Fälthammar, *Cosmical electrodynamics*, Clarendon, Oxford, 1963.

Balogh, A., et al., The Cluster Magnetic Field Investigation, *Space Science Reviews*, *79*, 65, 1997.

Bauer, T. M., Particls and Fields at the Dayside Low-latitude Magnetopause, Ph.D. thesis, Max-Planck-Institut für extraterrestrische Physik, Garching, Germany, 1997.

Baumjohann, W., and R. A. Treumann, *Basic space plasma physics*, London: Imperial College Press, 1996.

Berchem, J., and C. T. Russell, Magnetic field rotation through the magnetopause - ISEE 1 and 2 observations, *Journal of Geophysical Research*, *87*, 8139, 1982a.

Berchem, J., and C. T. Russell, The thickness of the magnetopause current layer - ISEE 1 and 2 observations, *Journal of Geophysical Research*, *87*, 2108, 1982b.

Biernat, H. K., M. F. Heyn, R. P. Rijnbeek, V. Semenov, and C. J. Farrugia, The structure of reconnection layers - Application to the earth's magnetopause, *Journal of Geophysical Research*, *94*, 287, 1989.

Cahill, L. J., and P. G. Amazeen, The Boundary of the Geomagnetic Field, *Journal of Geophysical Research*, *68*, 1835, 1963.

Cahill, L. J., Jr., and V. L. Patel, The boundary of the geomagnetic field, August to November, 1961, *Planetary and Space Science*, *15*, 997, 1967.

Carlson, C. W., D. W. Curtis, G. Paschmann, and W. Michel, An instrument for rapidly measuring plasma distribution functions with high resolution, *Advances in Space Research*, *2*, 67, 1982.

Chandrasekhar, S., *Hydrodynamic and hydromagnetic stability*, International Series of Monographs on Physics, Clarendon, Oxford, 1961.

Chapman, S., and T. Cowling, *The Mathematical Theory of Non-Uniform Gases*, Cambridge University Press, Cambridge, 1939.

Chapman, S., and V. C. A. Ferraro, A new theory of magnetic storms, Part I, The initial phase, *Terrestrial Magnetism and Atmospheric Electricity*, *36*, 171, 1931.

Clemmow, P. C., and J. P. Dougherty, *Electrodynamics of Particles and Plasmas*, Addison-Wesley Publishing Company, 1969.

Cowley, S. W. H., The causes of convection in the earth's magnetosphere - A review of developments during the IMS, *Reviews of Geophysics and Space Physics*, *20*, 531, 1982.

deHoffmann, F., and E. Teller, Magneto-Hydrodynamic Shocks, *Physical Review*, *80*, 692, 1950.

Dungey, J. W., Interplanetary Magnetic Field and the Auroral Zones, *Physical Review Letters*, *6*, 47, 1961.

Dunlop, M. W., and T. I. Woodward, Multi-spacecraft discontinuity analysis: Orientation and motion, in *Analysis Methods for Multi-Spacecraft Data*, edited by G. Paschmann and P. W. Daly, ISSI Scientific Reports, p. 271, ESA Publications Division, 1998.

Dunlop, M. W., and T. I. Woodward, Analysis of thick, non-planar boundaries using the discontinuity analyser, *Annales Geophysicae*, *17*, 984, 1999.

Dunlop, M. W., A. Balogh, P. Cargill, R. C. Elphic, K.-H. Fornaçon, E. Georgescu, F. Sedgemore-Schulthess, and The Fgm Team, Cluster observes the Earth's magnetopause: coordinated four-point magnetic field measurements, *Annales Geophysicae*, *19*, 1449, 2001.

Dunlop, M. W., A. Balogh, and K.-H. Glassmeier, Four-point Cluster application of magnetic field analysis tools: The discontinuity analyzer, *Journal of Geophysical Research (Space Physics)*, *107*, 24, 2002a.

Dunlop, M. W., A. Balogh, K.-H. Glassmeier, and P. Robert, Four-point Cluster application of magnetic field analysis tools: The Curlometer, *Journal of Geophysical Research (Space Physics)*, *107*, 23, 2002b.

Eastman, T. E., E. W. Hones, Jr., S. J. Bame, and J. R. Asbridge, The magnetospheric boundary layer - Site of plasma, momentum and energy transfer from the magnetosheath into the magnetosphere, *Geophysical Research Letters*, *3*, 685, 1976.

Escoubet, C. P., M. Fehringer, and M. Goldstein, The Cluster mission, *Annales Geophysicae*, *19*, 1197, 2001.

Fairfield, D. H., Observations of the Shape and Location of the Magnetopause: A Review, in *Physics of the Magnetopause*, edited by P. Song, B. U. Ö. Sonnerup, and M. F. Thomsen, vol. 90 of *Geophysical Monograph*, p. 53, American Geophysical Union, Washington, USA, 1995.

Fazakerley, A. N., S. J. Schwartz, and G. Paschmann, Measurement of plasma velocity distributions, in *Analysis Methods for Multi-Spacecraft Data*, edited by G. Paschmann and P. W. Daly, ISSI Scientific Reports, p. 91, ESA Publications Division, 1998.

Fuselier, S. A., Kinetic Aspects of Reconnection at the Magnetopause, in *Physics of the Magnetopause*, edited by P. Song, B. U. Ö. Sonnerup, and M. F. Thomsen, vol. 90 of *Geophysical Monograph*, p. 181, American Geophysical Union, Washington, USA, 1995.

Giovanelli, R. G., A theory of chromospheric flares, *Nature*, *158*, 81, 1946.

Goldston, R. J., and P. H. Rutherford, *Introduction to plasma physics*, Institute of Physics Press, Bristol, 1995.

Gustafsson, G., et al., First results of electric field and density observations by Cluster EFW based on initial months of operation, *Annales Geophysicae*, *19*, 1219, 2001.

Haaland, S., B. U. Ö. Sonnerup, M. W. Dunlop, E. Georgescu, G. Paschmann, B. Klecker, and A. Vaivads, Orientation and motion of a discontinuity from Cluster curlometer capability: Minimum variance of current density, *Geophysical Research Letters*, *31*, 10,804, 2004a.

Haaland, S., G. Paschmann, and B. U. Ö. Sonnerup, Comment on "A new interpretation of Weimer et al.'s solar wind propagation delay technique" by Bargatze et al., *Journal of Geophysical Research (Space Physics)*, *111*, 6102, 2006.

Haaland, S., et al., Four-spacecraft determination of magnetopause orientation, motion and thickness: comparison with results from single-spacecraft methods, *Annales Geophysicae*, *22*, 1347, 2004b.

Haerendel, G., Reconnection, in *The century of space science*, edited by J. A. M. Bleeker, J. Geiss, and A. Huber; history consultant, M. C. E. Russo, p. 1007, Kluwer Academic Publishers, Dordrecht, 2001.

Haerendel, G., and G. Paschmann, Entry of Solar Wind Plasma into the Magnetosphere, in *Physics of the Hot Plasma in the Magnetosphere*, edited by B. Hultqvist and L. Stenflo, p. 23, Plenum Press, New York, 1975.

Hasegawa, H., M. Fujimoto, T.-D. Phan, H. Rème, A. Balogh, M. W. Dunlop, C. Hashimoto, and R. TanDokoro, Transport of solar wind into Earth's magnetosphere through rolled-up Kelvin-Helmholtz vortices, *Nature*, *430*, 755, 2004.

Hasegawa, H., B. U. Ö. Sonnerup, B. Klecker, G. Paschmann, M. W. Dunlop, and H. Rème, Optimal reconstruction of magnetopause structures from Cluster data, *Annales Geophysicae*, *23*, 973, 2005.

Hill, T. W., Solar-wind magnetosphere coupling., in *Solar-terrestrial physics. Principles and theoretical foundations*, edited by R. L. Carovillano and J. M. Forbes, p. 261, 1983.

Hudson, P. D., Discontinuities in an anisotropic plasma and their identification in the solar wind, *Planetary and Space Science*, *18*, 1611, 1970.

Kawano, H., and T. Higuchi, A generalization of the minimum variance analysis method, *Annales Geophysicae*, *14*, 1019, 1996.

Kertz, W., *Einführung in die Geophysik. Band 2: Obere Atmosphäre und Magnetosphäre*, vol. 535 of *Hochschultaschenbücher*, Bibliographisches Institut, Mannheim, 1971.

Khrabrov, A., and B. U. Ö. Sonnerup, deHoffmann-Teller analysis, in *Analysis Methods for Multi-Spacecraft Data*, edited by G. Paschmann and P. W. Daly, ISSI Scientific Reports, p. 223, ESA Publications Division, 1998.

Khrabrov, A. V., and B. U. Ö. Sonnerup, Orientation and motion of current layers: Minimization of the Faraday residue, *Geophysical Research Letters*, *25*, 2373, 1998.

Kistler, L. M., TOF peak analysis, mass threshold and "spillover"determination, version 2.0, in *Cluster CODIF Calibration Report*, 2000.

Kivelson, M. G., and C. T. Russell, *Introduction to space physics*, Cambridge University Press, 1995.

Klumpar, D. M., et al., The Time-of-Flight Energy, Angle, Mass Spectrograph (Teams) Experiment for Fast, *Space Science Reviews*, *98*, 197, 2001.

Landau, L. D., and E. M. Lifshitz, *Electrodynamics of continuous media*, Course of theoretical physics, Pergamon Press, Oxford, 1960.

Lemaire, J., and M. Roth, Penetration of solar wind plasma elements into the magnetopause., *Journal of Atmospheric and Terrestrial Physics*, *40*, 331, 1978.

Levy, R. H., H. E. Petschek, and G. L. Siscoe, Aerodynamic aspects of the magnetospheric flow, *AIAA Journal*, *2*, 2065, 1964.

Longmire, C. L., *Elementary plasma physics*, Interscience, New York, 1963.

Lundin, R., Observational and Theoretical Aspects of Processes Other Than Merging and Diffusion Governing Plasma Transport Across The Magnetopause, *Space Science Reviews*, *80*, 269, 1997.

Lundin, R., et al., Evidence for impulsive solar wind plasma penetration through the dayside magnetopause, *Annales Geophysicae*, *21*, 457, 2003.

Marcucci, M. F., et al., Energetic magnetospheric oxygen in the magnetosheath and its response to IMF orientation: Cluster observations, *Journal of Geophysical Research (Space Physics)*, *109*, 7203, 2004.

Morse, P. M., and H. Feshbach, *Methods of Theoretical Physics*, McGraw-Hill, New York, 1953.

Mottez, F., and G. Chanteur, Surface crossing by a group of satellites: A theoretical study, *Journal of Geophysical Research*, *99*, 13,499, 1994.

Mozer, F. S., S. D. Bale, and T. D. Phan, Evidence of Diffusion Regions at a Subsolar Magnetopause Crossing, *Physical Review Letters*, *89*, 015,002, 2002.

Ogilvie, K. W., and R. J. Fitzenreiter, The Kelvin-Helmholtz instability at the magnetopause and inner boundary layer surface, *Journal of Geophysical Research*, *94*, 15,113, 1989.

Parks, G. K., *Physics of space plasmas: an introduction*, Westview Press, Advanced Book Program, 2004.

Paschmann, G., Comment on 'Electric field measurements at the magnetopause. I - Observation of large convective velocities at rotational magnetopause discontinuities' by T. L. Aggson, P. J. Gambardella, and N. C. Maynard, *Journal of Geophysical Research*, *90*, 7629, 1985.

Paschmann, G., Observational Evidence for Transfer of Plasma Across the Magnetopause, *Space Science Reviews*, *80*, 217, 1997.

Paschmann, G., Space Physics: Breaking through the lines, *Nature*, *439*, 144, 2006.

Paschmann, G., G. Haerendel, N. Sckopke, H. Rosenbauer, and P. C. Hedgecock, Plasma and magnetic field characteristics of the distant polar cusp near local noon - The entry layer, *Journal of Geophysical Research*, *81*, 2883, 1976.

Paschmann, G., B. U. Ö. Sonnerup, I. Papamastorakis, N. Sckopke, and G. Haerendel, Plasma acceleration at the Earth's magnetopause: evidence for reconnection, *Nature*, *282*, 243, 1979.

Paschmann, G., W. Baumjohann, N. Sckopke, I. Papamastorakis, and C. W. Carlson, The magnetopause for large magnetic shear - AMPTE/IRM observations, *Journal of Geophysical Research*, *91*, 11,099, 1986.

Paschmann, G., W. Baumjohann, N. Sckopke, T.-D. Phan, and H. Luehr, Structure of the dayside magnetopause for low magnetic shear, *Journal of Geophysical Research*, *98*, 13,409, 1993.

Paschmann, G., A. N. Fazakerley, and S. J. Schwartz, Moments of plasma velocity distributions, in *Analysis Methods for Multi-Spacecraft Data*, edited by G. Paschmann and P. W. Daly, ISSI Scientific Reports, p. 125, ESA Publications Division, 1998.

Paschmann, G., S. Haaland, B. U. Ö. Sonnerup, H. Hasegawa, E. Georgescu, B. Klecker, T. D. Phan, H. Rème, and A. Vaivads, Characteristics of the near-tail dawn magnetopause and boundary layer, *Annales Geophysicae*, *23*, 1481, 2005a.

Paschmann, G., S. J. Schwartz, C. P. Escoubet, and S. Haaland (Eds.), *Outer Magnetospheric Boundaries: Cluster Results*, chap. 8 and 10, Space Sciences Series of ISSI, Springer, 2005b.

Petschek, H. E., Magnetic field annihilation, in *AAS-NASA Symposium on the Physics of Solar Flares*, vol. SP-50 of *NASA Spec. Publ.*, p. 425, 1964.

Phan, T., et al., Cluster observations of continuous reconnection at the magnetopause under steady interplanetary magnetic field conditions, *Annales Geophysicae*, *22*, 2355, 2004.

Phan, T. D., and G. Paschmann, Low-latitude dayside magnetopause and boundary layer for high magnetic shear 1. Structure and motion, *Journal of Geophysical Research*, *101*, 7801, 1996.

Phan, T.-D., G. Paschmann, W. Baumjohann, N. Sckopke, and H. Luehr, The magnetosheath region adjacent to the dayside magnetopause: AMPTE/IRM observations, *Journal of Geophysical Research*, *99*, 121, 1994.

Phan, T.-D., G. Paschmann, and B. U. Ö. Sonnerup, Low-latitude dayside magnetopause and boundary layer for high magnetic shear 2. Occurrence of magnetic reconnection, *Journal of Geophysical Research*, *101*, 7817, 1996.

Puhl-Quinn, P. A., and J. D. Scudder, Systematics of ion Walén analysis of rotational discontinuities using E/Z measurements, *Journal of Geophysical Research*, *105*, 7617, 2000.

Rème, H., et al., First multispacecraft ion measurements in and near the Earth's magnetosphere with the identical Cluster ion spectrometry (CIS) experiment, *Annales Geophysicae*, *19*, 1303, 2001.

Roelof, E. C., and D. G. Sibeck, Magnetopause shape as a bivariate function of interplanetary magnetic field B_z and solar wind dynamic pressure, *Journal of Geophysical Research*, *98*, 21,421, 1993.

Rosenbauer, H., H. Gruenwaldt, M. D. Montgomery, G. Paschmann, and N. Sckopke, Heos 2 plasma observations in the distant polar magnetosphere - The plasma mantle, *Journal of Geophysical Research*, *80*, 2723, 1975.

Rossi, B., and S. Olbert, *Introduction to the physics of space*, McGraw-Hill, New York, 1970.

Russell, C. T., The Structure of the Magnetopause, in *Physics of the Magnetopause*, edited by P. Song, B. U. Ö. Sonnerup, and M. F. Thomsen, vol. 90 of *Geophysical Monograph*, p. 81, American Geophysical Union, Washington, USA, 1995.

Russell, C. T., M. M. Mellott, E. J. Smith, and J. H. King, Multiple spacecraft observations of interplanetary shocks Four spacecraft determination of shock normals, *Journal of Geophysical Research*, *88*, 4739, 1983.

Scholer, M., Magnetic Reconnection on the Sun and in the Earth's Magnetosphere, in *Energy Conversion and Particle Acceleration in the Solar Corona*, edited by L. Klein, vol. 612 of *Lecture Notes in Physics, Berlin Springer Verlag*, p. 9, 2003.

Scholer, M., and R. A. Treumann, The Low-Latitude Boundary Layer at the Flanks of the Magnetopause, *Space Science Reviews*, *80*, 341, 1997.

Scholer, M., D. Hovestadt, B. Klecker, F. M. Ipavich, and G. Gloeckler, Leakage of magnetospheric ions into the magnetosheath along reconnected field lines at the dayside magnetopause, *Journal of Geophysical Research*, *86*, 1299, 1981.

Scudder, J. D., P. A. Puhl-Quinn, F. S. Mozer, K. W. Ogilvie, and C. T. Russell, Generalized Walén tests through Alfvén waves and rotational discontinuities using electron flow velocities, *Journal of Geophysical Research*, *104*, 19,817, 1999.

Seon, J., L. A. Frank, A. J. Lazarus, and R. P. Lepping, Surface waves on the tailward flanks of the Earth's magnetopause, *Journal of Geophysical Research*, *100*, 11,907, 1995.

Sibeck, D. G., et al., Plasma Transfer Processes at the Magnetopause, Chapter 5, *Space Science Reviews*, *88*, 207, 1999.

Snare, R. C., A History of Vector Magnetometry in Space, in *Measurement Techniques in Space Plasmas – Fields*, edited by R. F. Pfaff, J. E. Borovsky, and D. T. Young, p. 101, 1998.

Sommerfeld, A., *Electrodynamics*, Academic Press, New York, 1964a.

Sommerfeld, A., *Mechanics of deformable bodies*, Academic Press, New York, 1964b.

Song, P., and C. T. Russell, Model of the formation of the low-latitude boundary layer for strongly northward interplanetary magnetic field, *Journal of Geophysical Research*, *97*, 1411, 1992.

Sonnerup, B. U. O., and L. J. Cahill, Jr., Magnetopause Structure and Attitude from Explorer 12 Observations, *Journal of Geophysical Research*, *72*, 171, 1967.

Sonnerup, B. U. Ö., and L. J. Cahill, Jr., Explorer 12 Observations of the Magnetopause Current Layer, *Journal of Geophysical Research*, *73*, 1757, 1968.

Sonnerup, B. U. Ö., and M. Guo, Magnetopause transects, *Geophysical Research Letters*, *23*, 3679, 1996.

Sonnerup, B. U. Ö., and M. Scheible, Minimum and maximum variance analysis, in *Analysis Methods for Multi-Spacecraft Data*, edited by G. Paschmann and P. W. Daly, ISSI Scientific Reports, p. 185, ESA Publications Division, 1998.

Sonnerup, B. U. O., G. Paschmann, I. Papamastorakis, N. Sckopke, G. Haerendel, S. J. Bame, J. R. Asbridge, J. T. Gosling, and C. T. Russell, Evidence for magnetic field reconnection at the earth's magnetopause, *Journal of Geophysical Research*, *86*, 10,049, 1981.

Sonnerup, B. U. O., I. Papamastorakis, G. Paschmann, and H. Luehr, Magnetopause properties from AMPTE/IRM observations of the convection electric field - Method development, *Journal of Geophysical Research*, *92*, 12,137, 1987.

Sonnerup, B. U. O., I. Papamastorakis, G. Paschmann, and H. Luehr, The magnetopause for large magnetic shear - Analysis of convection electric fields from AMPTE/IRM, *Journal of Geophysical Research*, *95*, 10,541, 1990.

Sonnerup, B. U. Ö., G. Paschmann, and T.-D. Phan, Fluid Aspects of Reconnection at the Magnetopause: In Situ Observations, in *Physics of the Magnetopause*, edited by P. Song, B. U. Ö. Sonnerup, and M. F. Thomsen, vol. 90 of *Geophysical Monograph*, p. 167, American Geophysical Union, Washington, USA, 1995.

Sonnerup, B. U. Ö., S. Haaland, G. Paschmann, M. W. Dunlop, H. Rème, and A. Balogh, Orientation and motion of a plasma discontinuity from single-spacecraft measurements: Generic residue analysis of Cluster data, *Journal of Geophysical Research (Space Physics)*, *111*, 5203, 2006.

Stern, D. P., A brief history of magnetospheric physics before the spaceflight era, *Reviews of Geophysics*, *27*, 103, 1989.

Stern, D. P., Modeling the Field of the Global Magnetopause, in *Physics of the Magnetopause*, edited by P. Song, B. U. Ö. Sonnerup, and M. F. Thomsen, vol. 90 of *Geophysical Monograph*, p. 45, American Geophysical Union, Washington, USA, 1995.

Stern, D. P., A brief history of magnetospheric physics during the space age, *Reviews of Geophysics*, *34*, 1, 1996.

Terasawa, T., et al., On the Determination of a Moving MHD Structure: Minimization of the Residue of Integrated Faraday's Equation, *Journal of Geomagnetism and Geoelectricity*, *48*, 603, 1996.

Treumann, R. A., and W. Baumjohann, Particle trapping at a tangential discontinuity: Multiple incidence, *Planetary and Space Science*, *36*, 1477, 1988.

Treumann, R. A., and W. Baumjohann, *Advanced space plasma physics*, London: Imperial College Press, 1997.

Treumann, R. A., and M. Scholer, The magnetosphere as a plasma laboratory, in *The century of space science*, edited by J. A. M. Bleeker, J. Geiss, and A. Huber; history consultant, M. C. E. Russo, p. 1495, Kluwer Academic Publishers, Dordrecht, 2001.

Treumann, R. A., J. Labelle, and T. M. Bauer, Diffusion Processes: An Observational Perspective, in *Physics of the Magnetopause*, edited by P. Song, B. U. Ö. Sonnerup, and M. F.

Thomsen, vol. 90 of *Geophysical Monograph*, p. 331, American Geophysical Union, Washington, USA, 1995.

Vaivads, A., Y. Khotyaintsev, M. André, A. Retinò, S. C. Buchert, B. N. Rogers, P. Décréau, G. Paschmann, and T. D. Phan, Structure of the Magnetic Reconnection Diffusion Region from Four-Spacecraft Observations, *Physical Review Letters*, *93*, 10,500, 2004.

Vasyliunas, V. M., Theoretical models of magnetic field line merging. I, *Reviews of Geophysics and Space Physics*, *13*, 303, 1975.

Vasyliunas, V. M., Interaction between the magnetospheric boundary layers and the ionosphere, in *Magnetospheric Boundary Layers*, edited by J. Lemaire, vol. 148 of *ESA Special Publication*, p. 387, 1979.

Weimer, D. R., D. M. Ober, N. C. Maynard, W. J. Burke, M. R. Collier, D. J. McComas, N. F. Ness, and C. W. Smith, Variable time delays in the propagation of the interplanetary magnetic field, *Journal of Geophysical Research (Space Physics)*, *107*, 29, 2002.

Yang, C.-K., and B. U. Ö. Sonnerup, Compressible magnetic field rreconnection: A slow wave model, *The Astrophysical Journal*, *206*, 570, 1976.

Yang, C.-K., and B. U. Ö. Sonnerup, Compressible magnetopause reconnection, *Journal of Geophysical Research*, *82*, 699, 1977.

Credits

In the present work we used extensively various software tools, either directly or as a basis to construct our own routines. We list them here, together with the corresponding teams or individuals who put effort in developing or maintaining these packages:

- to analyse CIS data we used mainly the CCAT software package which is based on TPLOT graphics package developed by Davin Larson from Space Sciences Laboratory (SSL) at Berkeley. The CIS routines for CCAT are developed and maintained by Doctors Chris Mouikis (University of New Hampshire), Markus Fränz (Max-Planck-Institut für Sonnensystemforschung, Lindau), Peter Schroeder (SSL) and Jim McFadden (SSL).
- for CIS data we also used two other packages: CL and IFSI-IDL. The first one is developed and maintained by Doctors Emmanuel Penou and Alain Barthe from Centre d'Etude Spatiale des Rayonnements, Toulouse while the latter by Doctors Ermanno Amata and Giuseppe Pallocchia from Istituto di Fisica dello Spazio Interplanetario, Rome
- The QSAS software package, provided by the United Kingdom Cluster Science Centre (Imperial College London and Queen Mary, University of London). We use extensively various plug-ins developed for QSAS by Dr. Stein Haaland from MPE. He also provided us the software useful in showing the orientations of the normals (the polar-plots).
- we based our programs for testing the Walén relation on one IDL routine written by Dr. Tai Phan from SSL, Berkeley

In this thesis, for the plasma (ions) data we used the Cluster CIS data base at MPE. We would like to express gratitude to the entire CIS team, (Principal Investigators being Dr. Henri Rème and Dr. Iannis Dandouras from Centre d'Etude Spatiale des Rayonnements, Toulouse) for the effort of building and operating the instrument.

The Cluster magnetic field data and electron density data were obtained from ESA's Cluster Active Archive on-line data base. We acknowledge the efforts of the FGM instrument team (present Principal Investigator, Dr. Elizabeth Lucek from Imperial College, London) and of the WHISPER instrument team (Principal Investigator Dr. Pierrette Décréau from Laboratoire de Physique et de Chimie de l'Environnement, Orléans).

The ACE magnetic field data and solar wind parameters were obtained from the ACE Science Center on-line data base. We thank the ACE MAG and SWEPAM instrument teams.

Acknowledgements

The work on this thesis was accomplished while at Max-Planck-Institut fur extraterrestrische Physik (MPE), in Garching. I am thankful for the conditions and hospitality offered by the institute throughout the past years, when I have been fortunate to interact with dedicated scientists who have greatly influenced me.

I would like to express my deepest gratitude to Dr. Berndt Klecker for the generosity and patience he showed me the entire time I was here. Berndt Klecker was always present to answer my questions or to dissect my ideas. His rational and witty way of approaching problems made me feel 'recalibrated' during more difficult times.

I had the privilege to work with Dr. Dr. Götz Paschmann and be contaminated by his enthusiasm. During the numerous fruitfull discussions we had, I took great benefit from his vast knowledge in the field of magnetospheric physics. Certainly, without his help and his seemingly unbound energy, this thesis would not appear in its present, more readable and accurate form.

I am thankful to Prof. Dr. Manfred Scholer and Prof. Dr. Rudolf Treumann for accepting to be my advisers at the Faculty for Geosciences of Ludwig-Maximilian-University in Munich. Their expertise in the field provided valuable comments and suggestions, helping me to improve on the conveyance of ideas in the thesis.

I would like to thank Prof. Dr. Gerhard Haerendel for the confidence he showed to me, while enabling my work at MPE through a stipend of the Max Planck Society.

I am pleased to thank other associates from MPE: Dr. Stein Haaland, for the valuable discussions and useful suggestions he made on many occasions, Hans Vaith, who was always eager to provide computer- and software-related help and who helped me translate the Summary in German and Jasmin Zanker-Smith, the assistant of our group, for all her help.

I am indebted to my colleagues at the Institute for Space Sciences in Bucharest for their serious effort to build an honest and stimulating environment in which to learn and grow: Doctors Mircea Ciobanu, Octav Marghitu, Marius Echim, Horia Comişel, and Dragoş Constantinescu and the younger researchers Costel Bunescu and Gabriel Voitcu.

And last but not least, I would like to thank my trusted non-physicist friends for encouraging and making me feel confident in pursuing this path.

Lebenslauf

von

Adrian Blăgău

Geboren am 16. August 1967 in Arad, Rumänien

Eltern:

Nicolae, Professor
Iavorca, Buchhalterin

Schulbildung:

Sep. 1973 – Juni 1981	Elementarschule, Arad
Sep. 1981 – Juni 1985	Ioan Slavici Gymnasium, Arad

Wehrdienst:

Sep. 1985 – Juni 1986	Mediaş

Universitätsstudium:

Sep. 1986 – Juni 1991	Universität Bukarest, Studienfach Physik Diplomarbeit: Bildverarbeitung – allgemeine Grundregeln und Anwendungen
Sep. 2002 – Juni 2005	Promotionsstudium an der Fakultät für Geophysik der Ludwig-Maximilians-Universität München

Anstellungen:

Nov. 1992 – Aug. 1993	Forschungsassistent, Institut für Kernphysik und Kerntechnik, Bukarest
Aug. 1993 – Apr. 1998	Forschungsassistent, Institut für Weltraumwissenschaften, Bukarest
Apr. 1998 –	Wissenschaftler, Institut für Weltraumwissenschaften, Bukarest

Stipendien:

September 1995	IPP Summer University for Plasma Physics, Garching
März 1997	Installation von FAST Software am MPE
Juli 2002	Sommerschule Alpbach "Space Weather - Physics, Impacts and Predictions"
März 2002 – Jan 2007	Mehrere Promotionsstipendien für Ausländer am MPE: Untersuchung der Erdmagnetopause mit Hilfe von Cluster Daten